Cranfield UNIVERSITY

Martin Berckmüller

"A Study of Mixture Formation in a Lean Burn Research Engine using Laser Fluorescence Imaging"

School of Mechanical Engineering

Ph.D. Thesis

Cranfield UNIVERSITY

School of Mechanical Engineering

Ph.D. Thesis
1996

Martin Berckmüller

"A Study of Mixture Formation in a Lean Burn Research Engine using Laser Fluorescence Imaging"

Supervisor: Prof. D. A. Greenhalgh

May 1996

This thesis is submitted in partial fulfilment of the requirements for the degree of Doctor of Philosophy.

This work has been supported by Honda R&D Co. Ltd. of Japan.

Abstract

Lean burn in spark-ignition engines offers a significant efficiency advantage compared with stoichiometric operation. The lean operation is restricted by increasing cyclic fluctuation in torque. In order to make use of the efficiency advantage and meet the mandatory emission standards the lean operation limit has to be further extended. This requires particular control of the mixing of fuel and air.

To study the effect of mixture formation on cyclic variability and to provide quantitative information on the mixing of air and fuel planar laser-induced fluorescence (PLIF) was developed and applied to an operating SI engine. The method is based on imaging the fluorescence of a fluorescent marker (3-pentanone) mixed with the fuel (iso-octane). 3-pentanone was found to have similar vaporisation characteristics to those of iso-octane as well as low absorption and suitable spectral properties.

The technique was applied to an one-cylinder SI engine with a cylinder head configuration based on the Honda VTEC-E lean burn system. The mixture formation process during the inlet and compression stroke could be described by measuring the average fuel concentration in four planes, between 0.7 and 15.2 mm below the spark plug, in a section of the cylinder orthogonal to the cylinder axis. The results showed that for 4-valve pent-roof cylinder head systems with swirl inlet flows, fuel impinging on the cylinder wall opposite to the inlet valves has a major influence on the mixture formation process.

In order to quantify the cyclic variability in the mixture formation process and its contribution to cyclic variability in combustion the fuel concentration in a plane near the spark plug was measured on a large number of cycles. It could be shown, that the fuel concentration in a small region close to the spark plug has a dominating effect on the subsequent pressure development for lean mixtures. Variations in the mixture concentration in the vicinity of the spark plug contribute significantly to cyclic variations in combustion.

In order to address the issue of nonuniformity in residual gas concentration prior to ignition a laser induced fluorescence method was developed to measure nitric oxide (NO) concentrations in the unburned charge in the same one-cylinder research engine. Measurements of average and instantaneous NO concentrations revealed, that the residual gas is not homogeneously mixed with the air and that significant cyclic variations in the local residual gas concentration exist.

Contents

PART I

OVERVIEW & BACKGROUND

Chapter 1

Introduction

In this chapter the basic concept of lean burn in spark-ignition engine combustion is introduced and the challenge of utilising its potential for improved efficiency and at the same time meeting the legislated emission standards is described. First a brief review of the combustion fundamentals relevant to lean burn is given. This is followed by a literature review of the problem of cyclic variability in combustion. Current theories of the causes of cyclic variability are highlighted and areas of limited understanding are identified. An overview of current implementations of lean burn concepts in automotive engines is given. The objectives and an outline of the work of this thesis completes the chapter.

1.1 Emissions & Legislation

Automotive engines are a major source of air pollution, particular in urban areas. The spark-ignition engine exhaust gases contain mainly carbon dioxide (CO_2), water (H_2O) together with small amounts of oxides of nitrogen (NOx), carbon monoxide (CO) and unburned hydrocarbons (HC). Legislation addressed this problem as early as 1970 in the USA limiting CO and HC emissions only because of their known impact on air quality and the toxicity for the human. Later the attention focused on the NOx which forms smog by interaction with sunlight and HC. This lead to NOx emission limits which could be met with a system using exhaust gas after treatment by a 3-way catalyst in conjunction with closed loop control of the mixture strength. In recent years the emission of CO_2 has been considered as an increasingly serious problem, due to its contribution to the greenhouse effect. The reduction of motor vehicle fuel consumption is seen as one of the most effective means of reducing CO_2 emissions in the medium term.

1.2 Combustion & Emission Basics

Amongst the methods to reduce the fuel consumption of spark-ignition engines (SI engines), lean burn is considered to be the most effective approach. Although, lean burn combustion achieves low primary exhaust emissions it is more difficult to reduce

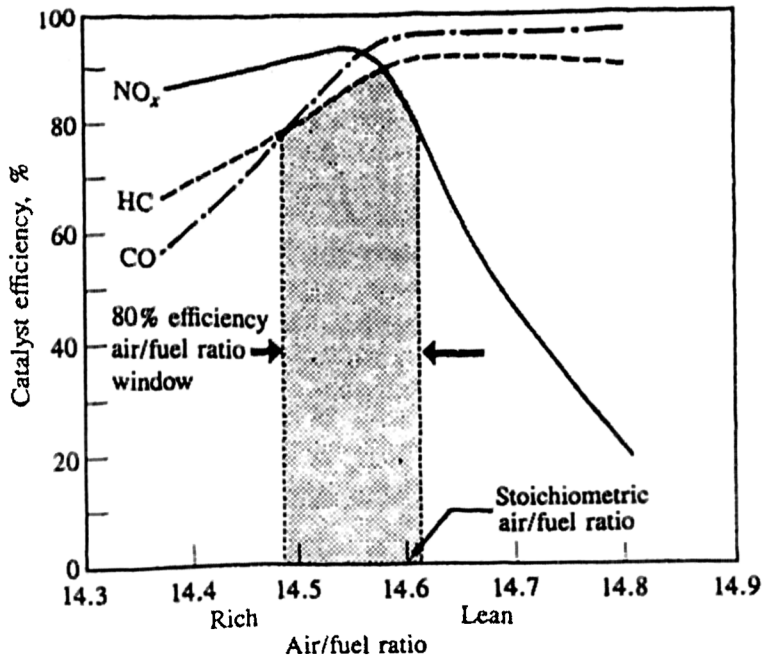

Fig. 1.1: Conversion efficiency for NO, CO and HC for a three way catalyst as a function of air/fuel ratio (from Heywood 1988)

NOx emissions to the mandatory level because exhaust gases from lean combustion generate an oxygen-rich condition in which a three-way catalyst does not work efficiently.

Operating a spark-ignition engine with a 3-way catalyst at optimum conversion efficiency requires a stoichiometric mixture strength where, by definition, the exact amount of air is supplied to burn the fuel completely. In theory there would be no HC or CO emissions, only water and CO_2. In practise combustion may not be quite finished when the exhaust valve(s) opens, particularly under transient conditions, quenching of the flame in the low pressure part of the expansion stroke is a source of unburned hydrocarbon and carbon monoxide. Another source of HC emission is fuel trapped in crevices, which are too narrow for the flame to enter, escaping unburned into the exhaust. Also at very high combustion temperatures, above 2000 K, high thermal energy leads to dissociation of the O_2, CO_2 and H_2O molecules to O, CO and H_2. The molecular oxygen in the burnt gas reacts with the nitrogen of the air and forms small quantities of nitrogen oxides. These are mainly nitric oxide (NO) and small amounts of nitrogen dioxide (NO_2). The higher the burnt gas temperature, the higher the rate of formation of NO. With catalytic converters NO can be removed by reduction using CO and H_2, while CO and hydrocarbons can be oxidised to CO_2 and water. If an engine is operated with a stoichiometric mixture, then both NO reduction and CO and HC oxidation can be achieved simultaneously in a 3-way catalyst (Fig. 1.1). In order to achieve optimum conversion efficiency the mixture strength is controlled around stoichiometric using systems such as closed loop control by an oxygen sensor in the exhaust. If the mixture is lean, a 3-way catalyst works perfectly well as an oxidising catalyst - but does little or nothing to reduce NOx.

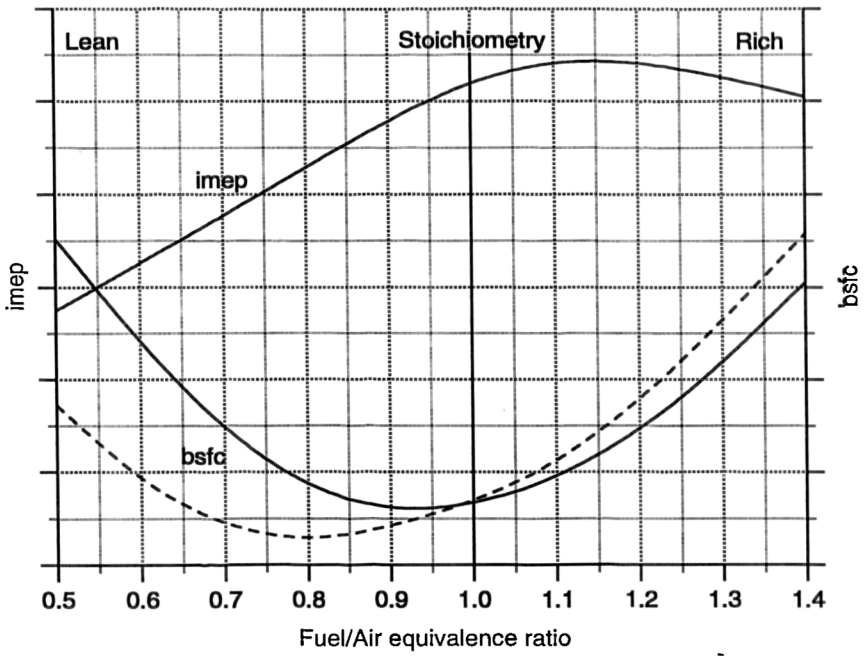

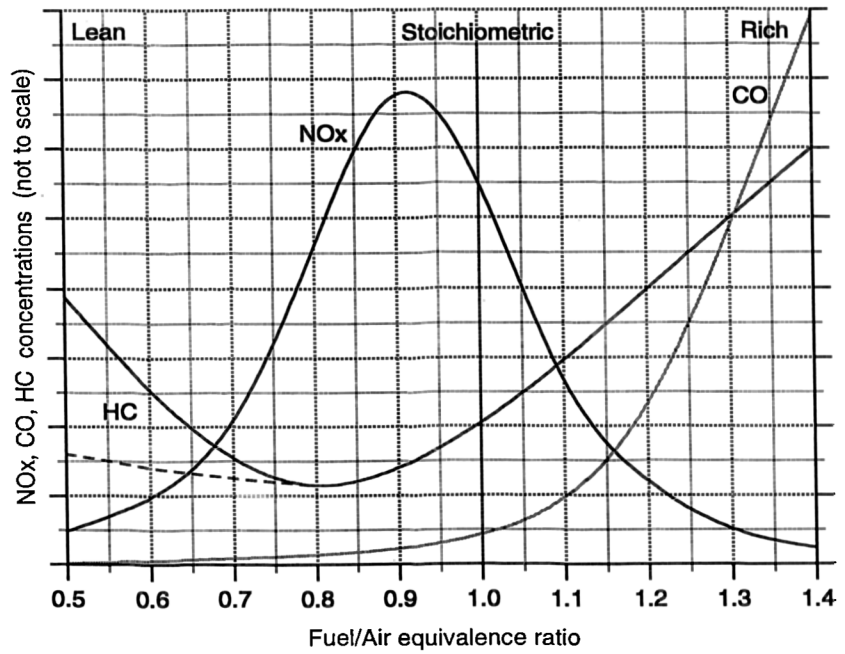

Fig. 1.2: Variation of the mean effective pressure, specific fuel consumption and primary pollutant concentrations in the exhaust of a conventional SI engine with fuel/air equivalence ratio.

Figure 1.2 shows typical responses of CO, HC and NOx to mixture strength. The NOx formation is strongly temperature dependent. The highest burnt gas temperatures occur in an operating regime with slightly rich mixtures (AFR 12 - 13), where engine power peaks; however at this air/fuel ratio oxygen concentrations are low. As the mixture is leaned out, increasing oxygen concentrations initially offset the falling gas temperatures and NOx emissions peak around an AFR of 15.5. For minimum NOx it would be advantageous to run very lean, with say an AFR of 24 or more. Although this would result in engine powers being reduced by about 40 % this has advantages because if, say 60 % of maximum power is required for motor way cruising, this can be achieved at nearly full throttle with a consequent reducing of throttle pumping losses. This is the major reason why lean burn can provide a significant advantage in fuel efficiency compared to stoichiometric running. Also with a full charge of air in the cylinder the combustion temperature is greatly reduced and this is why the NOx emissions decline. Carbon monoxide forms during the combustion process. With rich mixtures there is insufficient oxygen to burn fully all the carbon in the fuel to CO_2; also in the high temperature products even with lean mixtures, dissociation ensures there are significant CO levels. Hydrocarbon emissions, on the other hand, increase at some point on the lean side because of irregular combustion such as misfire or partial burning. This upturn in emissions of HC's can be postponed by speeding up the rate of combustion with the further benefit of improving fuel efficiency; burning more fuel early in the expansion stroke results in energy release at a higher expansion ratio.

1.3 Lean Burn Combustion in Spark-Ignition Engines

1.3.1 The Lean Operation Limit - Fundamentals

Operating a spark-ignition engine with a lean air/fuel mixture is limited to the air/fuel ratio, where further dilution leads to large cycle-by-cycle fluctuations in torque and subsequently to unacceptable levels of performance and hydrocarbon emissions and poor driveability - the lean operation limit.

Cyclic variations in torque are caused by cycle-by-cycle variations in the combustion. Variations of mixture strength and air motion in the combustion chamber lead to cyclic fluctuations in the burning rate. As the mixture in a SI engine is leaned out, the flame development period (the time to establish a flame kernel), the flame propagation period (the time to burn the bulk of the combustion gas) and the cyclic fluctuations in imep all increase (Young 1981). For slow burning cycles, where combustion is not completed before the exhaust valve(s) opens, the HC-emissions and the fuel consumption increase due to partial burning (Quader 1976). Further dilution of the mixture leads to misfire where the mixture fails to ignite altogether. Thus the slowest burning cycles determine the lean operation limit. For a fixed ignition timing, the slower-than-average burning cycle will be retarded, while the faster-than-average burning cycle will be over-advanced. Both will reduce torque and therefore high cyclic fluctuations not only affect engine driveability and smoothness but also reduce engine power.

Faster burning combustion chambers reduce the impact of cyclic variability, since a larger fraction of the heat release occurs near TDC when the chamber volume is changing slowly. Pressure variations are therefore mainly due to combustion variation. For slow-burning engines the effect of combustion variations on pressure is enhanced by the effect of volume change (Young 1981). This explains why dilute mixtures, which lead to reduced flame speeds, show higher cyclic fluctuations in pressure.

Fluctuations in combustion are caused by variations in gas velocity and turbulence during combustion and variations in mixture composition within a cylinder and between the cylinders of multi-cylinder engines (Heywood 1988). During the developed flame propagation process the average condition in the bulk gas will be the dominating factor, averaging local fluctuations. Variations in the overall flow pattern, turbulence intensity, length scale and variations in the amount of fuel fed into the cylinder from cycle-to-cycle are therefore important for the flame propagation (Heywood 1988). The mean flow influences the initial motion of the flame as it grows from the early flame kernel created by the spark. Cyclic fluctuations in the velocity of the overall flow field will influence the interaction between the flame and the cylinder walls and the spark plug (Gatowski 1984, Pischinger 1990). This will influence the flame surface area and the heat transfer and therefore the flame propagation rate (Keck 1987). The flame initiation is accelerated if the initial flame kernel is convected away from the spark plug due to the reduced heat loss (Le Coz 1992). In contrast the early interaction of the flame front with the cylinder wall increases the flame propagation period due to a reduced flame surface area (Witze 1982).

Variations in the flame development process will also influence the bulk combustion since the overall flow pattern will vary with time and the turbulence intensities decay with time (Liou 1983). Variations in the turbulence level will affect the development of the laminar-like flame kernel into the established turbulent flame. Studies of flame photographs (Gatowski 1985) and studies with a fibre optic instrumented spark plug (Witze 1988) have verified that there are substantial variations in the initial rate of flame growth and these variations are linked to dispersion in overall cycle performance (Swords 1982, Keck 1987, Witze 1988, Le Coz 1992). The flame initiation and development process will be determined by the local condition near the spark plug. In the early stages of combustion the flame is only weakly wrinkled and the flame growth is dominantly determined by the laminar flame speed (Tagalian 1986, Pischinger 1988). Laminar flame speed is a function of the mixture composition and gas temperature (Metghalchi 1982, Gülder 1984). Thus, if the inlet mixture is nonuniform, one may expect cycle-by-cycle variations in the gas composition near the spark electrodes at the time of spark, with corresponding variations in the flame development period and hence overall cycle performance.

1.3.2 Extending the Lean Operation Limit - Concepts

Cyclic variability increases with more dilute mixtures due to slower burning and the slowest burning cycles determine the lean operation limit. This explains why factors which accelerate flame development and propagation will extend the lean operation limit. These factors are compression ratio, spark location, mixture formation and turbulence level.

Increasing the compression ratio increases the charge temperature and thus aids combustion and extends the lean operation limit. Higher compression also reduces the fraction of residual gases which may affect the lean limit (Quader 1974). The compression ratio, however, can only be increased to the knock limit which is determined by the combustion chamber geometry and fuel quality (e.g. octane number). Short flame propagation distance will aid rapid combustion and extend the lean limit. This can be achieved either by locating the spark plug in a more central position (e.g. 4-valve head) or by dual spark location (Quader 1974). The effect of the spark location on burning rate is also influenced by the swirl level. For very high swirl, double ignition has been shown to be advantageous compared to central spark location (Witze 1982).

Higher turbulence levels lead to faster burning rates and therefore to a more stable combustion, provided that the initial flame is not extinguished due to excessive stretching or heat transfer. Small-scale turbulence is subject to dissipation (Liou 1983). Turbulence can be conserved by introducing kinetic energy to the cylinder during the intake process by large-scale vortices, which convert their energy into turbulence during compression. Swirl, or air which rotates horizontally round the cylinder axis, is effectively a large-scale vortex which will result in turbulence generation throughout the cycle (Liou 1983, Hall 1987). Swirl can be generated by helical inlet ports or shrouded valves. Inlet-generated turbulence is often gained at the expense of volumetric efficiency, especially with increasing engine speed. [These are the reasons why Honda and Toyota both employ a variable inlet system in their lean burn engine designs to increase swirl at low engine speeds in the lean operating regime whilst retaining high volumetric efficiency at high engine speeds (see *Section 1.4*)]. Tumble vortices are a large scale vertical rotational air motion; they are linked to improved flame burn by generating turbulence during their break-down in the second half of the compression stroke (Haddad 1991, Kiyota 1992). 4-valve configurations aid the generation of tumble, because strong tumble requires that the inlet port should be located as close as possible to the plane passing through the centre of the inlet and exhaust valves (Arcoumanis 1990). Turbulence may also be generated during compression by squish. Squish flow can only be generated in a few combustion chamber geometries (e.g. squish corner on the piston), they aid the flame development only when the spark plug is located directly in the squish flow (Gatowski 1985).

Since turbulence is a function of engine speed (Liou 1983, Hall 1987), adequate turbulence levels at low engine speeds leads to excessive turbulence levels at high

engine speeds. The turbulence intensities however are limited to levels where the stretch imposed by high fluctuations and strong mean flow causes local flame extinction (Bradley 1988), this is particularly important during ignition (Quader 1976, Pischinger 1988). Flame stretch can extinguish the flame when local velocity fluctuations exceed the local rate of chemical reaction. This phenomenon is not yet well documented and may affect the local burning velocity of slow-burning lean mixtures (Daneshyar 1983, Le Coz 1992). This effect may be important in 4-valve engines where high turbulence is readily generated by tumble and this will be detrimental to driveability and will increase HC emissions (Hu 1992). Iwamoto (1992) found that tumble ratios above 2.5 tended to increase misfire frequency and imep fluctuations for part load, ultra lean combustion (AFR 27). Inoue (1993) confirmed that swirl promotes turbulence, but found that above a certain level increasing turbulence did not result in a significant improvement to the lean limit; the effect of turbulence tended to saturate. Therefore, in a real engine, interaction of different effects limits the scope for improvement by a single parameter.

Several investigations have examined the contribution to combustion variability arising from nonuniformity of in cylinder fuel-air mixture. In-cylinder gas sampling showed that cyclic fluctuations in mixture strength in the vicinity of the spark plug exist (Matsui 1979), and that there is a linear relationship between cyclic variation in combustion and cyclic variation in mixture strength (Hamai 1986, Collings 1988, Sleightholme 1990). This is consistent with results from exhaust gas analysis by Pundir (1981) which also showed a linear correlation between cyclic variability and the level of mixture nonhomogeneity. To the contrary exhaust gas analyses made by Sztenderowicz (1990) showed that for increasing mixture uniformity, there was no significant impact on the statistics of the main combustion phase, nor on variation in imep. Also measurements of mixture strength by CARS showed *no* correlation between combustion variability and cyclic variations in the charge mixture near the spark plug (Williams 1991). Although these works indicate that there is a substantial variation in local fuel concentration at the spark electrodes and that differences in mixture preparation can be important to engine behaviour, the contribution to cyclic combustion variability due purely to mixture nonuniformity has, to date, not been clearly established.

The preceding review showed that the flame development period influences the subsequent in-cylinder pressure development. Ignition was found to be a function of mixture strength (Pischinger 1988, Le Coz 1992) and variations in the laminar flame speed to be the main reason for variations in the flame development period (Keck 1987). Since the laminar flame speed is a function of mixture strength, this gave rise to the concept of stratified charge to improve lean combustion. Stratifying the fuel in the combustion chamber such that it creates a potentially good mixture for ignition around the spark plug at the time of ignition extends partial burning and misfire limits. The potential advantages, in terms of igniteability through local charge stratification for overall air fuel ratios in excess of 50, has been demonstrated in a constant volume

combustion chamber by Arcoumanis (1994). Matsushita (1985) reported that a richer mixture near the spark plug extended the lean misfire limit; however local rich pockets, particularly near the spark gap, drastically increased the NOx emissions. He concluded, that the air/fuel ratio should be as homogeneous as possible to minimise NOx emissions.

Gas sampling analyses made by Quader (1982) has shown, that the top of the combustion chamber can be made leaner or richer than average, dependent on whether the fuel enters the cylinder early or late in the intake stroke. This result was confirmed by Matsushita (1985). Both authors found fuel injection, synchronised with the intake stroke of each cylinder, to extend the lean burn limit at part load conditions. The crank angle of injection during the inlet valve open period was found to be influential on cyclic variation in imep and NOx emissions under part load conditions. It was found that injection end should be between 60° - 110° after TDC of induction for reduced fluctuations in imep, but should be before inlet open for minimised NOx emissions (Matsushita 1985, Mikulic 1990, Horie 1992). The coefficient of variation of imep varied considerably with the injection timing during induction. Gas sampling at the spark plug location revealed richer than average mixture for low fluctuation in imep and the inverse for high fluctuations in imep (Matsushita 1985, Hardalupas 1995).

Swirl increases the turbulence level and therefore it is not surprising that the misfire limit could be extended by introducing swirl to the charge (Matsushita 1985, Horie 1993, Inoue 1993). Less clear is the influence of swirl on mixing. Quader (1982) observed that axial stratification by injection phasing only occurs with swirl. Gas samples showed no difference between studies with injection before and during inlet valve open period and studies of a premixed charge without swirl. This was again confirmed by Matsushita (1985) who found no improvement of the lean limit by injection phasing without swirl. Mikulic (1990) found that injection phasing with the inlet stroke increased cyclic variability and fuel consumption in absence of swirl, while the presence of swirl caused the inverse effect. On the other hand Quader (1974) and Ayusawa (1978) found that increasing mixture homogeneity extended the lean misfire limit in zero or low swirl configurations (though swirl is not mentioned in these papers, it is implicit that there was zero or little swirl since Quader used a Ricardo CFR engine and Ayusawa a side-valve engine). This implies that swirl tends to reduce mixing along the cylinder axis. If swirl is applied together with fuel injection during the inlet valve open period a positive axial fuel stratification can be achieved. In a non-swirl case inhomogeneties due to imperfect mixture preparation can have the opposite effect and therefore more homogeneous mixture can aid the flame initiation.

Also, increased tumble seems to have an adverse effect on mixing, as charge stratification was observed in a no-swirl high tumble configuration (Kiyota 1992). Baritaud (1992) reported that injection phasing influenced the mixture formation in a plane parallel to the cylinder head but found the effect depended on the flow field pattern. The mixture was found to be less homogeneous in swirling flows than in tumble flows for injection during inlet closed period, while for injection through the

open inlet valve there was little difference in the homogeneity of the mixture between the two flow fields.

These results and interpretations suggest that injection phasing can lead to charge stratification and can benefit the lean operation limit. However, there is little understanding of the mixing process and the role of swirl and injection phasing. Also the influence of charge stratification on cyclic variability has not been quantified.

1.3.3 Impact of Residuals on the Lean Operation Limit

The influence of residual gas or combustion products from the previous cycle on the lean operation is not very well documented. However, it is well known that the laminar flame speed is reduced by dilution with residuals (Metghalchi 1982, Rhodes 1985). Therefore variations in the mixing of residual gases with fresh charge and variations in the residual concentration and composition from cycle-to-cycle will affect the combustion process. Gas samples of the unburned gas taken with a rapid sampling valve just before spark discharge revealed an inverse relationship between the hydrocarbon concentration and the CO_2 concentration - the CO_2 concentration is a measure of the burned gas fraction in the unburned sample. There was a substantial fluctuation in the CO_2 concentration at a given fuel fraction, indicating significant fluctuations in the mixing of fresh gas and residual gas cycle-by-cycle (Matsui 1979). Galliot (1990) used gas sampling to measure the hydrocarbon concentrations in an engine charged with a homogeneous mixture of gaseous fuel and air. The residual gas concentration was calculated by comparing hydrocarbon concentrations between combusting and motored cycles. The residual gas fraction was found to decrease with load, and for high valve overlap, also decrease with speed. It was also found that fresh gas and residual gas appear to be well mixed. The fluctuations in hydrocarbon concentrations due to charge nonuniformity within the cycle were estimated to be less than one percent. The imep fluctuation did not correlate to residual concentration in the vicinity of the spark plug at high engine load but had an inverse correlationship for low load. Sztenderowicz (1990) analysed pressure data of a SI engine operated at light load and low speed with a stoichiometric mixture of fuel and air. Eliminating fresh charge nonuniformity was found to have no noticeable effect on fluctuations in either flame development angle (0 - 10 % mass fraction burned) or flame propagation angle (10 - 90 % mass fraction burned). Since skip firing did not lead to any reduction in flame development fluctuations, it was concluded that the residual gas and the fresh charge were well mixed and the residual fraction did not vary significantly from cycle-to-cycle. Keck (1987) observed significant cycle-by-cycle fluctuations in the early burning rate through analysis of Schlieren photographs. Since the laminar flame speed is a function of mixture strength, and fluctuations in the equivalence ratio were not expected because fuel and air were premixed, these fluctuations were attributed to incomplete mixing of fresh charge and residual gas. Early flame development studies, using a fibre optic instrumented spark plug, by Witze (1988), showed lower peak pressure later in the cycle with larger dispersion for unscavenged cycles compared with

completely scavenged cycles. Both of these features were also reflected in the flame velocity data, indicating variations in the residual concentration in the vicinity of the spark plug. Lebel (1992) made CO_2 and N_2 concentration measurements by CARS in a SI engine. High residual fractions were found to slow down the flame initiation but to aid fast combustion. It was concluded, that because an equivalence ratio of 1.1 was used where the laminar flame speed is not sensitive to small variations in mixture strength (which depends on residual gas fraction) but is strongly dependent on temperature, increased residuals lead to faster combustion. However Metghalchi (1982) and Rhodes (1985) found the laminar flame speed of iso-octane (the fuel used in Lebel's study) to be a strong function of the diluent fraction even at equivalence ratios of 1 and 1.2. This data seems to suggest that the effect of temperature increase due to higher residual fraction on the laminar flame speed is of the same order as the inverse effect due to dilution.

These results suggest that the influence of the residual fraction on the flame initiation and flame development process is dependent on engine characteristics and operating conditions. Under lean operation low load conditions with stratified charge inlet configuration, the mixing of fresh charge with residuals may well have a significant influence on cyclic variability and hence on the lean operation limit.

1.4 Lean Burn Spark-Ignition Engines

The problem in designing lean burn systems has been to extend the lean misfire limit sufficient to realise low NOx emission levels which achieve the mandatory emission standards whilst maintaining satisfactory driveability. This requires swirl or another means to improve or stabilise combustion; unfortunately this decreases the rated output power due to the low flow coefficient of swirl intake ports.

There are numerous concepts of lean burn engines; perhaps the ultimate expression of the lean burn stratified charge principle is the Diesel engine. The Diesel concept can be adapted to run on gasoline by combining direct injection and spark ignition as shown in the VW Futura concept engine (Emmenthal 1989). A SI engine with direct injection and such heterogeneous mixture composition can operate with equivalence ratios similar to those of diesel engines ($\phi > 0.2$) (Wurster 1988). The adaptation of this concept to a production engine has to date been prevented by the high cost for the mixture preparation system and it is limited in speed range.

In a concept which has been adopted in production engines at present by three Japanese manufacturers, the lean operation range is limited in order to meet the NOx emission standards. At low power, low speed when combustion temperature is low - and hence NOx output is naturally low - they operate as a lean burn engine for maximum fuel economy and then revert to controlled stoichiometric running for the high power condition. In the low power mode the catalyst just oxidises HC and CO while in the high power mode it also reduces NOx.

This is the basis of the Honda VTEC-E engine which is used in the Civic model; it also complies with the present European and Japanese emission regulations. The VTEC-E engine runs typically at AFR 22 below 3000 rpm at low power (below 75 % of max. inlet pressure). At high load and above 3000 rpm the engine reverts to a stoichiometric mixture (near full load to a rich mixture). The engine has a 4-valve pent-roof cylinder head with one centrally placed spark plug. One of the two inlet valves controls a high swirl port to ensure high turbulence for fast burning velocity. In the lean operating regime only this inlet valve opens fully, while the second opens only briefly about 1 mm to disperse unwanted fuel build up. At full load above 2500 rpm and at part load above 3200 rpm both inlet valves open fully for good volumetric efficiency and stoichiometric or rich running conditions. It is claimed for the lean operation mode, that by sequential injection during the inlet stroke the charge is stratified such that a rich mixture is present near the spark plug at ignition (Horie 1993, Hardalupas 1995, this work).

The Toyota lean burn engine follows a similar concept. It operates with an AFR of >20 below 4800 rpm and below 75 % of max. torque. At higher load and higher speed it reverts back to a stoichiometric mixture and at full load operates with an AFR of 12.5. Like the VTEC-E engine it also features a 4-valve pent-roof cylinder head with separated dual intake ports, one with a swirl control valve (SCV) and the other with a helical port shape for swirling inlet flow. In order to increase the volumetric efficiency, a small passage between the two ports allows a small air flow to the straight port when the SCV is closed at low load and low speed operation. By injecting into both ports at the appropriate time during the inlet stroke with a twin spray fuel injector, it is claimed that the fuel is finely atomised by the swirling bulk flow in the helical port and the high speed flow in the straight port resulting in a homogeneous charge (Inoue 1993).

It is noteworthy that though Honda and Toyota apparently follow the same strategy (swirl intake and sequential injection during inlet), the former's engine is claimed to be a stratified charge engine and the latter a homogeneous charge type.

The Mitsubishi MVV lean burn engine makes use of tumble instead of swirl to enhance turbulence and thereby reduces pumping losses. The fuel is injected through one port during the inlet stroke, with the second inlet port passing air only, therefore stratifying the charge. Due to tumble and the absence of swirl, it is claimed that the stratification is maintained during compression. In order to utilise the axial fuel stratification, the exhaust valve opposite the inlet valve which supplies the rich charge is replaced by the spark plug (Iwamoto 1992, Kiyota 1992).

In practice, under low load and low speed running conditions, all these engine designs offer an advantage in fuel consumption of about 5 - 10 % compared with their conventional counterparts. This brings them close to similar IDI-Diesel engines in terms of fuel efficiency. However, with an increasing proportion of high load and high speed running this advantage is reduced. Also low speed flexibility and refinement are below standard (AUTOCAR 17/06/1992, 26/04/1995).

Mitsubishi has announced that it will introduce a direct-injection petrol engine for the Japanese market in 1996. This engine operates with AFRs ranging from 30 to 40 at part load which allows operation with nearly unthrottled intake air, reducing pumping losses and improving fuel efficiency. The fuel is injected during the compression stroke with 50 bar pressure into a piston cavity. The piston cavity is claimed to direct the tumble air flow from a straight inlet port towards the centrally placed spark plug, generating a stratified charge with a rich mixture near the spark plug at the time of ignition. At medium and high load operation the fuel is injected during the inlet stroke. The high pressure swirl injector together with the intense tumble air motion are believed to generate a homogeneous charge. At medium load the engine is operated with an air-fuel ratio from 20 to 25 for improved fuel efficiency. In the lean operation mode EGR is used to minimise NOx. During high load operation the engine reverts to a stoichiometric mixture. This gives a conventional specific power output without turbo-charging and allows reduction of the NOx emission with a 3-way catalyst in the critical high power, high combustion temperature mode (Yamaguchi 1995, Kume 1996).

1.5 Summary

Operating a spark-ignition engine with a lean mixture can significantly improve efficiency compared with stoichiometric combustion. Although this type of engine offers low primary emissions of nitrogen oxides, its future success will primarily depend on its ability to meet the emission regulations on NOx without compromising performance or losing its advantage of efficiency. This involves reducing the cyclic variability of the lean combustion process and extending the lean operation limit. In order to meet even stricter future regulations, like those proposed for California, it might be necessary to use additional NOx reduction measures outside the combustion chamber.

The previous review showed the importance of cycle-by-cycle variations in combustion for the lean operation limit of spark ignition engines. The concept of stratified charge has been introduced as a means to reduce cyclic variability and to extend the lean operation limit. However, the contribution of mixture formation to cyclic variability in performance is not well established. There is only a limited understanding of the mechanism of in-cylinder mixture formation and to what extent stratification is generated and how this affects cyclic variability. Furthermore, the issue of residual gas concentration has not been considered in depth. It is not clear to what extent spatial variations in the residual gas concentration exist and how they affect the lean operation limit.

1.6 Aims of this Study

The primary aims of this study were to quantify the effect of mixture formation on cyclic variability and to provide quantitative information on the mixing of air and fuel.

The mixture formation evolution in a spark-ignition engine was to be characterised in order to provide an insight into the mechanism(s) influencing the fuel motion and mixing. For this purpose, it was intended to provide two-dimensional measurements of the average fuel concentrations at various crank-angle positions during inlet and compression stroke. To investigate the possible correlation between variations in the air-to-fuel ratio close to the spark plug and the variations in combustion, it was intended to provide sets of instantaneous two-dimensional fuel concentration measurements, close to the spark plug at the time of ignition, for different operating conditions. At the same time, by measuring simultaneously the in-cylinder pressure, the influence of the stoichiometry adjacent to the spark plug on engine performance could be studied in order to quantify some of the effects of charge stratification.

Another aim was to address separately mixture nonuniformity arising from potentially imperfect mixing between burned residual gases and incoming fresh charge and spatial variations in the residual gas concentration within the cylinder. Therefore it was intended to identify a method which could provide measurements of the spatial distribution and cyclic variation in residual gas concentration close to the spark plug at the time of ignition and apply it to an operating engine.

In order to achieve the above goals, laser fluorescence imaging has been developed to estimate air/fuel ratio distributions and residual distributions in a firing spark-ignition research engine which was based on the Honda VTEC-E lean burn concept.

1.7 Outline of this Thesis

This thesis is organised in 4 parts. *Part I* includes *Chapters 1* and *2* and provides background information to SI engine combustion and diagnostic methods applied in engine combustion research. *Part II* (*Chapters 3 - 5*) is concerned with fuel visualisation studies in an operating spark-ignition engine. The residual gas visualisation is described in *Part III* (*Chapters 6 - 8*). A summary of this work, references and acknowledgements are contained in *Part IV*.

Chapter 2 reviews diagnostic tools suitable for the study of the combustion and pollutant formation process in spark-ignition engines and gives examples of applications. The advantages and limitations of the most applicable techniques are discussed leading to an extended discussion of laser-induced fluorescence imaging for fuel visualisation studies in *Chapter 3*. A strategy is developed to quantify the measurements, resulting in equivalence ratio images. The experimental set-up, apparatus and procedures for the fuel visualisation are discussed in *Chapter 4*. The results of the fuel visualisation are presented in *Chapter 5* in two Sections. Section one describes the mixture formation process, while section two concentrates on the influence of stoichiometry on engine performance and cyclic variability. Finally the impact of the results on engine design is discussed. The strategy adopted to visualise residual gases at the time of ignition is described in *Chapter 6*. Apart from the engine, the experimental equipment and procedures of the residual gas visualisation study

differ from the fuel visualisation study and are described in *Chapter 7*. *Chapter 8* contains the results, discussion and conclusions of the residual gas study. *Chapter 9* (*Part IV*) summarises the work contained in this thesis and the principal conclusions.

Chapter 2

Combustion Diagnostics in Spark-Ignition Engines

A review of the diagnostic tools used to gain information on the mixing, combustion and pollutant formation processes in SI engines is given in this chapter. Examples of applications, the advantages and limitations of the most common techniques are presented.

2.1 Introduction

Traditionally engine configurations have been mainly developed by empirical methods. Therefore there is only limited understanding why one particular design is better than another. In order to optimise the balance between performance and efficiency whilst complying with the ever increasing demands for cleaner combustion, more specific insights into key phenomena such as mixing and combustion are required. The influence of fluid dynamics on the combustion process is seen as the primary target in developing and optimising spark ignition engine combustion. Therefore measurements of velocities and species concentration are essential if one is to gain a better knowledge, both of combustion fundamentals and of the design of a particular engine.

In order to obtain a better understanding of the mixing, ignition and combustion processes in the spark ignition engine, information on mixture strength and distribution, temperature, velocities, residual gas concentration, burning rate and their respective correlations to engine performance, as characterised by emissions, fuel efficiency and cycle-by-cycle fluctuations, is required. Particular problems for such measurements in the cylinder of a spark ignition engine are the high pressure and temperature fluctuations. Access to the combustion chamber is normally limited, particularly in modern 4-valve cylinder head configurations, and small clearance volumes render it difficult to introduce probes without perturbing the flow. High engine speeds for realistic running conditions require a high dynamic range of the data acquisition system if instantaneous cycle-resolved measurements are attempted.

Traditional engine diagnostics (reviewed by Amann 1985) have been expanded and supplemented by the application of optical (primarily laser based) diagnostic techniques (reviewed by Dyer 1985) for in-cylinder engine studies. With the introduction and

availability of reliable lasers, laser methods are assuming an increasingly important role in in-cylinder combustion diagnostics. Laser-based techniques supply the capability for remote, non-intrusive, in-situ, spatially and temporally precise in-cylinder measurements of properties. However, changes to the design of the engine required for optical access are often intrusive and influence the engine characteristics and performance.

2.2 Pressure Measurements

Piezoelectric transducers built into the engine head are commonly used for measuring the in-cylinder pressure. The transducer contains a quartz crystal which is exposed to the cylinder pressure by a diaphragm. An electrical charge proportional to the in-cylinder pressure is induced by the compression of the crystal and fed into a charge amplifier.

Pressure histories are a major source of information about the combustion characteristics. They directly measure peak pressure and the crank angle at which peak pressure occurs. The work per cycle may be calculated by integrating around a closed curve on a p-V diagram. This can be translated into the indicated mean effective pressure (imep) by dividing by the swept volume (Heywood 1988). Imep is a direct measure of the performance and efficiency of the combustion cycle. By making similar measurements over many cycles, the cycle-by-cycle fluctuations can be determined.

The piezoelectric pressure transducer is also the most useful monitoring device for knock. During knocking combustion, high frequency pressure fluctuations are observed whose amplitude decays with time (Heywood 1988). Once knock occurs, the pressure distribution across the cylinder is no longer uniform. Transducers located at different points in the chamber will record different pressure levels at a given time, thus allowing under certain circumstances location of the knock centre (Earp 1994).

It is also possible to extract approximate mass burning rates from the pressure curves (Heywood 1988). Sztenderowicz (1990) deduced flame development angle (0 - 10 % mass fraction burned) and flame propagation angle (10 - 90 % mass fraction burned) from pressure traces and compared them to fuel/air and residual gas nonuniformities.

2.3 Non Optical In-Cylinder Measurements

Cylinder composition information has been obtained by gas sampling directly from the combustion chamber through a fast-acting sampling valve built into the cylinder head and subsequent analysis of the sample. Most such valves use an electromagnetically or electrohydraulically controlled reciprocating needle to extract a small gas sample into an evacuated sampling chamber where a rapid drop in temperature and pressure quenches the combustion process. Sampling times are typically 1 ms for fast-acting valves. The sample can be analysed using conventional techniques, usually a flame ionisation detector (FID) for hydrocarbons, a non-dispersive infrared (NDIR) gas

analyser for CO, CO_2, NO, a chemiluminescent analyser for NO, a paramagnetic or a polarographic analyser for oxygen and a Bosch smoke meter for particulates.

With many sampling systems there are considerable uncertainties in where the gas sample originated and whether it is representative of the bulk composition. Even where the probe and lines are cooled to quench further reaction there remains considerable uncertainty due to potential chemical reaction after sample withdrawal from the combustion chamber. If the valve protrudes into the chamber, it also affects the in-cylinder gas behaviour.

Collings (1988) developed a fast response FID system by introducing the sample directly into the detector's hydrogen flame via short, small-diameter tubes. This enables frequency response of up to 500 Hz, but because of the pressure dependence of the transient time it cannot be used to continuously sample over a whole cycle. By introducing the sample tube into the spark plug Collings was able to correlate the local hydrocarbon concentration to the subsequent in-cylinder pressure at TDC. Sleightholme (1990) used the Collings technique to correlate hydrocarbon concentration to cyclic pressure fluctuations.

Galliot (1990) used the same gas sampling technique to measure the residual gas concentration in a SI engine. Using propane fuel premixed with air, the hydrocarbon concentrations near the spark plug were measured. By comparing the hydrocarbon concentrations of combusting and motored cycles, the residual gas concentration was estimated - the use of premixed gaseous fuel has the advantage of separating the issues of evaporation and mixing of a liquid fuel.

2.4 Optical Fibre Techniques

Optical fibres built into the cylinder head, piston or the spark plug give optical access to the combustion chamber requiring only minor modification to the engine. An optical fibre is a light guide with extremely high transmission efficiencies. The fibre itself consists of two concentric silica regions, called the 'core' and the 'cladding'. Light rays entering the fibre at angles within its acceptance cone are reflected by the core/cladding interface and thus are guided by the fibre. Contrasting light rays outside the fibre's acceptance cone are absorbed by the cladding. The light is usually guided to some sort of photodetector.

By building several separate fibres into the cylinder head the direction of the flame development can be determined (Haagensen 1991). A tool which allows detection of the early flame development on every spark ignition engine without modification was developed by Witze (1988). He installed eight optical fibres in a ring at the base of the threaded region of a standard spark plug. The effects on flame kernel development caused by differences in residual gas scavenging, differences in the ground electrode orientation and differences in swirl and turbulence levels were detected. This tool may also be used to investigate the cause and effect relationship between early flame

development and engine performance. Ohyama (1990) built an optical fibre bundle into the centre electrode of a spark plug. This enables detection of knock using the effect of the pressure fluctuation on the intensity of the combustion gas light emissions. By building several fibres into the piston, the knock onset location could be detected (Spiccher 1990). Detecting the light intensity of CH (450 nm) and C_2 (750 nm) radicals after the spark discharge cycle-by-cycle, allows the fluctuation of the air/fuel ratio near the spark plug to be monitored (Ohyama 1990) - though no quantitative results have been reported.

2.5 Laser Schlieren Photography

While direct flame photographs show the location and the shape of the actual reaction zone which radiates in the blue region of the visible spectrum (Bates 1989), Schlieren photography can give insight into the structure of the flame. It allows the gross features of the flame to be illustrated. The Schlieren technique makes use of the fact that when a collimated beam of light is passed through a gas of nonuniform density, individual rays are deflected through different angles. If the rays are focused by a lens after they pass through the chamber section, a deflected ray misses the focal point and can be blocked by an aperture. Regions responsible for ray deflection appear darker when subsequently refocused onto film.

Gatowski (1984) used Schlieren photography to illustrate various stages of combustion in a SI engine with a square-piston. The influence of bulk gas motion on variations in cycle by cycle convection of the flame centre, the influence of turbulence and of the spark location on the early flame development could be illustrated. In the same engine Gatowski (1985) investigated the flame development phase and its cyclic fluctuation for swirl and squish flows by Schlieren photography.

Keck (1987) used a model to perform a more detailed analysis of the flame from successive time resolved Schlieren images. Based on the assumption of a spherical flame kernel, the flame front radius was determined according to the spherical surface which best fitted the silhouette observed in the photograph, and subsequently the flame frontal area and flame volume could be calculated. Assuming that early in the combustion process the rate of growth of the burnt volume is proportional to the rate of growth of the flame front as observed in the frames, the early burning velocities could be determined solely from the Schlieren film - in a phase of combustion where pressure data do not yield much information. This analysis of Schlieren film complemented by analysis of pressure data for the developed flame propagation was used to examine the influence of swirl and squish on combustion and the influence of the location and growth rate of the early flame kernel on cyclic variability.

Pischinger (1988) used a Schlieren system which provided two orthogonal views of the developing flame to define the initial flame growth process. The influence of different breakdown ignition systems on the initial flame development period for swirling and non-swirling combustion chambers were investigated.

2.6 Rayleigh & Raman Scattering

The scattering techniques are based on an incident high-energy laser beam interacting with the molecules along its path, resulting in light scattering at incident wavelength (elastic process) or other wavelength (inelastic process). The scattered light is collected and its intensity and spectral characteristics measured with a spectrometer. Species concentrations are usually inferred from the intensity of the incident scattering and temperatures from the spectral distribution.

Rayleigh scattering is an elastic process and as such is not specific to any species in a spectral sense. It can be used to measure mixing of gases with significantly different Rayleigh cross sections. Temperature measurements can be made in constant pressure environments. Rayleigh scattering suffers from Mie (scattering from particles or droplets) interference and scattered laser light (Long 1993).

Raman scattering is an inelastic process. The frequency shift of the Raman spectrum is species specific and proportional to number density. Temperature measurements can be made from the distribution of the scattering. Raman scattering is very weak due to small scattering cross sections and is usually limited to single point measurements of major species or mean measurements over many laser pulses.

Rayleigh scattering was applied to measurement of the local gas temperatures in a methane-fuelled spark ignition engine (Kadota 1991). These measurements were performed in a low compression ratio (4:1), L-head, side-valve type engine configuration in order to minimise Mie and laser scattering.

Arcoumanis (1991) has made Rayleigh scattering measurements from fuel simulated with gaseous Freon-12 in a port-injected model engine. The engine was fabricated from acrylic with a low compression ratio (3.5:1) and a flat cylinder head with a single valve used for inlet and exhaust. It was motored, with no combustion taking place, running at 200 rpm. Spatial and temporal information about the fuel/air mixing was obtained by mean point measurements in a plane. Similarly Kadota (1989) made vapour concentration measurements in a transparent cylinder via Rayleigh scattering. An engine cylinder head was mounted on a cylinder made from acrylic resin. Air was supplied by a compressor and fuel (Freon) injected continuously. Time-averaged measurements at more than 100 points and two planes were made and extrapolation between the measurement points allowed determination of contours of fuel concentration.

Vapour concentration measurements using Rayleigh scattering under more realistic conditions were performed by Kadota (1991) in a motored (n = 650- 850 rpm), non-combusting 4-valve engine with a compression ratio of 3.1:1. Time-averaged measurements during the inlet and compression stroke were performed with n-pentane, n-hexane and gasoline as fuel at a point close to the spark plug. There was a good resemblance among the time histories of vapour concentration for the different fuels.

The Rayleigh scattering technique was compromised by the need to use a fuel marker with a large Rayleigh cross section in order to achieve an adequate signal-to-noise ratio. Freon-12 is gaseous and its molecules large, so it may not be representative of the true fuel distribution in a production engine - Kadota's (1991) work showed similar time histories comparing gaseous fuels and gasoline, but did not compare the vapour distribution. Since the method relies on a weak elastic scattering process, all other sources of scattering need to be minimised. This imposes constraints on the design of a suitable experimental engine, hence the simplified cylinder head geometry in a non-firing engine.

Raman spectroscopy was used by A. O. zur Loye (1983) to make cycle-averaged spatially and temporally resolved measurements of the gas temperature, using the spectra of nitrogen, and CO concentrations in the post-flame gases in a skip-fired SI engine. Johnston (1979) used laser Raman spectroscopy to measure fuel-air distribution in a motored (n = 456 rpm) research engine using propane as fuel. The engine had a flat fused silica cylinder head and radially mounted and pushrod operated valves. Time-averaged point measurements along a line across the cylinder were taken for pentane and nitrogen concentrations during the inlet and compression stroke. The mixing process was described on an equivalence ratio scale and compared to flow visualisation photographs.

The major short-coming of the spontaneous Raman technique is an inherently low signal level. This is especially problematic at low pressure and in environments with high background luminosities. This makes cycle-by-cycle single-shot measurements difficult.

2.7 Laser-Doppler Anemometry (LDA) & Phase-Doppler Anemometry (PDA)

LDA and PDA are based on the same principle. They make use of the interference fringes generated by incident coherent laser beams of equal intensity. A particle moving through the interference fringe planes scatters intensity-modulated light which is detected with a photodetector. LDA measures the rate of intensity variation of the scattered light, which is proportional to the velocity normal to the fringes. By generating three orthogonal interference fringes of different wavelength in the same measurement volume, all three velocity components can be obtained (3D-LDA). PDA makes use of three photodetectors which are spaced at different angles to the measurement volume. Each detector will see the same modulated signal as in the LDA case, but with a time delay. This time delay is effectively a phase shift which is proportional to the particle diameter. Because the instrument is based on the LDA principle, it also gives the droplet velocity vector normal to the fringes and hence droplet size, velocity and position simultaneously (Heitor 1993). Understanding droplet size and trajectory is particularly important for good fuel/air mixing because large droplets contain higher fuel mass than small ones and tend to follow the air flow

less faithfully. PDA/LDA is therefore a good instrument for droplet velocity/size measurement in Diesel or SI engine fuel injector sprays. LDA is also widely used for in-cylinder three-dimensional air velocity measurements by seeding particles into the flow. By making average point measurements over a grid in a plane, spatial mean flow characteristics can be obtained.

LDA/PDA is a very well established technique and is now widely used in the combustion and flow diagnostics community. First applications of LDA in firing SI engines were reported as early as 1979 by Rask and Asanuma. More recently Vafidis (1987) studied the effect of intake port and combustion chamber geometry on in-cylinder turbulence in a motored engine. Foster (1987) used a SI engine with a transparent cylinder head and side-wall located valves and spark plug to measure the velocity and turbulence profile in a fired engine. They made these measurements in the boundary layer and quantified the increase in boundary layer thickness for low and high swirl. Arcoumanis (1990) showed, that tumbling motion is a mechanism for turbulence enhancement using LDA. This was done by rotating the inlet port such that in a plane passing through the centre of the inlet and exhaust valves, either only tumble, or only swirl, or both tumble and swirl were generated. Hadded (1991) used scanning LDA measurements to obtain a spatial turbulence characterisation of a pent-roof 4-valve engine for four different inlet configurations with differing tumble magnitudes. Le Coz (1992) measured the local flow field in the spark gap by two-component LDA and compared it with the combustion initiation duration. Hardalupas (1995) reports on droplet characteristics and air velocity in an engine of similar design to the one examined here. The results and conclusions to be drawn from this work are incorporated in *Chapter 5*.

2.8 Particle Image Velocimetry (PIV)

While LDA is limited to point measurements, PIV is used to extract 2-dimensional velocity fields. PIV is based on small tracer particles introduced to the flow and subjected to intensive multiple-illumination by a laser sheet. The light scattered from seed particles is recorded photographically or electronically, with one image for each laser pulse. Due to the short laser pulse duration each image contains the instantaneous position of the particles. The local velocity in the flow is measured by determining the displacement of a particle between two laser pulses (images). If the seeding density is sufficiently high, a two-dimensional velocity map of the illuminated region can be generated. [Up-to-date reviews of PIV can be found in Buchhave (1994) and Farrugia (1996).]

PIV was first applied to in-cylinder measurements by Reuss (1989) in a motored engine. The velocity of the swirling bulk flow could be measured in a portion of the engine cylinder, parallel to the piston crown. Vorticity structures and strain rates with >1 mm resolution were derived from instantaneous flow fields. It was suggested, that the magnitude of the observed strain rates and the random distribution of high strain

regions could affect the early flame growth and therefore contribute to cyclic variations in engine performance. Nino (1993) demonstrated PIV in a fired two-stroke engine with high swirl inlet configuration. Instantaneous and ensemble averaged velocity fields parallel to the piston crown and velocity fluctuations could be obtained in the unburned gas. Reeves (1994) measured the instantaneous velocity field in a motored 4-valve engine. Illumination of a plane parallel to the cylinder axis through a piston window allowed the study of large scale tumble vortices.

2.9 Coherent Anti-Stokes Raman Spectroscopy (CARS)

CARS is used for temperature and species concentration measurements. It makes use of two lasers of different wavelength (pump and Stokes beams) to stimulate a non-linear interaction with the gas molecules contained in the measurement volume. An anti-Stokes shifted laser-like (coherent) signal beam is generated by this interaction which is directed into a spectrometer for measurement of intensity and spectral structure. By comparing the measured spectrum of a species with a calculated spectrum, the temperature in the measurement volume can be determined. The concentration of the measured species in the measurement volume can be obtained from the signal intensity. [Complete reviews of CARS theory can be found in Eckbreth (1988) and Greenhalgh (1988).] Advantages of CARS in engine combustion applications are that the laser-like signal beam allows for efficient collection with limited optical access and the spatial rejection of the combustion luminosity and laser scattering. Since CARS is a point measurement technique, spatial information can only be obtained by measuring the mean signal at several locations in the cylinder.

CARS has been applied to temperature and species concentration measurements in the internal combustion engine. Lucht (1987) measured the cylinder temperature in the unburned gas of a fired SI engine with an accuracy of better than 10 %. Marie (1987) performed temperature measurements for light load, full load and knocking engine running conditions and analysed dispersions due to cycle-by-cycle variations. Williams (1991) used CARS for simultaneous measurement of HC and O_2 in the unburned gas of a firing SI engine. Quantitative results of the local AFR in the vicinity of the spark plug were presented and correlated to engine performance. Lebel (1992) studied the influence of the mixing between fresh gas and residual gas in the vicinity of the spark plug on engine performance by simultaneous measurement of CO_2 concentrations and temperature in a firing SI engine.

2.10 Planar Laser-Induced Fluorescence (PLIF)

PLIF involves exciting certain molecules from a specific initial stage to an excited electronic state and then collecting the resulting fluorescence as they relax radiatively. In an uniform quenching environment, the PLIF signal is proportional to species concentration. LIF scattering cross sections for one photon transitions are sufficiently large that minor species can be detected. The signal can be spectrally filtered from laser

light scattering, since the fluorescence wavelength is often shifted compared to the excitation wavelength.

The feasibility of observing the flame front in a SI engine by PLIF from OH radicals has been demonstrated by Felton (1988) and Suntz (1988). Qualitative information about the turbulent flame structure was obtained with this method in a square-piston engine simulator by Becker (1990). Acetaldehyde mixed into the fuel was used as a fluorescence dopant for two-dimensional imaging of the flame front in the same engine simulator by Arnold (1990). It was demonstrated that in this way the flame front could be marked by mapping regions of unburned fuel. Andresen (1990) imaged NO, OH and fuel distribution in an optical 4-cylinder Volkswagen engine. Quartz windows in the engines flat 2-valve cylinder head (parallel inlet and exhaust valves) allowed an 18 mm wide laser sheet. Broad band fluorescence attributed to iso-octane was used to describe the gross fuel distribution in a qualitative manner. It was also demonstrated that the distribution of nitrogen oxide could be imaged with LIF at 193 nm during the exhaust stroke (200° after TDC). During the combustion stroke no fluorescence of NO could be detected. This was attributed to absorption by an unspecified species.

Baritaud (1992) made fuel concentration measurements in a motored model engine by PLIF of biacetyle mixed with iso-octane. Quantitative comparisons of the fuel concentration fluctuations in the measurement plane for different fuel injection timings, engine speeds, swirl and tumble inlet were presented. Lawrenz (1992) made quantitative 2D LIF measurements of air/fuel ratios during the intake stroke in a motored square-piston model engine. Single images taken at different crank angle positions in subsequent cycles showed that appreciable inhomogeneities existed until ignition timing for injection at 30° CA after inlet TDC. Arnold (1993) imaged simultaneously fuel and OH radicals in a realistic SI engine. The fuel was iso-octane doped with acetone as fluorescence marker. The start and propagation of combustion were studied for different AFRs in a ribbon 10 mm below the spark plug from both the fuel and the OH images. This work also gave a qualitative description of the fuel inlet process over 6° crank angle after the inlet valve opened for different AFRs.

2.11 Other In-Cylinder Combustion Diagnostic Approaches

Swords (1982) described a high resolution optical flame-speed detector and its application to a SI engine. The attenuation of two parallel He/Ne laser beams, each focused on an optical detector, was used to mark the arrival of the flame front. From the time delay between the attenuation of each beam by the flame front, and the spacing of the beams, the flame speed was calculated. With this method correlations between the flame speed of the early flame kernel, engine speed and stoichiometry could be described. The technique was also used together with LDA for multi-sampling of combustion variables such as early flame speed, mean flow and turbulence levels and allowed the correlation with engine performance.

Winkelhofer (1992) described a method for observation of the vaporised fuel in the cylinder of a motored IC engine, based on absorption of infra-red laser light radiation by hydrocarbon molecules. An IR beam is focused through the combustion chamber and its transmitted intensity is measured by a photo sensor. Variations in the transmitted radiation intensity are produced by the presence of fuel vapour and can be scaled for fuel vapour concentration levels. The technique is limited to the line-of-sight integral of the fuel concentration along the optical path. The cycle-by-cycle variations in fuel concentration levels and the mapping of the temporal development of the in-cylinder fuel distribution with some limited degree of spatial resolution could be demonstrated.

Shoji (1992) studied the behaviour of the OH, CH and C_2 radicals by means of emission and absorption spectroscopy in a research SI engine. The combustion luminosity is introduced into a polychromator through an optical fibre. The light is then dispersed by a diffraction grating and transmitted to four optical detectors by four fibres at positions corresponding to the desired wavelengths. In the emission mode, the combustion luminosity was detected, whereas in the absorption mode, a xenon lamp was used and the absorption of the light at the wavelength of the corresponding species was detected. The apparatus was used to study the behaviour of the radical emissions during normal and knocking combustion.

2.12 Summary

A limited review of diagnostic tools for combustion research in SI engines showed that the measurements most often sought have involved cylinder-gas pressure, temperature and composition, and in-cylinder fluid motions such as bulk gas velocity, turbulence and flame travel. Measurement of the in-cylinder pressure development with piezoelectric transducer is the major source of information about combustion characteristics. Laser based diagnostic tools enabled in-cylinder studies of velocities and species concentration. LDA has been widely used for point measurements of air velocity and turbulence. More recently PIV has been applied to operating engines for measurement of 2-dimensional velocity fields. Concentration measurements, laser based (CARS, Rayleigh) or traditional (gas-sampling), are often limited to a single point. However, the laser techniques offer the potential to get some spatial information by measuring the mean concentration of several points in a grid and assembling 2D-maps of average concentrations. In the same way velocity maps can be assembled using LDA. Few such measurements have been reported so far, probably due to the long measurement time required for collecting sufficient data points. A technique which is effective enough to allow instantaneous planar (2D) measurements of species concentration, is LIF. Planar LIF offers therefore great potential for real time in-cylinder concentration measurements which might have an impact on engine design. 'But there is much to be done in turning promises into reality. This can only happen by careful design of critical experiments - those that answer important questions - and the application of diagnostic techniques that will lead to those answers'(T. M. Dyer 1985).

PART II

FUEL VISUALISATION STUDIES

Chapter 3

Strategy for Fuel Visualisation

Planar LIF is presented as the means of visualising the fuel distribution in an operating SI engine. The criteria for the selection of the fuel and a suitable fuel marker are shown and the issue of fuel vaporisation and mixing is discussed. A strategy to quantify the measurements, resulting in maps of equivalence ratios, is described.

3.1 Introduction

Quantitative measurement of the mixture formation process and the influence of cycle-by-cycle fluctuation in fuel concentration on engine performance requires a measuring technique which is both instantaneous and two-dimensional. Probe sampling and CARS can be instantaneous, but they are limited to a single measurement point. The previous review showed that planar laser-induced fluorescence is an effective diagnostic method for species concentration measurements in operating SI engines. PLIF is attractive because, unlike other planar laser diagnostics, such as Raman or Rayleigh scattering, it is a relatively efficient scattering process. Raman or Rayleigh possess small scattering cross sections and are therefore very susceptible to contamination from laser scattering from windows or particles in the flow. This makes them unsuitable for applications in "real" engines. Fluorescence scattering cross sections are large enough to allow instantaneous 2D imaging of species concentration with pulsed lasers, generating 10 - 40 ns pulses. By analysing instantaneous images it is not only possible to obtain average concentrations, but also the fluctuating concentration as say a standard deviation. This is a particularly important feature because cycle resolved measurements can be related to the performance of an individual engine cycle. For these reasons, the experiments discussed in this thesis are based on laser-induced fluorescence.

3.2 Concept of Quantitative Measurements by PLIF

LIF is a well-established, sensitive technique for detecting population densities of atoms and molecules in specific quantum states. The principles of LIF are well known and up to date reviews can be found in Eckbreth (1988), Seitzman (1988) and

Greenhalgh (1994). The principle of LIF is illustrated in Figure 3.1. After the laser has raised a proportion of the probed molecules to an excited electronic state, there are several possible relaxation routes from the upper to the lower level. If the energy is emitted in the form of a photon as the excited species returns to the ground state, it is called fluorescence. But there are other important competing processes. One is relaxation to the ground state stimulated by the laser, and the second is excitation by the laser to higher electronic levels. High laser intensities can lead to ionisation, where the molecules acquire sufficient energy to allow one or more electrons to escape. Collision with other molecules can lead to radiationless energy transfer (quenching). Interaction between separate atoms of the molecule can produce internal energy transfers, called dissociation. These internal collisions or interactions with the bath gas can also lead to relaxation and energy exchange processes in the vibrational and rotational levels in the upper state. This, plus the opportunity to relax to other rotational and vibrational levels in the lower state, causes the fluorescence to be broad band and, normally, shifted to longer wavelength. For practical purposes quenching and rotational and vibrational relaxation are the most important because they are environment specific and therefore a function of the local gas composition, pressure and temperature.

The quenching rate depends on the molecule probed and the available collision partner. Some molecules are better than others in carrying away the excess energy after absorption of laser light. This gives rise to differing quenching rates for different gas compositions. If the quenching rate is the dominant form of relaxation then the fluorescence quantum yield will also be composition dependent. Oxygen is often found to be a good quencher. For fuel visualisation, the quenching effect due to oxygen is most important, since for an inhomogeneous fuel/air mixture the quenching

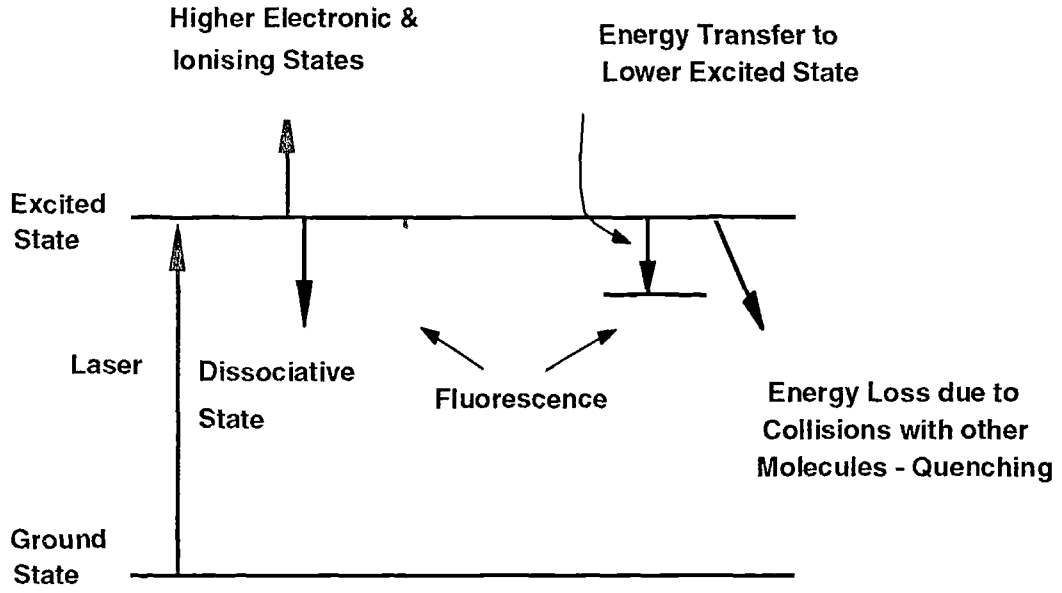

Fig. 3.1: Schematic diagram of the primary energy transfer processes in fluorescence.

environment for the fluorescence marker varies.

The fluorescence is proportional to the number of molecules in the measurement volume, the laser intensity and, if the transition is not saturated, inversely proportional to the quenching rate. If the laser intensity is very large, absorption and stimulated emission dominate the energy transfer such that the quenching does not significantly decrease the population in the upper level. Thus, if the laser intensity is significantly above the saturation intensity, fluorescence becomes independent of both quenching and laser intensity. Saturated fluorescence is not without problems however. Many hydrocarbons do not saturate at laser intensities available at absorption wavelengths. Furthermore, it is difficult to achieve saturation during the entire laser pulse due to the temporal variation in the laser intensity. It is also difficult to maintain saturation over the whole sheet profile (Eckbreth 1988).

In order to allow quantitative concentration measurements, the photo-physical properties of the species under investigation and its sensitivity to the quenching environment has to be known. Ideally the probed species should be insensitive to quenching and it should yield a strong fluorescence signal independent of temperature and pressure. Alternatively the temperature and pressure dependence of the fluorescence as well as the quenching cross sections of the most important quenching partner have to be measured and the measured images corrected for these effects. However any ambiguity in the precise magnitude of the conditions in the probed volume will affect the accuracy of the measurement. Unfortunately most commonly used fuels are not suitable for detection by LIF since they either do not have a sufficiently strong absorption at an accessible wavelength or they dissociate in

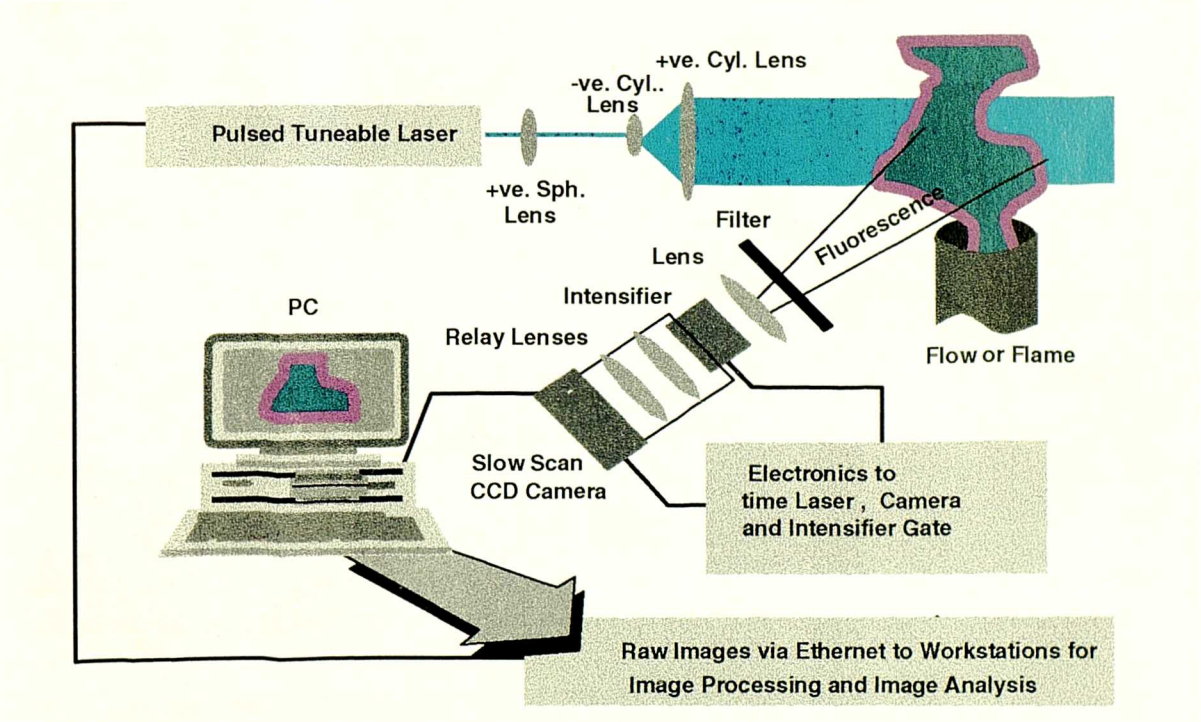

Fig. 3.2: Schematic of Planar Laser Induced Fluorescence (PLIF), (from Greenhalgh 1994).

preference to fluorescing. Natural markers, such as aromatics can be problematic and produce weak signals at high pressures; also these are very sensitive to oxygen quenching. For such fuels a carefully chosen fuel marker must be used. This can be added to the fuel or, if it is physically and chemically similar to the normal fuel, used instead.

The basic layout of a PLIF experiment is shown in Figure 3.2. The laser beam, which is tuned to a molecular absorption, is formed into a sheet by a set of cylindrical lenses and focused onto the measurement volume by a spherical lens. The fluorescence is typically detected at right angles to the incident laser light with a CCD (charge-coupled device) camera in conjunction with a gated signal intensifier. Short gate durations (50-100 ns) of the intensifier allow weak images to be recorded against bright background e.g. flames or roomlight. Since CCDs are digital devices, recorded images can be transferred on line to a PC for instant display, storage or processing. In most PLIF applications pulsed lasers are used for their short pulse duration of typically 10-30 ns which, along with short intensifier gate-times, enable instantaneous imaging of species concentrations.

3.3 Choice of a Fluorescence Marker

Commercial-grade gasoline emits very strong fluorescence signals when excited at 308 nm. However, since gasoline consists of many components, this fluorescence is not specific, and may vary for different fuels. The influence of pressure and temperature on the fluorescence signal is difficult to quantify. Nevertheless, qualitative information can be gained from these unspecific signals (Fansler 1995). In this investigation, iso-octane was used as the fuel since it consists of only one component. Although iso-octane will fluoresce when excited at 248 nm it tends to be heavily quenched at pressure. Andresen (1990) detected broad band fluorescence emissions which were attributed to iso-octane. This broad band emission was probably predominantly from polycyclic aromatic hydrocarbons (PAH) formed during combustion and not iso-octane. The quantum efficiencies of fluorescence for PAHs tend to be several orders of magnitude larger and give rise to similar spectra (Tait 1994). For this reason, a dopant with a well defined fluorescence and chemical behaviour had to be chosen and mixed into iso-octane. The choice of a possible tracer is limited by the requirement that it must not only have suitable fluorescence properties, but must also be soluble in iso-octane and have similar combustion and molecular transport characteristics. These conditions can be met by choosing a low molecular weight hydrocarbon, like a ketone or an aldehyde, as a fluorescence marker.

A further limitation to the choice of a fuel marker is that it must absorb at an available laser wavelength. If a planar image is to be obtained covering a substantial part of the cylinder cross section, then typically 50-200 mJ of excitation energy is required. The only laser sources available for this study which could obtain this power were KrF and

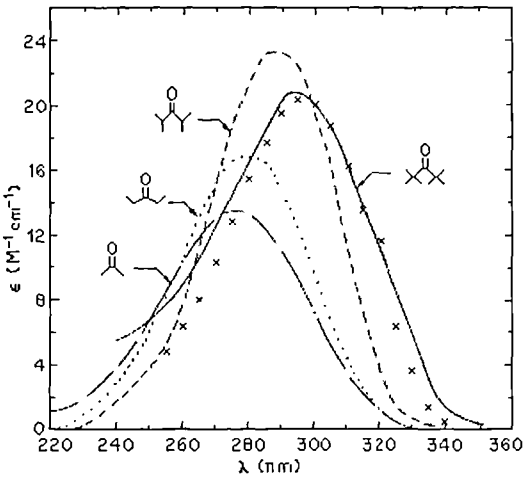

Fig. 3.3: Gas phase absorption spectra of acetone, 3-pentanone, 2,4-dimethyl-3-pentanone, and 2,2,4,4-tetramethyl-3-pentanone (from Hansen et al 1975).

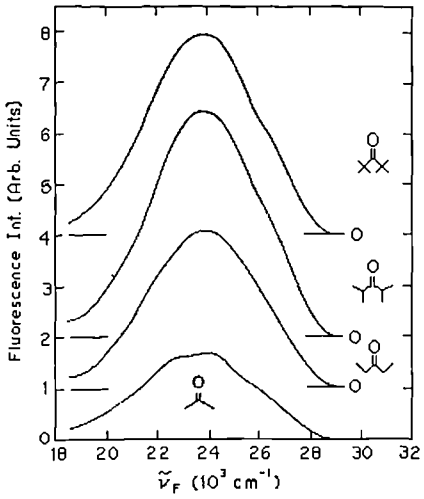

Fig. 3.4: Fluorescence emission spectra of acetone, 3-pentanone, 2,4-dimethyl-3-pentanone, and 2,2,4,4-tetramethyl-3-pentanone (from Hansen et al 1975)

XeCl Excimer lasers which lase at 248 and 308 nm respectively and Nd:YAG (third harmonic) at 266 nm. Excitation at 248 nm gives rise to large background signals from traces of oils absorbed into engine surfaces and may result in contamination of the fluorescence signal by PAHs formed during combustion. To minimise this problem the 308 nm radiation of the XeCl Excimer laser was the preferred choice.

Ketones and aldehydes have been used as fluorescence markers for hydrocarbon fuels. Becker (1990) and Tait (1992) used Acetaldehyde in combustion while Lozano (1992) and Tait (1993) used Acetone in cold-flow situations. Ketones and aldehydes have similar absorption and fluorescence spectra. The ketones acetone and pentanone have absorption bands ranging from 230 to 320 nm with a maximum near 280 nm (Fig. 3.3), which is very similar to the absorption band of acetaldehyde (Tait 1994). This allows efficient excitation with large planar sheets using UV Excimer lasers operating at 308 nm (XeCl) or 248 nm (KrF). The fluorescence, after excitation with 308 nm exhibits a featureless broadband structure from 330 to 600 nm, with the maximum around 430 nm (Fig. 3.4). The shift towards longer wavelength of the fluorescence compared with the excitation is important from a spectroscopy stand point, since it permits discrimination between the laser light and the fluorescence signal. This discrimination can be easily achieved without a special UV-filter by using standard glass optics for the detection system, because the peak emission at about 430 nm is in the visible range and 308 nm radiation is not transmitted by standard glass.

The fluorescence properties of acetone have been subject to numerous investigations over the years and have been shown to be favourable. Acetone fluorescence was found to be linear with laser fluence (Lozano 1992, Tait 1994). Experiments established that the self quenching of acetone is negligible and the fluorescence intensity is directly proportional to concentration (Lawrenz 1992, Lozano 1992, Tait 1994). Tait (1994)

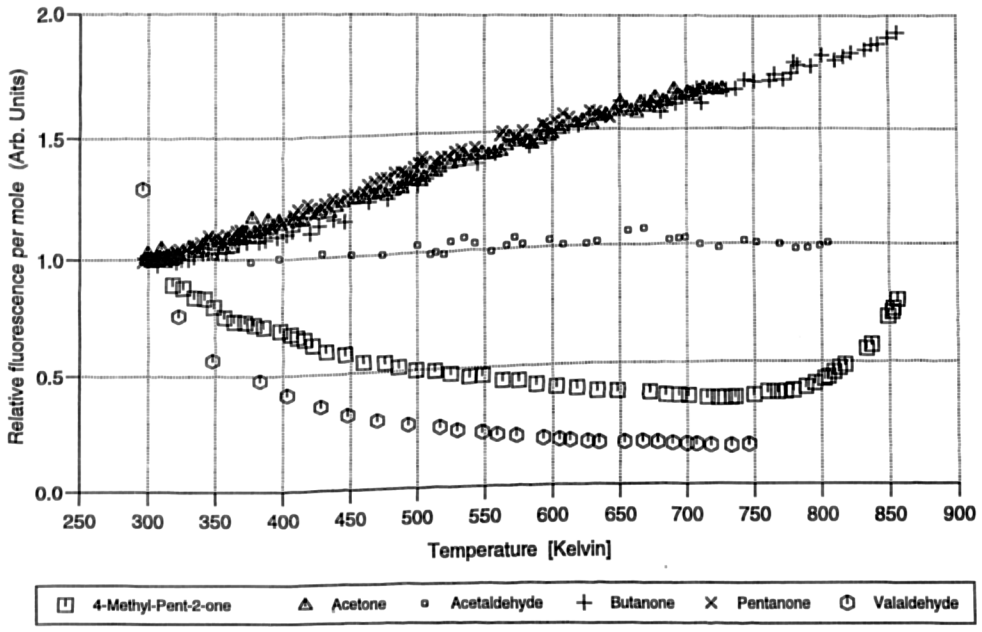

Fig. 3.5: Relative fluorescence of various carbonyl compounds with temperature (from Tait et al 1992).

showed that different carrier gases (nitrogen and air) did not change the fluorescence behaviour between 300 and 700 K at atmospheric pressure. This suggests that the fluorescence from acetone is insensitive to quenching by oxygen over this range of conditions. Studies by Lawrenz (1992) and Bryce (1996) revealed only a small pressure dependence of the fluorescence from acetone up to 10 bar when excited with 308 nm at room temperature. The temperature dependence of the acetone fluorescence was found to be linear at atmospheric pressure (Fig. 3.5). The effect of temperature on fluorescence at elevated pressures has not yet been studied, due to the complex nature of such an experiment (Bryce 1996). It is unlikely that the temperature dependency of the fluorescence is significantly different at pressures up to 2 bar (the maximum cylinder pressure during measurements in the current work) compared to ambient pressure. However this remains an area of slight uncertainty until quantitative data is available.

The fluorescence properties of acetaldehyde has been less intensively studied. Lawrenz (1992) found fluorescence intensities from acetaldehyde to be directly proportional to concentration. The fluorescence of acetaldehyde was found to be almost independent of pressure at room temperature (Bryce 1996) and independent of temperature at atmospheric pressure (Fig. 3.5) when excited with 308 nm.

Both acetaldehyde and acetone are soluble in iso-octane. However, acetaldehyde was rejected as a fuel marker because of a large difference in vaporisation characteristics compared with iso-octane. Acetaldehyde has a vapour pressure of 1 bar at 21 °C whereas iso-octane attains this pressure at 99 °C. Fuel injection into an inlet port, where the fuel is allowed to vaporise and mix with the intake air, would lead to a

Table 1: Physical properties of various fuel marker

Fuel Marker	Molecular Weight [g/mole]	Boiling Point [°C]	Density [g/cm^3]	Vapour Phase Mass Diffusion[1)] [10^{-6} m^2/s]
Iso-Octane	114.23	99.2	0.6919	10.0
Acetaldehyde	44.05	20.8	0.7831	18.3
Acetone	58.08	56.2	0.7899	15.6
Butanone	72.12	79.6	0.8054	
3-Pentanone	86.14	101.7	0.8138	12.4

[1)] in air at a pressure of 1 bar and a temperature of 373 K.

separation of the iso-octane and the doped acetaldehyde (Harding 1996). It is also doubtful whether acetone (b.p. 56 °C) would be likely to follow the iso-octane sufficiently closely, due to the difference in vaporisation characteristics (see Table 1).

One species with an almost perfect match of its rate of vaporisation to that of iso-octane is 3-pentanone, also known as diethyl-ketone. The absorption and fluorescence spectra of 3-pentanone are displayed in Figure 3.3 and 3.4 respectively. The emission spectrum is identical to that of acetone, i. e. broadband emission from 330 nm to 600 nm with a maximum at 430 nm. The fluorescence intensity of 3-pentanone, is like acetone, proportional to temperature at atmospheric pressure (Fig. 3.5) and essentially independent of pressure at room temperature when excited at 308 nm (Lawrenz 1992, Bryce 1996). Bryce (1996) also found that like acetone 3-pentanone is insensitive to quenching by oxygen. Neij (1994) and Johansson (1995) reported that the fluorescence intensity is directly proportional to the laser intensity for excitation energies from 10 to 100 mJ. They also established a linear relationship between the fluorescence intensity and pentanone concentration when excited at 248 nm. The close spectral similarity of pentanone to acetone fluorescence is most likely due to the chemical similarity; effectively the methyl group in acetone is substituted by an ethyl group in pentanone.

The rate of vaporisation of 3-pentanone (b.p. 101.7 °C) almost perfectly matches that of iso-octane (b.p. 99.7 °C). Also the vapour phase mass diffusion in air is similar to iso-octane. Therefore 3-pentanone was chosen as fuel marker in preference to acetone. By experiment it was found that a mixture of 75 vol% of iso-octane and 25 vol% of 3-pentanone gives a good signal to noise ratio, was optically thin and produced stable combustion.

3.4 Influence of Vaporisation Characteristics on Mixing

Measurements with two different markers, butanone and acetone, were compared to evaluate the influence of the vaporisation characteristics of different fuel markers on apparent fuel distribution. Sets of 20 single shot fluorescence images were recorded and subsequently averaged for both butanone and acetone as fuel markers. The fuel was a blend of three parts of iso-octane and one part of seed. The measurements were taken in the Honda Mk 1 research engine (see *Chapter 4.1*), operated with 1500 rpm, with ignition at 680° CA ATDC and an AFR of 16.

The resulting images for both fuel markers were corrected for background contribution and flatfielded against the same calibration image, which used butanone as seed. Figures 3.6 shows the mean fuel distribution for both fuel markers. Both images were normalised by their respective mean and multiplied by the factor 100 in order to correct for the difference in the fluorescence yield between the two seeds. The apparent fuel distribution is very similar. Normalising the acetone image by the butanone image and multiplication with the factor 100 results in the percentage difference in the fuel concentration between the two seeds (Fig. 3.7). On average the fuel concentration varies by 2.7 % between the two seeds. This reflects approximately the repeatability of the measurement of 2.9 %, as observed in the difference of subsequent normalising images (Fig. 3.8).

These measurements suggest that the different volatilities of the seeds with a boiling point range between 56 - 80 °C result in only very small differences in the observed fuel distribution. However, this conclusion might not hold for species with substantially differing volatilities, such as fractions of a commercial grade gasoline near the lower end and near the upper end of the gasoline boiling range (b.p. ≈ 20 - 200 °C). The effect on mixing of low and high boiling fuels was observed by Harding (1996) in a gas turbine. By imaging the vapour concentration in the duct of a gas turbine combuster, S. Harding (1996) found that acetaldehyde (b.p. 21 °C) followed the airflow in the centre of the duct, whereas kerosene (b.p. range 150 - 260 °C) exhibited a near uniform distribution over the whole duct area. It was concluded that the low boiling acetaldehyde will vaporise instantaneously after injection and the vapour phase will follow the air stream parallel to the injector axis. Since gas-gas mixing is slow, the mixture remains heterogeneous. In the case of kerosene, after injection the droplets will traject throughout the air stream and gradually vaporise, leading to a near homogeneous mixture. For IC engines with concentric swirling inlet flows with little mixing orthogonal to the flow direction the effect as observed by Harding (1996) could be important. Therefore, by using 3-pentanone (b.p. 101.7 °C) as fuel marker which has a boiling point close to the middle of the boiling range of a typical commercial-grade gasoline, the fuel marker will not only represent the distribution of iso-octane (b.p. 99.2 °C) but is also likely to give a realistic picture of the fuel distribution of a typical pump-fuel.

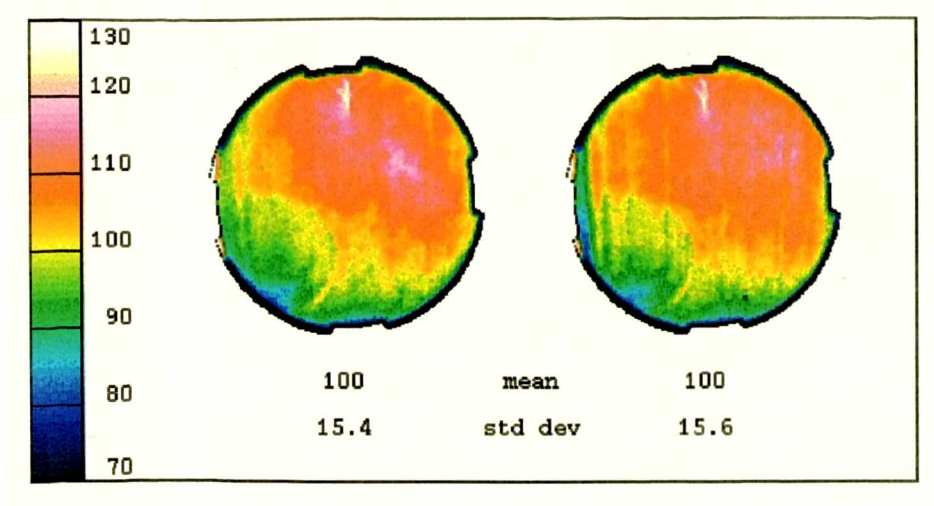

Fig. 3.6: Mean fuel concentration in a plane parallel to the piston with acetone (left) and butanone (right) as fluorescence marker as measured in the Mk 1 engine under the same conditions. Mean fuel concentrations were normalised to 100.

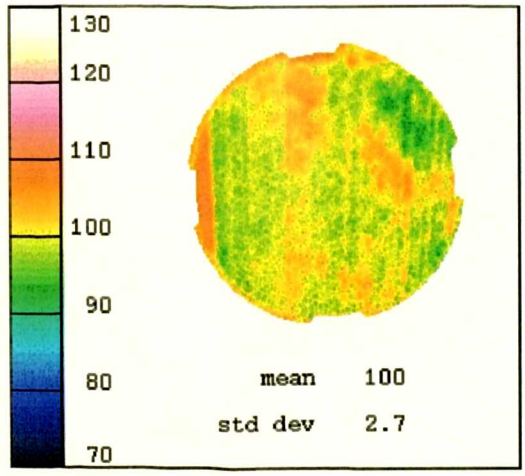

Fig. 3.7: Fractional difference between acetone distribution and butanone distribution multiplied by the factor 100. The mean variation across the image is 2.7 %.

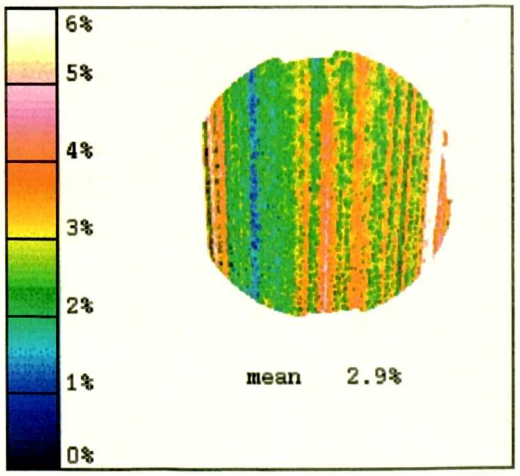

Fig. 3.8: Fluctuation around the mean signal of 10 successive calibration images. On average the fluctuation is 2.9 %.

3.5 Image Processing

The raw images of the fuel distributions have to be post-processed in order to generate quantitative data.

3.5.1 Noise and Laser Profile Inhomogeneity

The signal collected at each pixel of the camera is formed from several contributions; a part of it is proportional to the fuel concentration, laser intensity and collection efficiency and a second part arises from laser-generated background fluorescence, intensifier noise, thermal CCD noise and CCD electronic offset.

Spatial variations in the laser sheet profile, intensifier gain profile, CCD sensitivity and collection optics efficiency result in a scalar factor to be multiplied to the signal arising from the fluorescence of the seed. This causes the effective gain of the detection system to vary from pixel-to-pixel. Thus the data images need to be corrected for these spatial variations by normalising against a calibration image. A calibration image can be obtained from a uniform concentration of the fuel marker homogeneously mixed across the cylinder of the engine.

When the image is read from the CCD chip, a constant offset is added to each pixel to prevent amplifier noise causing any of the signal integrations becoming negative. The finite dark current, even at the temperature of the thermo-electrically or water-cooled CCD's adds a random contribution to each pixel - thermal noise. Scattered laser light gives rise to fluorescence of species absorbed on surrounding engine surfaces. All these effects add an unwanted contribution which is independent of fuel concentration. This can be corrected for by subtracting a background image from each of the images of interest. An exposure, taken while the engine is motored, provides a suitable background image. Ideally several background images should be averaged, this reduces errors due to shot noise and thermal noise.

The calibration and background corrections are made on the basis of mean laser sheet characteristics. This introduces an error due to shot noise and pulse-to-pulse fluctuations in the laser sheet. This error was found by measurement using calibration images to be usually between 2 - 3% (see also *Chapter 5*). On some of the images it resulted in a slight linear modulation orthogonal to the laser propagation direction.

The corrected fuel fraction image intensity, I_{Final}, is given by:

$$I_{Final} = \frac{I_{Raw} - I_{Back}}{I_{Calib} - I_{Back}} \tag{3.1}$$

where I_{Raw} is the raw image intensity collected whilst running the engine, I_{Calib} is the calibration image intensity and I_{Back} is the background image intensity. The processed image I_{Final} therefore displays a relative fuel concentration distribution at the measurement condition.

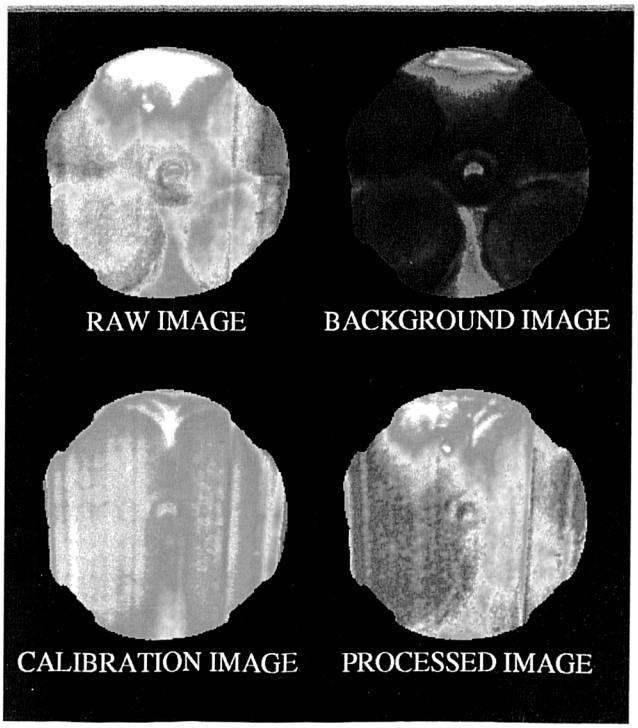

Fig 3.9: Image processing

3.5.2 Density and Temperature Normalisation

With 3-pentanone as seed, the fluorescence signal is proportional to number density and temperature in the measurement volume (see *section 3.3*):

$$I_{Final} \propto \frac{n_f}{V} \cdot (a + b \cdot T) \tag{3.2}$$

where n_f is the number of seed molecules per unit volume (V); a and b are coefficients which account for the temperature (T) dependence and have been estimated from the data in Figure 3.5. Equation 3.2 shows that at a given temperature the fluorescence signal is proportional to the number density. However, the most important parameter is the ratio of fuel-to-air, not the density of the fuel molecules. Since pressure is constantly changing in an IC engine, images must be corrected for density effects in order to represent fuel-to-air ratios. The following describes a procedure which corrects the images for pressure and temperature to give estimates of fuel-to-air ratios.

Images taken during Compression Stroke

During compression, after the inlet valve has closed, the number density of fuel molecules in the cylinder increases and the fluorescence signal increases correspondingly. However, the number density of air molecules also increases during compression. Therefore the ratio of the number of fuel molecules to the number of air molecules remains constant and the apparent increase in fluorescence signal does not indicate an increase in the fuel-to-air ratio. To create an AFR image, this effect must be taken into account.

Consider an equation for intensity I_1 normalised to a reference condition intensity I_0 :

$$\frac{I_1}{I_0} = \frac{n_{f1} \cdot V_0}{n_{f2} \cdot V_1} \cdot \frac{(a + b \cdot T_1)}{(a + b \cdot T_0)} \tag{3.3}$$

Using the ideal gas law, number density can be expressed in terms of pressure p and temperature T by,

$$\frac{n}{V} = \frac{p}{\tilde{R} \cdot T} \tag{3.4}$$

and relation 3.3 can be rewritten:

$$\frac{I_1}{I_0} = \frac{p_{f1} \cdot T_0}{p_{f0} \cdot T_1} \cdot \frac{(a + b \cdot T_1)}{(a + b \cdot T_0)} \tag{3.5}$$

where p_f is the partial pressure of the fuel vapour. The total pressure in the cylinder will be the sum of the partial pressures of air and fuel vapour. With

$$\frac{p_1}{p_0} = \frac{p_{f1}}{p_{f0}} = \frac{p_{a1}}{p_{a0}} \text{ [1]} \tag{3.6}$$

the normalising factor can then be written as:

$$\boxed{f_N = \frac{I_1}{I_0} = \frac{p_1 \cdot T_0}{p_0 \cdot T_1} \cdot \frac{(a + b \cdot T_1)}{(a + b \cdot T_0)}} \tag{3.7}$$

p_1 and p_0 can be taken from the indicated cylinder pressure. This will also take the effect of blow-by into account.

---

[1] The air/fuel ratio (AFR) is defined as the ratio of the mass (m) of air and fuel:

$$AFR = \frac{m_a}{m_f} = \frac{n_a \cdot M_a}{n_f \cdot M_f} \qquad \Rightarrow \qquad \frac{n_a}{n_f} = \frac{M_f}{M_a} \cdot AFR = k$$

where the suffix a denotes air, f the fuel vapour and M is the molecular mass. According to the ideal gas law

$$p_f \cdot V = n_f \cdot \tilde{R} \cdot T \qquad \text{and} \qquad p_a \cdot V = n_a \cdot \tilde{R} \cdot T .$$

Equating: $$\frac{p_f}{p_a} = \frac{n_f}{n_a} = \frac{1}{k}$$

The total pressure p is the sum of the partial pressures of fuel vapour p_f and air p_a:

$$p = p_f + p_a = p_f + k \cdot p_f = p_f \cdot (1 + k)$$

Equating: $$\frac{p_1}{p_2} = \frac{p_{f1} \cdot (1 + k)}{p_{f2} \cdot (1 + k)}$$

With $AFR_1 = AFR_2$: $$\frac{p_1}{p_2} = \frac{p_{f1}}{p_{f2}} = \frac{p_{a1}}{p_{a2}}$$

Images taken during Inlet Stroke

During the inlet stroke (inlet valve open) air and fuel enter the cylinder and therefore the AFR is not constant. The inlet stroke can be separated into two independent processes. Consider first the change in cylinder volume. If the mass of the charge remains constant ($n_{f1} = n_{f2}$) during the volume change, the signal intensity is reduced due to a reduction in the number density of fuel molecules. Yet the AFR remains constant. To account for this effect, the normalising factor f_1 can be written as:

$$f_1 = \frac{I_1}{I_0} = \frac{V_0}{V_1} \cdot \frac{(a + b \cdot T_1)}{(a + b \cdot T_0)}. \tag{3.8}$$

In the second process, fuel and air are introduced to the cylinder charge through the inlet valve. The additional fuel increases the number density of molecules and the fluorescence signal increases proportionally. Thus the decrease in AFR has to be accounted for by the signal intensity. Adding air to the cylinder charge increases the AFR, whilst maintaining a constant signal intensity. This is accounted for by a normalising factor f_2:

$$f_2 = \frac{n_{a1}}{n_{a0}} \tag{3.9}$$

where n_a is the number of air molecules. According to the ideal gas law the number of molecules can be expressed as

$$n_a = \frac{p_a \cdot V}{\tilde{R} \cdot T}. \tag{3.10}$$

Therefore equation 3.9 can be rewritten as:

$$f_2 = \frac{p_{a1} \cdot V_1 \cdot T_0}{p_{a0} \cdot V_0 \cdot T_1}. \tag{3.11}$$

The normalising factor for both change in volume (eq. 3.8) and change in air mass (eq. 3.11) is therefore:

$$\boxed{f_N = f_1 \cdot f_2 = \frac{p_{a1} \cdot T_0}{p_{a0} \cdot T_1} \cdot \frac{a + b \cdot T_1}{a + b \cdot T_0}} \tag{3.12}$$

where p_{a1} and p_{a2} can be obtained from the indicated cylinder pressure. This will introduce an error, since the measured pressure is the sum of the partial pressure of air and the partial (vapour) pressure of the fuel and the AFR is not constant during the inlet stroke. However, this error is expected to be small, because of the order of magnitude difference between the partial pressures of air and fuel vapour.

The images were normalised by the factor f_N to give relative fuel concentration distributions at a reference condition (p_0, T_0).

3.6 Calibration of Images

Following the initial post-processing, as outlined above, the images represent the actual LIF signal from the doped fuel at a certain condition (density, temperature). This signal can be converted into absolute fuel concentration by relating it to the signal level of a known fuel concentration field. In conjunction with every measurement sequence in the engine, measurements of homogeneous fuel distributions were recorded. These calibration images have already been used to normalise the laser profile and the intensifier gain profile as described in the previous section. If the concentration of the seed for the calibration images is known, the measured images can be converted to images of absolute fuel concentration distributions.

3.6.1 Seed Concentration in Fluorescence Image

The processed image represents a ratio of a data image and a calibration image as shown in relation (3.1):

$$I_{Final} = \frac{I_{Data}}{I_{Calib}}. \tag{3.13}$$

Since the fluorescence signal is proportional to the concentration of the species in the measurement volume probed it follows that

$$I_{Final} \propto \frac{X_{Data}}{X_{Calib}} \tag{3.14}$$

where X_{Data} is the seed concentration as represented by the data image and X_{Calib} the seed concentration represented by the calibration image. The fluorescence signal intensity also depends on the temperature and pressure conditions and the actual seed used for the data and calibration images. By introducing factors of proportionality, the relation (3.14) can be re-arranged as

$$I_{Final} = f_N \cdot f_F \cdot \frac{X_{Data}}{X_{Calib}}. \tag{3.15}$$

The factor f_N corrects for the difference in temperature and pressure between the data and calibration condition (see *3.5.2*).

$$f_N = \frac{p_{Data} \cdot T_{Calib}}{p_{Calib} \cdot T_{Data}} \cdot \frac{a + b \cdot T_{Data}}{c + d \cdot T_{Calib}} \tag{3.16}$$

If different fluorescence markers are used for the calibration and the fuel visualisation, the difference in the fluorescence yield of the two seeds at the calibration condition has also to be accounted for and the factor f_F is:

$$f_F = \frac{Fluorescence\ \ Yield_{Seed\ Data}\ (p,T)}{Fluorescence\ \ Yield_{Seed\ Calibration}\ (p,T)}. \tag{3.17}$$

Where the seed concentration in the calibration gas is known and the measurement conditions in both calibration and fuel visualisation are well defined, the seed concentration can be obtained from the signal intensity in the processed data image.

$$\boxed{X_{Data} = I_{Final} \cdot \frac{X_{Calib}}{f_N \cdot f_F} \qquad \left[\frac{mol}{m^3}\right]} \tag{3.18}$$

3.6.2 Fuel Concentration as Function of Seed Concentration

In this investigation a mixture of three parts of iso-octane and one part of 3-pentanone by volume was used as fuel.

$$\frac{V_{Oct}}{V_{Pent}} = \frac{3}{1}$$

The volume V can be expressed in terms of number of molecules n, molar Mass M and density ρ by

$$n = \frac{m}{M} = \frac{V \cdot \rho}{M} \qquad \Rightarrow \qquad V = n \cdot \frac{M}{\rho}.$$

Using the above expressions it follows that:

$$\frac{V_{Oct}}{V_{Pent}} = \frac{n_{Oct} \cdot M_{Oct} \cdot \rho_{Pent}}{n_{Pent} \cdot M_{Pent} \cdot \rho_{Oct}} = \frac{3}{1} \tag{3.19}$$

and the number of iso-octane molecules can be expressed as a function of the number of 3-pentanone molecules:

$$n_{Oct} = 3 \cdot \frac{M_{Pent} \cdot \rho_{Oct}}{M_{Oct} \cdot \rho_{Pent}} \cdot n_{Pent}. \tag{3.20}$$

With M and ρ from Table 1:

$$n_{Oct} = 3 \cdot \frac{86 \cdot 7025}{114 \cdot 8103} \cdot n_{Pent} = 1.962 \cdot n_{Pent}, \tag{3.21}$$

and the number of fuel molecules becomes:

$$n_{Fuel} = n_{Oct} + n_{Pent} = 1.962 \cdot n_{Pent} + 1 \cdot n_{Pent} = 2.962 \cdot n_{Pent} \qquad [mol], \tag{3.22}$$

or, expressed as concentrations;

$$\boxed{X_{Fuel} = 2.962 \cdot X_{Pent} \qquad \left[\frac{mol}{m^3}\right]}. \tag{3.23}$$

The concentration of the fuel can be calculated from the concentration of the seed as obtained from the data images (eq. 3.18), if the fuel composition is known.

3.6.3 Air Concentration in the Engine Cylinder

The total number of molecules per unit volume in the cylinder can be expressed as:

$$X_{Total} = X_{Air} + X_{Fuel} + X_{Residual} = X_{Air} + 2.962 \cdot X_{Pent} + X_{Residual} \qquad \left[\frac{mol}{m^3}\right]. \qquad (3.24)$$

Using the ideal gas law, the total concentration can be expressed in terms of temperature T and pressure p:

$$X_{Total} = \frac{n_{Total}}{V} = \frac{p}{\tilde{R} \cdot T} \qquad \left[\frac{mol}{m^3}\right]. \qquad (3.25)$$

Relation 3.24 can be rewritten:

$$X_{Air} = X_{Total} - 2.962 \cdot X_{Pent} - X_{Residual}, \qquad (3.26)$$

and introducing eq. 3.25 results in

$$X_{Air} = \frac{p}{\tilde{R} \cdot T} - 2.962 \cdot X_{Pent} - X_{Residual} \qquad \left[\frac{mol}{m^3}\right]. \qquad (3.27)$$

The 3-pentanone concentration X_{Pent} can be obtained from equation (3.18) for the calibration condition. Therefore, pressure p and temperature T in eq. (3.27) are as measured during calibration. The residual concentration $X_{Residual}$ can so far only be estimated. Galliot (1990) measured residual gas fractions of between 5 and 10 % at full load and about 20 % at part load condition (0.45 bar inlet pressure) in an engine with a compression ratio of 8.3:1 and a valve overlap of 3° CA operating at 1500 rpm. These engine parameter and operation conditions match very closely those used for this investigation (see *Chapter 4.1 and 5*). Using Galliot's residual gas concentration measurement as an approximation, the air concentration X_{Air} can be expressed as a function of seed concentration X_{pent}:

$$\boxed{X_{Air} = 0.8 \cdot \frac{p_{Calib}}{\tilde{R} \cdot T_{Calib}} - 2.962 \cdot X_{Pent} \qquad \left[\frac{mol}{m^3}\right]} \qquad (3.28)$$

3.6.4 Equivalence Ratio as Function of Seed Concentration

The air/fuel ratio is defined as:

$$AFR = \frac{m_{Air}}{m_{Fuel}} = \frac{n_{Air} \cdot M_{Air}}{n_{Fuel} \cdot M_{Fuel}} \qquad (3.29)$$

where m denotes the mass, n the number of molecules and M the molar mass. Since pressure and temperature in the cylinder are the same for air and fuel, the AFR can also be written in terms of concentrations:

$$AFR = \frac{X_{Air} \cdot M_{Air}}{X_{Fuel} \cdot M_{Fuel}}. \tag{3.30}$$

Introducing eq. 3.23 and 3.28 and the molar mass of air and fuel[1], eq. 3.30 becomes

$$\boxed{AFR = \frac{\left(0.8 \cdot \frac{p_{Calib}}{\tilde{R} \cdot T_{Calib}} - 2.962 \cdot X_{Pent}\right) \cdot 28.74}{2.962 \cdot X_{Pent} \cdot 104.55}}, \tag{3.31}$$

and the AFR can be expressed as a function of the 3-pentanone concentration as observed in the fluorescence image (eq. 3.18). The AFR can easily be converted to an equivalence ratio:

$$\phi = \frac{AFR_{Stoichiometry}}{AFR} = \frac{14}{AFR}. \tag{3.32}$$

Data images converted using relations 3.31 and 3.32 will display absolute equivalence ratio maps.

3.7 Gas Temperature during Inlet and Compression Stroke

As explained in the previous section, fluorescence and density are temperature and pressure dependent. In order to normalise fluorescence images such that they display absolute fuel concentrations, the temperature and pressure in the cylinder at the measurement time have to be known. Pressure can readily be obtained from a pressure transducer mounted in the cylinder head (see *Chapter 4.2*). Unfortunately there is no simple way to measure bulk temperature in a firing SI engine. Thermocouples do not have the frequency response to deliver a meaningful temperature profile. Hot wire probes which would give a sufficiently fast response, will not survive in the hostile conditions encountered in a firing SI engine. The only way to measure an instantaneous temperature profile is by CARS (Lucht 1987, Marie 1987) and possibly LIF (Seitzman 1985, Chang 1991, McMillin 1991). However, such measurements are complex and were beyond the scope of this study.

---

[1] The molar mass M of the fuel used in this investigation (0.75 Vol% iso-octane + 0.25 Vol% 3-pentanone):

$$m_{Fuel} = m_{Oct} + m_{Pent} \quad \Rightarrow \quad n_{Fuel} \cdot M_{Fuel} = n_{Oct} \cdot M_{Oct} + n_{Pent} \cdot M_{Pent}$$

$$M_{Fuel} = \frac{n_{Oct}}{n_{Fuel}} \cdot M_{Oct} + \frac{n_{Pent}}{n_{Fuel}} \cdot M_{Pent}$$

$$M_{Fuel} = \frac{1.962 \cdot n_{Pent}}{2.962 \cdot n_{Pent}} \cdot 114 + \frac{n_{Pent}}{2.962 \cdot n_{Pent}} \cdot 86 \quad \Rightarrow \quad M_{Fuel} = 104.55 \ Kg / Kmol$$

An alternative approach is to calculate the temperature. Therefore a very simplified model for the treatment of the inlet and compression strokes was considered.

The process was assumed to be reversible and adiabatic. Initially the inlet valve was considered to open and the cylinder pressure fall to that of the inlet. Since the pressure in the inlet was less than atmospheric some of the residual gases enter the manifold. These residual gases were assumed to re-enter the cylinder at the start of the intake stroke, prior to entry of fresh charge. The inlet manifold was assumed to have an infinitely large area and pressure was not increased when the inlet valve opened. No valve overlap was allowed to occur, as mass flowrates through the valves would than have to be considered; valve overlap is indeed negligible on the engine used in this work (Fig. 4.2). Exhaust valve closing and inlet valve opening were assumed to occur at TDC.

The inlet process was considered in 20° crank angle increments. The temperature of the fresh charge was assumed to be 300 K. The cylinder pressure was taken from the indicated pressure curve as measured in the engine. The temperature of the residual gas was estimated to be 1100 K from calculations using the LEEDS ENGINE SIMULATION MODEL (Merdjani 1993), and the internal energy of the residual charge was calculated at this temperature. The fresh charge and residual fraction were then considered to mix. The process is adiabatic i. e. $Q = 0$, hence the energy balance can be expressed as:

$$m_{in} \cdot h_{in} = W_{12} + m_2 \cdot u_2 - m_1 \cdot u_1 \tag{3.33}$$

The temperature of the mixture in the inlet manifold is constant throughout the stroke, i. e. $h_{in} = c_{p_{in}} \cdot T_{inlet}$ and using the caloric equations the mass induced can be calculated:

$$m_{in} = \frac{W_{12} + m_2 \cdot c_{v_2} \cdot T_2 - m_1 \cdot c_{v_1} \cdot T_1}{c_{p_{in}} \cdot T_{inlet}} \tag{3.34}$$

where the work done is given by the mean pressure during the increment times the swept volume i. e. $W_{12} = (p_1 + p_2)/2 \cdot (V_2 - V_1)$ and the mass of the charge at the beginning and the end of the increment is given by:

$$m_1 = \frac{p_1 \cdot V_1}{R_1 \cdot T_1} \qquad m_2 = m_1 + m_{in} = \frac{p_2 \cdot V_2}{R_2 \cdot T_2}$$

Knowing the induced mass, the temperature at the end of the increment can be calculated using the following expression:

$$T_2 = \frac{p_2 \cdot V_2}{R_2 \cdot (m_{in} + m_1)} \tag{3.35}$$

Since the specific heat c_{v2} is a function of temperature and mixture composition and the gas constant R_2 a function of mixture composition the temperature T_2 at the end of the increment was found by an iterative procedure. First the specific heat c_{v2} and the specific gas constant R_2 were calculated for the conditions (mixture composition and

temperature) at the beginning of the increment using the empirical equations and coefficients of McBride (1993). The induced mass and the temperature were then calculated using Equations 3.34 and 3.35. For the next iteration step the specific heat c_{v2} and the gas constant R_2 were calculated from this new approximation. This process was repeated until the specific heat changed by less than 0.05% between iteration steps. The next increment was then considered.

When the piston reached the crank angle of inlet valve closing an isentropic compression was assumed and an isentropic exponent γ was estimated so as to closely match the measured pressure curve up until ignition.

In this model heat transfer between the cylinder walls and the gas was neglected and a gaseous fuel assumed. More elaborate models taking into account the heat transfer and heat of vaporisation may be used in future studies. However, given the precision required for the temperature it was considered that these estimates of temperature would be sufficient to give sizeable estimates of AFR. Estimating the temperature with an accuracy of 50 K causes an uncertainty of approximately 10 % in estimating the AFR represented by the image intensity at the time of ignition. The error in estimating the relative temperature sequence during the important compression stroke is expected to be small since the temperature estimates are based on the measured pressure profile; blow-by and heat transfer will be reflected in the cylinder pressure.

3.8 Summary

Planar LIF has the potential for real time in-cylinder fuel concentration measurements in an operating SI engine. However, LIF measurements require the species which is to be probed, to have suitable fluorescence properties. Unfortunately, multi-component commercial-grade gasoline is unsuitable for fluorescence measurements and therefore had to be replaced by a blend of a single component fuel, iso-octane, and a fluorescence marker, 3-pentanone; 3-pentanone has favourable spectroscopic properties and is chemically and physically similar to iso-octane. The in-cylinder distribution of 3-pentanone will also give a good estimate of the distribution of a pump fuel, since the boiling point of the fluorescence marker is in the middle of the boiling range of a commercial-grade gasoline. In order to provide quantitative results, fluorescence images require post-processing, i.e. removing of background signal and normalising of laser-sheet inhomogeneities. Fluorescence images can be calibrated by comparison with an image of known fuel concentration. This requires measurement and calibration conditions to be well defined.

Chapter 4

Experimental Set-Up for Fuel Visualisation

The equipment used for the planar LIF measurements of fuel concentration in this work is described; the research engine, the laser system with the sheet-forming optics and the fluorescence detection system. Additionally, the timing and synchronisation of the experimental equipment and the measurement and calibration procedure for fuel visualisation are described.

4.1 Introduction

A schematic of the experimental set-up for planar LIF fuel concentration measurements in the cylinder of an optical research engine is shown in Figure 4.1. A laser beam was formed into a sheet using spherical and cylindrical lenses and passed through the windows in the cylinder of the research engine, illuminating a plane parallel to the piston crown. Fluorescence from the fuel molecules was collected at right angles via a window in the piston and a 45° mirror with an intensified CCD camera.. The resulting instantaneous concentration images were transferred on-line to a Personal Computer for instant display and storage. Simultaneously in-cylinder pressure may be recorded.

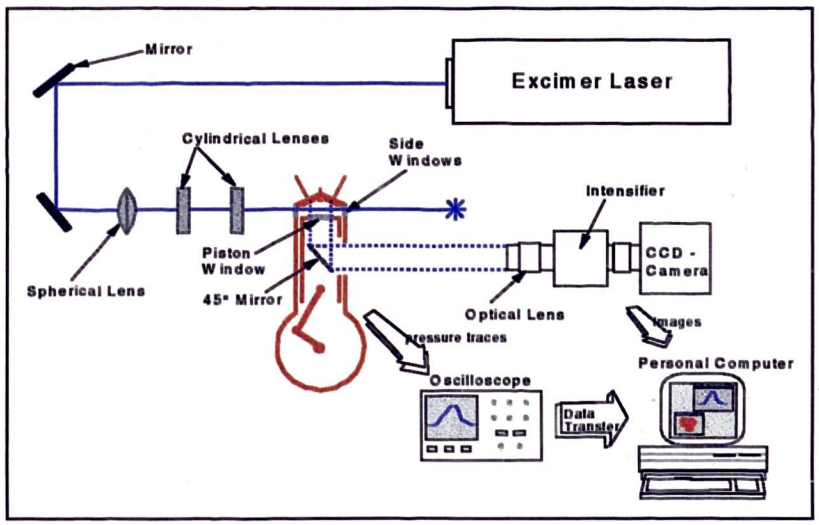

Fig. 4.1: Schematic of Experimental Set-Up.

Table 2: Engine Parameters

	Optical Engine BKR-E-0003	Production Engine Honda VTEC-E
Number of Cylinders	1	4 in line
Displacement (ccm)	360	1493
Bore x Stroke (mm)	75 x 81.5	75 x 84.5
Compression Ratio	Mk 1: 9.1 Mk 2: 7.6	9.3
Valve Mechanism	sohc VTEC-E	sohc VTEC-E
Number of Valves	4	4
Valve Diameter (mm)		
Inlet	27.5	27.5
Exhaust	23.5	23.5

4.2 Engine Configuration

A single-cylinder research engine with optical access was used and it is shown in Figure 4.3 - 4.6. The engine was designed specifically for this project by Honda R&D, Japan, to give good optical access while retaining most of the engine characteristics of a typical production engine.

A notable feature of this particular engine is the valve train which is based on the Honda sohc VTEC-E valve deactivation mechanism. This mechanism has been previously described by Horie (1993). The engine has a 4-valve pent-roof cylinder head with high-swirl and non-swirl inlet ports. In the *VTEC-E mode*, only the valve controlling the high-swirl inlet port (referred to as primary inlet valve) opens to its maximum lift of 8 mm. This generates the high in-cylinder swirl required for stable lean burn operation. The VTEC-E mechanism reduces the lift of the valve on the non-swirl inlet port (secondary inlet valve) to 0.65 mm. This valve is not fully closed so as to permit drainage of the fuel that would otherwise remain trapped in the secondary port. In the production engine, to achieve good volumetric efficiency, the secondary valve opens fully to 8 mm at engine speeds above 2500 and 3200 rpm, depending on the load condition (see also 1.4). For this study the engine was only operated in the VTEC-E mode with a speed of 1500 rpm. The corresponding primary and secondary valve lifts are shown in Figure 4.2. The resulting swirl ratio[1] at this running condition is about 2.1

[1] In an operating engine the *swirl* and *tumble ratio* are defined as the angular velocity of a solid body rotational flow (ω_S, ω_T), devided by the crankshaft angular rotational speed $2\pi N$ (Heywood 1988).

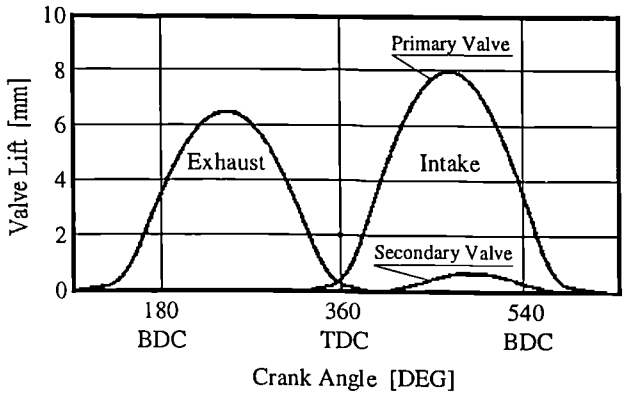

Fig. 4.2: Valve lift in the VTEC-E mode for the exhaust, primary inlet and secondary inlet valves.

and the tumble ratio[1] 1.9. Table 2 provides the principal parameters of the research engine and compares these with the equivalent for the production version which is used in the Honda Civic.

Two types of engines, offering differing optical access to the combustion chamber, were employed in this study. Both engines had a spacer placed between the cylinder head and the engine block with a 45° mirror mounted inside the spacer on the cylinder block. The piston was elongated and hollow, with the inlet and exhaust side walls removed, such that the fixed 45° mirror could be positioned directly under the cylinder axis. These modifications permitted a view of the combustion chamber through a fused silica window of 54 mm diameter, located in the piston top (Fig. 4.3). The visible area of the combustion chamber through the piston window is displayed in Figure 4.4.

In the engine referred to as Mk 1, a fused silica cylinder was mounted in the spacer directly beneath the head gasket (Fig. 4.3, 4.6). Window ports of 50 mm width, placed in the inlet and exhaust side of the cylinder spacer, enabled a UV laser sheet to pass across the combustion chamber and exit at the opposite side of the cylinder. This allowed, depending on the piston position, laser illumination of planes between 10 and 30 mm below the spark plug perpendicular to the pent-roof gable.

The engine referred to as Mk 2 had two fused silica window inserts on opposite sides in the elongated cylinder head providing a view along the pent-roof axis (Fig. 4.5). This allowed laser illumination of planes between the gable of the pent roof and a plane 15 mm below the spark plug (again depending on piston position). The cylinder head of the Mk 2 engine was made of cast iron instead of aluminium, but had otherwise the same geometries as the Mk 1 version. The elongated cylinder head of the Mk 2 version required the piston rings to be repositioned lower on the piston in order to avoid contact with the cylinder head gasket. This increased the crevice volume which in turn reduced the compression ratio from 9.1 to 7.6.

The production engine has a piston bowl providing a squish area 0.75 mm thick and 55 mm in diameter. A similar bowl was created in the optical engine, by receding the 55 mm diameter quartz window by 3 mm from the piston crown, thus providing a combustion chamber shape closely matching that of the production engine.

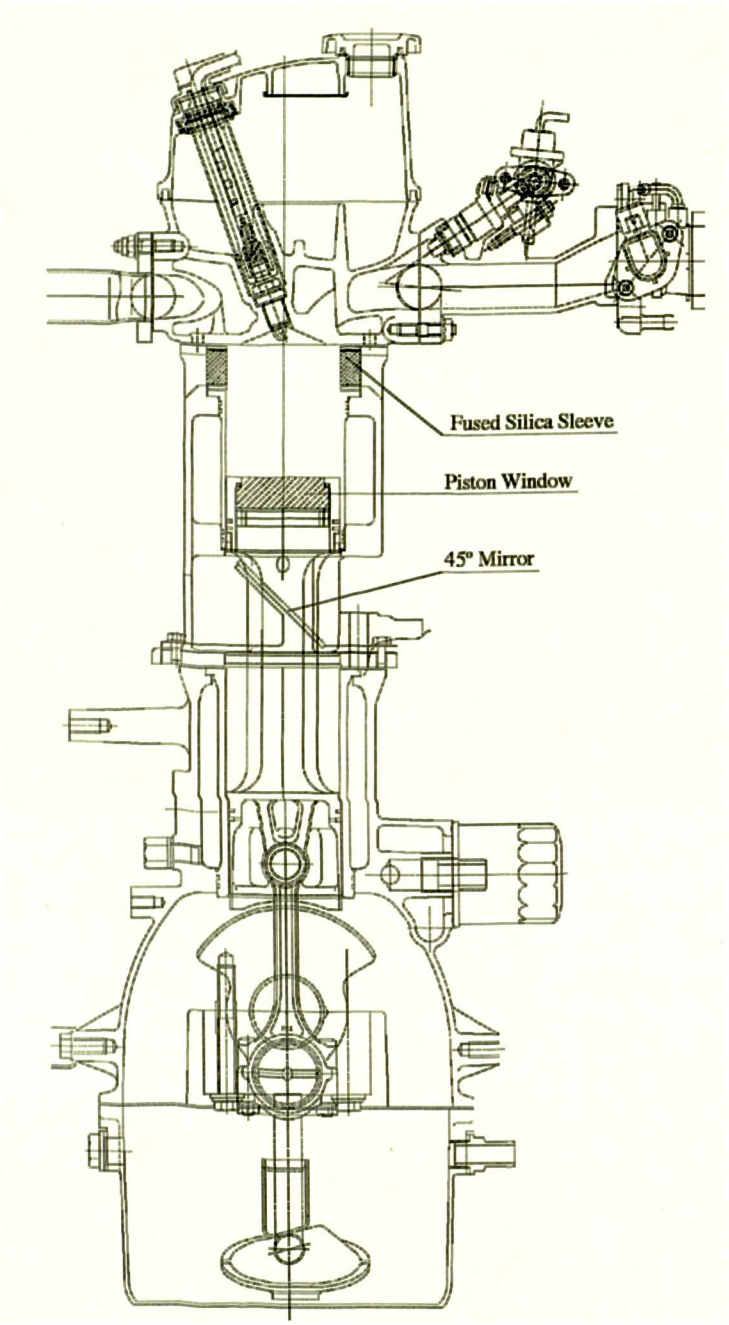

Fig. 4.3: Honda one-cylinder optical research engine (Mk 1).

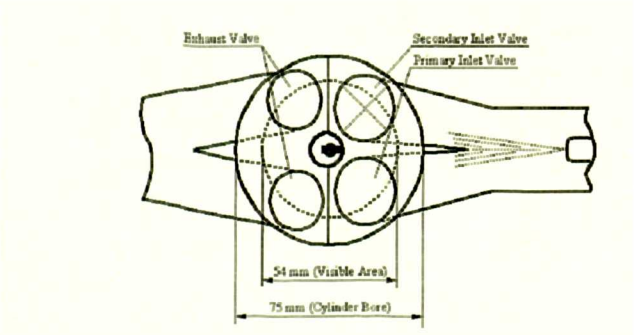

Fig. 4.4: Plan view of valve layout and visible area of the combustion chamber in the Honda VTEC-E research engine.

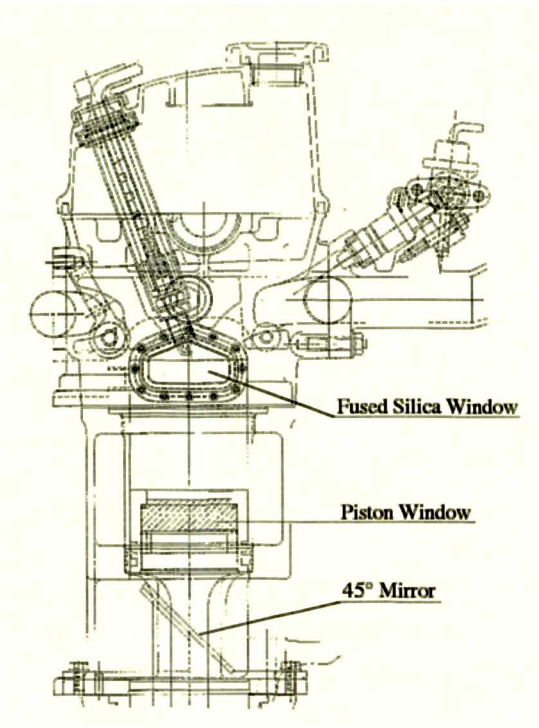

Fig. 4.5: Optical access to Mk 2 one-cylinder research engine for laser from timing side.

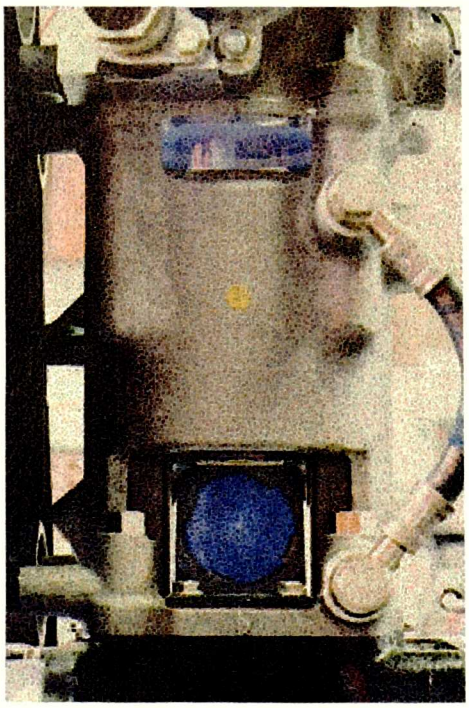

Fig. 4.6: Optical access to Mk 1 one-cylinder research engine for laser and camera from inlet side

To avoid fouling of the windows, oil had to be prevented from entering the combustion chamber. Therefore the cylinder liner in the spacer, connecting engine block and cylinder head, and the piston rings located near the piston crown were coated so as to allow unlubricated operation of this part of the engine. A vacuum pump attached to the sump and the cylinder head, removed oil vapour which otherwise could have passed the piston rings located at the bottom of the piston, which seal the engine block. Oil passing these rings could have misted up the 45° mirror and the lower surface of the piston window.

Air entered the engine through a throttle body and passed via an inlet plenum chamber; the manifold depression was measured in the inlet plenum. Fuel was drawn from the fuel tank by an electrical pump and supplied to the injector. Excess fuel returned via a pressure regulator to the fuel tank. This ensured a continuous supply of cool fuel to the injector. However, like all ketones, pentanone attacks rubber and since fuel pumps, regulators and injectors contain rubber components - mostly O-rings for sealing purposes - the fuel supply system of the engine had to be modified. The standard fuel lines, which are made of rubber, were replaced with copper lines and a PTFE ring was substituted for the O-ring on the inlet manifold. The only ketone-resistant fuel pumps available were of a diaphragm type. Since diaphragm pumps supply a pulsating flow, two accumulators were required to dampen out fluctuations in the fuel pressure. A modified Hoke ball and spring pressure regulator maintained a constant pressure of 2.5 bar. In a commercial gasoline fuel injector (Keihin 16450-PD5-A000) a rubber O-ring protects the solenoid from the fuel. This O-ring was replaced with a Teflon version which is ketone-resistant. Continuous operation for several hours was therefore possible using fuels seeded with ketones.

Crank angle was measured by a 1° resolution encoder attached to the crankshaft pulley. The encoder generated signals to trigger the custom-built engine controller which allowed to set the crank angle at which injection started, the duration of injection, the crank angle of ignition and the ignition duration. Ignition was pre-set for all experiments to 40° CA before TDC and 4 ms duration. The injection timing was the principal parameter for the measurements presented here. The injection duration controlled the value of the air-to-fuel ratio supplied to the engine. The stoichiometry of the charge entering the cylinder was continuously monitored by a heated, linear air-to-fuel (LAF) ratio zirconia-based high-speed sensor, which was mounted in the exhaust pipe. The exhaust sensor used was a calibrated version of the same type as described by Yamada (1992). The output voltage of the LAF sensor was displayed by a digital voltmeter and could be converted to AFR by means of a corresponding calibration curve. The fluctuations in the output voltage of the LAF sensor lead to an uncertainty of about 0.5 AFR in adjusting the injector pulse width.

The engine was mounted on an English Electric dynamometer regulated by a Saftronics controller to provide constant speed, which was 1500 rpm for the fuel visualisation experiments and 1200 rpm for the residual imaging experiments. The

engine was water cooled and the coolant preheated to 58 °C before operation. During firing operation the water temperature was controlled around 78 °C.

4.3 Pressure Measurements

In-cylinder pressures were recorded using an uncooled Kistler pressure-transducer (6121A1), which was fitted into the cylinder head. A Kistler charge amplifier (5011A1) converted the transducer signal into a voltage proportional to pressure. The pressure data was recorded by a Tektronix 2224 digital oscilloscope, connected to a PC via an IEEE bus. The oscilloscope had an 8 bit A-D converter and recorded single traces with either 1024 or 4096 data-points. The oscilloscope recorded the pressure of just over a full cycle plus a TDC mark as reference. The trigger point, corresponding to ignition, was set to be in the middle of the trace. The TDC signal was provided from the engine controller. The resolution of the pressure trace was calculated from the correspondence between ignition and TDC.

The piezoelectric pressure transducer only measures relative pressures. The pressure traces were corrected to absolute pressures on the assumption that the cylinder pressure at the end of the exhaust stroke is equal to the atmospheric pressure. In reality the pressure will be slightly higher than atmospheric, owing to the back pressure of the exhaust system.

Limited access to the combustion chamber did not permit the use of a cooling adapter for the pressure transducer. The pressure transducer was exposed to combustion gases reaching temperatures of more than 1500 K. This short term heating in the range of milliseconds provides a measuring error due to thermal stress in the sensor - short term drift. This short-term drift is less than 1 bar for the transducer used (Kuratle 1992).

The short-term drift mainly affects the low pressure part of the cycle. In this study the engine was operated heavily throttled (inlet manifold depression Pb = 450 mmHg) with the initial part of the compression stroke occurring below atmospheric pressure. Therefore the indicated mean effective pressure, calculated from the indicated pressure, contains a systematic error. Figure 4.7 illustrates this point. It shows the mean indicated pressure of 200 fired cycles and a motored cycle for the same inlet depression of 450 mmHg in a p-V diagram. The difference between the pressure in the exhaust and the inlet stroke should be the same in both cases. The measurement error in the low pressure part of the cycle also affects the slope of the compression curve, which will modify the imep. Comparison of the indicated pressure of 200 fired cycles showed only small variations in the low pressure part of the cycle. However, it is considered reasonable to use the measured imep for comparison of individual cycles taken under the same operating conditions, bearing in mind of course that the real imep will be higher than that indicated. Values derived from the pressure traces were gross imep, peak pressure and the crank angle of peak pressure.

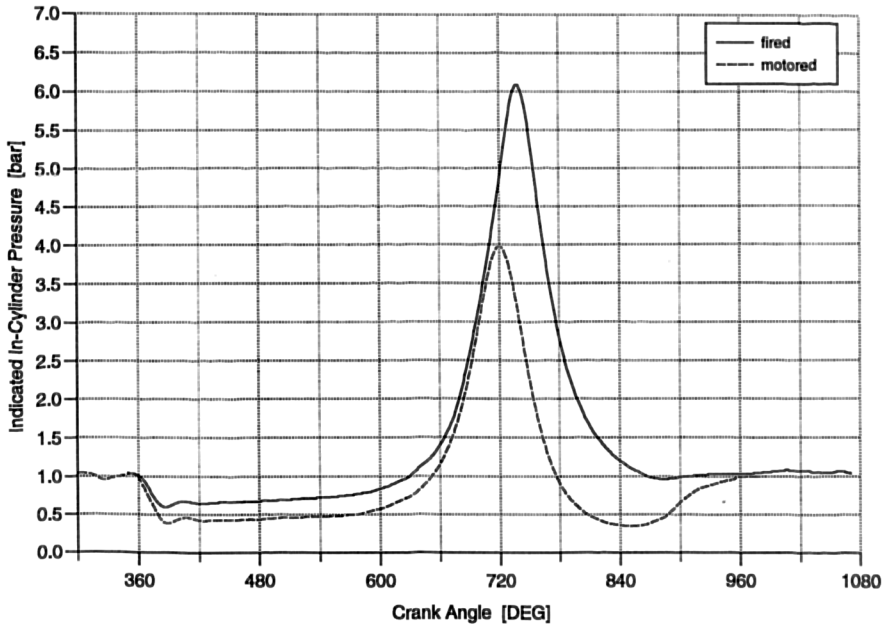

Fig. 4.7: Averaged indicated in-cylinder pressure of 200 fired cycles and 20 motored cycles. Inlet manifold depression 430 mmHg.

4.4 Laser and Sheet Forming Optics

A Lambda Physic EMG 150 MSC XeCl Excimer laser was used as the illumination source. It produces about 150 mJ of 308 nm radiation in 17 ns pulses. The laser can be triggered externally or from an internal clock at a pulse repetition rate of up to 80 Hz.

The laser output beam had the shape of a rectangular block. In order to match its geometry to that of the required sheet, the laser beam was rotated through 90° by two Ø50 mm steering mirrors. The rotated beam was then directed towards the engine by another two Ø50 mm 45° steering mirrors before passing through the sheet forming optics. The laser sheet was formed using three fused silica lenses. A spherical lens of 1 m focal length thinned the beam to below 0.5 mm. Two cylindrical lenses with a focal length of -75 mm and 150 mm acted as a Galilean telescope, expanding the beam in one direction to give a sheet of approximately 5 cm width.

For the measurements in the Mk 1 engine the laser sheet was directed by a 45° mirror so that it passed from the inlet side, 5 mm below the cylinder head gasket, through the quartz cylinder, exiting the combustion chamber on the exhaust side (Fig. 4.8a).

For the measurements in the Mk 2 version of the engine the laser sheet was directed by two 45° mirrors to the appropriate height to pass from the timing side (front) of the engine through the quartz window into the combustion chamber and exit on the gearbox side. The second of the two 45° mirrors was mounted on a vertical traverse, which enabled the height of the laser sheet to be set precisely to the required value with a micrometer screw (Fig. 4.8b).

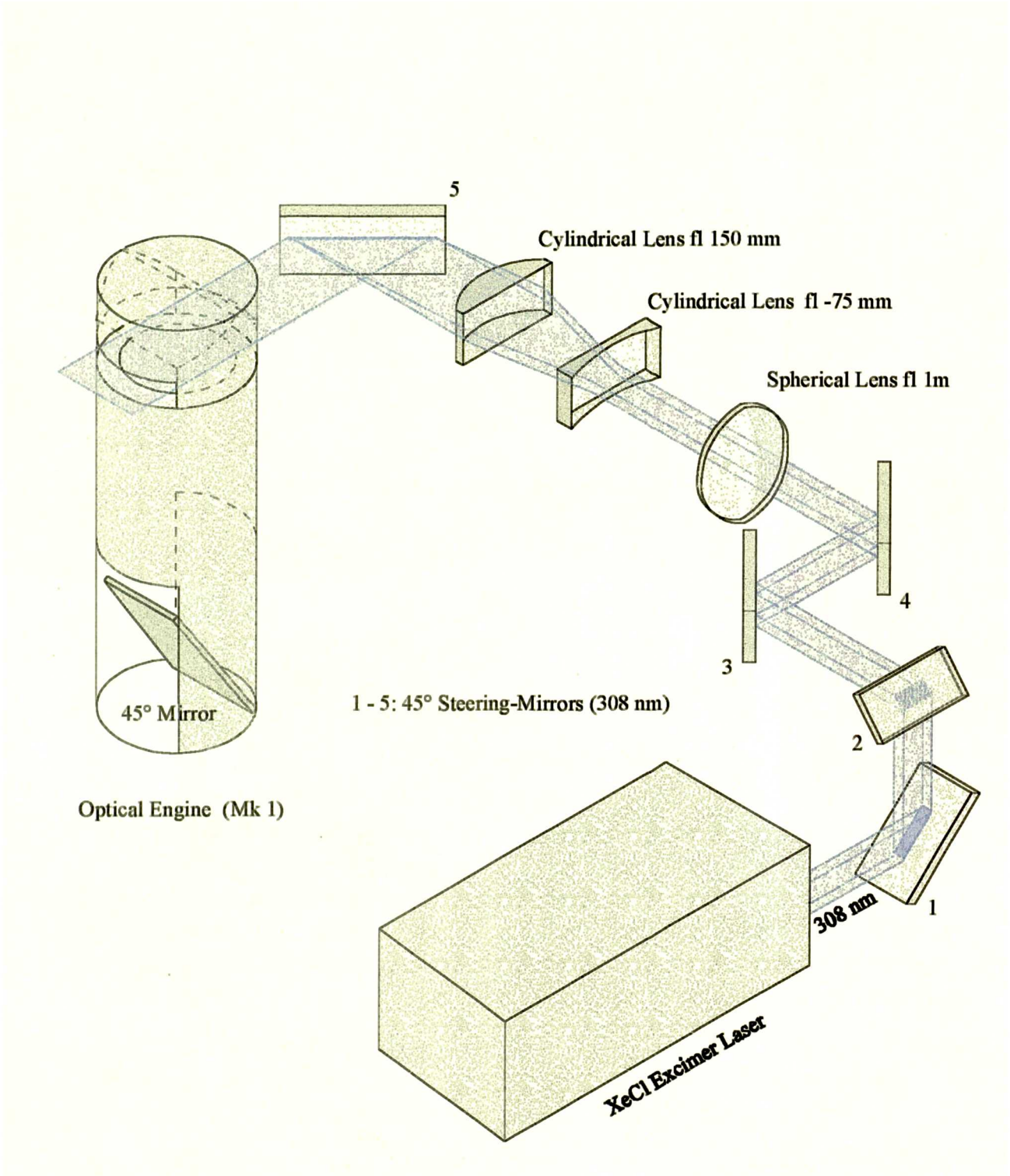

Fig. 4.8a: Optical set-up for planar LIF measurements in the **Mk 1** engine.

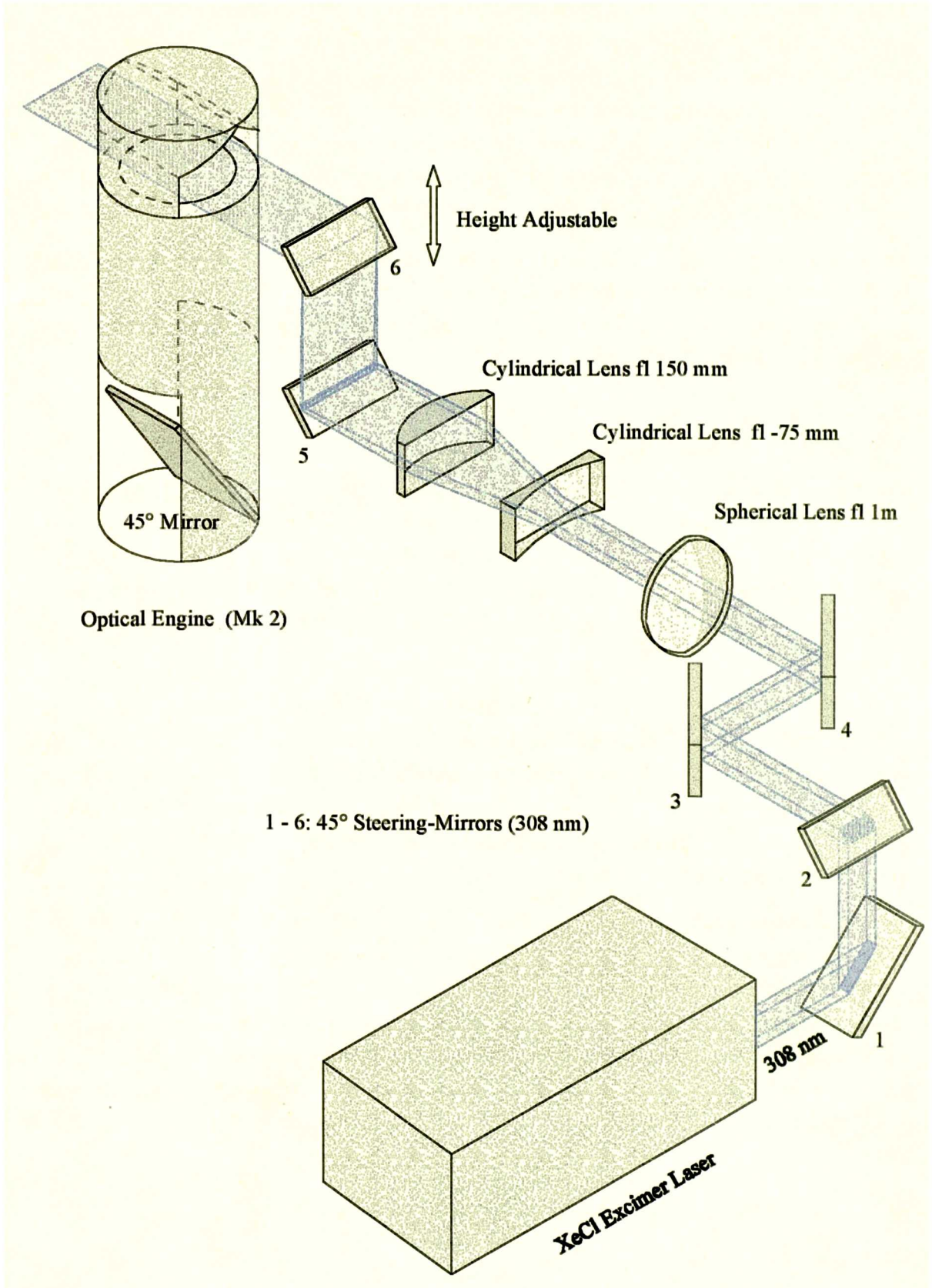

Fig. 4.8b: Optical set-up for planar LIF measurements in the **Mk 2** engine.

The quartz-window in both engines was a 50 mm wide annulus with an inner diameter equivalent to the cylinder-bore. The window in the Mk 1 engine was recessed by 12.5 mm from the outer cylinder surface and the window in the Mk 2 engine was flush with the cylinder surface. Therefore, the window in the Mk 2 engine had double the width compared to the window in the Mk 1 engine. The spherical surface of the window caused a refraction of the laser sheet. Because of the wider window in the Mk 2 engine, this caused the laser sheet to be narrower compared to the Mk 1 engine.

Reflections of laser light from the exit window affected LIF images on the exhaust side of the combustion chamber for measurements below a plane 5 mm from the spark plug. This required the laser sheet to be masked, compromising the viewed area in this part of the combustion chamber.

4.5 Fluorescence Detection System

The fluorescence signal was imaged using a 15-bit CCD-camera (Wright Instruments) coupled to a gated image intensifier (Princeton Instruments) with two front-to-front mounted Pentax f 1.2 50 mm lenses. The intensifier was synchronised with the laser and gated for approximately 200 ns to discriminate against room light and combustion luminosity. The signal was focused with a Nikon f 1.2 50 mm lens onto the image intensifier.

All camera focusing adjustments were made while the engine was stationary. The cylinder was filled with nitrogen and pentanone vapour and a 1 mm wide wire was used to obscure part of the laser sheet. The camera could then be focused on the laser sheet by maximising the sharpness of the edge that is generated by the wire in the fluorescence image. Typically the sharp edge spread over approximately two pixels for an optimal focus.

The CCD camera has a framing rate of 1 Hz which did not permit the recording of images from consecutive cycles. The CCD was controlled by a PC and the images were read out and stored on this computer. The use of 2 x 2 binning of the images reduced the image size from 500 Kbytes to 125 Kbytes, also by reading only the part of the image of interest from the chip onto the PC, the size of single images could be reduced to 80 Kbytes. This reduced the readout time by a factor of 5 and allowed more images to be taken during one measurement campaign.

4.6 Hardware Limitations on Image Quality

Resolution

An area of approximately 15 x 10 cm was focused onto the 600 x 400 pixel CCD chip. Hence, each pixel corresponds to a measurement volume of 0.25 x 0.25 x 0.25 mm - the sheet is approximately 0.25 mm thick. However a photon incident on the intensifier phosphor screen does not excite a single pixel. Due to blooming of the intensifier

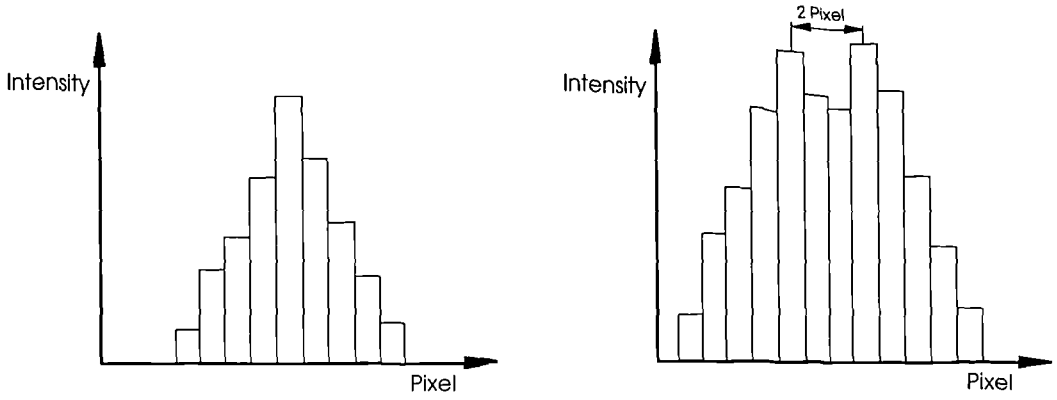

Fig. 4.9: Intensifier blooming results in a point-spread function[1] of signal intensities for a single photon event. Only events which are at least 2 pixel apart can be resolved.

phosphor, adjacent pixels will also be excited. Instead of a delta function, the real signal will be a point-spread function[1] (Fig. 4.9). Therefore, only structures which are at least two pixels apart can be resolved. In addition, the lens coupling between the intensifier and the camera was not able to focus on a single pixel. It spreads the signal over about four pixels (intensifier crosstalk) and the blooming from the phosphor screen of the intensifier will be amplified on the CCD chip. As a result, the true resolution will be less than 0.5 x 0.5 mm when one also considers the distortions caused by viewing through the heterogeneous charge. For these reasons 2 x 2 binning of the images resulted in no measurable loss of resolution. The true resolution was estimated to be better than 1 mm.

Intensifier Gain and Noise

There are several sources of noise on the camera/intensifier system:

- shot noise from the intensifier
- shot noise from the CCD
- readout noise from the CCD
- thermal noise from the CCD

The total noise on the system is:

$$\text{Noise} = \sqrt{(\text{gain} \cdot \text{shot}_{Int})^2 + \text{shot}_{CCD}{}^2 + \text{readout}_{CCD}{}^2 + \text{thermal}_{CCD}{}^2} \qquad (4.1)$$

The readout noise is constant (20 counts) and the thermal noise is a function of temperature. Not every photon event on the CCD chip or intensifier cathode will lead to an electron event. The resulting error is called shot noise and has a Poisson

[1] Also the finite accuracy of the focusing optics will lead to a point-spread function of a point light source. However, this effect is very small (typical resolution of a f1.2, 50 mm lens is about 25 µm) compared to the intensifier blooming and can therefore be neglected in this considerations.

distribution. Therefore the shot noise is proportional to the square root of the number of counts on the CCD chip/intensifier cathode ($\sqrt{X}$, where X is the number of counts).

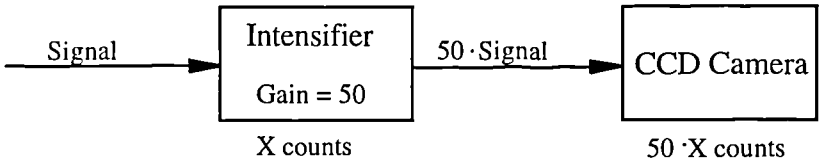

Shot noise on the Intensifier: $\sqrt{X}$

Shot noise on the CCD: $\sqrt{50 \cdot X}$

The total shot noise of the system consists of shot noise on the intensifier x the gain and shot noise on the CCD:

$$\sqrt{(50 \cdot \sqrt{X})^2 + (\sqrt{50 \cdot X})^2}$$

Shot noise is random. Blooming and intensifier crosstalk average the signal over several pixels and random noise is cancelled out. Binning the image by 2 x 2 increases the signal per pixel by a factor of four. This effectively doubles the signal-to-noise ratio, since the shot noise is proportional to the square-root of the number of counts.

4.7 Timing and Synchronising of the Experimental Equipment

A schematic of the instrumentation used for single exposure LIF measurements is shown in Fig. 4.10. The Controller of the dynamometer kept the engine speed constant at a pre-set value, which was 1500 rpm for this work. This required that the engine had to act as master in the timing sequence of the experiment. An optical sensor generated timing pulses of 1° crank angle resolution from a slotted disk fitted to the crank shaft pulley. TDC was marked by the absence of a slot. The engine management translated this signal into TTL pulses and provided a 360° pulse/revolution and a 1 pulse/2-revolution (TDC) output. A crank-angle counter used the TDC pulse as reference and counted the one degree pulses to give a TTL output pulse at every previously selected crank angle. This allowed the experiment to be triggered at every desired crank angle between 1° and 720° after combustion TDC with 1° crank angle resolution. The trigger signal was fed to a timing controller which gave a 12 V output to trigger the laser and a TTL output to trigger the digital oscilloscope only after it had been armed by the computer controlling the camera. This sequence ensured that the laser was triggered only once per exposure.

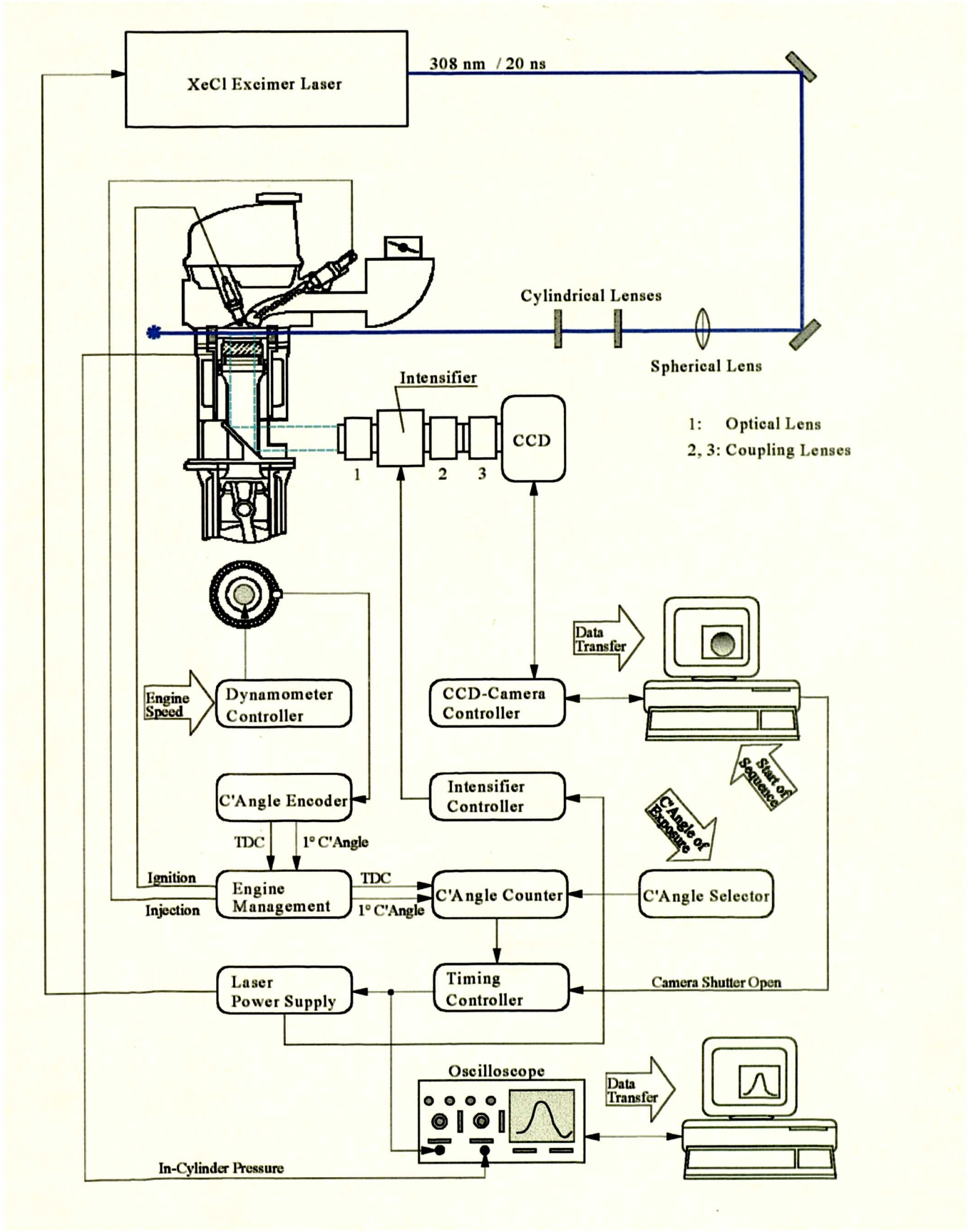

Fig. 4.10: Schematic of instrumentation used to measure the fuel concentration in the single-cylinder research engine.

For single shot imaging the sequence of events was (Fig. 4.11):

1. The computer controlling the camera initiates a new exposure of shutter duration 0.5 ms.
2. 5 ms later the software sends a TTL pulse from the output bus of the computer. (This time delay allows the mechanical camera shutter to open fully before the laser fires)
3. The TTL pulse is used to arm the timing controller.
4. The timing controller waits until it receives a trigger from the crank angle counter (occurring at a pre-set crank angle position) before it sends a trigger pulse to the laser power supply and the digital oscilloscope.
5. The timing controller resets itself and stays dormant until the next exposure.
6. The laser power supply triggers the intensifier controller. After an adjustable delay of typically 900 ns, the intensifier gate is opened for 200 ns.
7. After the camera shutter closes, the camera controller sends a signal to the computer and subsequently the chip is read out and the image saved onto the hard disk.
8. After an adjustable delay, the computer initiates a new exposure and the sequence is repeated.

The Excimer laser has a 3 μs delay between when it receives a triggering pulse and when it lases. Approximately 1 μs before the laser pulse a TTL output signal is generated by the laser power supply. This TTL pulse was used to trigger the intensifier rather than the input trigger from the timing controller since it provided a cleaner (less noisy) signal. The intensifier power supply allows the user to set a precise delay between the input pulse and the output gate. This delay was set to 900 ns and the gate length to 200 ns to ensure that the 20 ns laser pulse occurred in the centre of the gate and that non-laser generated signals such as room light were strongly discriminated against.

The digital oscilloscope recorded the pressure traces. It was controlled by a PC via an IEEE bus. The computer software arms the oscilloscope which then waits until it receives a trigger from the timing controller. After receiving the trigger pulse it stores the 512 data points before and after the trigger which are subsequently read out by the computer and saved in a file. The software then re-arms the oscilloscope. Because the data transfer from the oscilloscope is much quicker than the readout of the images from the CCD chip, it was not necessary to synchronise both PCs and the acquisition of pressure traces did not reduce the framing rate of the camera.

To record average images of the fuel concentration the camera exposure was set to 10 seconds and the laser was directly triggered by the engine timing controller. This resulted in the averaging of 125 consecutive cycles onto the CCD chip before the images were transferred to the computer (with the engine operating at 1500 rpm). This

allowed the acquisition of large sample averaged data sets in a short period of time. Pressure traces were not recorded in this mode.

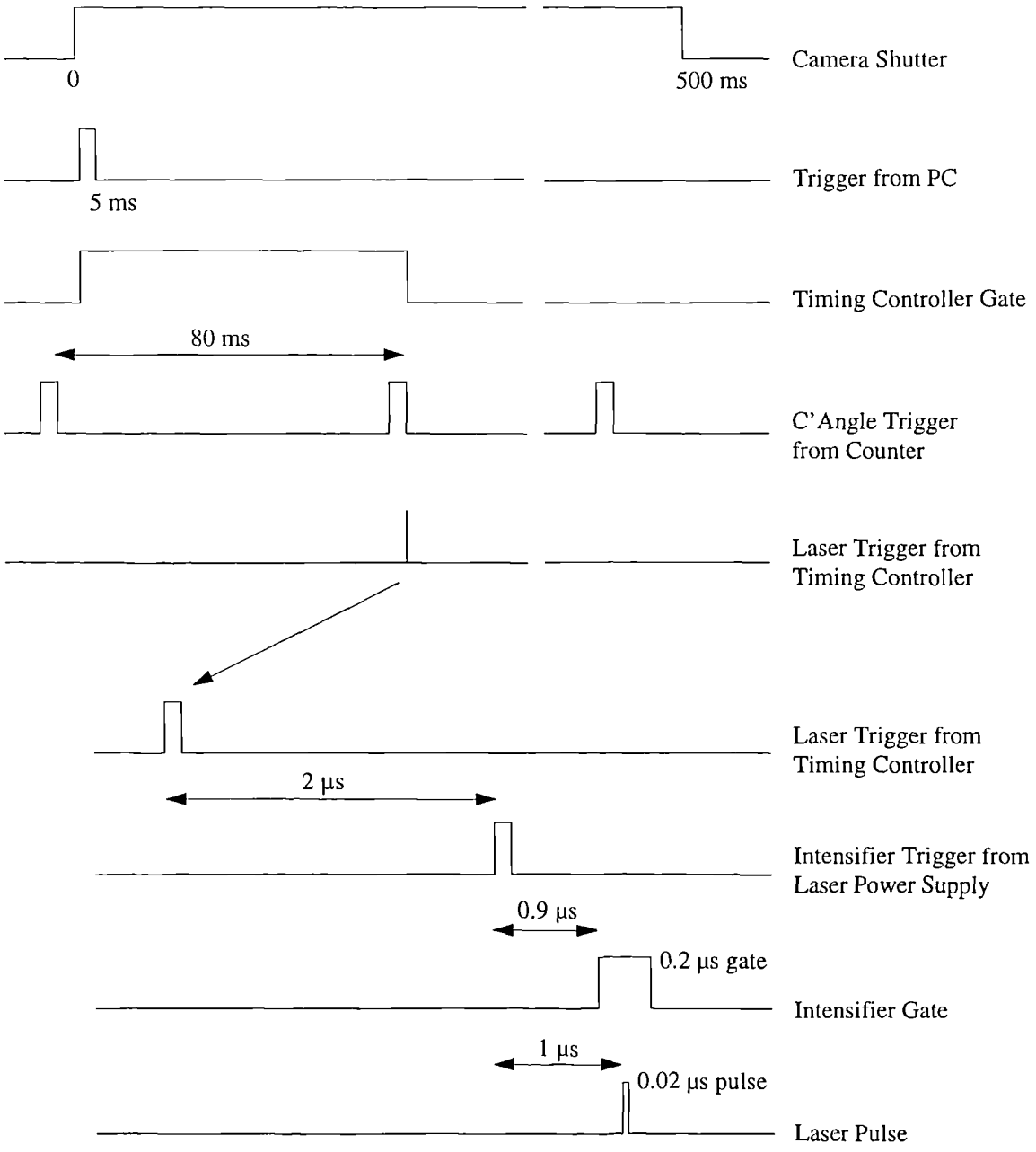

Fig. 4.11: Sequence of timing events for single exposure LIF measurements.

4.8 Measurement Procedure

The procedure of a typical test run for taking single shot images, was as follows:

- Warm the engine cooling water to 58 °C using a heater in the coolant system.
- Switch on the fuel pump, to allow the accumulator to be filled and the fuel pressure to settle to a constant 2.5 bar.
- Check the laser sheet alignment - adjust if necessary.
- Alter the timing set-up to allow the camera to trigger the laser directly.
- Crank the engine to inlet valve open position and connect calibration gas tank to the inlet plenum chamber. Fill the engine with calibration gas.
- Obscure part of the laser beam with a fine wire. Re-focus the camera and remove the wire.
- Take a series of at least 10 images of this uniform seed concentration - these are the raw calibration images. Adjust the intensifier gain so that these images make the best use of the camera's dynamic range, while ensuring that the intensifier is not saturating.
- Flush the engine with nitrogen without cranking.
- Take a second series of at least 10 images - these contain the background signal which is subtracted from the raw calibration images. If the background signal is too high, the laser sheet must be altered to minimise the background noise level and the calibration images repeated.
- Change the timing set-up so that the laser is triggered once per exposure.
- Dial the desired crank angle into the timing controller.
- Switch on the vacuum pump and exhaust sensor heater.
- Open the throttle on the inlet plenum chamber.
- Start the engine. Switch on the engine controller and bring the engine speed up to 1500 rpm (check speed with oscilloscope using TDC signal from engine controller).
- Check that ignition and injection occur on the compression stroke - switch TDC mark if necessary. Set the injection timing for the first test condition.
- Take a series of background images (pressure traces are also taken).
- Close the throttle on the inlet plenum chamber and adjust the inlet manifold depression
- Switch on injection, adjust the injection pulse length to desired AFR (as measured by the exhaust sensor).
- Fire the engine until it has settled down (approximately 2 minutes). Re-adjust the injection pulse width and the inlet manifold depression if necessary.

- Take a series of images and pressure traces.
- Switch the injection off and open the throttle.
- Take a series of background images.
- Repeat for other conditions.
- Stop the engine and switch off the engine controller.
- Crank the engine to the same position as for the previous calibration images. Take another set of calibration background images.
- Fill the engine with calibration gas. Take a further set of calibration images.

4.9 Calibration Procedure

In order to yield images proportional to fuel concentration the fluorescence images have to be corrected for spatial variations in the laser intensity and the collection efficiency of the detection system[1] (see *Chapter 3.5)*. These spatial variations in the effective gain of the system are reflected in the signal obtained when the engine is filled with a uniform concentration of the fuel marker (Fig. 3.9). Therefore a homogeneous mixture of fluorescence marker and nitrogen was filled through the inlet port into the cylinder of the stationary engine. Several images (usually 20) were recorded and subsequently averaged. This minimises errors due to noise and temporal laser intensity fluctuations. The calibration image was corrected for background contributions; background images were obtained before filling the cylinder with calibration gas.

The intensity of the data images normalised by the such obtained calibration image is proportional to the fuel concentration (*Chapter 3.5*) and can be written as:

$$I_{Final} = \frac{I_{Data}}{I_{Calib}} = f \cdot \frac{Seed\ Concentration\ in\ Data\ Image}{Seed\ Concentration\ in\ Calibration\ Image}$$

where f is a factor for the pressure and temperature difference between measurement and calibration.

It follows that if temperature and pressure during measurement and calibration were known, the seed concentration and hence the equivalence ratio in the data image could be calculated from the seed concentration represented in the calibration image (see *Chapter 3.6*). Two different attempts were made to quantify the seed concentration of the calibration gas.

---

[1] The overall collection efficiency of the detection system includes vignetting, aberration, transmission losses and inefficiencies of intensifier and CCD camera.

Seeder Method

In order to obtain a calibration gas of known composition, nitrogen was passed through a sealed vessel filled with pentanone so as to cause the exit gas to contain a vapour pressure of the seed. The nitrogen passed through a fine wire mesh sprayer which distributes its flow as small bubbles through the pentanone. The nitrogen carrier gas then became saturated with pentanone vapour. This procedure ensured a homogeneous mixture of nitrogen and seed. For safety reasons nitrogen was chosen as the carrier gas, as this ensures that a flammable pentanone/air mixture was never present in the system. The temperature in the seeder was measured with a thermocouple and the pressure was monitored with a pressure gauge.

However, the calculated seed concentrations of the calibration gas turned out to be too low compared to the signal obtained and did not lead to sensible results in the conversion of the fuel images. This result suggested that more pentanone entered the cylinder than expected for a saturated vapour. Further investigations indicated, that a fine aerosol was probably being created, causing higher seed concentrations in the cylinder compared to the calculation based on saturated vapour. As a result, images corrected by calibration images obtained using the seeder method could not be placed on an absolute scale. Therefore, an alternative calibration method was sought.

Premixed Calibration Gas

In order to obtain a well-defined seed concentration for the calibration images the calibration gas was premixed to a known concentration in a 61 litre tank. This tank was evacuated with a vacuum pump. 27 ml of liquid acetaldehyde was metered into the tank, which was then filled to 7 bar with nitrogen. The resulting acetaldehyde concentration of 2.73 Vol% was chosen to give a similar fluorescence signal strength as the fuel-air mixture in the engine. The tank had to be large enough to hold the calibration gas for a whole measurement campaign. It is also noted that the bigger the tank, the higher the accuracy with which the seed can be metered.

Acetaldehyde was chosen as calibration seed in preference to 3-pentanone because of its lower boiling point (20.8 °C vs. 101.7 °C) which makes it more volatile and as such, gives better mixing with the nitrogen. The calibration gas composition was confirmed by a spectral analysis of a sample at the beginning and the end of the measurement campaign using a mass spectrometer. The difference in fluorescence yield of acetaldehyde and 3-pentanone can be accounted for by the following correction factor:

$$f_f = f_{rel} \cdot \frac{a + b \cdot T_{cal}}{1}, \tag{4.2}$$

where f_{rel} is the difference in absolute fluorescence yield of 3-pentanone and acetaldehyde at 293 K. The coefficients a and b are taken from Figure 3.5 for 3-pentanone. The fluorescence yield from acetaldehyde is independent of temperature (Fig. 3.5).

Chapter 5

Engine Application of Fuel Visualisation - Results

Results from the visualisation of the mixture formation process in the one-cylinder research engine are presented, as well as correlations of pressure variations to image data. The impact of the results on engine design and possible future extensions are discussed. The first part of this chapter concerns the mixture formation process whilst the second concentrates on the influence of the mixture distribution on cyclic variability in performance.

5.1 Mixture Formation Process

5.1.1 Measurements

To study the evolution of the mixture formation in the one-cylinder research engine measurements of the fuel concentration during the inlet and compression stroke were needed. However, the framing rate of the CCD camera (1 Hz) did not permit instantaneous imaging of the mixture formation process during a single cycle. Therefore the average fuel concentration at different crank-angle positions was measured on several cycles in both the Mk 1 and Mk 2 Honda research engines.

The measurements taken in the Mk 1 engine comprised 31 sets of 20 single shot planar LIF images each taken at a different crank-angle during the inlet and compression strokes between 468° CA and 680° CA ATDC in a plane approximately 13 mm below the spark plug. Injection begin was set to 405° CA ATDC. The 20 instantaneous LIF images of each crank-angle position were subsequently averaged in order to give a picture of the mean mixture formation evolution.

Two further data sets (Data Set 2 and 3) were acquired in the Mk 2 engine. For these data sets, the images of 125 consecutive cycles were averaged on the chip of the CCD camera before the data was transferred to the PC. Because the readout time limits the framing rate of the CCD camera, this strategy reduced the measurement time required for the acquisition of average fuel concentration images by a factor of 10 compared with reading each instantaneous image onto the PC, for subsequent averaging. Therefore bigger data sets could be accumulated in the same period of time. In this

Table 3: Experimental conditions

	Data Set 1 [Fig.: 5.2]	Data Set 2 [Fig.: 5.3a, b]	Data Set 3 [Fig.: 5.4a, b]
Engine Type	Mk 1	Mk 2	Mk 2
Engine Speed [rpm]	1500	1500	1500
Inlet Depression [mmHg]	450	430	430
Ignition [° CA ATDC]	680	680	680
Injection [° CA ATDC]	***405***	***405***	***0***
AFR	20	19	19
Fuel	3 parts of Iso-octane + 1 part of 3-Pentanone		
Measurement Plane [in mm below spark plug]	13	0.7, 5.2, 10.2, 15.2	0.3, 5.2, 10.2, 15.2
Calibration Method	Seeder	Premixed	Premixed
Calibration Gas	3-Pentanone/N_2	Acetaldehyde/N_2	Acetaldehyde/N_2

way the average fuel concentration was measured in 20° crank-angle steps during the inlet and compression strokes between 360° CA and 740° CA ATDC, for injection at combustion TDC (0°) and 405° ATDC. These measurements were taken in different planes, 0.7 (0.3) mm, 5.2 mm, 11.2 mm and 15.2 mm below the ground electrode of the spark plug, thus giving a quasi 3-dimensional picture of the mixture flow during the cycle. For this experiment, a 45° turning mirror was mounted on a vertical traverse which could be adjusted by a micrometer screw, thus allowing precise setting of the height at which the laser sheet entered the combustion chamber. Background images and calibration images were taken at the same height of laser sheet as the corresponding data images. The background images were also taken at the same crank-angle as for the corresponding data images. The engine operation and experimental conditions for all three data sets are given in Table 3.

5.1.2 Image Processing

Each image was corrected for background contribution, mean laser and intensifier structure by subtracting a mean background image and dividing by a mean calibration image. The LIF images processed in this way represent seed densities at the relevant measurement condition. In order to display relative fuel/air ratios the images had to be corrected for temperature and density. Therefore all images were normalised to the calibration condition employing equation 3.15:

$$f_N = \frac{p_{Data} \cdot T_{Calib}}{p_{Calib} \cdot T_{Data}} \cdot \frac{0.51 + 0.001683 \cdot T_{Data}}{0.51 + 0.001683 \cdot T_{Calib}} , \qquad (5.1)$$

The coefficients which account for the temperature difference were estimated from the data in Figure 3.5. The denominator of the second term becomes unity when acetaldehyde was used as the calibration gas because the fluorescence yield of

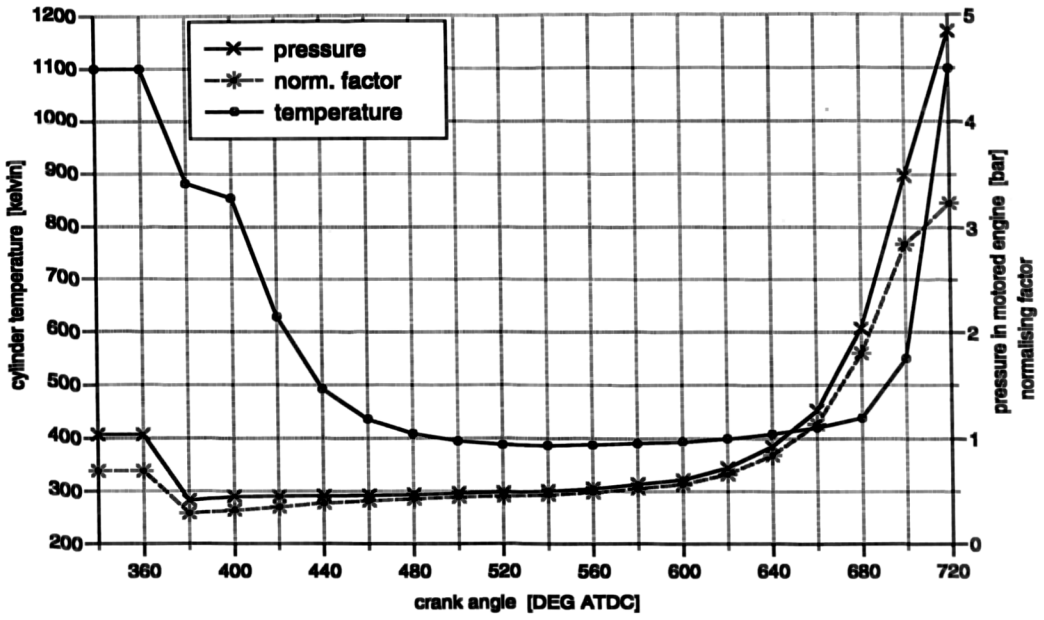

Fig. 5.1: Temperature and pressure with the resulting correction factor for normalising the crank-angle resolved data.

acetaldehyde is independent of temperature (Fig. 3.5). In order to make these corrections, it is necessary to know the temperature and the pressure throughout the inlet and compression strokes. The cylinder pressure was measured by a Kistler pressure transducer and the temperature was calculated using a model which assumed adiabatic mixing between air and residuals (see *Chapter 3.7* for more detail). Figure 5.1 shows the pressure and temperature together with the resulting normalising factor calculated with equation 5.1.

5.1.3 Image Calibration

The images flatfielded with calibration images obtained from a premixed calibration gas should display the same image intensity for the same conditions. However, this was not the case. The signal intensity in the calibration images varied substantially between the different data sets. An explanation for this initially mysterious result could be the fact that acetaldehyde is absorbed by gasket material used in the engine cylinder. Discussion of this problem with N. Tait from Shell Research (Thornton) revealed a similar problem in a combustion cell. In the evacuated, heated (150 °C) cell, injection seeding of toluene (b.p. 110 °C) and methanol (b.p. 60 °C) did not yield the expected vapour pressure. It was found that the gasket material used in the cell absorbed the seeded species. The cylinder head gasket on the research engines used for this investigation is made of the same material as the gaskets employed in the combustion cell at Shell and acetaldehyde, like toluene and methanol, is also polar. These facts may explain the unreliable results of the calibration procedure.

Inspite of this limitation in the calibration the images can still provide quantitative information on the mixture formation process. The main limitation is that images taken under different conditions and flatfielded against different calibration images can only be compared qualitatively. In order to allow semi-quantitative comparisons, the images were calibrated on the basis of the exhaust sensor reading.

The Data Sets 2 and 3 contain averaged images taken in four different planes of the cylinder during inlet and compression. At 680° CA ATDC, the piston has reached a position just below the lowest measurement plane. Therefore, at this crank-angle, the images represent four slices through the remaining cylinder volume. If it is assumed that there are no step changes in the axial fuel distribution, the averaged signal of all four planes should correspond to the overall air/fuel ratio as indicated by the exhaust sensor. Although the images cover only a part of the cylinder cross section, the average fuel concentration outside the measurement plane is not expected to differ significantly from that displayed by the images. On this basis the images were converted to equivalence ratios by the following procedure.

Using equation 3.31, the pentanone concentration can be expressed as a function of the air/fuel ratio:

$$X_{Pent} = \frac{23 \cdot \frac{p_{Calib}}{\tilde{R} \cdot T_{Calib}}}{309.7 \cdot AFR + 85.1} \tag{5.2}$$

With the calibration conditions (p_{calib} = *1 bar* and T_{Calib} = *331 K*) and for an indicated air/fuel ratio of 19 the above equation yields:

$$X_{Pent}(AFR\ 19) = 0.14 \qquad \left[\frac{mol}{m^3}\right].$$

The intensity I of the sum of the four images taken at 680° CA ATDC and normalised to calibration conditions is proportional to the pentanone concentration expected for AFR 19:

$$\sum_{i=1}^{4} I_i \propto X_{Pent}(AFR\ 19) \tag{5.3}$$

and the factor of proportionality can be expressed as:

$$f = \frac{X_{Pent}(AFR\ 19)}{\sum_{i=1}^{4} I_i} \qquad \left[\frac{mol/m^3}{Count}\right]. \tag{5.4}$$

With f from equation 5.4 the signal intensities of each image can be converted to pentanone concentrations:

$$X_{Pent} = f \cdot I_{Data} \qquad \left[\frac{mol}{m^3}\right]. \tag{5.5}$$

The images can now be further converted to display equivalence ratios by using equations 3.31 and 3.32.

5.1.4 Results

The results are displayed in Figures 5.2 to 5.6. Figure 5.2 shows the ensemble average of 20 single shot images (previously referred to as Data Set 1) for a range of different crank-angles taken in the Mk 1 engine with start of injection set to 405° CA ATDC. The laser sheet entered from the inlet side 13 mm below the spark plug and exited on the exhaust side. The four recessed areas on the circumference of the images are caused by the locking nut which holds the piston window in place and extends into the viewing area. These images were normalised by calibration images obtained using the seeder method and could only be displayed on a relative scale since the seed concentration in the calibration image was not well defined. The arbitrary scale is based on the mean fuel concentration of the ensemble-averaged image taken at 680° CA which corresponds to 100 on this scale.

Figures 5.3a, b and 5.4a, b show the crank-angle resolved 3D data for injection beginning at 405° and 0° CA (TDC) respectively, as measured in the Mk 2 engine. The laser sheet entered from the primary side (top) and exited on the secondary side (bottom). At crank-angles 380°, 400° and 700° the laser sheet in the lower measurement planes was clipped by the descending/ascending piston, and subsequently no image could be taken. The images in the top plane (0.7, 0.3 mm) from 380° to 540° CA and for the second plane (5.2 mm) from 400° to 520° CA were clipped by the open inlet valve. The focusing effect of the cylindrical entrance window reduced the width of the laser sheet, leading to a smaller imaged area compared to Data Set 1 (Fig. 5.2) obtained in the Mk 1 engine. In order to partly compensate for this, the laser sheet was made slightly diverging. The images in the top plane (0.7, 0.3 mm) view the pent-roof combustion chamber and are therefore smaller. The measurement planes 5 to 15 mm below the spark plug were affected by scattered laser light in a region near the exhaust side of the cylinder. Therefore, the laser sheet had to be masked, compromising the field of view. The 3D data was converted to an equivalence ratio scale as described in *Section 5.1.3*. The average equivalence ratio as measured by the exhaust sensor was 0.72. The mean equivalence ratio in each image in Figures 5.3a, b and 5.4a, b is displayed in Figures 5.5 and 5.6.

Some of the images have stripes perpendicular to the laser propagation direction. These have resulted from fluctuations in the laser profile and need to be disregarded when interpreting the images. Tait (1994) showed that such artificial features can be removed with a Fourier filter. For the current set of images, such image enhancement was discarded on grounds of the risk of distorting the true profile and the fact that the observed modulations are very small (< 1 %).

Included in Figures 5.2 to 5.4 is a colour bar showing the correspondence between the false colour scale and the data values. In the schematic displayed together with the

images the crossed valve indicates the inlet valve with the reduced lift referred to as the secondary inlet valve. The fully-opening main inlet valve will be referred to as the primary inlet valve in the following discussion. The exhaust valves will be accordingly dubbed primary and secondary exhaust valves.

The primary inlet valve opens at 360° CA ATDC. Subsequently the pressure in the cylinder drops to that present in the inlet manifold (Fig. 5.5, 5.6). Thus, at 380° the flow is from the cylinder into the manifold and unburned hydrocarbons sucked from the long piston crevices lead to an increase in signal. The descending piston then reverses the flow and in the case of injection at 405° CA air enters the cylinder between 400° CA and 420° CA, together with fuel vapour, left from the previous cycle in the manifold (Fig. 5.3a). This mixture is then diluted with air between 440° CA and 460° CA. At the same time the secondary inlet valve opens and fuel vapour trapped behind the valve from the previous cycle enters the cylinder. This can clearly be seen in the 0.7 mm and 5.2 mm planes at 460° CA and 10.2 and 15.2 mm planes at 480° CA, where the two primary quadrants are leaner than the two secondary quadrants due to the air flow through the main inlet valve.

Between 460° and 480° CA, fuel injected at 405° CA reaches the 0.7 mm plane through the primary inlet valve. Most of it moves down outside the measurement plane, near the cylinder wall and only a little of it can be seen in the exhaust half in lower planes. Between 480° CA and 500° CA, the fuel injected at 405° CA enters the top plane through the secondary inlet valve. Here as well, most of the fuel is actually outside the measurement plane, near the cylinder wall. While the fuel pocket which entered the cylinder via the primary valve is carried quickly down the cylinder by the incoming air flow, the fuel stemming from the secondary inlet valve stays in the top of the cylinder, and is carried by the swirl motion in a clockwise direction (images 500° to 600° CA).

After 580° CA the primary inlet valve lift is less than 1 mm and no further dilution with air occurs. During the compression stroke vapour stemming from the secondary valve, sitting outside the viewed area, mixes into the measurement planes (Fig. 5.3b) which leads to an increased mixture strength (Fig. 5.5). Between 640° CA and 680° CA a fuel-rich cloud appears in the secondary exhaust quadrant, and in the secondary inlet quadrant the secondary vapour cloud becomes diluted. At 700° CA ATDC the flame kernel reaches the top measurement plane. The flame burns to the lean primary exhaust side rather than towards the rich secondary exhaust quadrant of the cylinder.

For injection beginning at 0° CA ATDC, the fuel enters the cylinder through the main inlet valve as soon as the cylinder pressure has fallen to the manifold pressure, between 380° and 400° CA (Fig. 5.4a and Fig. 5.6). The second charge of air-fuel mixture enters the cylinder through the secondary inlet valve between 440° and 520° CA. The subsequent development is much the same as for injection 405°. The mixture which entered through the main valve moves down the cylinder with the air flow, while the mixture from the second inlet valve stays in the top of the cylinder. The mixture is also

influenced by the clockwise swirl motion. Again between 640° and 680° CA a fuel rich cloud appears opposite the secondary inlet valve (Fig. 5.4b). The final fuel distribution at 680° CA is very similar for injection 0° and 405° CA. Also, in this case the flame growth in the direction of the lean primary exhaust quadrant can be observed at 700° CA.

In the ensemble-averaged crank-angle resolved images taken in the Mk 1 engine (Fig. 5.2) a bigger area of the cylinder was imaged. These images show that most of the fuel actually sits close to the cylinder wall. The first fuel trace can be observed between the inlet valves moving to the exhaust side along the two secondary quadrants between 468° and 480° CA. This fuel stems from the back of the primary inlet valve. The bulk of the fuel appears near the cylinder wall between the two exhaust valves 480° CA ATDC. In the subsequent images the fuel cloud moves through the measurement plane, with the tail just disappearing at 588° CA. At 528° CA, a second fuel cloud becomes visible in the secondary exhaust quadrant. Conversely to the primary cloud, this cloud remains in the measurement plane which can be observed in the subsequent images and is highlighted by the separation of the two clouds. This fuel cloud must stem from the secondary valve as observed in the 3D images. The primary fuel cloud is convected by the onset of a clockwise swirl motion at bottom dead centre (BDC). The difference in the convection angle between the primary and the secondary cloud is evidence for the fact that the former is moving axially and the latter is stationary in the plane. These measurements also show the mixing of the vapour of the secondary cloud from outside the viewed area into the measurement plane. At the end of compression a fuel-rich cloud appears in the secondary exhaust quadrant and the inlet half is leaned out in the same way as observed in the 3D images.

5.1.5 Interpretation of Results

The results identified two mechanisms which influence the mixture formation process:

1. the fuel entering through the secondary inlet valve stays in the top of the cylinder.
2. the fuel entering the cylinder through the primary inlet valve strikes the opposite cylinder wall and remains in the vicinity of the wall.

The 3D crank-angle resolved data show the previously unrecognised effect of the secondary inlet valve on the fuel distribution. Due to the small lift of the secondary inlet valve, the air flow velocity is very small compared with the main valve. Therefore, the fuel entering the cylinder through the secondary valve tends to stay in the top of the cylinder, whereas the fuel coming through the primary inlet valve follows the air motion along the exhaust side cylinder wall, down the cylinder. This, together with the different phasing of the opening of the two inlet valves, leads to two distinct rich clouds of fuel in the cylinder. The fuel stemming from the primary inlet valve is carried across the cylinder by the air flow and thereby impinges onto the opposite cylinder wall. Particular fuel droplets which are likely to follow a more or less ballistic path will hit the cylinder wall. This causes a film of liquid fuel to form on the exhaust side

cylinder wall. Vaporising of liquid fuel from the cylinder walls would explain the appearance of a rich mixture below the secondary exhaust valve during compression.

Previously it was thought that injection synchronised with the inlet stroke is the major source of fuel stratification and that fuel injection before inlet open will lead to a homogeneous fuel distribution (Horie 1993, Hardalupas 1995). The current study showed that injection timing does indeed influence the above described mechanisms. Fuel injection at 405° or 0° CA has only a small effect on the stratification pattern of the fuel in the measurement planes at the time of ignition, however it affects the degree of axial stratification. Fuel injection during the inlet stroke will cause fuel droplets to enter the combustion chamber through the primary inlet valve and impinge on the opposite cylinder wall. Fuel injected at combustion TDC hits the hot inlet valve and has approximately 2 ms to evaporate. Therefore more fuel in vapour form will enter the cylinder through the primary inlet valve and fewer droplets will strike the opposite cylinder wall. This is reflected in the stronger signal during the inlet stroke for injection at 0° CA, since droplets yield a weaker signal than vapour. Hardalupas (1995) found that the spray motion in the port is determined mainly by the speed of the spray generated by the injector, rather than by the air speed in the ports. This implies that the droplet velocity for injection at 0° CA is lower than for injection at 405° CA and therefore fewer droplets will impinge on the opposite cylinder wall. This explains the fact that the fuel-rich mixture observed during compression below the secondary exhaust valve is weaker in the case of injection at 0° CA. The injection timing also affects the quantity of fuel entering through the secondary inlet valve. Fuel injected behind the secondary valve at TDC has time to evaporate and as soon as the primary inlet valve opens will be drawn by the air flow into the cylinder. This effect is reflected in the leaner secondary cloud present in the images taken with injection at 0° CA compared to those taken with injection at 405° CA. Since the mixture in the rich cloud near the exhaust side cylinder wall is also leaner, the rest of the cylinder contains a richer mixture, which is reflected in the smaller degree of axial stratification.

With the fuel concentrated in the cylinder head and near the cylinder wall of the exhaust side, the rest of the cylinder must contain a very lean air-fuel mixture. Consequently the ascending piston pushes lean air-fuel mixture up and compresses the fuel into the upper regions of the cylinder, thus creating the stratification along the cylinder axis. The axial stratification is more pronounced when the fuel is injected during the inlet stroke, but the mixture is far from homogeneous when injecting at combustion TDC. On average the difference between the top and bottom plane at the time of ignition is 0.32 and 0.21 equivalence ratio for injection at 405° CA and at 0° CA respectively (Fig 5.5, 5.6). The top plane is 4.8 % richer when the fuel is injected through the open inlet valve rather than behind the closed valve. However, 20° CA before ignition the top plane for injection at 405° CA was 8.4 % richer. This is caused by the ascending piston pushing leaner mixture from lower in the cylinder into the measurement planes. Up to 20° CA before ignition, this is offset by mixing with fuel from the rich clouds outside the measurement plane. From 660° CA on, the leaning of

the mixture due to the piston movement becomes dominant. The effect is less pronounced in the case of fuel injection at TDC since the degree of axial stratification is smaller. This implies that for more retarded ignition the mixture in the plane closest to the spark plug will become leaner and the difference in the mixture concentration between the two injection strategies will be further reduced.

Following Pages:

Fig. 5.2: Fuel concentrations in a plane 13 mm below the spark plug during inlet and compression stroke in the Mk 1 engine with fuel **injection at 405° CA** (Data Set 1). Each image is the ensemble-average of 20 single images. The images are scaled according to the mean fuel concentration at ignition (680° CA) which was set to 100. 360° CA is inlet TDC and 720°/0° CA is combustion TDC. The laser direction is from left to right.

Fig. 5.3a, b: Fuel concentrations in four planes during inlet (5.4a) and compression (5.4b) stroke in the Mk 2 engine with fuel **injection at 405° CA** (Data Set 2). Each image is the mean of 125 consecutive cycles. The images are displayed on an equivalence ratio scale. The laser direction is from top to bottom.

Fig. 5.4a, b: Ditto except for fuel **injection at 0° CA** after TDC (Data Set 3).

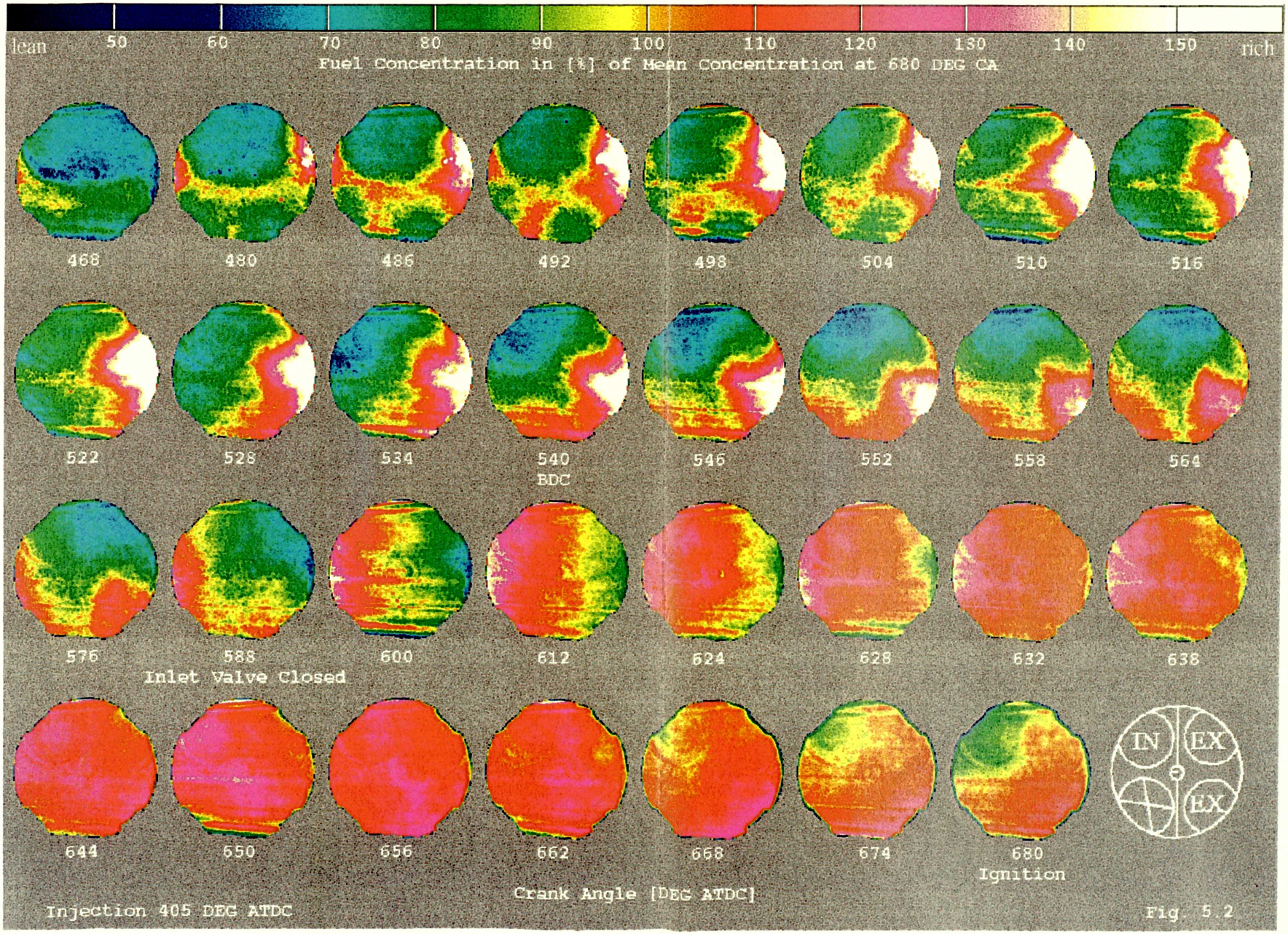
lean
50
60
70
80
90
100
110
120
130
140
150
rich
Fuel Concentration in [%] of Mean Concentration at 680 DEG CA
468
480
486
492
498
504
510
516
522
528
534
540
BDC
546
552
558
564
576
588
600
612
624
628
632
638
Inlet Valve Closed
644
650
656
662
668
674
680
Ignition
IN
EX
EX
Crank Angle [DEG ATDC]
Injection 405 DEG ATDC

Fig. 5.2

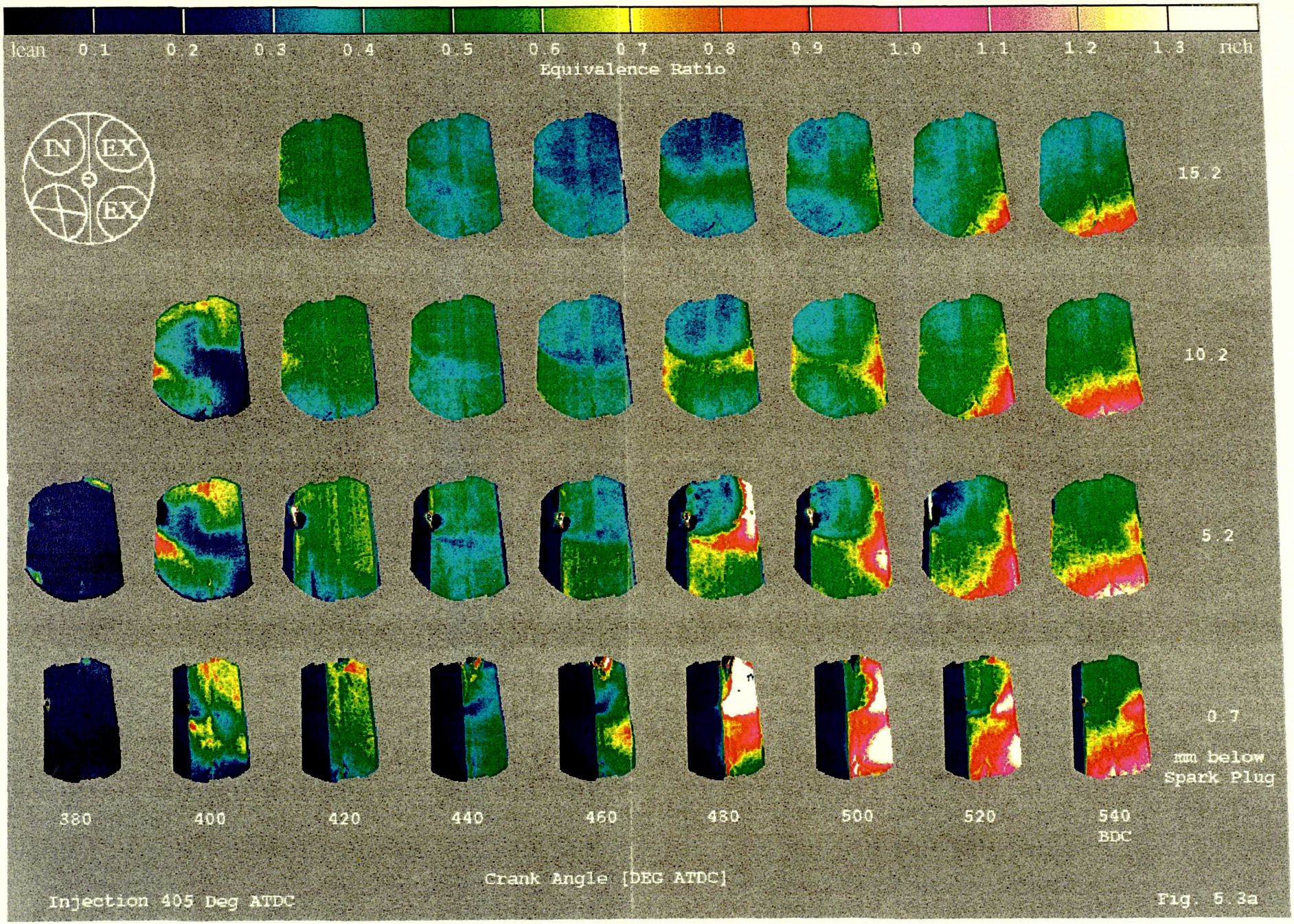
lean
0.1
0.2
0.3
0.4
0.5
0.6
0.7
0.8
0.9
1.0
1.1
1.2
1.3
rich
Equivalence Ratio
IN
EX
EX
15.2
10.2
5.2
0.7
mm below
Spark Plug
380
400
420
440
460
480
500
520
540
BDC
Crank Angle [DEG ATDC]
Injection 405 Deg ATDC

Fig. 5.3a

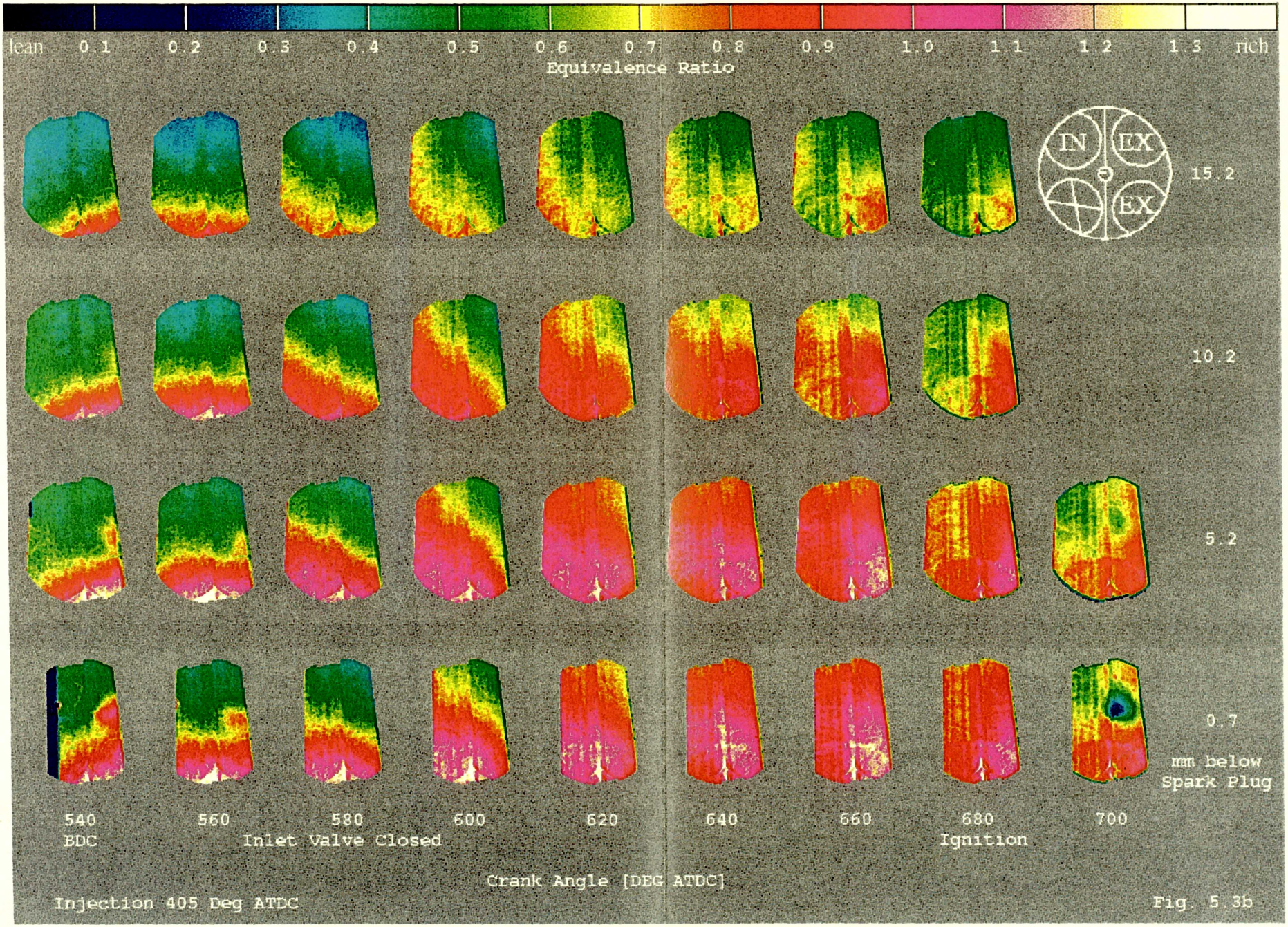
lean 0.1 0.2 0.3 0.4 0.5 0.6 0.7 0.8 0.9 1.0 1.1 1.2 1.3 rich
Equivalence Ratio
IN
EX
EX
15.2
10.2
5.2
0.7
mm below Spark Plug
540 560 580 600 620 640 660 680 700
BDC
Inlet Valve Closed
Ignition
Crank Angle [DEG ATDC]
Injection 405 Deg ATDC

Fig. 5.3b

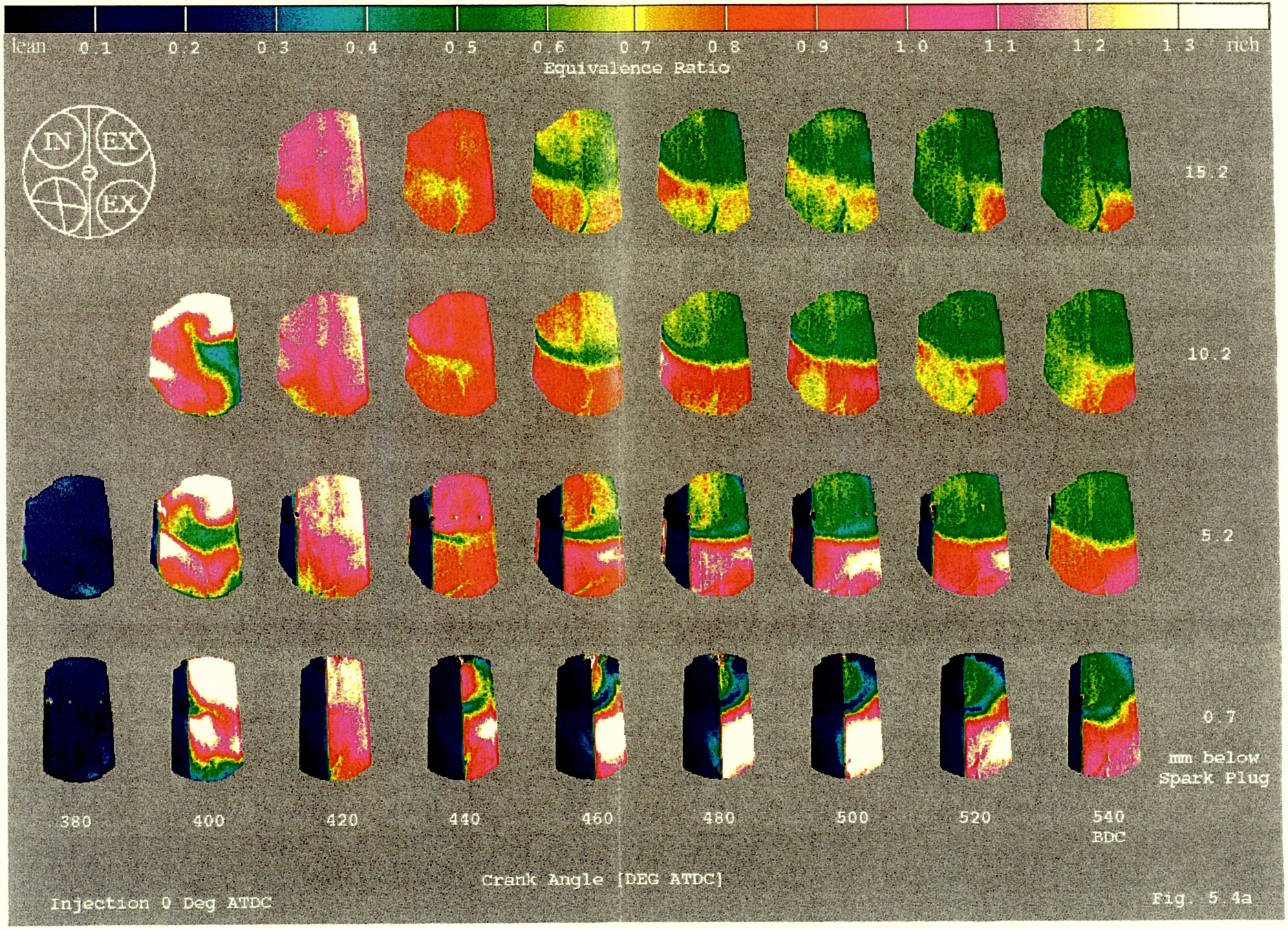
lean 0.1 0.2 0.3 0.4 0.5 0.6 0.7 0.8 0.9 1.0 1.1 1.2 1.3 rich
Equivalence Ratio
IN
EX
EX
15.2
10.2
5.2
0.7
mm below Spark Plug
380 400 420 440 460 480 500 520 540 BDC
Crank Angle [DEG ATDC]
Injection 0 Deg ATDC

Fig. 5.4a

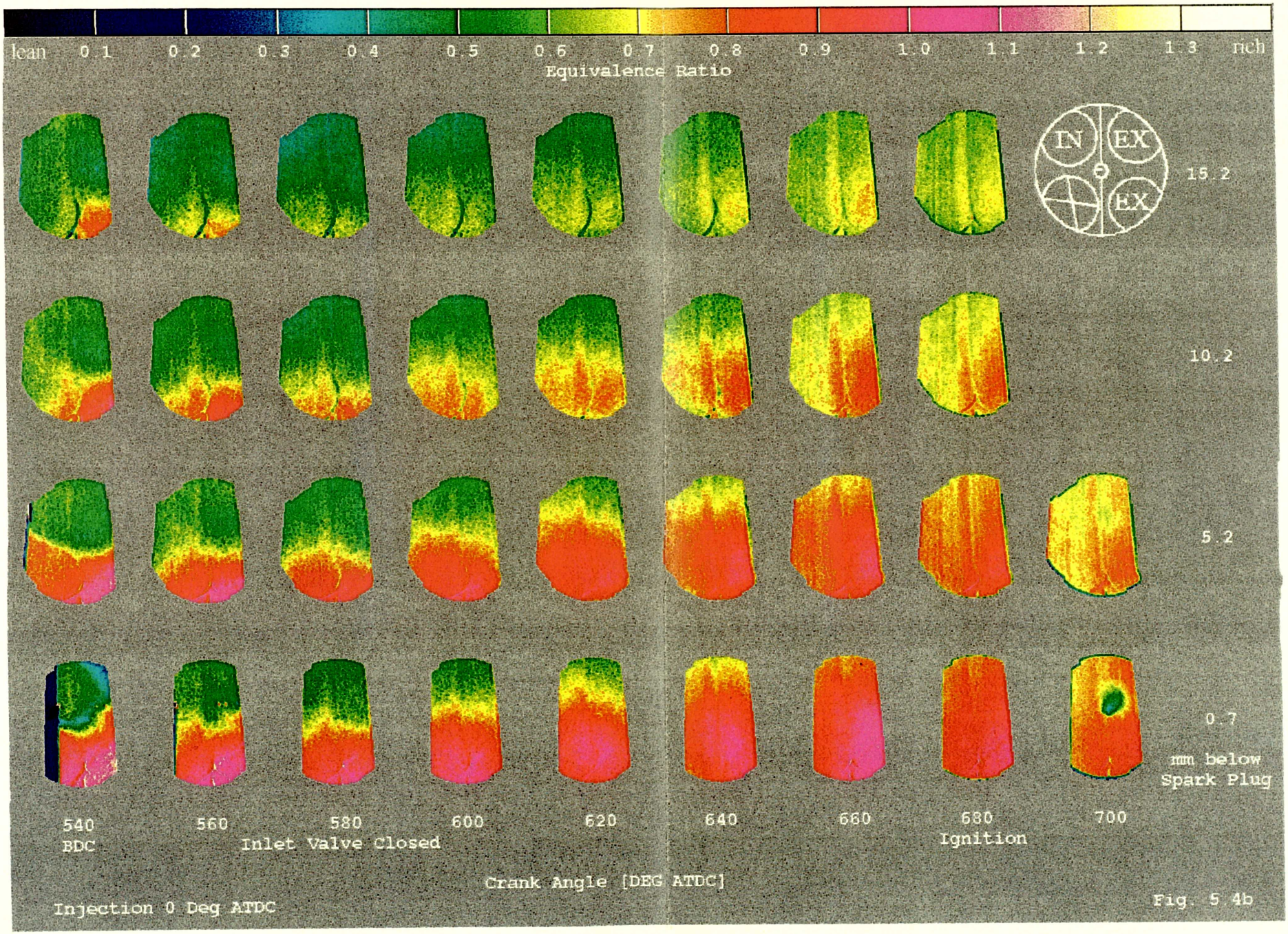
lean 0.1 0.2 0.3 0.4 0.5 0.6 0.7 0.8 0.9 1.0 1.1 1.2 1.3 rich
Equivalence Ratio
IN
EX
EX
15.2
10.2
5.2
0.7
mm below Spark Plug
540 BDC
560
580
600
620
640
660
680 Ignition
700
Inlet Valve Closed
Crank Angle [DEG ATDC]
Injection 0 Deg ATDC

Fig. 5 4b

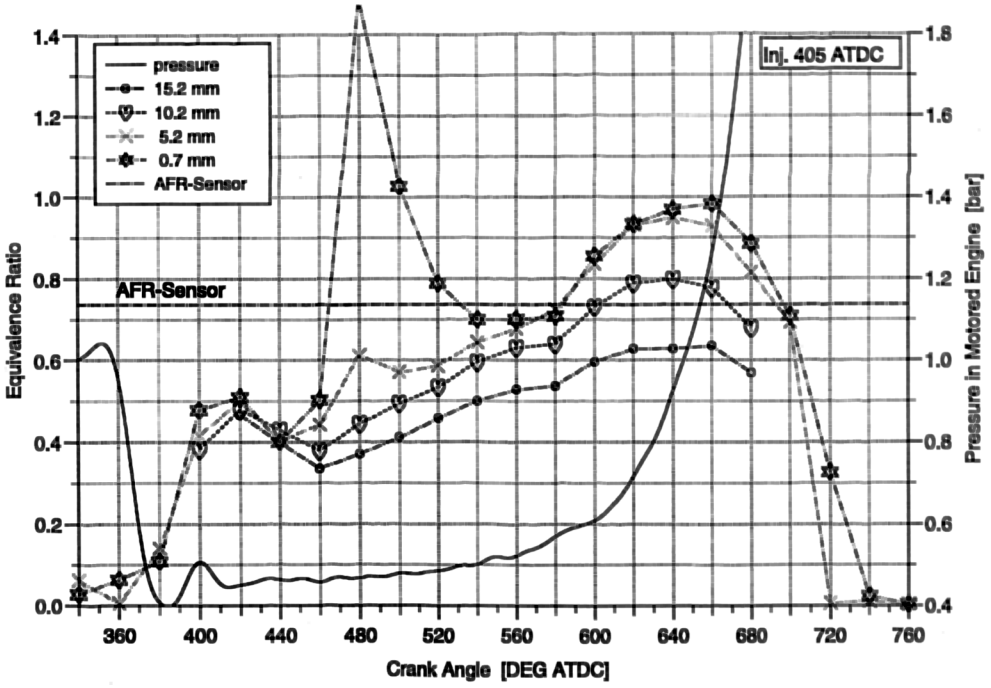

Fig. 5.5: Mean equivalence ratio across the images taken in four different planes during inlet and compression stroke with fuel **injection at 405° CA.**

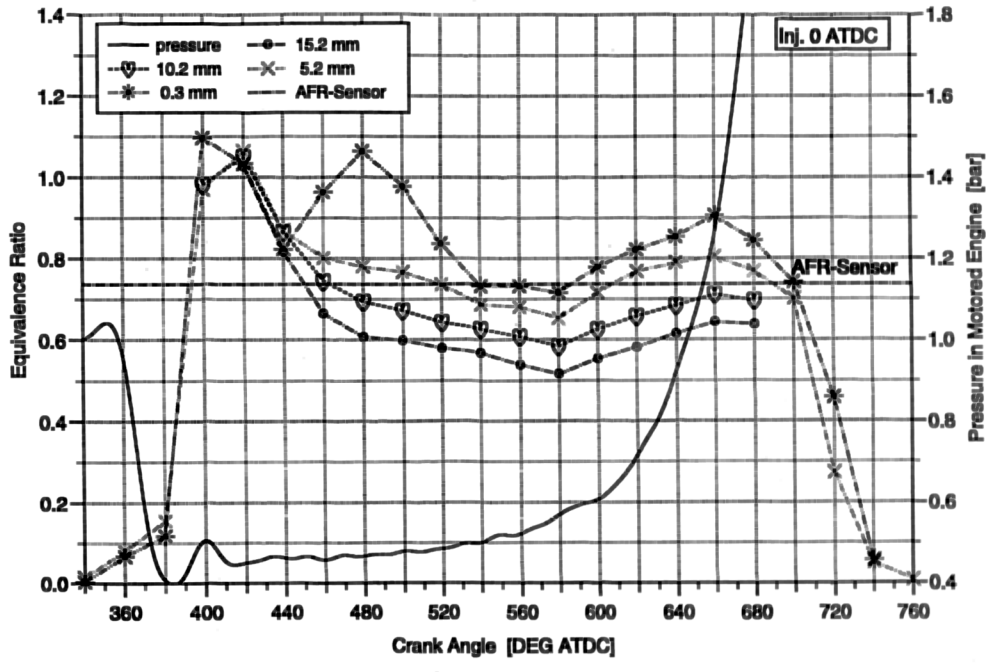

Fig. 5.6: Mean equivalence ratio across the images taken in four different planes during inlet and compression stroke with fuel **injection at 0° CA.**

5.1.6 Comparison of Spray Characteristics and Air Velocities with Fuel Vapour Concentrations

A research group at Imperial College (London) and Honda R&D (Japan) studied spray characteristics and air velocities in similar engines under similar conditions to those of the current study. The results were jointly published in the SAE paper 950507 (Hardalupas 1995). The spray characteristics were studied using high-speed cine equipment. Droplet arrival time and droplet density were thus measured by illuminating a plane 16 mm below the spark plug with a pulsed laser sheet. In the same measurement plane 2D grids of mean droplet size and velocity were measured with PDA and 3 dimensional air velocities by LDA. Since the results of Hardalupas (1995) are complementary to the results of this study they are presented here and are compared with the PLIF results.

PDA measurements of droplet size and velocities obtained from a measurement grid 16 mm below the spark plug are summarised in terms of liquid volume flux and liquid droplet concentration averaged over the whole inlet stroke in Fig. 5.7 (Hardalupas 1995). The contours show a maximum droplet concentration near the sleeve in the primary exhaust quadrant, extending into the secondary exhaust quadrants. This is where the PLIF images of vapour concentrations (Fig. 5.2) show the bulk of the fuel for crank-angle between 480° - 528° CA. The fuel concentration images in Figure 5.2 also show a second fuel cloud appearing near the sleeve in the secondary exhaust quadrant at 516° and 528° CA. The droplet concentrations in this region is very small as shown in Figure 5.7, suggesting that the fuel entering through the secondary inlet valve is mainly in vapour phase.

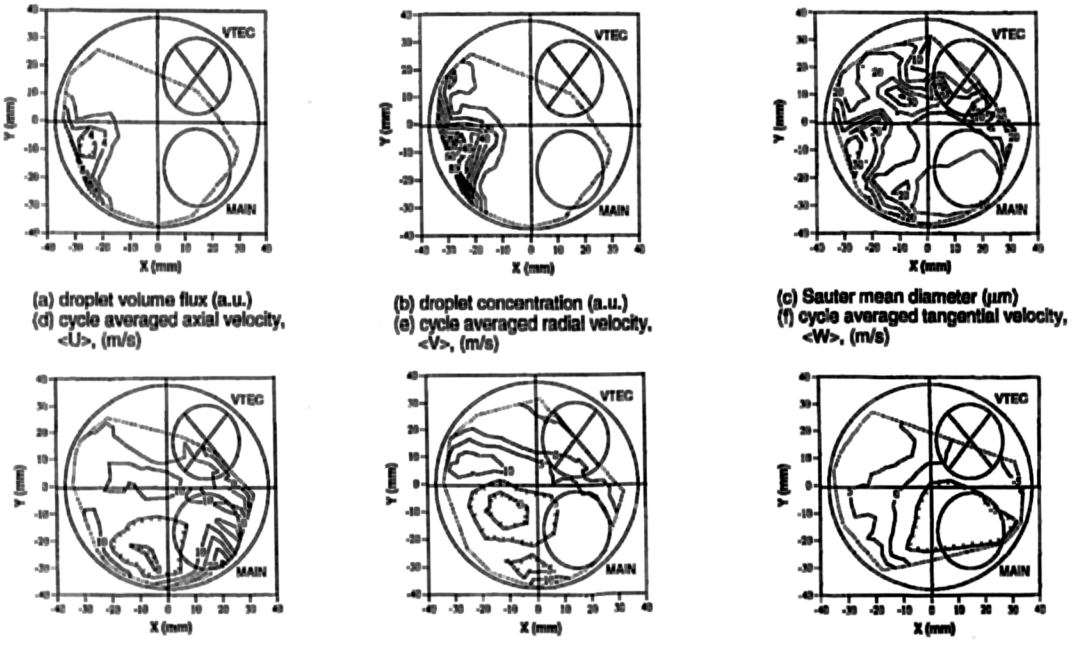

Fig. 5.7: Spray characteristics for **injection at 420° CA** in a plane 16 mm below the spark plug (Hardalupas et al 1995).

Figure 5.8 shows maps of in-cylinder gas velocities measured by LDA in a grid 16 mm below the spark plug averaged over ±10° CA. The flow pattern in the LDA data at 450° CA is reflected in the fuel motion as observed in the PLIF data. The images in Figure 5.2 at 468° CA and 480° CA show a fuel stream from between the inlet valves and the secondary inlet quadrant, where the velocity vectors, as indicated in the LDA images (Fig. 5.8), are directed downwards and towards the secondary exhaust quadrant. In the primary exhaust quadrant, where the velocity vectors are directed towards the head, and in the primary inlet quadrant, the fuel images show a very lean mixture i. e. mainly air. The same flow pattern is observed in the 3D LIF data (Fig. 5.3a, 5.4a) between 440° and 500° CA where an air stream dilutes the near homogeneous vapour concentration followed in the case of injection 405° CA by a fuel stream.

The PLIF data images in Figure 5.2 show the fuel cloud which stemmed from the primary inlet valve, moving through the measurement plane and disappearing by 600° CA, whereas the cloud originating from the secondary inlet valve stays in the measurement plane. The air velocity data in Figure 5.8 shows an axial velocity of 10 m/s towards the piston crown in the quadrant of the primary cloud at 540° CA, whereas the quadrant of the secondary cloud has zero or slightly negative axial velocity vectors. The primary cloud is carried by the air flow from the primary inlet valve along the exhaust side towards the piston, while the secondary cloud sits in an area of low axial flow, since it is not followed by a significant air flow through the secondary inlet valve. This is also reflected in the droplet measurements of Figure 5.7. The contours averaged over the whole inlet stroke show a maximum droplet volume flux near the primary exhaust sleeve. During compression, at 660° CA, the axial velocity vectors of -5 to -10 m/s are directed towards the cylinder head in the two secondary quadrants (Fig. 5.8). This is consistent with the vapour cloud appearing in the secondary exhaust quadrant between 640° and 680° CA (Fig. 5.2 - 5.4). This cloud stems from the fuel film evaporating from the exhaust side cylinder wall pushed back into the measurement planes by the ascending piston.

The formation of a clockwise swirl motion at bottom dead centre as shown by the LDA measurements is reflected in a clockwise displacement of the fuel vapour clouds beginning at 540° CA after TDC. According to Figure 5.8 the swirl motion is maintained during compression up to 660° CA. However, the effect of the swirl on the fuel-rich clouds seems to decay slowly during compression and appears to be terminated after 600° CA. Hardalupas (1995) does not give the magnitude of the swirl velocities, but the PLIF data suggests a gradual decay during compression. The swirl pattern in Figure 5.8 is very concentric with little flow orthogonal to the swirl. This explains the slow mixing of the rich patches near the cylinder wall with the rest of the cylinder charge (Fig. 5.2 - 5.4) and implies that swirl might be important for maintaining both the axial and cross-bore stratification.

There is very good agreement between the PLIF results and the results of Hardalupas

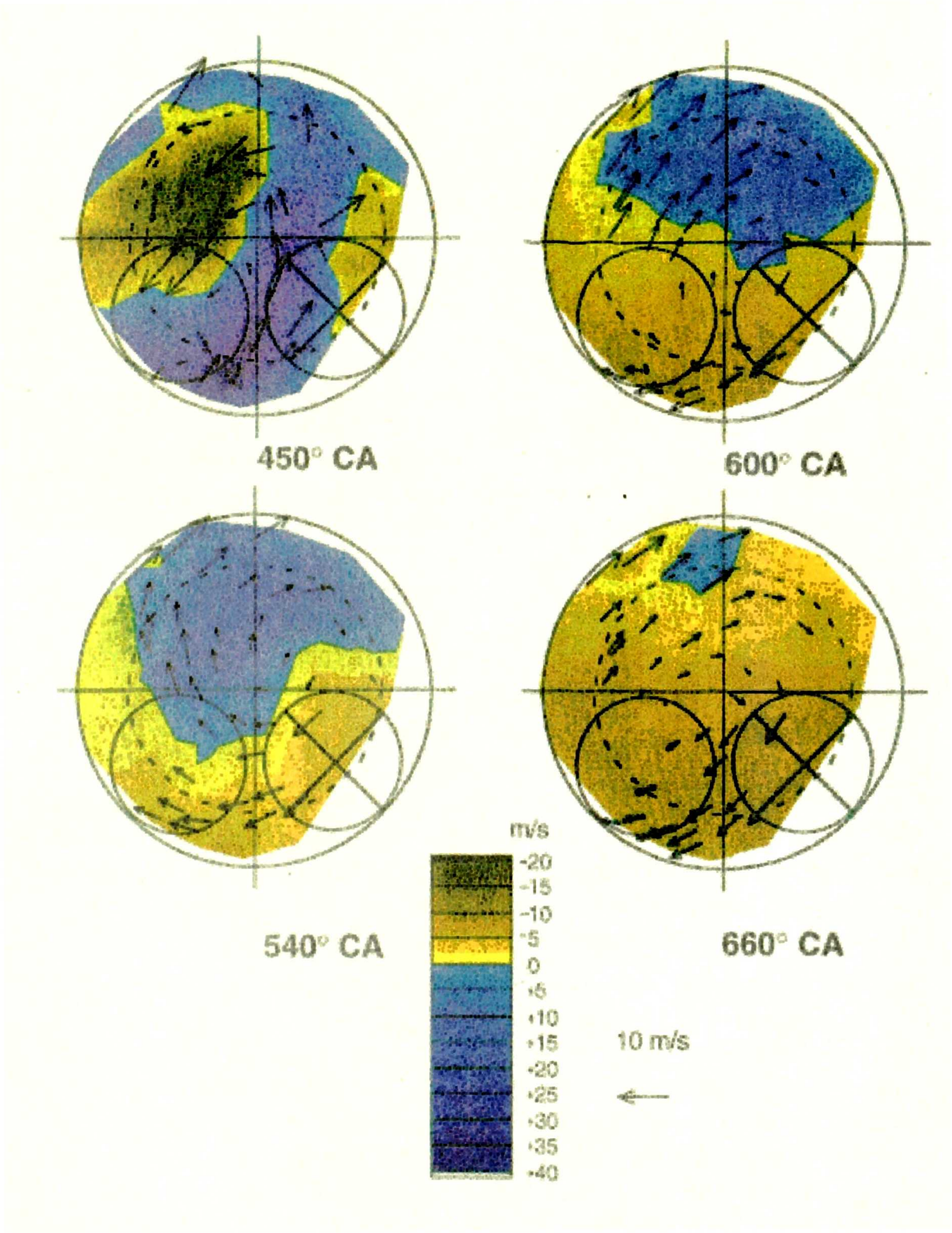

Fig. 5.8: Contours of averaged air velocity measured by LDA in a plane 16 mm below the spark plug gap in a Mk 1 type engine (Hardalupas et al 1995).

(1995). The vapour phase shows an identical distribution as the droplets during the inlet stroke and follows the air flow as indicated in the LDA measurements.

5.1.7 Fuel Vapour Motion during Inlet and Compression Strokes

On the basis of the crank-angle resolved PLIF fuel concentration images and the PDA and LDA data published by Hardalupas (1995), the motion of the fuel entering the cylinder through the primary inlet valve is described in (Fig. 5.9 a, b).

Assuming the axial air velocity of 10 m/s (Fig. 5.8) to be constant throughout the inlet and compression strokes, the fuel vapour from the primary inlet valve is moving down the cylinder at a rate of 10 mm/ms. Based on this assumption, the head of the vapour cloud which appears at 480° CA in the plane 15 mm below the spark plug should have moved 66 mm down the cylinder along the exhaust side cylinder wall by the time the piston reaches BDC. At 580° CA ATDC the last traces of vapour move through the top measurement plane and the leading part of the vapour cloud should be convected to the inlet side. According to Figure 5.8, at 620° CA ATDC the head of the vapour stream moves upwards to the cylinder head while the tail is still on the move down at about 30 mm below the 15 mm plane. Between 620° and 660° CA the tumble vortex will break down (Fig. 5.8) and, as well, the part of the vapour stream which still remains in the exhaust half of the cylinder is pushed upwards by the ascending piston. Also by this crank angle, the swirl motion will have deflected the fuel vapour cloud such that the head of the fuel cloud is likely to reappear between the inlet valves, while the tail should be in the secondary exhaust quadrant. The fuel vapour cloud will lean out during the inlet and compression strokes due to turbulent mixing with both, the air and the residuals in the cylinder. By the time it reaches the cylinder head the remaining fuel cloud it actually leaner than the rich cloud from the secondary valve which is sitting in the upper and inlet half of the cylinder. This explains the dilution of the mixture in the inlet half of the cylinder head during compression (Fig. 5.3b).

Based on an air flow path estimated by Hardalupas (1995) fuel droplets entering the cylinder through the primary inlet port will hit the cylinder wall at the exhaust side between 10 and 20 mm below the 15 mm measurement plane where they probably form a fuel film. During compression the fuel film will gradually vaporise and this vapour will be gradually convected towards the piston due to the now slower moving air and hence form an axially-stratified richer mixture near the exhaust cylinder wall. Between 620° and 660° CA, after the break down of the tumble vortex, this fuel-rich mixture will be pushed upwards by the ascending piston. This is consistent with the enrichment of the secondary exhaust quadrant during the later stages of compression (Fig. 5.3b, 5.4b). The measured reduction in mixture strength between 660° CA and 680° CA suggests that the fuel vaporised from the cylinder wall is axially stratified and that a leaner mixture exists lower in the cylinder. Near the end of the compression stroke, this leaner mixture dilutes the bulk of the mixture in the upper part of the cylinder.

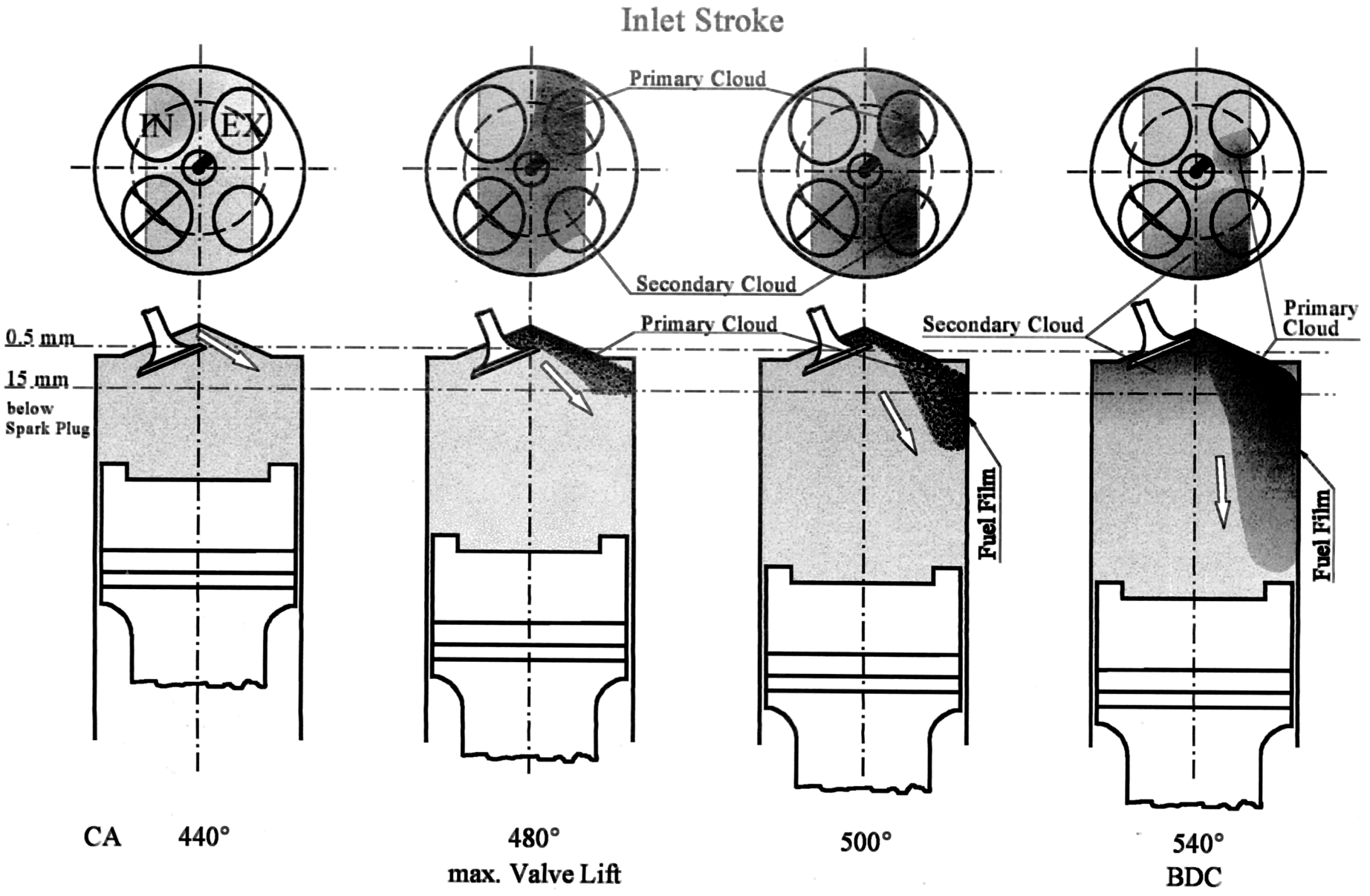

Fig. 5.9a: Schematic of mixture formation process in the cylinder of the Honda VTEC-E engine; injection 405° ATDC (Scale 1:2).

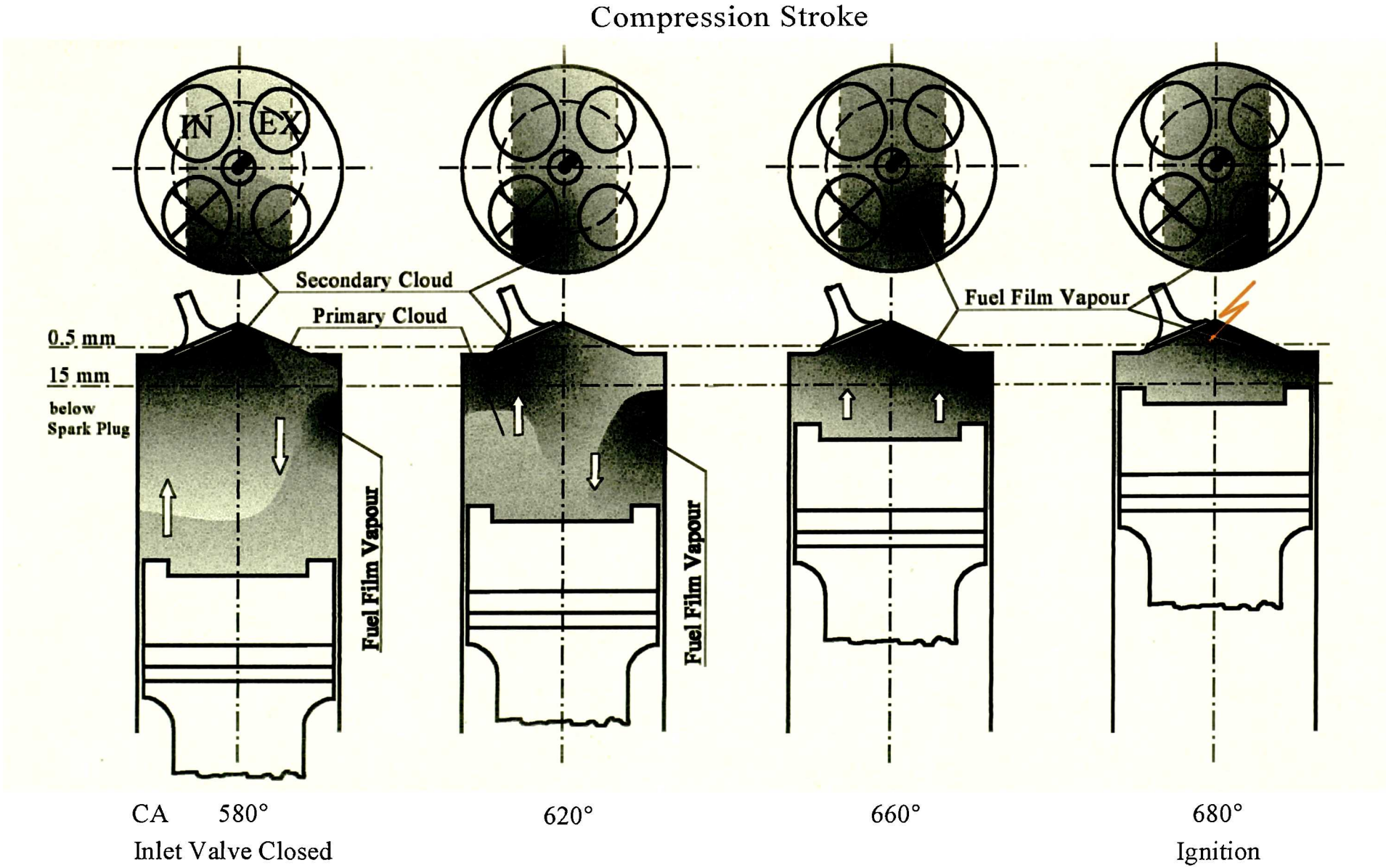

Fig. 5.9b: Schematic of mixture formation process in the cylinder of the Honda VTEC-E engine (Scale 1:2).

5.1.8 The Toyota Lean Burn Engine

The review of lean burn SI engines in *Chapter 1.4* revealed that Toyota uses a very similar strategy to Honda's VTEC-E engine for the mixture preparation in their 3rd generation lean burn engine. Both engine concepts have 4-valve pent-roof cylinder-head configurations. They make use of one high-swirl inlet port with a swirl ratio of 2.05 (Honda) and 2.4 (Toyota) to supply the bulk of the mixture and utilise a second inlet port to supply the richer mixture. In the Honda engine this is controlled by the VTEC-E valve and in the Toyota engine by the SCV valve. The SCV valve is located in the inlet port and is closed in the lean operation mode thus preventing any air entering through the non-swirl inlet port. A small passage between the swirl inlet port and the non-swirl inlet port permits a small airflow to enter with high velocity through the second inlet valve. The fuel entering through the non-swirl inlet port is therefore accompanied only by a small quantity of air, just as in the VTEC-E mode of the Honda engine. Both engine concepts use sequential injection during inlet open period at about 400° CA ATDC (Horie 1992, Inoue 1993). However, Toyota claim that their engine is a homogeneous charge engine (Inoue 1993) whereas the results of this work identified a strong axial stratification in the Honda lean burn engine.

Toyota supports its view of the mixture distribution with crank-angle resolved LIF measurements of fuel concentration in a single plane parallel to the piston and 23 mm below the spark plug (Shimizu 1992). The engine was operated at 1200 rpm with ignition at 690° CA ATDC. It was found that at ignition the mean fuel concentration in this plane was almost equal to the overall equivalence ratio and it was concluded that the fuel and air are homogeneously mixed.

The Toyota research workers used N,N-dimethylaniline (DMA) as the fluorescence tracer and mixed it with gasoline. The boiling point of DMA is 193 °C which corresponds to the upper end of the gasoline range (b.p. range 20 - 215 °C). As discussed in *Chapter 3.3*, it is doubtful whether a fuel marker with such different vaporisation characteristics from the bulk of the gasoline will be representative of the fuel distribution. Shimizu et al (1992) do not provide any detailed specification about the gasoline used for the experiment. However, commercial-grade gasoline is known to exhibit strong fluorescence when excited at 308 nm. It is not clear how the fluorescence of DMA and gasoline was distinguished.

Also, measurements in only one plane can be very deceptive. For example, the 3D images in Figure 5.5 show that at 680° CA ATDC in the plane 5 mm below the spark plug the mixture is slightly richer than the average, whereas that in the plane 10 mm below the spark plug is slightly leaner. If the fuel concentration is measured only in one plane between 5 and 10 mm below the spark plug, the result may not be typical for the whole cylinder.

5.1.9 Further Implications and Recommendations

In the Honda VTEC-E engine, the formation of a fuel film on the exhaust side cylinder wall opposite to the inlet valve was found to play a major role in the mixing process. Even for fuel injection behind the closed inlet valve, fuel wetting the cylinder wall was found to be important. The mixture formation for injection earlier or later than the 405° CA chosen in this study will mainly be affected by the valve lift. At injection 405° CA the bulk of the fuel enters the cylinder in a period around maximum valve lift. For earlier or later injection timing more fuel droplets will impinge on the back of the inlet valve as it opens or closes. This will tend to scatter more of the fuel droplets and will subsequently reduce the amount of fuel hitting i.e. the opposite cylinder wall. The resulting mixture distribution is therefore expected to be between the two cases studied here. For injection late in the induction stroke, where only part of the injected fuel is able to enter the combustion chamber, the picture might be very different. The fuel remaining in the inlet port will behave in the same way as we observed for the fuel injected at 0° CA. The fuel entering late in the induction stroke will almost certainly remain in the exhaust half of the cylinder and will therefore increase the axial and radial stratification.

To allow the fuel to impinge on the exhaust side wall a tumbling inlet flow directed towards the exhaust side is required. Such a flow is readily produced in pent-roof 4-valve cylinder head configurations. Flat 2-valve cylinder head designs, which are still commonly used, will produce low tumble and a flow directed towards the piston. In this case injection timing is likely to have a different effect on the mixture formation process compared to the observations of this study. It is likely to follow the concept proposed by A. Quader (1982). For fuel injection before the inlet valve opens, the mixture formation will initially follow the same pattern as observed in this study for fuel injection at 0° CA through the primary valve. A rich mixture of fuel and air enters the cylinder after the inlet opens. This is followed by gradually leaner mixture until the end of induction. With an inlet port directed towards the piston, the fuel will not hit the exhaust side cylinder wall and will follow the flow straight down the cylinder, possibly wetting the piston crown. In the absence of tumble, the rich mixture is likely to stay close to the piston, which will lead to negative axial stratification at the end of compression. For the same reasons, injection timing during inlet open can lead to a positive axial stratification.

In Quader's (1982) study it was also observed that fuel stratification occurs only in the presence of swirl, which suggests that swirl inhibits mixing. The current study seems to support this view, since radial mixing is slow and axial mixing is dominated by compression by the ascending piston. However, whether no swirl leads to a more homogeneous mixture in pent-roof combustion chamber geometries will not be seen with the current experiment. To answer this question, a similar study on a cylinder head with non-swirl inlet ports would be necessary.

The important effect of the secondary inlet valve on mixture formation is evident from the data presented here. Operation in 4-valve mode will change the mixture formation process significantly. The second inlet port imposes no swirl on the air which will change the flow field in the engine substantially. Due to the larger effective inlet area, the air velocity will be reduced during 4-valve operation. This makes it difficult to estimate from the available data the mixture formation in 4-valve operation. PLIF measurements in the 4-valve mode with swirl and non swirl second inlet ports would allow the picture of the mixture formation process in pent-roof cylinder-head configurations to be completed.

5.1.10 Conclusions on the Mixture Formation Process

- The mixture formation process in a research engine with 4-valve pent-roof cylinder-head could be described quantitatively by means of quasi 3-dimensional crank-angle resolved PLIF images.
- Two major causes of fuel stratification could be identified:
  - fuel forming a film on the exhaust side cylinder wall
    (vaporising of fuel wall film during compression causes locally richer mixture),
  - fuel entering the cylinder through the secondary inlet valve
    (low axial flow behind secondary inlet valve causes fuel to stay at top of the combustion space).
- Injection timing is an important parameter for mixture formation:
  - injection phasing during the inlet open period causes more droplets to strike the opposite cylinder wall where they form a fuel film,
  - injection timing influences the quantity of fuel entering through the secondary inlet valve.
- Swirl motion determines the location of richer mixture clouds.
- Fuel vapour motion measurements are consistent with air velocity and droplet measurements.
- The implication is that swirl is important for maintaining fuel/air stratification.
- Further studies of non-swirling engine configurations are required.

5.2 Mixture Formation and Cyclic Variability

In this chapter the correlation between engine performance and the mixture distribution at ignition, its cyclic variability and the early flame growth are investigated.

5.2.1 Measurements

This study is based on four data sets. Two data sets of 200 (189) single fuel concentration images together with corresponding in-cylinder pressure traces were taken ***at ignition*** in a plane 0.7 mm below the spark plug for injection at 405° and 0° CA ATDC. In order to image the early flame kernel, two further data sets of 200 (186) single images each were taken ***20° after ignition*** together with corresponding in-cylinder pressure traces. The same conditions as for the images taken at ignition were used. The engine operation and experimental conditions for all four data sets are given in Table 4.

5.2.2 Image Processing and Calibration

Each image was corrected for mean background contribution and mean laser and intensifier structure by subtracting a background image and dividing by a calibration/normalising image. The signal intensity in the calibration images could not

Table 4: Experimental conditions

	Data Set 1	Data Set 2	Data Set 3	Data Set 4
Engine Type	Mk 2	Mk 2	Mk 2	Mk 2
Engine Speed [rpm]	1500	1500	1500	1500
Inlet Depression [mmHg]	430	430	430	430
Ignition [° CA ATDC]	680	680	680	680
Injection [° CA ATDC]	***405***	***405***	***0***	***0***
AFR	20	20	20	20
Fuel	3 parts of Iso-octane + 1 part of 3-Pentanone			
Measurement Plane [mm below spark plug]	0.7	0.7	0.7	0.7
Measurement Crank-angle [° CA ATDC]	***680***	***700***	***680***	***700***
No. of Images	200	200	189	186
Indicated Cylinder Pressure	yes	yes	yes	yes
Calibration Method/Gas	Premixed Acetaldehyde/N_2			

be related to the known composition of the premixed calibration gas, probably due to absorption of seed material by the cylinder head gasket (see *Section 5.1.3).* This prevented the image intensity from being correlated to an absolute seed concentration: However, all four data sets were normalised by the same calibration image, thus allowing a quantitative intercomparison between the images for the two different injection timings.

5.2.3 Results

Mixture Distribution and Variation

On average, the fuel distribution between injection 0° CA and 405° CA is near identical (Fig. 5.11, 5.12). However, injection during the inlet stroke causes the plane 0.7 mm below the spark plug to be richer, on average by 4.3 %. This corresponds closely with the images from the 3D-data sets, taken at ignition, which show on average a difference of 4.7 % between injection at 0° CA and 405° CA (Fig. 5.13, 5.14). The 3D data corresponds to an average of 125 consecutive cycles and they were converted to an equivalence-ratio scale as described in *Section 5.1.3.* The average mixture concentration in the centre of the cylinder, near the spark plug, is 4 % higher for injection at 405° CA compared to injection at 0° CA. However, there is also a small region close to the spark plug where the mixture is about 2 % leaner than with injection at 0° CA. The difference in fuel concentration between the two injection strategies is largest in the exhaust half of the cylinder where the mixture is 8 to 10 % richer for fuel injection synchronised with the inlet stroke (Fig. 5.15).

On a single cycle basis the mixture concentration distribution varies substantially. This point is illustrated by Figure 5.17 which shows 49 single images of the 200 measurements taken at ignition for injection 405°. Both the overall fuel concentration and the fuel distribution in the measurement plane vary from cycle to cycle. The mean fluctuation of the fuel concentration around the mean value of the 200 (189) single shot images is 10.9 % for injection 405° compared to 8.6 % for injection 0° CA (Fig. 5.18 and 5.19). This is a difference of 26 % in the cyclic dispersion of the overall fuel concentration between the two injection strategies. Locally the fluctuations can be considerably higher. They are particularly large around the spark plug; 10.5 % (0°) and 12.9 % (405°). The highest fluctuations are observed in the secondary inlet quadrant with 15 % and 13 % for injection at 405° CA and 0° CA respectively.

The repeatability of the measurements can be estimated from a set of 20 calibration images which, on average, show a fluctuation of 2.3 % (Fig.: 5.16). Because this value is small (2.3 %) compared to the fluctuations present due to cycle-by-cycle variability (8 - 11 %), subtracting it in quadrature hardly affects the result (see *Section 5.2.5*). The small error in repeatability within the calibration images is due to errors of shot noise, intensifier noise and fluctuations in the laser power and profile. This represents the lower limit of the possible error associated with a single laser pulse measurement. The true error may be larger than this due to systematic errors particularly introduced

during the calibration measurements. Additional error sources which are not accounted for may include effects due to engine vibration (calibration images were taken with the engine stationary) or distortions of the images due to viewing through a heterogeneous charge.

The sets of 200 (189) images taken at ignition were classified according to peak pressure p_{max} in "good" ($p_{max} \geq 7$ bar), "fair" (7 bar > p_{max} > 5 bar) and "bad" ($p_{max} \leq 5$ bar) cycles and the images within each group were subsequently averaged. The overall fuel distribution for all cycles is shown in Figure 5.11 and 5.12 for the different injection periods. To highlight the important characteristics in the fuel distribution between "good" and "bad" cycles, each image was normalised by the mean of all images at the relevant injection timing. This allows the factors which distinguish between a "good" and a "bad" cycle to be analysed.

The resulting images from this analysis show the importance of having a richer mixture near the spark plug for the subsequent pressure development (Fig. 5.24 - 5.27). The average "bad" cycle is overall 5.8 % (405°), 4.4 % (0°) leaner than an average cycle. However, in the centre of the cylinder, near the spark plug, the "bad" cycle is up to 12 % (405°), 8 % (0°) leaner than the average. This contrasts with the fuel concentration for "good" cycles, which are on average 5.6 % (405°), 4.4 % (0°) richer than an average cycle, but are up to 12 % richer in the vicinity of the spark plug.

In Figure 5.22 and 5.23 the average peak pressure for "good", "fair" and "bad" cycles is compared with the relative fuel concentration in the whole image and in a circle centred on the spark plug, with a radii covering half the image width. On average differences in fuel concentration in the vicinity of the spark plug of ± 7 % (6 %) from the average cycle mark a difference in peak pressure of about ± 25 %. This sensitivity in the relationship between fuel concentration and peak pressure is reflected in the higher fluctuations in peak pressure of 19.3 % and 17.7 % for injection at 405° and 0° CA respectively (Fig. 5.20, 5.21) compared to the observed fluctuations in the fuel concentration.

Figures 5.20 and 5.21 illustrate the relationship between peak pressure and the crank-angle location of its occurrence for all 200 (189) measurements at injection 405° CA and 0° CA. The fastest burning cycles reach peak pressure between 10° and 12° CA ATDC. Slower burning cycles reach a lower peak pressure later in the expansion stroke, up to a point where the expansion due to the downwards moving piston exceeds the pressure rise caused by combustion. Cycles with very slow burning velocities will gradually approach the peak pressure of the non-combusting cycle, closer to TDC. In order to illustrate the relationship between the fuel concentration in the vicinity of the spark plug and the mass burning rate of the bulk combustion, the fuel concentration images for which peak pressure was above 7 bar in a range between 9.3° and 15.9° CA after TDC were averaged and normalised by the mean fuel concentration image of all cycles (Fig. 28, 29). Overall the fast burning cycles are 7 % (405°), 5.5 % (0°) richer than an average cycle. In the centre, near the spark plug, they

are up to 20 % (405°), 16 % (0°) richer than an average cycle. That is about 6 % richer than the average of all cycles with a peak pressure above 7 bar.

Despite these correlations between local mixture strength and peak pressure and the overall richer mixture in the vicinity of the spark plug for injection during the inlet stroke compared to injection at TDC, the corresponding average peak pressures are almost identical for both injection strategies (Fig. 5.20, 5.21). Also, the "good" cycles for both injection strategies have on average the same peak pressure, notwithstanding a difference of 6 % in fuel concentration in the vicinity of the spark plug.

The correlation between the fuel concentration in a particular region of the image and the peak of the in-cylinder pressure curve can be estimated by calculation of the sample correlation coefficient between each pixel value and the corresponding peak pressure. The sample correlation coefficient is the quotient of the sample covariance and the product of the sample standard deviations[1]. Its value approaches a maximum of one for a linear correlation of the two parameters.

The correlation between fuel concentration and peak pressure as shown in Figures 5.30 and 5.31 is highest, between 0.6 and 0.7, in the centre of the image in the vicinity of the spark plug. The correlation in the primary half (top) of the image is only 0.1 - 0.3, while it is 0.3 - 0.4 in the secondary half (bottom) of the image. The higher correlation between the fuel concentration in the secondary half of the cylinder and the peak pressure can be explained by the mixture distribution in the cylinder, where a fuel-rich cloud is located in the secondary exhaust quadrant. (Fig. 5.11, 5.12, 5.17). The richer the cloud is, the further it extends towards the centre of the image; thus the fuel concentration in the vicinity of the spark plug is correlated to the mixture strength in the secondary half of the cylinder. Overall, the results demonstrate the importance of the mixture strength near the spark plug for both injection timings.

---

[1] **Sample Correlation Coefficient**

Sample Correlation Coefficient is defined as:

$$r_{xy} = \frac{S_{xy}}{S_x \cdot S_y}$$

where S_x and S_y are in this case the standard deviations of the fuel concentration and peak pressure respectively:

$$S_x = \sqrt{\frac{1}{n-1}\sum_{i=1}^{n}(x_i - \bar{x})^2} \qquad S_y = \sqrt{\frac{1}{n-1}\sum_{i=1}^{n}(y_i - \bar{y})^2}$$

S_{xy} is the sample covariance of the variables fuel concentration and peak pressure:

$$S_{xy} = \frac{1}{n-1}\sum_{i=1}^{n}(x_i - \bar{x})(y_i - \bar{y})$$

For each pixel of the 200 (405°), 189 (0°) images the sample correlation coefficient r_{xy} between fuel concentration and peak pressure was calculated. Figure 5.30 and 5.31 are contour plots of the sample correlation coefficient.

An important measure for engine performance is the indicated mean effective pressure. No correlation was found between gross imep, derived from the indicated pressure traces, and the fuel concentration in the measurement plane (Fig. 5.32, 5.33). This results from use of an ignition timing of 40° CA BTDC which was chosen as a compromise to fit the average cycle. For faster-than-average burning cycles ignition is too early, while for slower-than-average burning cycles it is too late. Both, faster and slower than average burning cycles will have an adverse effect on the work done during the cycle; for the faster-burning cycles this is due to the pressure rise during the compression stroke and increased heat transfer caused by the higher temperature and for the slower-burning cycles this is due to the increased volume change caused by the descending piston.

The effect on engine performance due to variations in fuel concentration is illustrated in Figures 5.34 and 5.35, where the pressure development and the corresponding fuel concentration for three individual cycles is displayed. Cycle A, with a peak pressure of 9.5 bar at 10° CA after TDC, shows a rich mixture near the spark plug at the time of ignition, while Cycle C, with an initial pressure development similar to a motored cycle, shows a lean mixture near the spark plug. For the fast-burning Cycle A, ignition is clearly over-advanced, leading to a strong pressure rise during compression which has an adverse effect on imep. Conversely for the slow-burning Cycle C, ignition is not sufficiently advanced, leading to combustion late in the expansion stroke, at a low expansion ratio causing a low imep. The pressure development of Cycle B, with peak pressure of 7.9 bar 17° CA after TDC, indicates an ignition phasing close to optimum which is reflected in a high imep. The fuel concentration for this cycle is similar to the average fuel concentration which is indicating that the chosen spark timing is appropriately close to MBT timing.

In Figures 5.36 and 5.37, the imep is displayed against the crank-angle at which peak pressure occurred. It is evident that slow-burning cycles (θ_{max} > 20° CA), which are associated with low peak pressure (Fig. 5.20, 5.21) reach the same if not higher imep values as fast burning, but not overadvanced cycles (12° < θ_{max} < 20° CA) with high peak pressure. The vertical spread in imep for peak angles over 10° CA is normally associated with a variation in the total amount of fuel in the cylinder (Heywood 1988). However, the vertical spread observed here is larger than variations in fuel-charging would suggest. These results are believed to be caused by abnormally high heat losses in the optical research engine. An increased surface area due to a large crevice volume and the recessed piston window, a high heat capacity of the elongated piston and the large window areas will lead to a enhanced heat transfer compared to a production engine. Since the heat transfer rate is governed by the temperature difference between the gas and the solid structures, the hotter fast-burning cycle will generate a bigger heat loss than the cooler slow-combusting cycle, leading to a reduced difference in imep. This is illustrated in Figures 5.38 and 5.39, where a fast and a slow burning cycle are displayed. The corresponding peak pressures are 8.3 bar and 4.7 bar respectively at 14° CA after TDC. Despite the different peak pressure, both cycles produce the same

imep. This result could be explained by either a higher heat transfer rate of the fast-burning cycle, fuel charging variations or a combination of both. If fuel charging differences were solely responsible, then a reduced or even negative axial fuel stratification would be required in the slow-burning cycle case, because the top measurement plane was found to be 3 % leaner compared with the fast cycle (Fig. 5.39).

Early Flame Kernel

Figures 5.40 and 5.41 show the average of the images taken 20° CA after ignition for each injection strategy. The region of low signal intensity indicates the area of burnt gas. This can be determined from individual images and used to estimate the size of the flame in the measurement plane. The results, given in Figures 5.42 and 5.43, show the flame area, as a percentage of the image area, plotted against peak pressure of the corresponding cycle for both injection timings. In spite of the 2-dimensional measurement of a 3-dimensional flame kernel there is a good correlation of the flame area in the measurement plane to peak pressure. Cycles which have a high peak pressure despite having a small flame kernel suggest either flame growth away from the measurement plane, e.g. into the pent-roof, or a more rapid bulk combustion. Differences in the bulk combustion phase can be caused by cyclic variations in the amount of fuel delivered to the cylinder.

Classifying the images taken 20° CA after ignition into "bad", "fair" and "good" cycles in the same way as those taken at ignition, demonstrated that, on average, the pressure development and the flame-kernel size are linked (Fig. 5.44, 5.45). The richer mixtures for injection during the inlet stroke rather than at TDC result, on average, in a larger flame area in the measurement plane 20° CA after ignition (Fig. 5.44, 5.45). This is consistent with a strong correlation between the fuel concentration in the vicinity of the spark plug and the pressure development.

Just as in the case of measurements at ignition, the average peak pressure for both injection strategies is nearly identical, despite a smaller average flame area in the case of injection at TDC. This is also consistent with a number of cycles with no flame in the measurement plane 20° CA after ignition which still result in "fair" peak pressure values in the case of injection at TDC.

The mean images in Figures 5.40 and 5.41 show an average flame convection towards the primary exhaust side. Also the centroid of the individual flames is, in all but a few cycles, displaced from the spark plug towards the fuel-lean primary exhaust side, independent of the injection strategy employed (Fig. 5.46). The implication from these plots is that once the flame is established, factors other than the fuel concentration influence the direction of flame growth.

5.2.4 Interpretation of the Results

These results show that the fuel concentration in the vicinity of the spark plug influences the subsequent pressure development. The pressure development is mainly a function of the mass burning rate. In the initial phase of the combustion process, the mass burning rate will be dependent on the laminar flame speed, which is in turn a function of mixture strength. Therefore, the strong correlation found between peak pressure and the fuel concentration in the vicinity of the spark plug shows that the early stages of combustion have a strong influence on the phasing of the subsequent bulk combustion. The richer mixtures near the spark plug result in faster combustion, leading to a higher pressure peak early in the expansion stroke. During the propagation of the developed flame, the overall amount of fuel in the cylinder will be important, since the turbulent flame grows to consume fuel in nearly all parts of the cylinder, thereby in effect averaging out the local fluctuations in fuel concentration. Therefore, these results give experimental support to the hypothesis (Young 1981, Gatowski 1985, Keck 1987, Witze 1988, Pischinger 1990, Le Coz 1992) that cyclic variability has its origin very early in the cycle.

The speeding up of the combustion process by a richer mixture in the vicinity of the spark plug shows that charge stratification can indeed extend the lean operation limit. However, whether this benefits the engine performance depends on the extent of the cyclic variation in combustion, since both faster and slower than average burning cycles will reduce imep at a given static ignition advance. Both the correlation calculations between peak pressure and fuel concentration and the difference in fuel distribution between "good" and "bad" cycles indicate that fluctuations of the fuel concentration in the vicinity of the spark plug are a major cause of the cyclic variations in combustion for lean mixtures.

The injection strategy influences both the charge stratification and the cyclic variation in the fuel distribution. Higher fuel concentrations near the spark plug for injection phasing during the inlet stroke compared with injection at combustion TDC are linked with a higher cyclic dispersion in the mixture distribution. The lower fluctuations in fuel concentration for injection at 0° CA compared to injection at 405° CA do not result in a substantial reduction in the cyclic dispersion in peak pressure. The leaner mixture near the spark plug for injection at 0° CA leads on average to a slower flame development and hence a slower combustion. This will lead to enhanced variations in pressure due to an enhanced effect of the volume change caused by the descending piston late in the cycle.

Note that the longer flame development period when the fuel is injected at TDC is supported by the measurement of a smaller flame area 20° CA after ignition. The strong correlation between the size of the early flame kernel and the subsequent pressure development is again indicative of the fact that cyclic dispersion has its origin early in the combustion process. The stoichiometry in the vicinity of the spark plug is an important factor establishing the flame. Once the flame kernel is established, the

mixture formation is less important for the flame development. This is clearly demonstrated by the fact that the flame develops towards the leaner rather than the richer side of the combustion chamber. This is probably caused by convection of the flame kernel by a mean flow field directed towards the primary exhaust valve and/or by the temperature distribution in the cylinder. Temperature is well known to have a strong influence on laminar flame speed (Metaghalchi 1982, Rhodes 1985) and this will be particularly important during the early stages of combustion. The temperature will be higher near the exhaust side due to the radiation and conduction from the hot valves. On the richer side of the cylinder, the heat of vaporisation of the fuel will have a slight cooling effect. Subsequently the temperature is likely to be highest on the lean exhaust side. Also, the residual gas distribution will influence the temperature profile in the cylinder and this is discussed in more detail in *Part 3* of this thesis.

The above results show two clear points; a strong correlation between the pressure development and the fuel concentration at ignition in the vicinity of the spark plug and a similar correlation with the flame size 20° CA after ignition. These conclusions are true for both of the injection strategies. Also, in line with the lower fuel concentration, the flame area for injection at TDC was smaller than in the case of injection during inlet. However, for injection at TDC, neither the lower fuel concentration nor the resulting slower flame development, produced lower peak pressures. This suggests that the developed flame propagation must be faster for TDC injection compared to injection at 405° CA. The developed flame propagation will be governed by the mean flow, the overall turbulence level and the overall stoichiometry. The mean flow is the same for both injection strategies. Also the turbulence level should be virtually identical for both injection strategies; variations from cycle-to-cycle will be averaged to close to zero for 200 cycles. The mean fuel concentration was measured using an oxygen sensor in the exhaust system. The fluctuation of the output voltage on the display can lead to an error of about 0.5 AFR in adjusting the injector pulse width (see *Chapter 4.2*). Therefore, it is conceivable, that the amount of fuel injected could be up to 2.5 % different for each measurement run. At ignition the measurement plane was found to be on average 4.3 % leaner for fuel injection at TDC which was consistent with the smaller flame size 20° CA after ignition. This is due to a stronger axial stratification in the fuel concentration when injecting during the inlet stroke (see *Chapter 5.1*). Therefore, in the case of fuel injection at TDC, the top plane can still be leaner despite an overall richer mixture. Data from Metaghalchi (1982) suggests that for an iso-octane air mixture of equivalence ratio $\phi = 0.8$ at atmospheric pressure and room temperature, a difference of 2.5 % in mixture strength can lead to a difference of 10 % in the laminar burning velocity and this difference is likely to be larger for leaner mixtures. The difference in axial stratification between the two injection strategies is not expected to influence the flame speed of the well developed flame significantly, because by the time the piston reaches TDC, most of the stratification will have been mixed out.

5.2.5 Error Analysis of Single Exposure Data

Each of the final fuel concentration images (F) was formed from four separate images:

- a raw data image (R),
- a background taken with the engine motoring (B),
- a calibration image (C)
- and a background for the calibration image (B_{cal}).

Each of these can potentially add to the total noise on the final fuel image. The errors that will arise from the background images and the calibration image can be evaluated by measuring the fluctuation in sets of these images (denoted σ) and comparing them to the mean values. The fractional error in the raw data image is harder to estimate but will be at least as large as for the calibration image. The final fuel image was calculated as:

$$F = \frac{R - B}{C - B_{cal}} \tag{5.6}$$

The expected fractional error in measuring F will be:

$$\frac{\varepsilon_F}{F} = \sqrt{\left(\frac{\varepsilon_R}{R-B}\right)^2 + \left(\frac{\sigma_B}{R-B}\right)^2 + \left(\frac{\sigma_C}{C-B_{cal}}\right)^2 + \left(\frac{\sigma_{Bcal}}{C-B_{cal}}\right)^2} \tag{5.7}$$

200 Single Shot Fuel Images at Injection 405° ATDC

The data set comprises of 200 single shot data images and 20 single shot images each for background, calibration and calibration background. Below are the mean and the fluctuation around the mean for each of the data sets:

	CCD Counts
- Mean raw data image intensity (R)	7134
- Mean background intensity (B)	288
- Mean calibration image intensity (C)	16736
- Mean calibration background intensity (B_{cal})	522
- Fluctuation in raw images (ε-estimated as 2.5% of R)	178
- Fluctuation in background images (σ_B)	17
- Fluctuation in calibration images (σ_C)	398
- Fluctuation in calibration background images (σ_{Bcal})	33

With the above values, equation 5.7 gives an **expected fractional error of 3.6%** for the final images. The resulting values for the final image F (calculated from eq. 5.6) are:

	CCD Counts
- Mean final image intensity (F)	4273
- Fluctuation in final images (σ_F)	466 (10.9%)
- Uncertainty in final images (ε_F)	154 (3.6%)

Therefore, the actual fluctuation in fuel concentration within the signal F will be:

$$\sigma = \sqrt{\sigma_F^2 - \varepsilon_F^2} \tag{5.8}$$

With the above values, equation 5.8 gives an **expected cyclic fluctuation of 10.3 %** for the fuel concentration around the mean value.

189 Single Shot Fuel Images taken at Injection 0° ATDC

The data set comprises of 189 single shot data images and 20 single shot images each for background, calibration and calibration background. Below are the mean and the fluctuation around that mean for each of the data sets:

	CCD Counts
- Mean raw data image intensity (R)	6857
- Mean background intensity (B)	214
- Mean calibration image intensity (C)	16736
- Mean calibration background intensity (B_{cal})	522
- Fluctuation in raw images (ε-estimated as 2.5% of R)	172
- Fluctuation in background images (σ_B)	14
- Fluctuation in calibration images (σ_C)	398
- Fluctuation in calibration background images (σ_{Bcal})	33

With the above values, equation 5.7 gives an **expected error of 3.6 %** for the final images. The resulting values for the final image F (calculated from eq. 5.6) are:

	CCD Counts
- Mean final image intensity (F)	4101
- Fluctuation in final images (σ_F)	353 (8.6%)
- Uncertainty in final images (ε_F)	148 (3.6%)

With the above values, equation 5.8 gives an **expected cyclic fluctuation of 7.8 %** for the fuel concentration around the mean value.

The uncertainty in the measurement of a single image is 3.6 % for both strategies. If all the uncertainty is only due to the single measurement, in other words it is random and no systematic error occurs, the error in measuring the mean of a set of 200 images is:

$$\sigma = \frac{3.6\%}{\sqrt{200}} = 0.25\%$$

However, not all the uncertainty is due to random error. There are systematic errors caused for example by viewing through an inhomogeneous charge, reading the AFR

meter, engine vibration, background correction and laser sheet normalisation on the basis of mean characteristics etc. Therefore the uncertainty in measuring mean characteristics will be between 3.6 % (all the error is systematic) and 0.25 % (all the error is random). The difference in the mean fuel concentration between the two data sets of 4.3 % is bigger than the expected uncertainty and it can be concluded that the measurement plane is richer in the case of injection phasing with the inlet stroke compared to injecting at TDC.

5.2.6 Conclusions on Mixture Formation and Cyclic Variability

- The correlation between fluctuations in mixture formation and the pressure development could be described quantitatively.
- Strong cycle-by-cycle variations in fuel distribution exist.
- Cycle-by-cycle variations in mixture distribution are a dependent on injection timing.
- Mixture fluctuations near the spark plug are a major cause for cyclic variability in combustion.
- Fuel stratification can extend the lean operation limit.
- Cyclic variations in mixture formation limit lean operation.
- Fuel concentration in the vicinity of the spark plug has a dominating effect on the subsequent pressure development for lean mixtures.
- The concept of "early flame development to determine the subsequent pressure development" is supported by the results of this study.
- The results also support the hypothesis that cyclic variability in combustion has its origin early in the cycle.
- The flame propagation data suggests that heating of the mixture by exhaust valves could be important.

Fig. 5.10: Location and image size in relation to cylinder head configuration. Solid lines indicate the pent-roof area 0.7 mm below the spark plug in proportion to image size. Dashed outer circle represents bore diameter. The crossed valve marks "inactive" (secondary) inlet valve. The image width is limited due to focusing of the laser sheet by the curved entrance window in the cylinder head. In order to partly offset the focusing effect, the laser sheet was made diverging. The diameter of the image is limited by the diameter of the piston window. Bore and spark plug diameter are in scale with image size (scale: 1:1). Valves are not in scale due to the pent-roof shape of the combustion chamber.

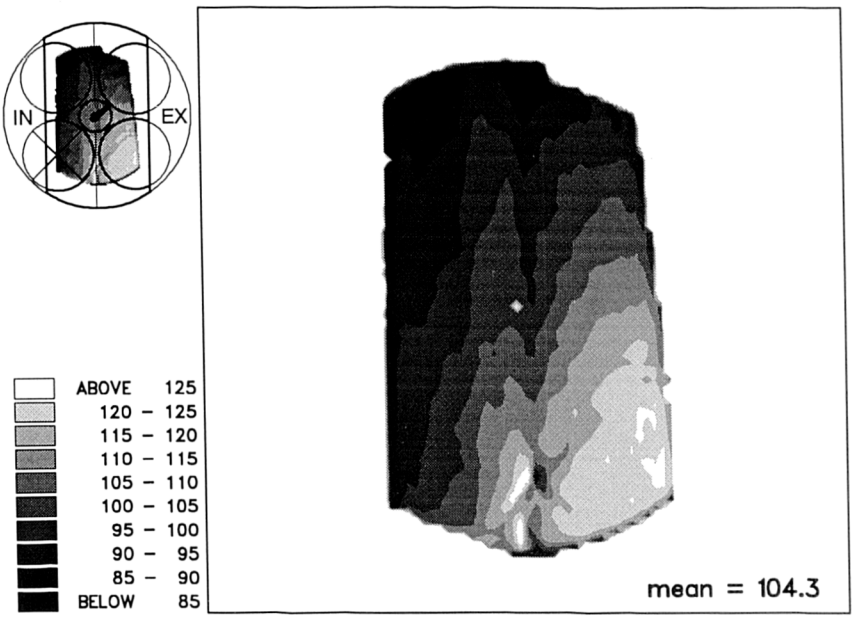

Fig. 5.11: Mean fuel concentration of 200 single images taken at the time of ignition (680° CA after combustion TDC) 0.7 mm below the spark plug with **injection 405° CA** after combustion TDC. The fuel concentration is displayed on the basis of the mean concentration in the image of Fig. 5.12 which was set to 100.

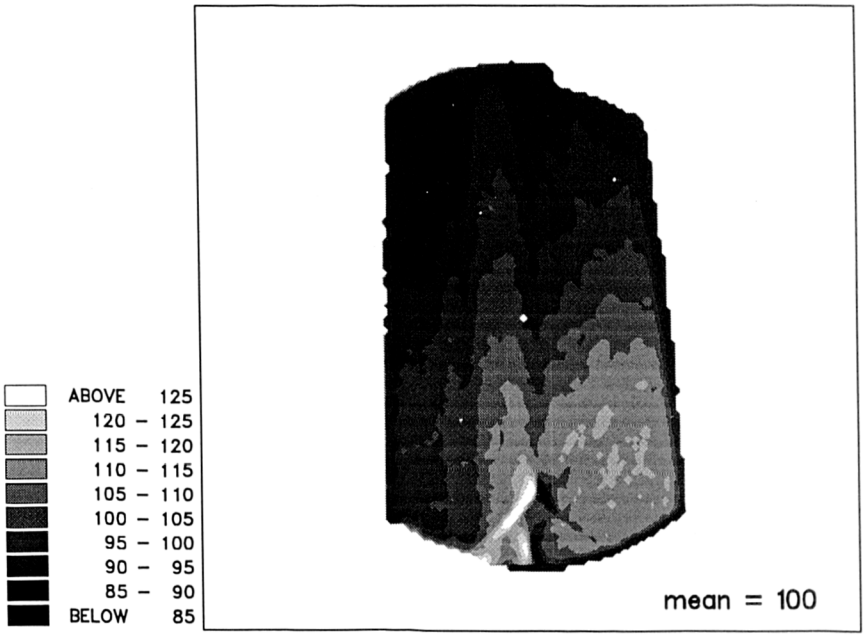

Fig. 5.12: Mean fuel concentration of 189 single images taken at the time of ignition (680° CA after combustion TDC) 0.7 mm below the spark plug with **injection 0° CA** after combustion TDC. The average fuel concentration in the image was set to 100.

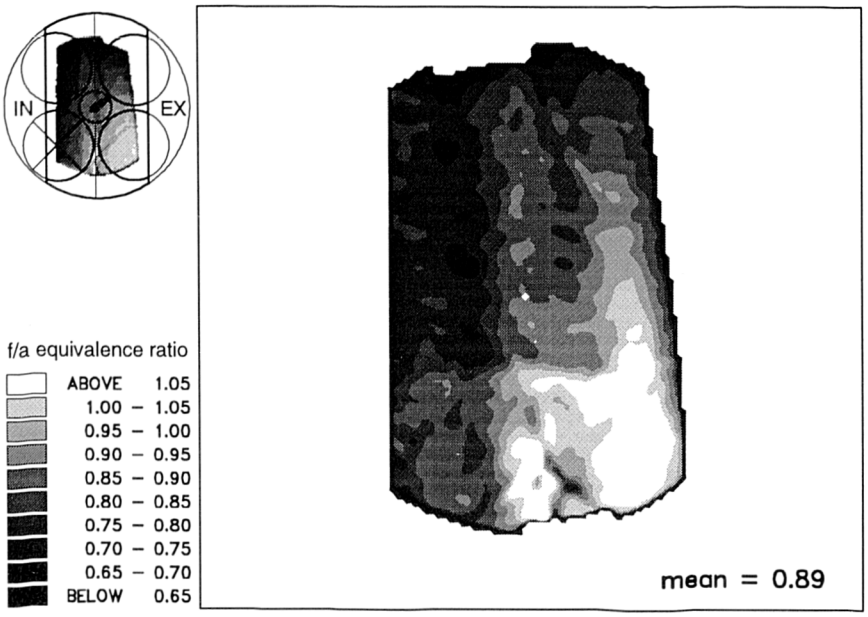

Fig. 5.13: Fuel concentration averaged over 125 consecutive cycle at the time of ignition (680° CA) 0.7 mm below the spark plug with **injection 405° CA** ATDC.

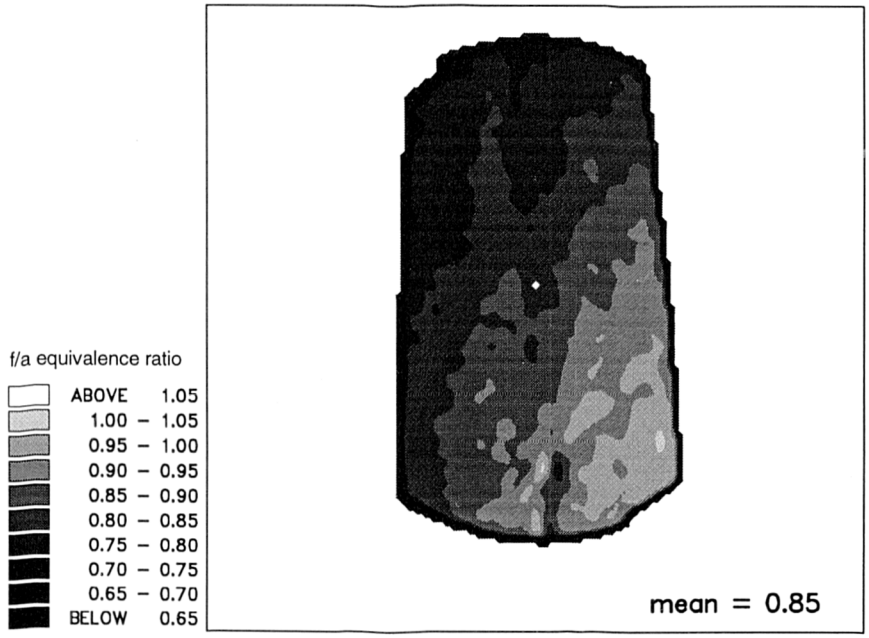

Fig. 5.14: Fuel concentration averaged over 125 consecutive cycle at the time of ignition (680° CA) 0.7 mm below the spark plug with **injection 0° CA** ATDC.

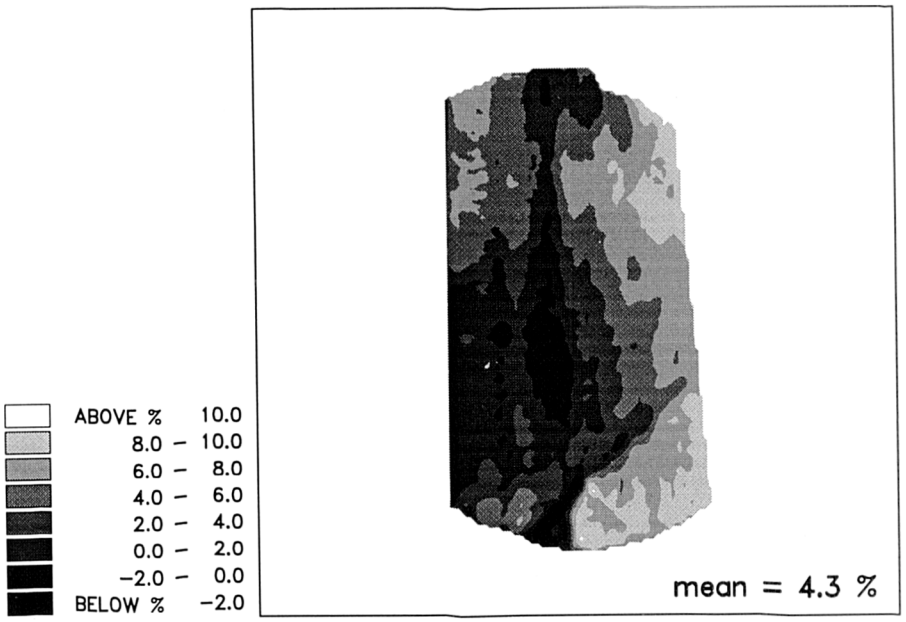

Fig. 5.15: Fractional difference between mean fuel distribution for injection at 405° CA and 0° CA. Fuel injection at 405° CA results on average in a 4.3 % higher fuel concentration in a plane 0.7 mm below the spark plug.

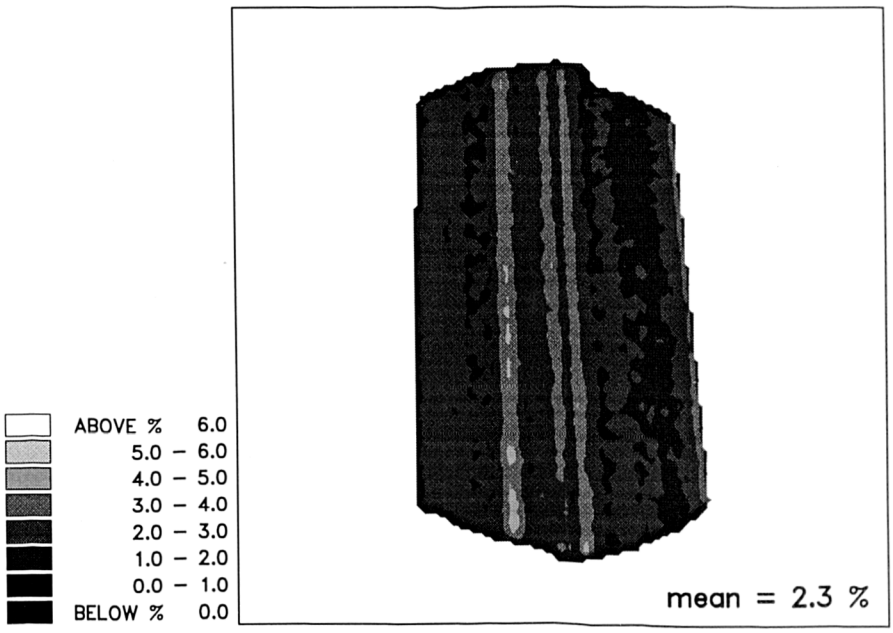

Fig. 5.16: Percentage fluctuation around the mean signal of 20 calibration images. The mean fluctuation is 2.3 %.

Following Page:

Fig. 5.17: Cycle-by-Cycle mixture fluctuations illustrated on 49 out of the 200 single exposure fuel concentration images taken at ignition (680° CA) in a plane 0.7 m blow the spark plug with fuel **injection at 405° CA** after combustion TDC. The average fuel concentration of 200 cycles is 100 in the measurement plane. First number in top row below images refers to the mean fuel concentration in the respective image. The second number represents the mean fuel concentration in a circle centred on the spark plug with a radius of half the image width. The numbers in the bottom row show the corresponding peak pressure p_{max} and peak c'angle θ_{max}.

160
150
140
130
120
110
100
90
80
70
60
IN
EX
EX
mean/mean-center-pixel
peak-pressure/6°-angle

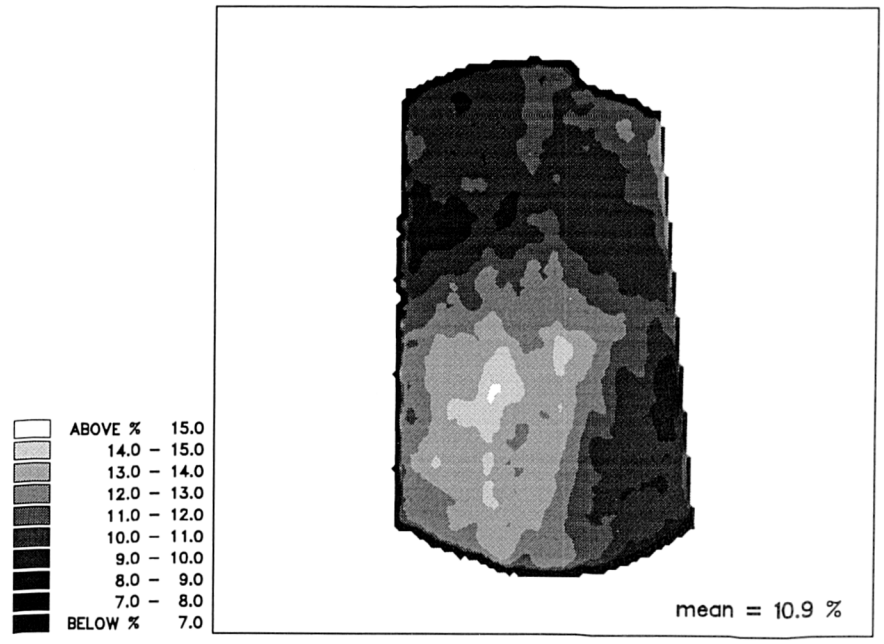

Fig. 5.18: Percentage fluctuation in fuel concentration around the mean of 200 single images for **injection 405° CA**. The average fluctuation across the image is 10.9 %.

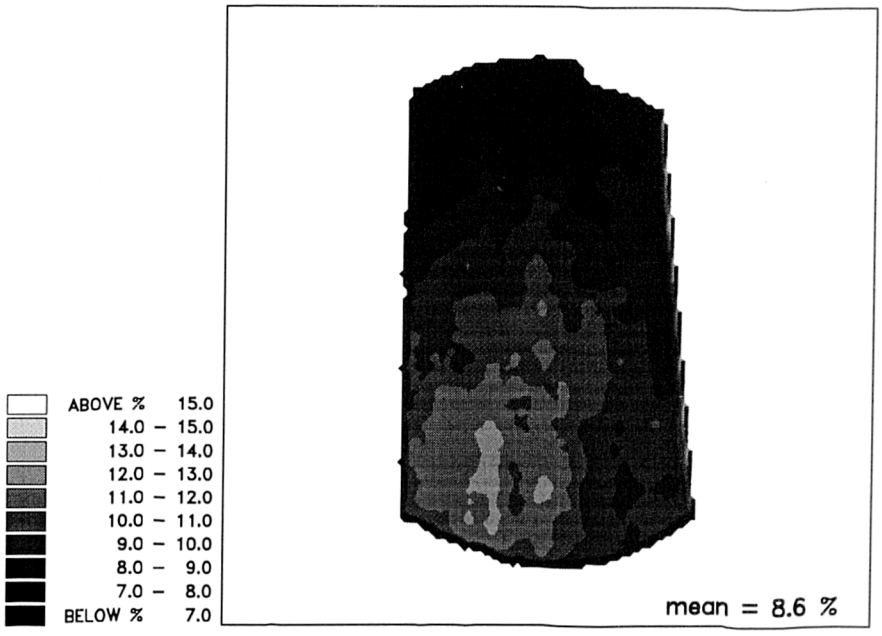

Fig. 5.19: Percentage fluctuation in fuel concentration around the mean of 189 single images for **injection 0° CA**. The average fluctuation across the image is 8.6 %.

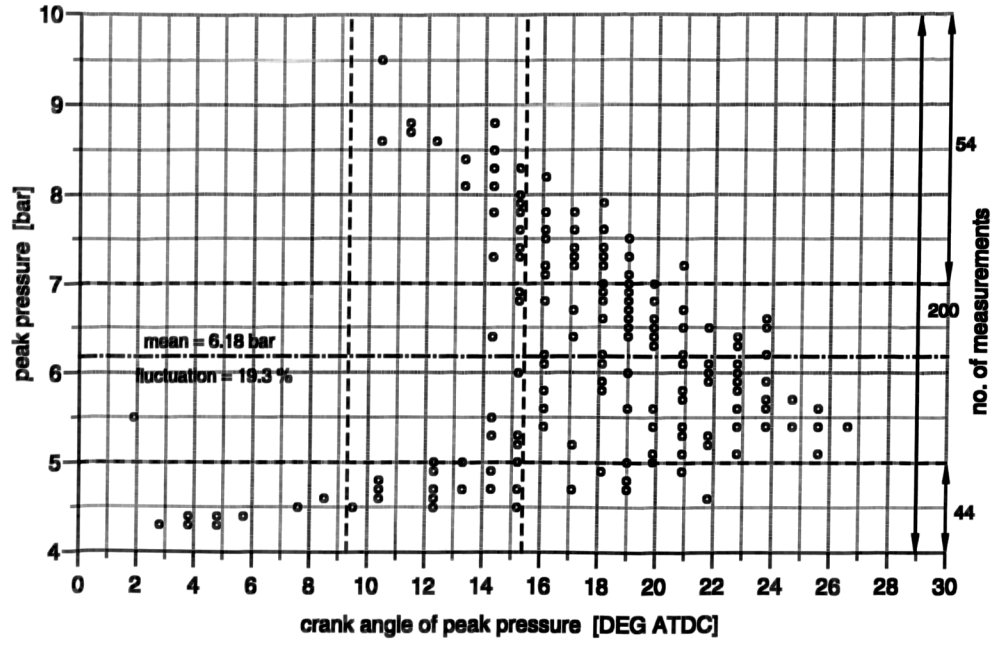

Fig. 5.20: Peak pressure versus crank angle for **injection 405° CA**. There are 54 "good" ($p_{max} \geq 7$ bar) and 44 "bad" ($p_{max} \leq 5$ bar) cycles out of 200 measurements. The peak pressure fluctuates by 19.3 % around the average of 6.18 bar.

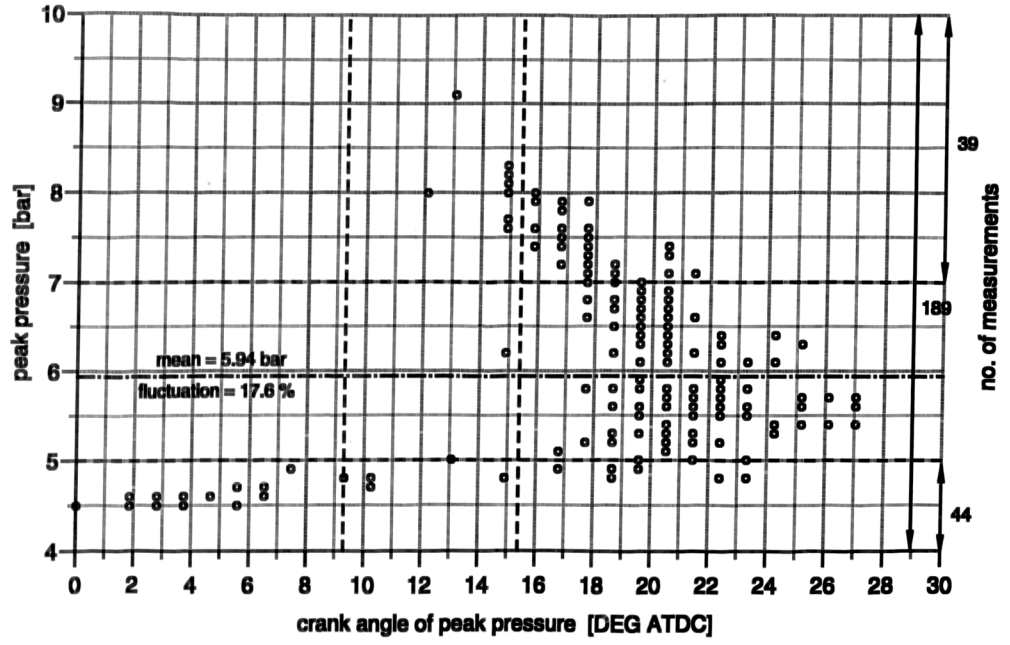

Fig. 5.21: Peak pressure versus crank angle for **injection 0° CA**. There are 39 "good" ($p_{max} \geq 7$ bar) and 44 "bad" ($p_{max} \leq 5$ bar) cycles out of 189 measurements. The peak pressure fluctuates by 17.6 % around the average of 5.94 bar.

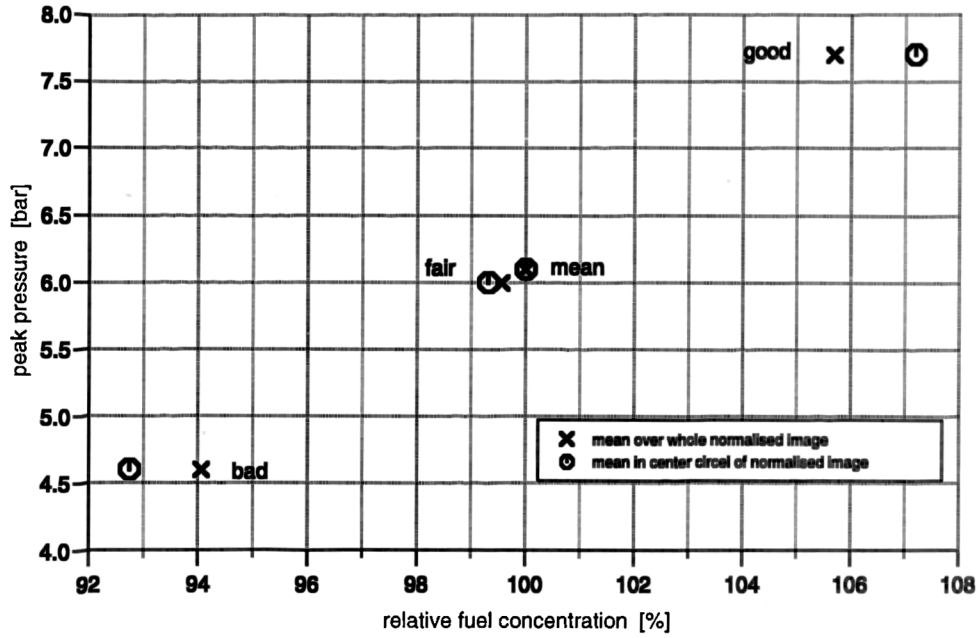

Fig. 5.22: Average peak pressure versus average fuel concentration of "good" ($p_{max} \geq 7$ bar), "bad" ($p_{max} \leq 5$ bar), "fair" ($5 \leq p_{max} \leq 7$ bar) cycles and the mean of all cycles for **injection 405° CA**. The fuel concentration is measured over the whole image and in a circle (radii = half width of image) centred on the spark plug.

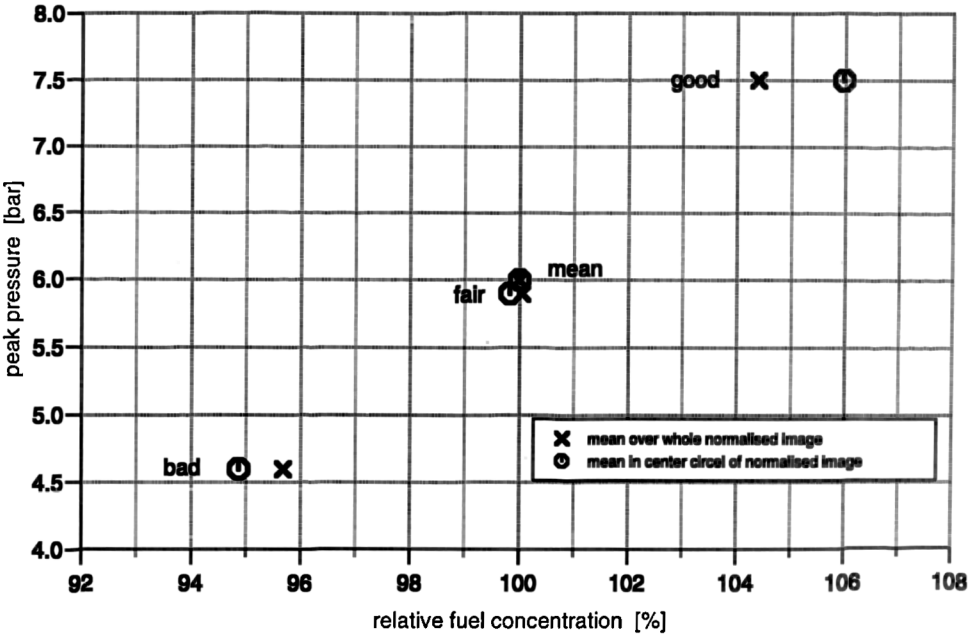

Fig. 5.23: Average peak pressure versus average fuel concentration of "good" ($p_{max} \geq 7$ bar), "bad" ($p_{max} \leq 5$ bar), "fair" ($5 \leq p_{max} \leq 7$ bar) cycles and the mean of all cycles for **injection 0° CA**. The fuel concentration is measured over the whole image and in a circle (radii = half width of image) centred on the spark plug.

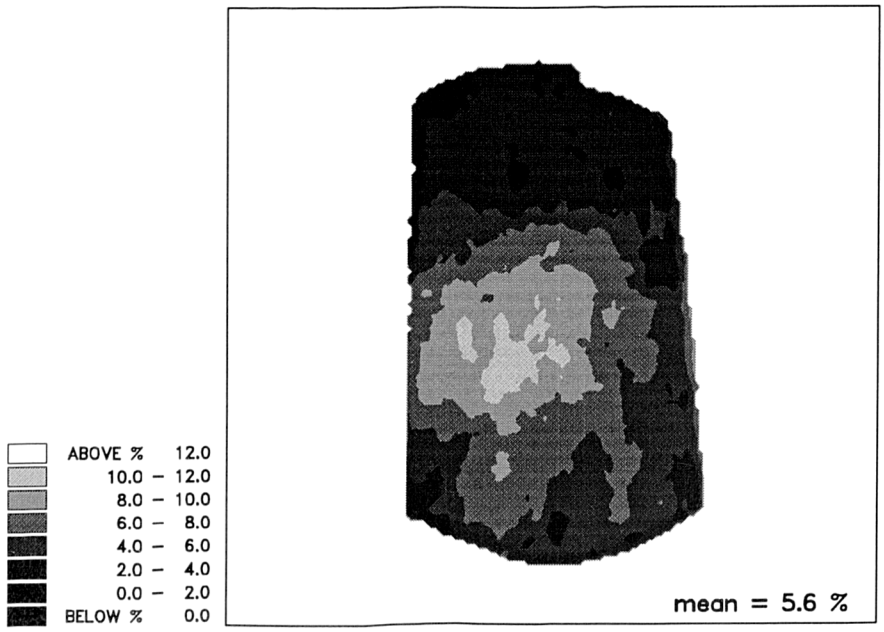

Fig. 5.24: Fractional difference of "good cycles" ($p_{max} \geq 7$ bar) from the mean fuel concentration of all 200 measurements for **injection 405° CA**. The average "good cycle" is 5.6 % richer than an average cycle.

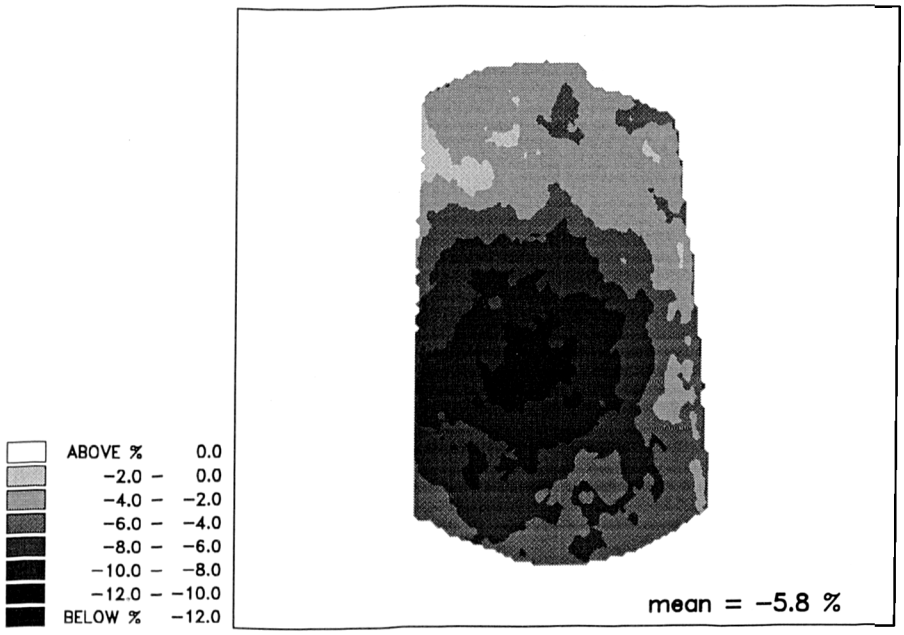

Fig. 5.25: Fractional difference of "bad cycles" ($p_{max} \leq 5$ bar) from the mean fuel concentration of all 200 measurements for **injection 405° CA**. The average "bad cycle" is 5.8 % leaner than an average cycle.

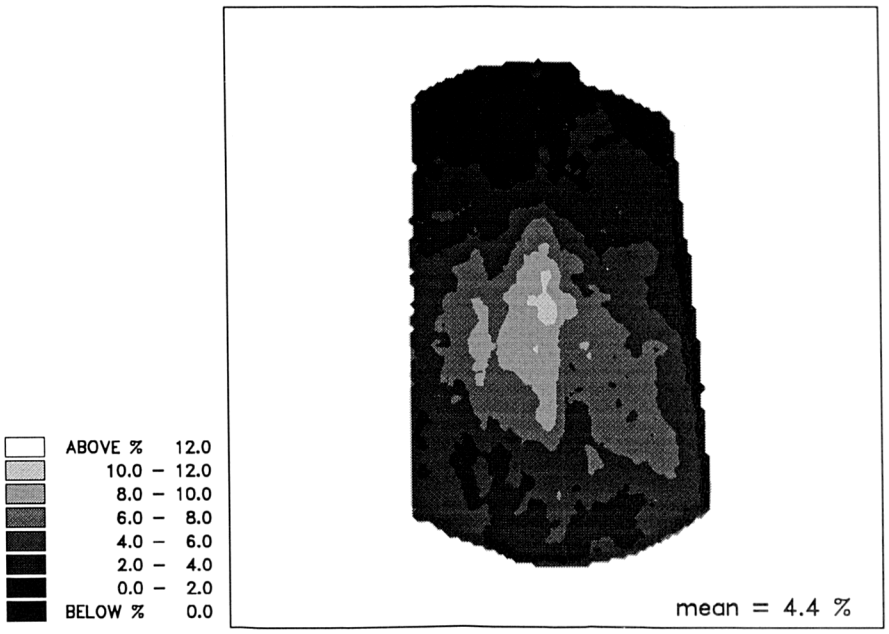

Fig. 5.26: Fractional difference of "good cycles" ($p_{max} \geq 7$ bar) from the mean fuel concentration of all 189 measurements for **injection 0° CA**. The average "good cycle" is 4.4 % richer than an average cycle.

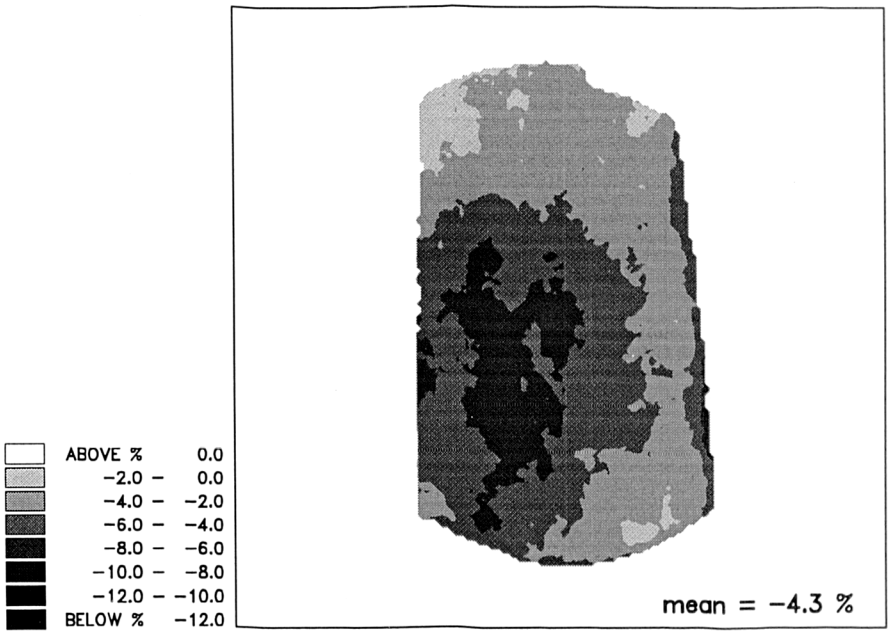

Fig. 5.27: Fractional difference of "bad cycles" ($p_{max} \leq 5$ bar) from the mean fuel concentration of all 189 measurements for **injection 0° CA**. The average "bad cycle" is 4.3 % leaner than an average cycle.

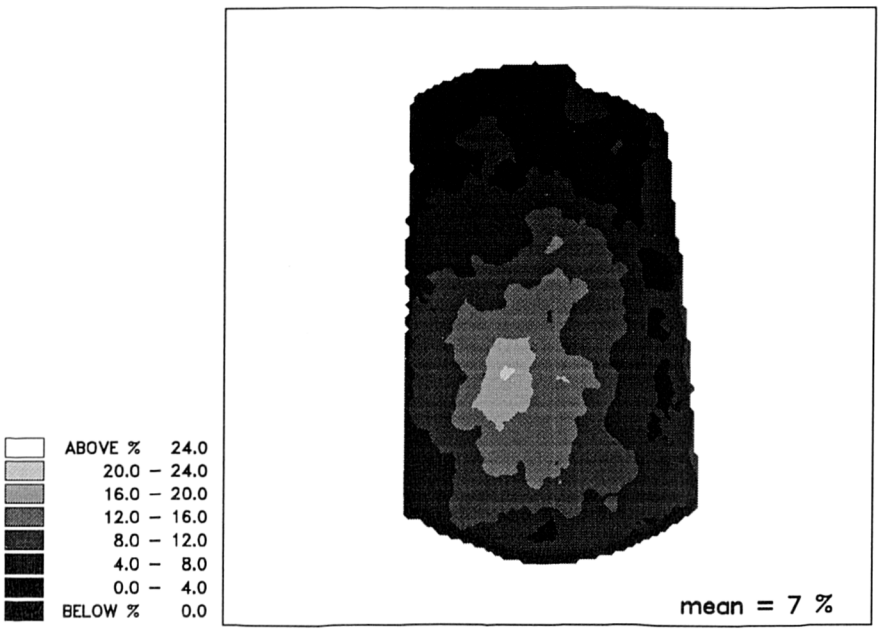

Fig. 5.28: Fractional difference of "good cycles" ($p_{max} \geq 7$ bar between 9° and 16° CA ATDC) from the mean fuel concentration of all 200 measurements for **injection 405° CA**. The average "good cycle" is 7 % richer than an average cycle.

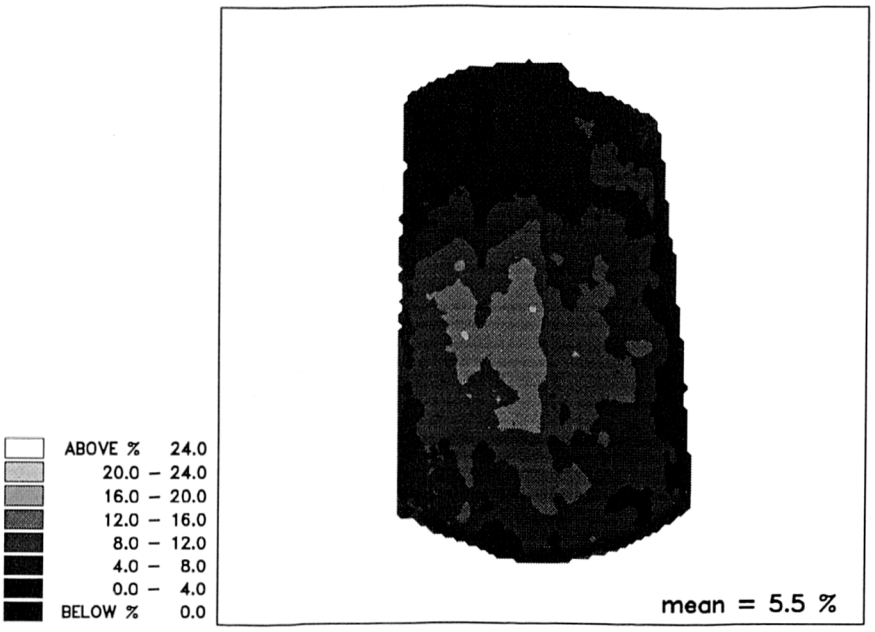

Fig. 5.29: Fractional difference of "good cycles" ($p_{max} \geq 7$ bar between 9° and 16° CA ATDC) from the mean fuel concentration of all 189 measurements for **injection 0° CA**. The average "good cycle" is 5.5 % richer than an average cycle.

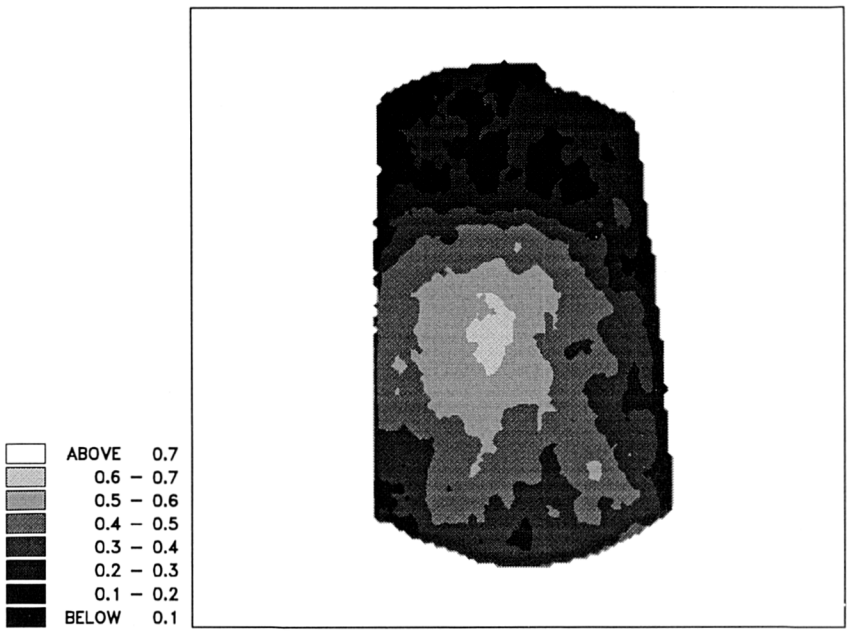

Fig. 5.30: Sample correlation coefficient between peak pressure and fuel concentration for **injection 405° CA.**

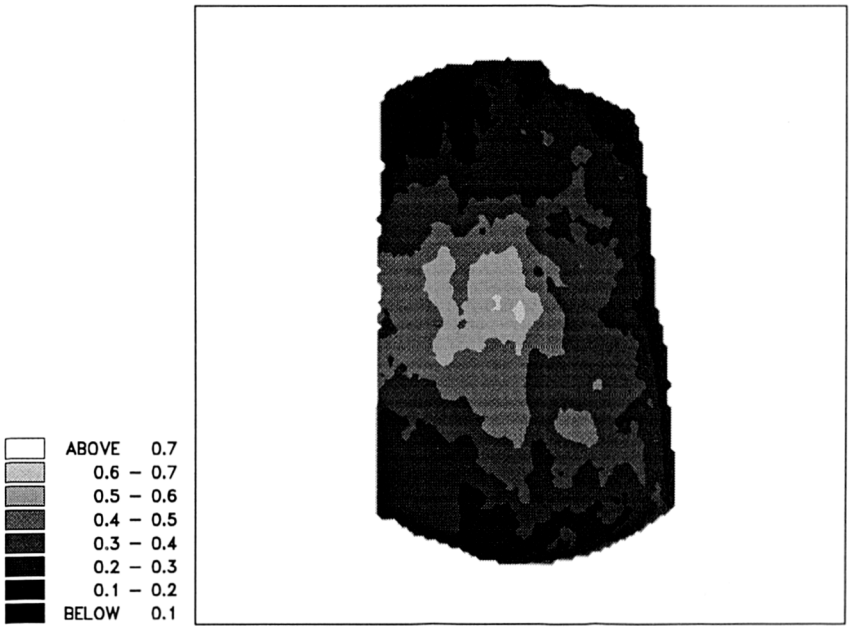

Fig. 5.31: Sample correlation coefficient between peak pressure and fuel concentration for **injection 0° CA.**

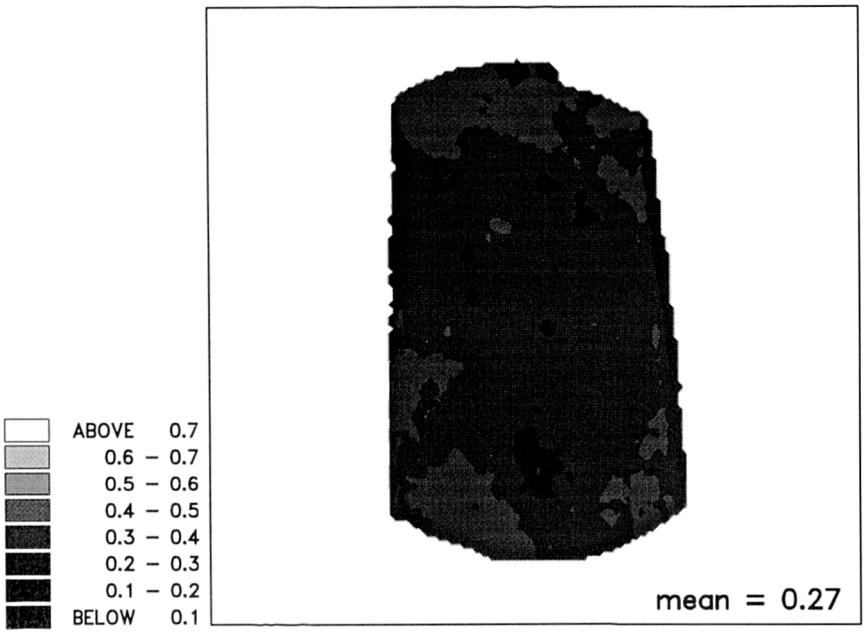

Fig. 5.32: Sample correlation coefficient between imep and fuel concentration for **injection 405° CA.**

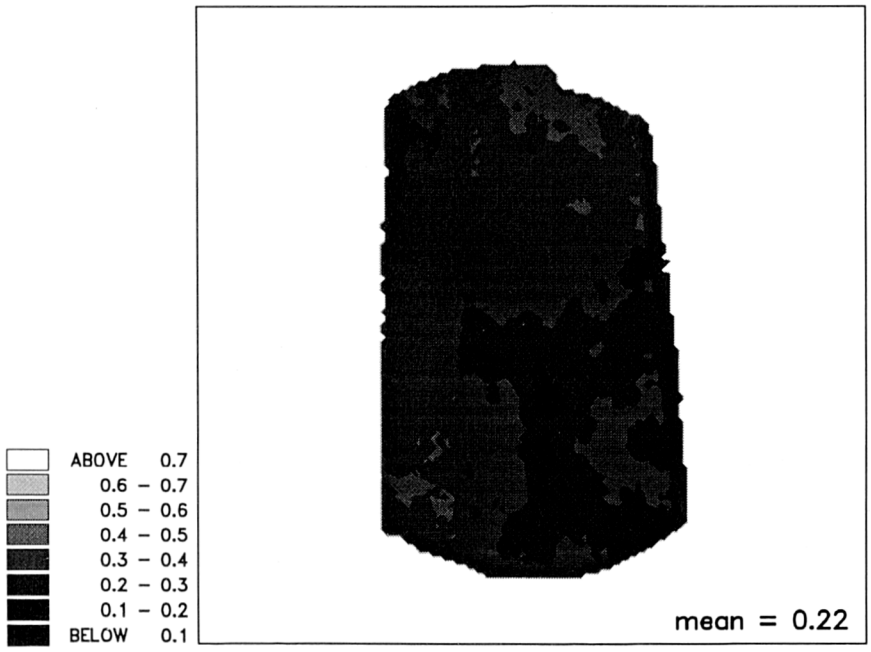

Fig. 5.33: Sample correlation coefficient between imep and fuel concentration for **injection 0° CA.**

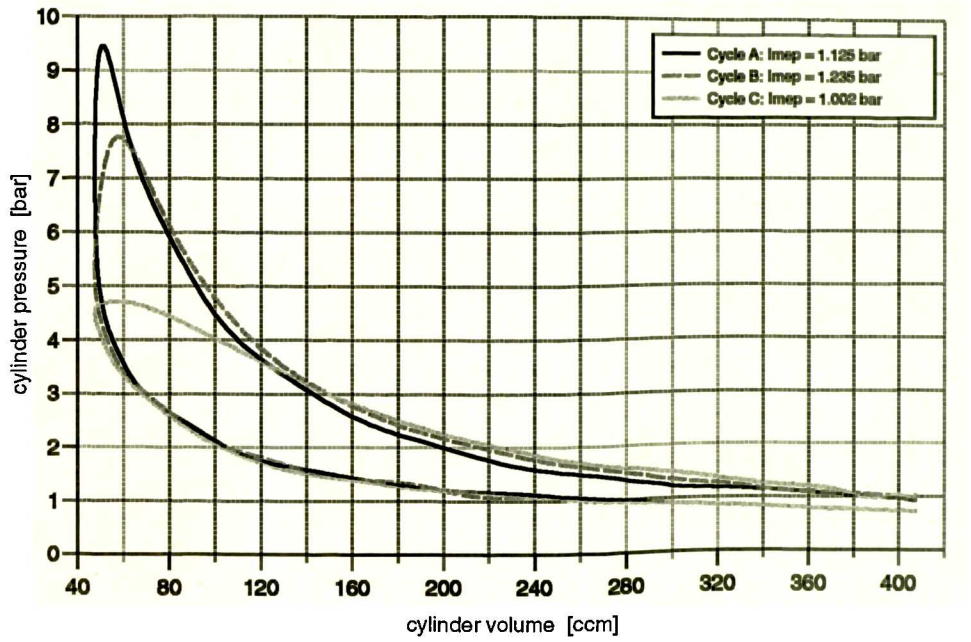

Fig. 5.34: p-V diagram of a fast (Cycle A), normal (Cycle B) and slow (Cycle C) burning cycle with resulting gross imep.

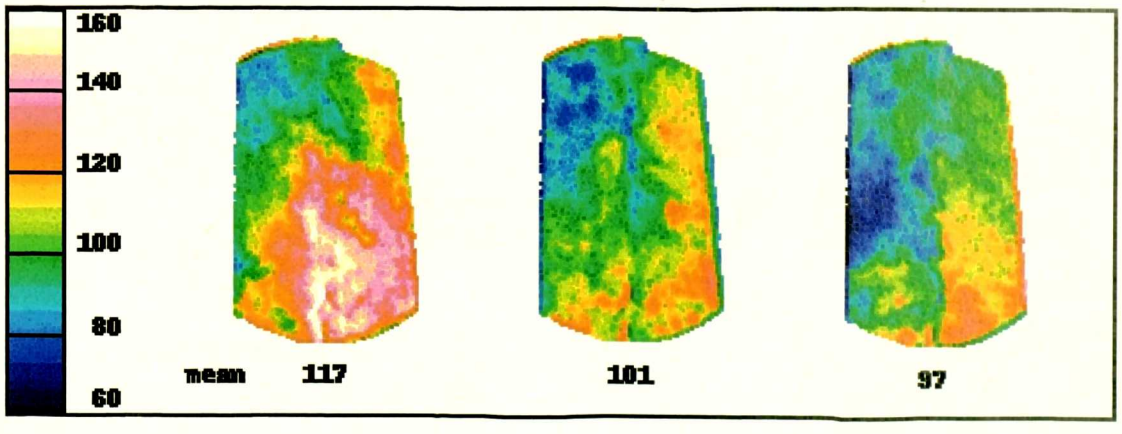

Fig. 5.35: Mixture concentration 0.7 mm below the spark plug of Cycle A, B and C (*from left*) corresponding to p-V diagram in Figure 5.34. Mixture concentration of 100 corresponds to the average fuel concentration of 200 cycles.

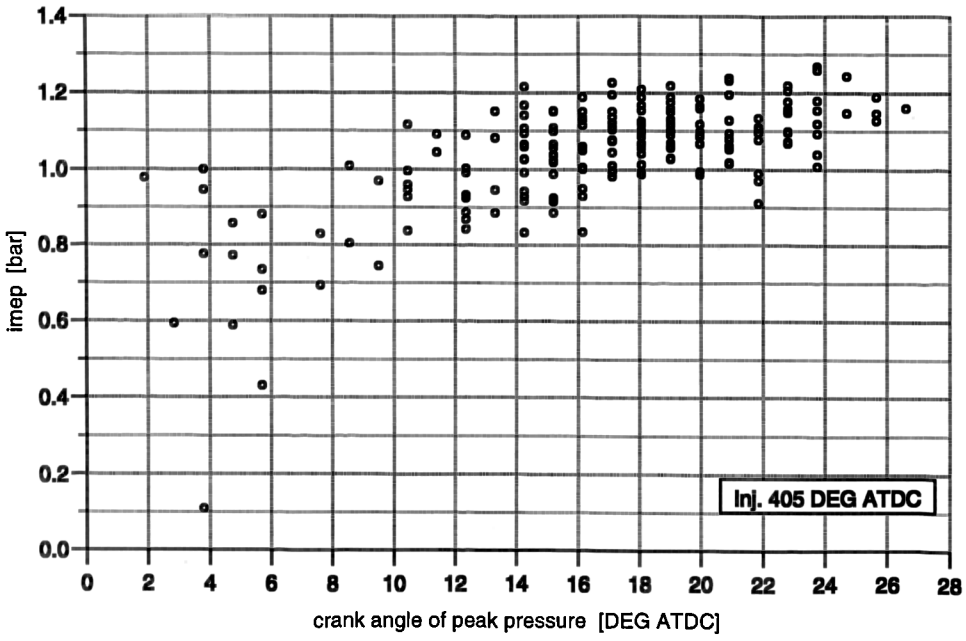

Fig. 5.36: Gross imep against crank angle of peak pressure from 200 in-cylinder pressure measurements corresponding to the fuel concentration measurements with fuel **injection at 405° CA.**

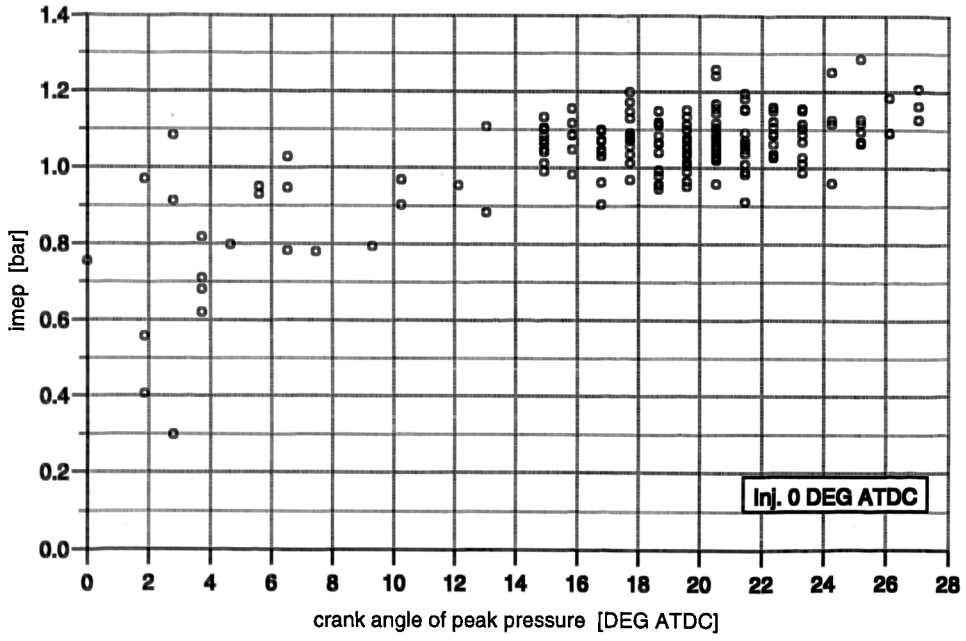

Fig. 5.37: Gross imep against crank angle of peak pressure from 189 in-cylinder pressure measurements corresponding to the fuel concentration measurements with fuel **injection at 0° CA.**

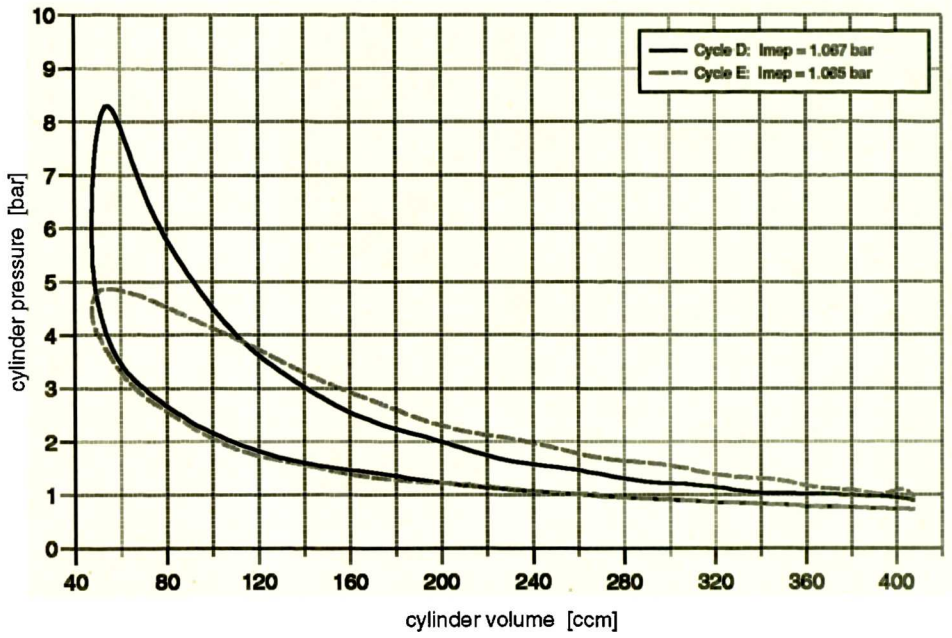

Fig. 5.38: p-V diagram of a fast (Cycle D) and a slow (Cycle E) burning cycle. Both cycles have the same gross imep.

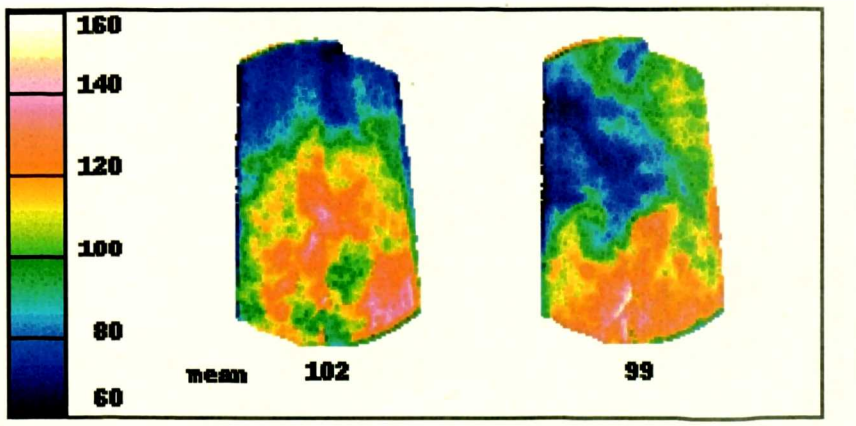

Fig. 5.39: Mixture concentration 0.7 mm below the spark plug of Cycle D and E (from left) corresponding to p-V diagram in Figure 5.38. Mixture concentration of 100 corresponds to the average fuel concentration of 200 cycles.

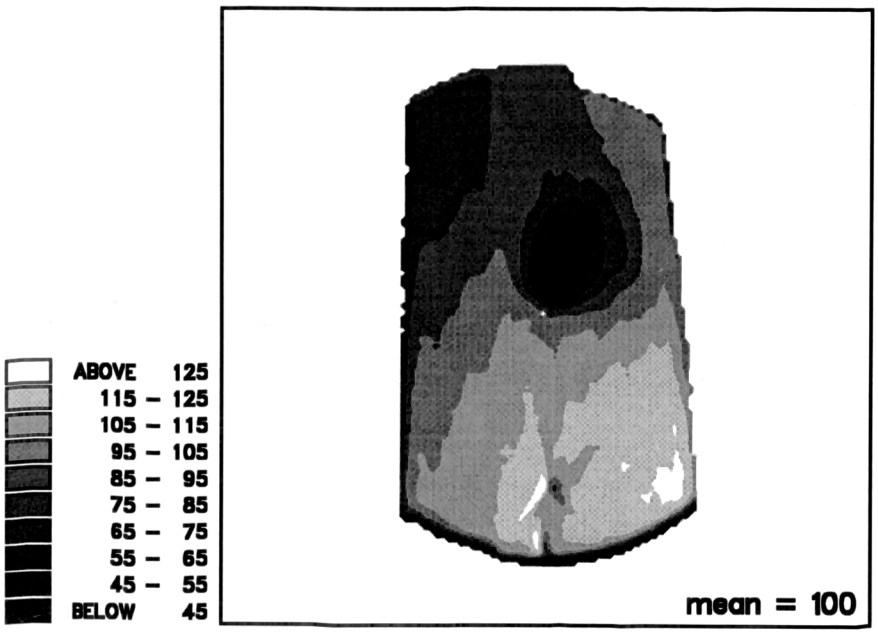

Fig. 5.40: Average of 200 images taken 20° CA after ignition (680° CA after TDC) for **injection 405° CA** after combustion TDC in a plane 0.7 mm below the spark plug. Low fuel concentration in image centre indicates the burned area. The average fuel concentration outside the burned area was set to 100.

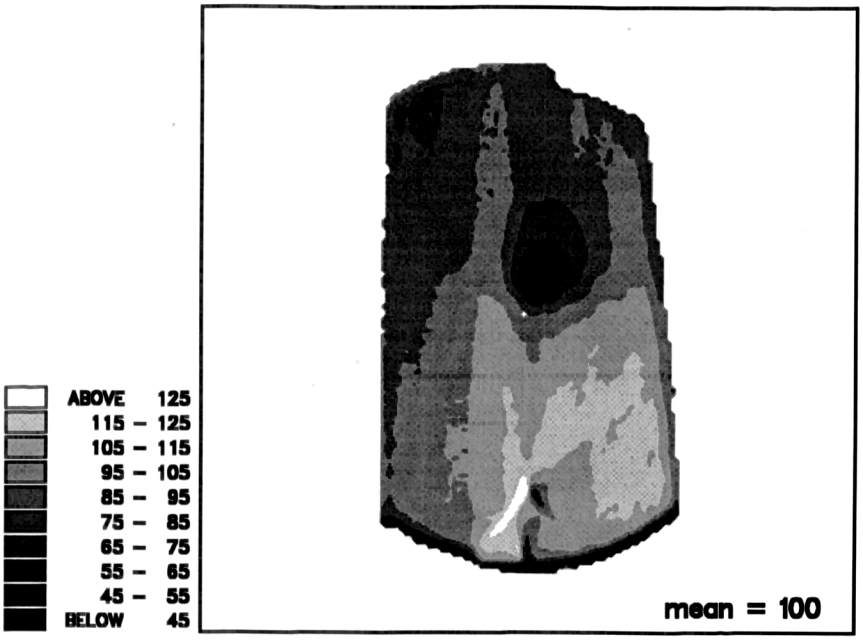

Fig. 5.41: Average of 186 images taken 20° CA after ignition (680° CA after TDC) for **injection 0° CA** after combustion TDC in a plane 0.7 mm below the spark plug. Low fuel concentration in image centre indicates the burned area. The average fuel concentration outside the burned area was set to 100.

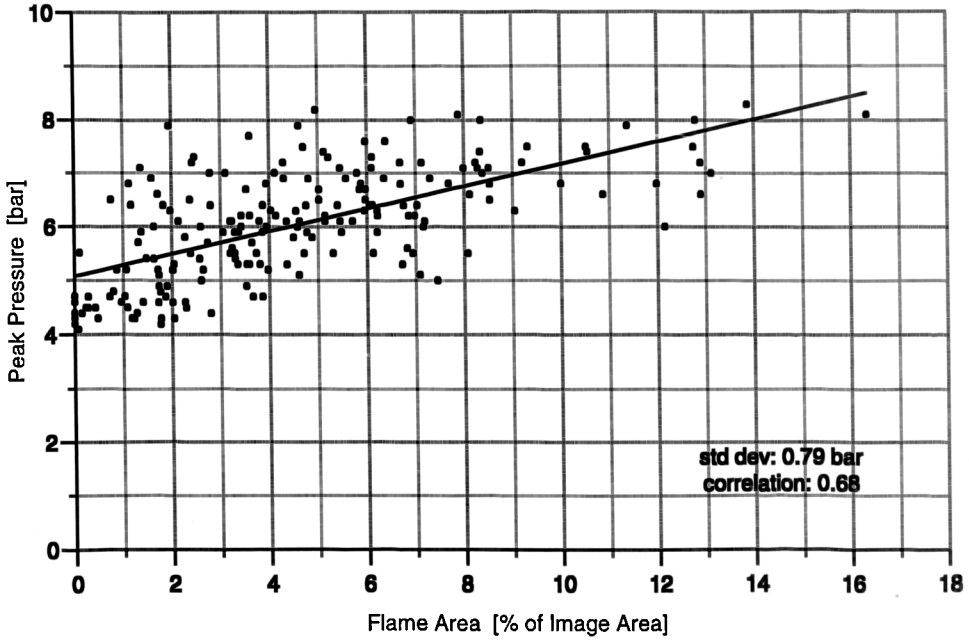

Fig. 5.42: Peak pressure versus flame area of images taken 20° CA after ignition (680° CA) in a plane 0.7 mm below the spark plug for **injection 405° CA**. The flame area is expressed as a percentile of the image area. The linear regression has a correlation coefficient of 0.68 and a standard deviation of 0.79 bar.

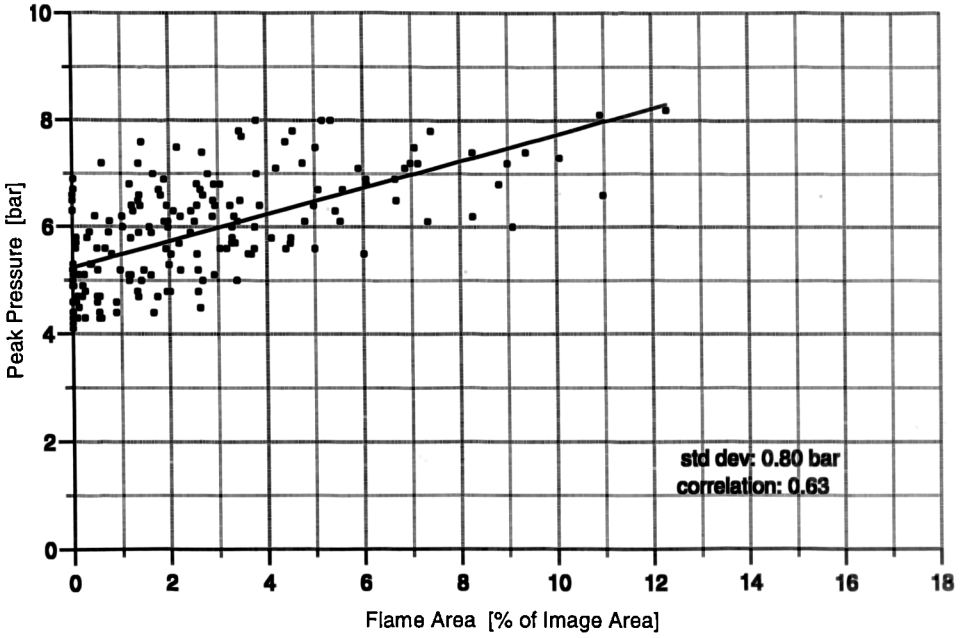

Fig. 5.43: Peak pressure versus flame area of images taken 20° CA after ignition (680° CA) in a plane 0.7 mm below the spark plug for **injection 0° CA**. The flame area is expressed as a percentile of the image area. The linear regression has a correlation coefficient of 0.63 and a standard deviation of 0.80 bar.

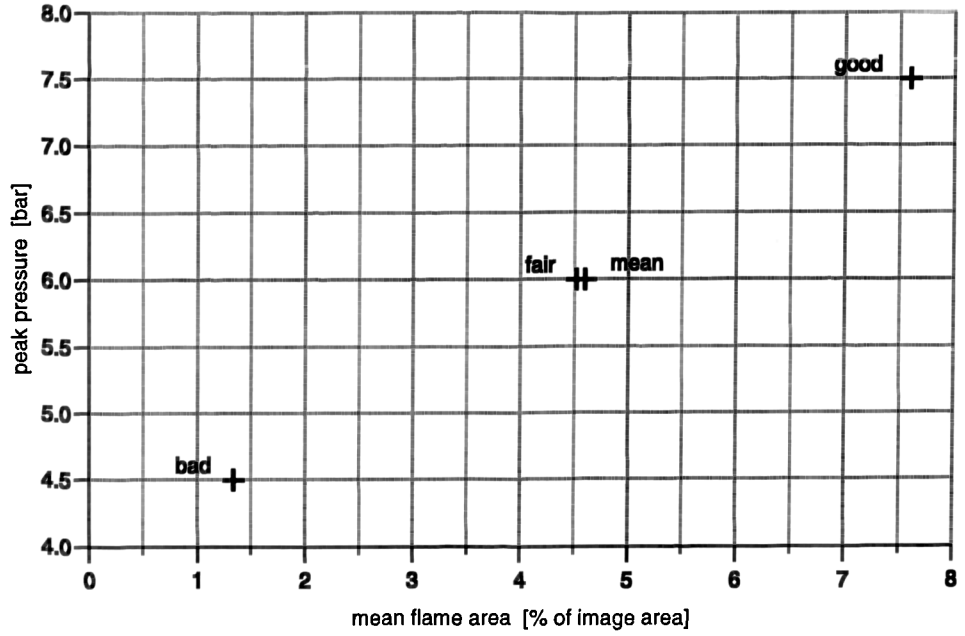

Fig. 5.44: Average peak pressure versus average flame area as percentage of image area of "good" ($p_{max} \geq 7$ bar), "bad" ($p_{max} \leq 5$ bar), "fair" ($5 \leq p_{max} \leq 7$ bar) cycles and the mean of all cycles for **injection 405° CA.**

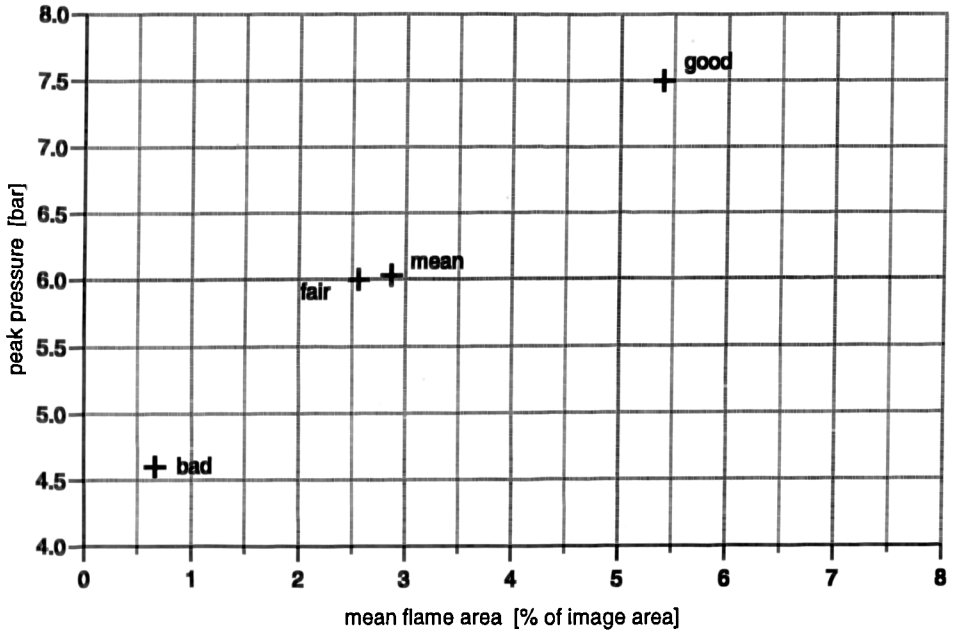

Fig. 5.45: Average peak pressure versus average flame area as percentage of image area of "good" ($p_{max} \geq 7$ bar), "bad" ($p_{max} \leq 5$ bar), "fair" ($5 \leq p_{max} \leq 7$ bar) cycles and the mean of all cycles for **injection 0° CA.**

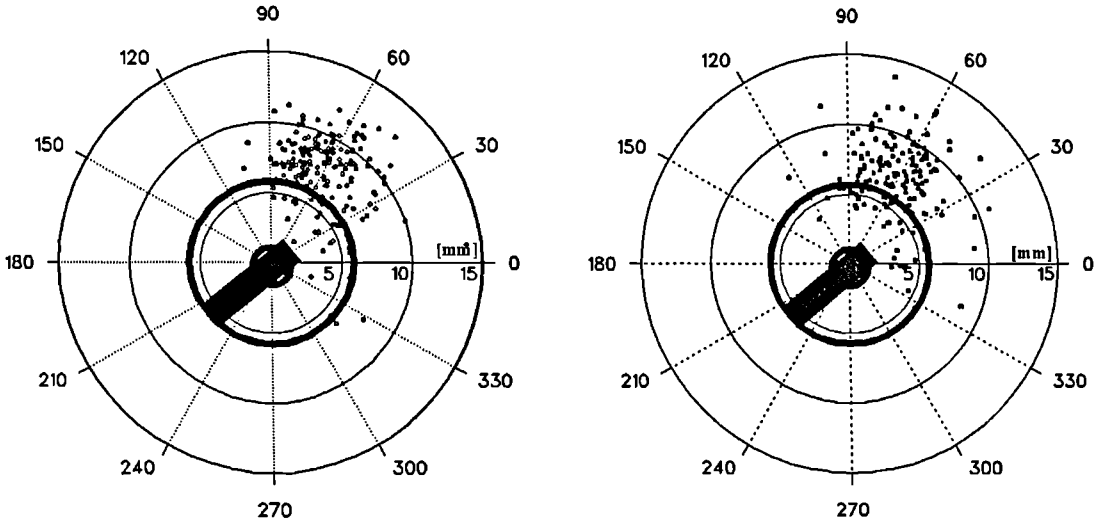

Inj. 405° CA

Inj. 0° CA

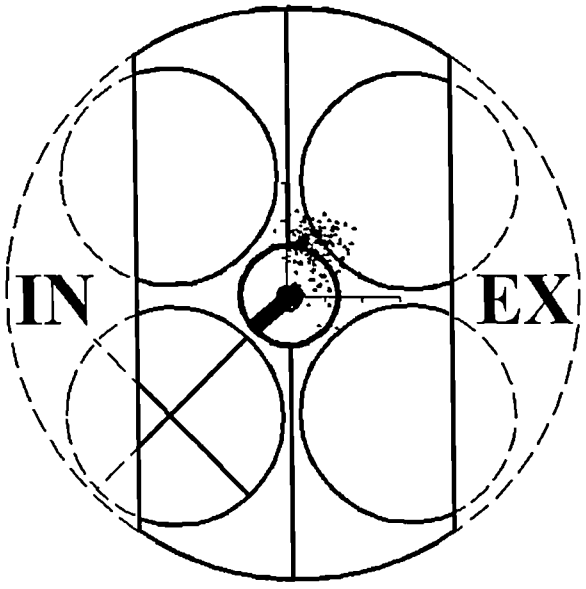

Fig. 5.46: Displacement of the centroid of the flame area relative to the spark plug for both injection timings (405° CA and 0° CA).

5.3 Implications for Engine Design

The objective of the design of the Honda lean burn engine was to extend the lean operation limit (Horie 1992). Introducing swirl was found to stabilise the combustion process. In order to avoid compromising performance due to the low volumetric efficiency of swirl inlet ports at high load and high speed operation, the second inlet port was specified without swirl. This required prevention of the air from entering through the non-swirling port during the lean operation mode. Therefore, the VTEC-E valve mechanism was utilised to reduce the valve lift during lean operation (Horie 1992). Injection phasing during the inlet valve open period was found to further extend the lean operation limit. Gas sampling near the spark gap revealed that, depending on when the fuel was injected, the mixture could be made leaner or richer (Matsushita 1985, Horie 1992, Hardalupas 1995). It was concluded that injection through the open inlet valve lead to axial fuel stratification (Horie 1992, Hardalupas 1995). Thus, the aim was not to generate a homogeneous fuel-air mixture but a stratified mixture. This objective has been achieved, as the results of this work clearly demonstrate. However, these results revealed some surprising and significant points for the engine designer. First, the influence of the reduced lift of the VTEC-E valve on charge stratification has not been previously considered. Second, the main mechanism governing the mixture distribution was found to be liquid fuel which formed a film on the exhaust-side cylinder wall. Injection timing influences the amount of liquid phase depositing on the cylinder wall and therefore the degree of axial stratification. However, contrasting to the previous understanding, even for fuel injection at combustion TDC the mixture was far from homogeneous. It remains unclear, whether tumbling inlet flows directed towards the cylinder wall, as generated in 4-valve pent-roof configurations, will in general lead to an inhomogeneous mixture, or if swirl prevents the fuel from mixing with the air. This aspect needs further investigation.

These results show the importance of the mixture strength in the vicinity of the spark plug. However the fuel images also revealed that the richest mixture sits opposite the secondary inlet valve on the exhaust side. As clearly shown by the correlation results in *Chapter 5.2*, it would be beneficial to the performance of the engine to position this cloud closer to the spark plug. This should reduce cycle-by-cycle variations in performance, since ignition and early flame development will be less sensitive to cyclic fluctuations in an "ignition happy" rich mixture, rather than in a mixture closer to the lean ignition limit (as shown in *Chapter 5.2*).

One possible strategy for achieving this goal might be to inject more of the fuel into the inlet port of the secondary inlet valve. By doing so, more of the fuel will remain in the top of the cylinder in the inlet half and less droplets will impinge on the exhaust cylinder wall. This would move the rich cloud from the side opposite the secondary inlet valve to the side beneath it. By increasing the swirl ratio from the present 2 to about 3, this fuel-rich cloud should move towards a position between the two inlet valves and extend more towards the middle of the cylinder. This is because the pent

roof head is not symmetrical - the width of the combustion chamber at a plane close to the spark plug is less between the exhaust and the inlet side than between the windows. However, an increased swirl ratio might compromise the engine performance at higher engine speeds. Also the effect of non-symmetric fuel injection on performance and emissions in the four-valve mode is not clear.

An alternative, more promising strategy would be to move the spark location towards the fuel-rich cloud. In order to avoid excessively long flame paths which would compromise high speed operation and could lead to a lower knock limit, a smaller second spark plug could be placed at the edge of the cylinder head between the secondary inlet valve and the exhaust valve. This might yield a further advantage. The locally rich mixture is not likely to benefit low NOx emissions. By moving the spark plug to the rich mixture it would be possible to reduce the level of inhomogeneity without compromising the combustion stability. Since the mixture between the inlet and exhaust valve is considerably richer than in the centre of the combustion chamber, injection during the inlet-valve-closed period might be possible and this should reduce NOx emissions (Hardalupas 1995).

5.4 Improvement of Fuel Visualisation Strategy

The previous section showed that with laser induced fluorescence imaging of a fluorescence marker, quantitative information on mixture formation and its influence on engine performance can be obtained. However the calibration of the fluorescence signal to an absolute equivalence ratio proved to be difficult. Despite preparation of a calibration gas of known concentration, the fluorescence signal of the calibration images could not be reliably related to the known concentration. A possible cause for this is absorption of seed material by gaskets used in the engine. Replacement of the cylinder head and window gaskets with metal gaskets would be a possible solution, but this requires re-engineering of certain parts of the engine.

Due to the problems incurred with the current method, a different approach to calibration of fluorescence images may be considered. Calibration images can be obtained in a firing engine supplied with a homogenous premixed air-and-fuel mixture. The mixture strength can be monitored using the exhaust gas sensor. If the calibration images are taken at the same crank-angle as the data images, using the same fuel, density and temperature effects are automatically accounted for. There will be an error due to imperfect mixing of the residual gas with the fresh charge (see Part 3 of this thesis). By taking an image of premixed fuel and air in a motored (non-combusting) engine the calibration image can be corrected for incomplete mixing of residual gas. This requires the collection of several calibration images to average out cyclic fluctuations in residual distribution. In order to obtain a good premix of fuel and air, it is suggested that the fuel is injected upstream of the inlet port into an elongated and heated inlet pipe. If necessary a large inlet plenum chamber can be used to further promote mixing.

PART III

RESIDUAL GAS VISUALISATION STUDIES

Chapter 6

Strategy for Residual Gas Visualisation

The potential for detection of major combustion products by planar LIF and their suitability as residual markers is reviewed. Problems and limitations associated with the chosen strategy are discussed. The criteria for selecting an excitation line are described.

6.1 Introduction

Information on residual gas fraction and fluctuation has been previously obtained by the use of probe-sampling (Matsui 1979, Galliot 1990) or CARS (Lebel 1992). Probe-sampling is advantageous since it possesses a low detection limit, is easy to use and is less expensive than laser-based techniques. Problems with probe-sampling can arise, however, if the sample probe interferes with the flow and if the sampling period is long compared to the mixing time scale of the in-cylinder flow. Gas sampling as well as CARS allow only point measurements with considerable uncertainty as to whether they are representative of the bulk composition. Precise spatial resolution can be achieved with the planar laser-induced fluorescence technique. Compared to other planar imaging techniques such as Raman or Rayleigh, LIF should be sufficiently sensitive to allow imaging of species naturally present in the residual gas. Typical exhaust gas concentrations of the major species formed in spark ignition engine combustion are shown as a function of equivalence ratio/air-fuel ratio in Figure 6.1. The concentration at the time of ignition will depend on the amount of residual gas remaining in the cylinder, which in turn is a function of compression ratio, valve overlap, engine load and speed. Galliot (1990) measured residual gas fractions of between 5 - 10 % at full load and about 20 % at part load (0.4 bar inlet pressure) in an engine with a compression ratio of 8.3:1 operating at 1500 rpm. Thus, at the time of ignition, the concentrations of residual species are at least an order of magnitude lower than given in Figure 6.1.

For this study lean combustion is of particular interest. There is no obvious reason why the residual distribution and fluctuation should be significantly different in a rich environment. However, if there is an influence of the residuals on the combustion

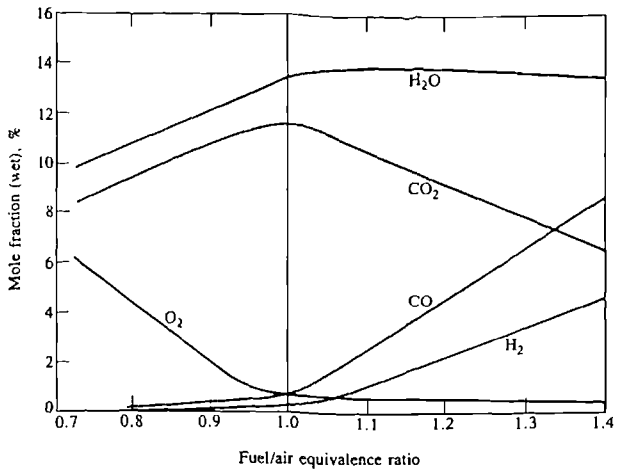

Fig. 6.1: Wet exhaust gas species concentrations as function of fuel/air equivalence ratio (Heywood 1988).

process on a cycle-to-cycle basis it is expected to be more pronounced for lean mixtures. This is because, as mixture strength is reduced from stoichiometric, flame speed becomes increasingly sensitive to the precise mixture strength (Metaghalchi 1982, Rhodes 1985). Therefore, residual imaging is of great potential importance in the study of lean combustion. [There is an important side aspect in that the windows of the optical engine tend to foul more quickly during rich combustion.]

6.2 Choice of a Residual Gas Marker

There are primarily six species in the combustion gas which could, potentially, be used as residual markers. Oxygen is obviously discarded since it is a major constituent of the intake air and is a reactant, not a product. Because of its high concentration in the exhaust gas the most promising species is CO_2, but there have been no reports in the literature on laser-induced fluorescence of CO_2. The next obvious choice from a concentration point of view is water vapour. Water vapour concentrations in the combustion gas are expected to be about 10 % which translates into about 1 % at the time of ignition. However the natural water content in the intake air at 300 K is of the same order. The use of dry air was regarded as impractical with our facilities due to the large air capacity required for operating an engine. CO and H_2 concentrations will be below 100 ppm at ignition for lean combustion. LIF detection of CO is possible with two photon excitation (Seitzman 1987). The detection limit for CO at flame temperatures and atmospheric pressure was estimated to be 100 ppm for 2 mJ pulse energy (Seitzman 1987). The lower temperatures in the unburned gas of an SI engine would improve that limit. The increase in number density due to the higher pressure at engine conditions will probably be offset by increased quenching. The application of a multi-pass cell, as used by Seitzman (1987), to an engine might be difficult from a

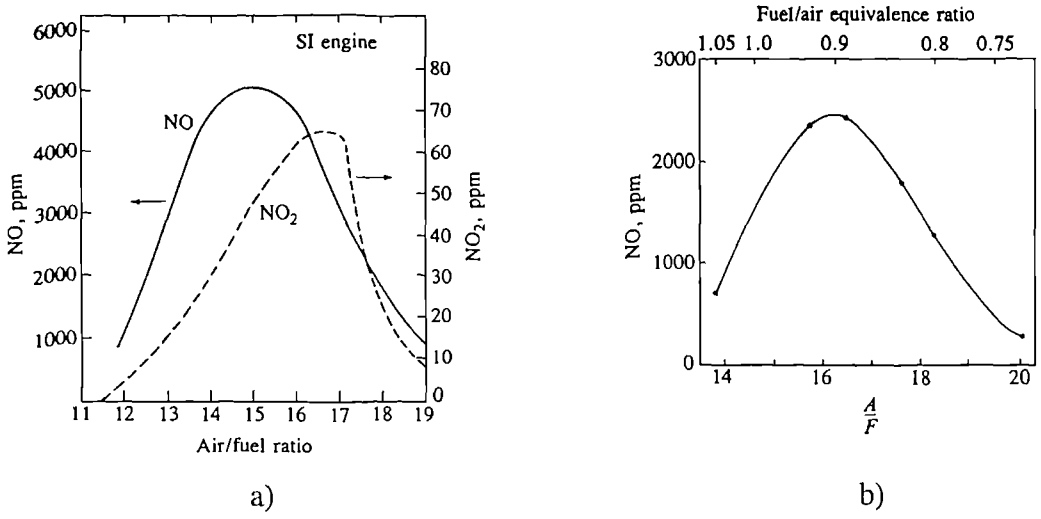

Fig. 6.2: **a)** NO and NO_2 concentration in SI engine exhaust as function of air/fuel ratio, 1500 rpm wide-open throttle; **b)** Variation of exhaust NO concentration with A/F and fuel/air equivalence ratio, 1600 rpm, η_v = 50 percent, MBT timing; Heywood (1988).

stability and alignment point of view. Focusing using cylindrical lenses could lead to a signal decline of about an order of magnitude. Additionally the probability of excitation for two-photon absorption is not linearly proportional to laser intensity. Therefore, normalisation of laser fluctuations and sheet inhomogeneities is very difficult. Another problem is photochemistry which may occur when using a short wavelength UV laser with power levels strong enough to induce two photon transition. It might be possible to overcome these problems. However, the concentrations in the unburned gas will be close to or less than the detection limit and therefore CO is not an attractive choice as a residual marker for lean combustion. Like CO, LIF detection of H_2 is possible with two photon excitation (Lempert 1991) and faces therefore, similar difficulties as LIF of CO when applied under engine running conditions. In addition, the temperature and pressure dependence, and the species dependent quenching of the H_2 fluorescence are not well documented.

This leaves nitric oxide (NO) and nitric dioxide (NO_2) as potential residual gas markers. The use of LIF for measuring of NO_2 has been reported frequently in the literature (Cole 1980, Cattolica 1986, Cattolica 1987). The concentration level of NO_2 in the combustion gas is about two orders of magnitude below that of NO and below the detection level associated with planar LIF measurements in an operating engine at the time of ignition (Figure 6.2a). On these grounds, NO_2 had to be discarded as a practical residual marker.

LIF has been widely used for measurement of NO concentration in flames (Morley 1982, Kychakoff 1984, Reisel 1993). At flame temperatures and atmospheric pressure the detection limit for NO has been estimated between 1 and 10 ppm (Reisel 1993, Kychakoff 1984). In a SI engine the NO concentration level will range from 4000-

5000 ppm (full load) to 500-1000 ppm (idle), which is well within the detection limit associated with LIF, even after dilution with the fresh charge.

The NO production in combustion is temperature dependent. Therefore the amount of NO in the exhaust gas will depend on the combustion temperature of that particular cycle. Since cycle-to-cycle fluctuations in combustion exist, the NO concentration in the exhaust gas will vary. Fluctuations in NO concentrations will therefore contain contributions due to fluctuations in the residual gas concentration and fluctuations due to the amount of NO generated in the previous cycle. This effect can be minimised by choosing a stable operation condition with low cycle-by-cycle variation in combustion. Chen (1976) showed that the NO production is approximately proportional to peak pressure of the corresponding cycle. This allows fluctuations in peak pressure to be used as a measure for cycle-by-cycle fluctuations in NO production. The nitric oxide concentration in a SI engine exhaust peaks at about AFR 16 (see *Chapter 1.2*). The absolute concentrations are depending on load condition and spark timing. Reducing the load on an SI engine, reduces the amount of mixture in the cylinder leading to a lower combustion temperature and therefore lower NO concentrations in the burnt gas. The further ignition is retarded from MBT timing the lower the combustion temperature and hence the NO concentration in the exhaust.

Planar imaging of the NO concentration can potentially provide a picture of the residual gas distribution and a measure of the cycle-by-cycle variation in residual concentration. Therefore nitric oxide has been chosen from the combustion products as a marker for the residual gas, because of its potential for giving the most accurate picture of the distribution and fluctuation at realistic engine operating conditions.

6.3 Laser Induced Fluorescence of Nitric Oxide

LIF on NO was previously used to study the kinetics of NO formation in flames (Morley 1982, Reisel 1993). Reisel (1993) excited a temperature independent line from the $X^2\ \Pi$ to the $A^2\ \Sigma$ state near 226 nm. The resulting fluorescence was detected between 234 and 238 nm. The detection limit was estimated to be 1 ppm at flame temperatures and atmospheric pressure. The same transition was used by Kychakoff (1984) and Paul (1989) for two-dimensional LIF measurement of Nitric Oxide. In an athmospheric methane-air burner the detection limit was estimated to 10 ppm (Kychakoff 1984). In operating IC engines LIF was used to image the NO distribution during expansion and exhaust strokes by Andresen (1990), Arnold (1992) and Burgman (1993). All three workers used the $D^2\ \Sigma\ (v' = 0) \leftarrow X^2\ \Pi\ (v'' = 0)$ transition in the (0,1) band near 193 nm for fluorescence imaging of NO. Andresen (1990) imaged the average distribution of NO at 200° CA after combustion TDC (exhaust stroke) in a 18 mm wide ribbon below the spark plug in a SI engine. Arnold (1992) used LIF to image the NO distribution during the expansion stroke in a DI-Diesel engine. The average distribution of NO could be obtained at 47° and 65° CA after combustion TDC in a narrow ribbon in the centre of the combustion chamber.

Burgman (1993) used 2D-LIF to image the in-cylinder NO distribution in a Diesel engine. Averaged NO distributions and typical single snapshots as a function of crank angle, engine load and fuel were presented for the expansion and exhaust strokes. The images presented by Andresen (1990), Arnold (1992) and Burgman (1993) give only qualitative information due to the effect of collision quenching of the $D^2\ \Sigma$ state and the effect of laser sheet inhomogeneity which has not been accounted for.

Linear fluorescence is complicated by the dependence of the signal on both the laser power and the quenching environment in the cylinder. The influence of laser sheet inhomogeneity can be quantitatively corrected using laser energy normalisation. The collision quenching will be dependent on pressure and temperature. For comparison of NO images taken at different conditions, the quenching rate coefficient must be determined to allow for collisional effects. Drake (1993) measured the quenching cross sections for laser induced fluorescence from NO for the most important combustion species and products as a function of temperature between 300 and 1750 K. NO is efficiently quenched by O_2, H_2O, CO_2 and is also an efficient self-quencher. O_2 quenching cross sections were found to decrease with increasing temperature, whereas the self-quenching cross section of NO was independent of temperature. With this data-base, quantitative measurements of NO concentrations in engines should be feasible. Cell measurements showed that at room temperature the NO fluorescence is independent of iso-octane concentrations, but is heavily quenched by 3-pentanone. This might cause a problem in future attempts to simultaneously image fuel (marked by 3-Pentanone) and residuals (marked by NO).

One way to avoid the dependence on laser power and quenching rate is to employ saturated laser induced fluorescence. To achieve saturation of the NO transition of interest, the laser fluence must be large enough to ensure that the laser excitation rate is much greater than the collisional quenching rate. When this condition is met, the population in the excited state is equal to that in the ground state to within the ratio of the degeneracies of the two states. A drawback of saturated LIF is that saturation can not be maintained in the wings of the laser beam where the fluence is low. This, together with the fact that it is not possible to achieve complete saturation during the entire duration of the laser pulse, results in simultaneous generation of saturated and non-saturated fluorescence. Previously, saturated laser-induced fluorescence has been used for successful quantitative point measurements of NO in flames by Reisel (1993). Planar saturated laser-induced fluorescence measurements would be difficult to quantify, because the partially saturated wings of the sheet will cover a substantial proportion of the measurement volume.

6.4 Choice of an Excitation Line

Previous NO fluorescence studies in IC engines excited the $D^2\ \Sigma\ (v' = 0) \leftarrow X^2\ \Pi\ (v'' = 0)$ transition in the (0,1) band near 193 nm (Andresen 1990, Arnold 1992, Burgman 1993). This wavelength is readily produced by an Argon-Fluoride (ArF) Excimer laser.

UV laser light at power levels strong enough to produce fluorescence signals may induce photochemical reactions. The species being probed might then be created through photo-dissociation of other molecules. Also ionisation might occur. These processes become more important in the short wavelength UV. In addition absorption of the UV laser by oxygen increases with shorter wavelength. For these reasons the $A^2 \Sigma (v'' = 0) \leftarrow X^2 \Pi (v' = 0)$ transition in the $\gamma(0,0)$ band near 226 nm was chosen for this work in preference to excitation from the $D^2 \Sigma$ to the $X^2 \Pi$ state (193 nm).

The temperature in the combustion chamber will be dependent on the residual distribution. This requires the use of a NO excitation line which has a temperature independent ground state population. The energy-level equations from Engleman (1970) were used to calculate the rotational energy levels for the $^2\Sigma$ and $^2\Pi$ states of the NO. Population level for temperatures between 300 and 700 Kelvin were calculated using Boltzmann's distribution law. The $Q_2(22.5)$ transition (225.967 nm) in the $\gamma(0,0)$ band was found to have a ground state population which varies by only 2% over a temperature range from 350 to 700 K.

In order to identify the $Q_2(22.5)$ transition, a fluorescence spectrum was measured between the excitation wavelength of 225.9 nm and 226.1 nm in 0.04 nm steps in a test cell containing 1000 ppm NO in Nitrogen at room temperature. The obtained LIF excitation spectrum was compared with a significant part of the complete spectrum in Engleman (1970). In Figure 6.3, the relevant rotational transitions as given by Engleman (1970) are indicated by vertical lines. All lines in the measured spectrum could be identified. Because the population of the different rotational levels in the ground state is strongly temperature dependent, one must be careful in drawing conclusions from the intensity differences of individual lines at room temperature, to the likely signal level at elevated temperatures in an engine. Figure 6.3 shows the results of an excitation scan between 225.955 and 225.975 nm (around the $Q_2(22.5)$ line) in 0.001 nm steps. The $Q_2(22.5)$ line is well separated from nearby main branch transitions. The results of an excitation scan between 225.5 and 225.6 nm are presented in Figure 6.4. Background images were taken by tuning-off resonance to 225.55 nm.

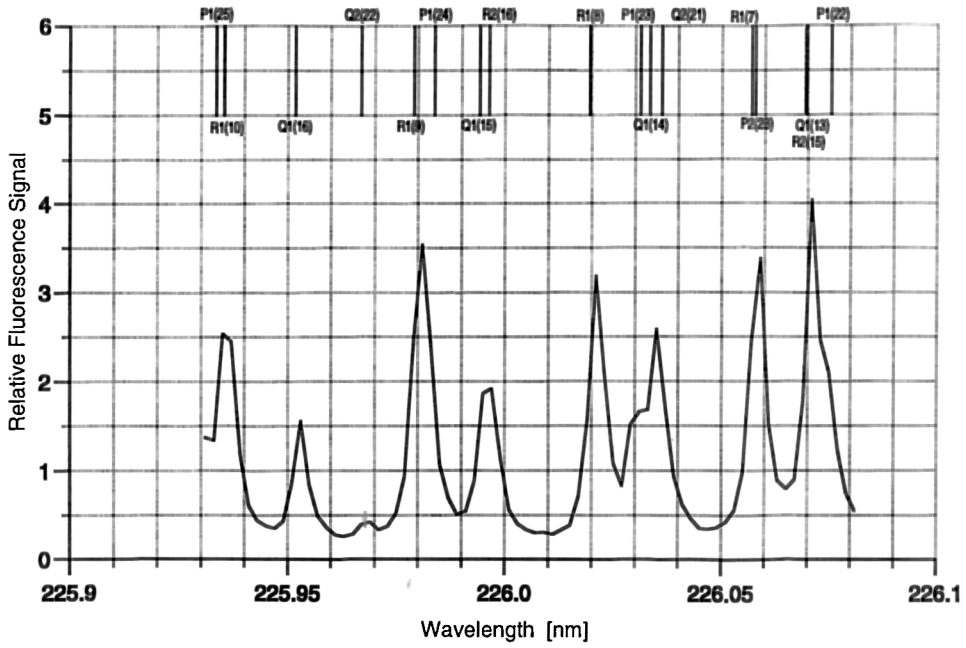

Fig. 6.3: Excitation scan of $\gamma(0,0)$ band of NO in a cell containing 1000 ppm NO in N_2 at room temperature and atmospheric pressure. The fluorescence was detected from the $\gamma(0,2)$ band. The wavelengths of the spectral lines are taken from Engleman (1970).

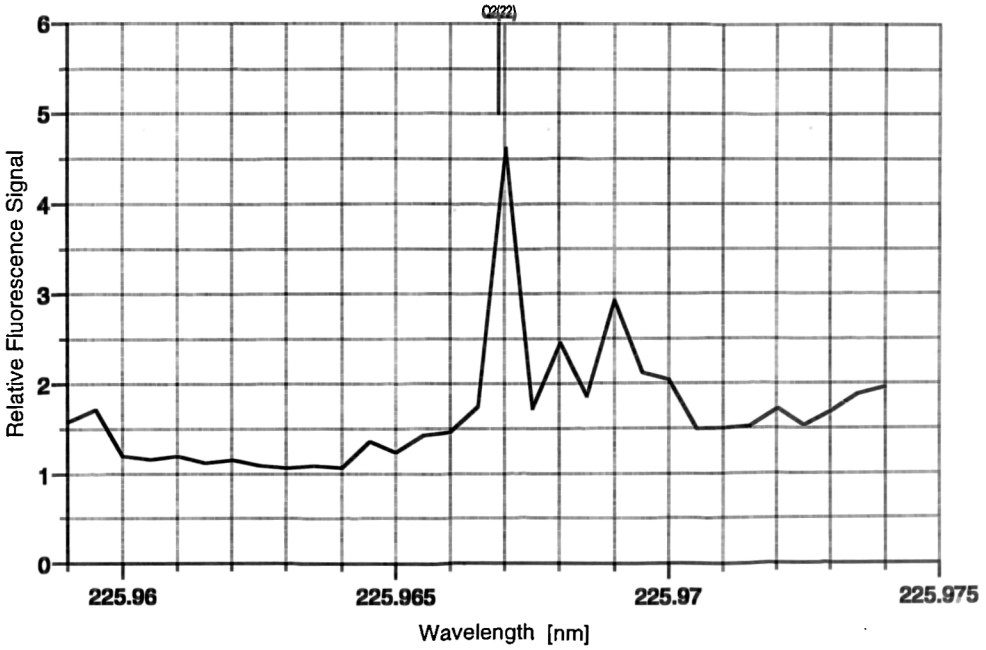

Fig. 6.4: Excitation scan around the $Q_2(22.5)$ line in the $\gamma(0,0)$ band of NO at room temperature.

Chapter 7

Experimental Set-Up for Residual Gas Visualisation

The equipment used for the planar LIF measurements of NO concentration in this thesis is described, including the laser system with the sheet-forming optics and the fluorescence detection system. Additionally, the timing and synchronisation of the experimental equipment and the measurement procedure for NO visualisation are described.

7.1 Laser and Sheet Forming Optics

The $Q_2(22.5)$ line of the $\gamma(0,0)$ band ($\lambda \cong 225.967$ nm) was used for excitation of NO. The laser system producing this wavelength comprised a Quanta-Ray GCR-200 Nd:YAG laser, with a Lambda Physik Scanmate dye laser and a Lambda Physik doubling crystal. The third harmonic ($\lambda = 355$ nm) of the Nd:YAG laser was used to pump the dye laser, which was configured for transverse pumping of the oscillator and both the first and second amplifier. The dye laser output at $\lambda = 440$ - 484 nm, with a peak conversion efficiency of the dye (Coumarin 47) at $\lambda = 456$ nm, was frequency-doubled, producing an output beam with a tuning range between $\lambda = 220$ - 242 nm. The laser system was purchased just prior to these experiments and unfortunately did not operate to specification. The maximum energy obtained for the frequency-doubled beam ($\lambda \cong 226$ nm) was 4 mJ/pulse with a corresponding pump beam ($\lambda = 355$ nm) energy of $\cong$ 400 mJ/pulse. Improvements on the laser since have more than doubled the conversion efficiency so that now 10 mJ of energy at 226 nm are available. Doubling the laser energy will double the fluorescence signal, but will also increase the background signal. In spite of this, the signal-to -noise ratio will slightly improve, since the background signal will not rise proportionally with laser energy.

The dye laser grating was calibrated against a NO spectrum from Dodge (1980) by comparison with a NO spectrum obtained between 226.5 and 226.7 nm. Figure 7.1 shows that the measured spectrum matches the one from Dodge (1980) when it is shifted by 0.031 nm. However this shift is temperature-dependent and retuning using the $Q_2(22.5)$ line was required on a daily basis.

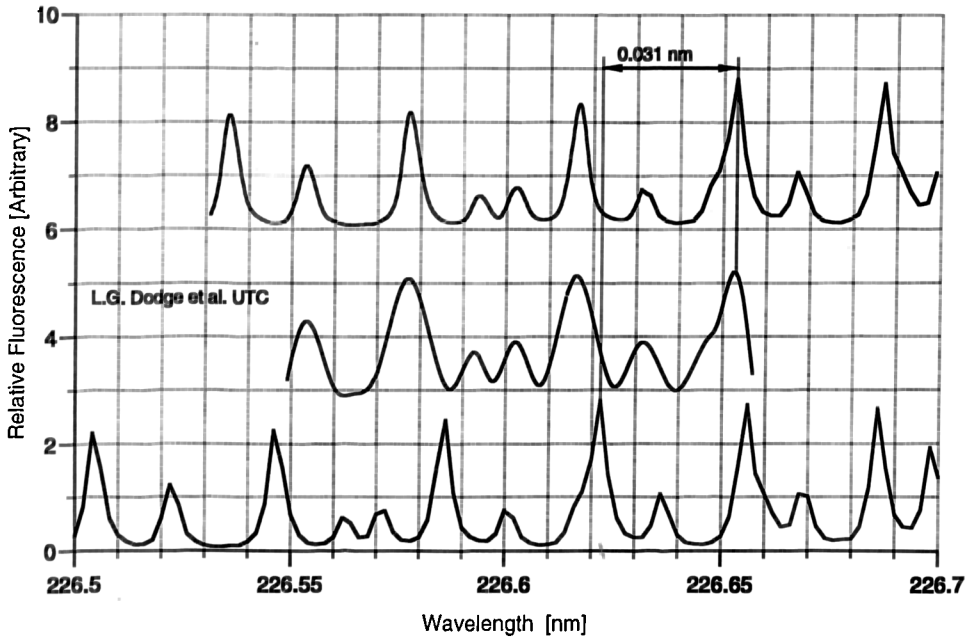

Fig. 7.1: Calibration of dye laser grating. NO excitation scan matches NO absorption spectrum from Dodge (1980) when shifted by 0.031 nm.

The laser sheet was formed using two fused silica cylindrical lenses (-25 and 300 mm) which formed a Galilean telescope, expanding the beam such that the resulting laser sheet was approximately 50 mm wide and ≅ 2 mm thick when passing through the combustion chamber. This allowed averaged planar NO distributions to be obtained. For measurements of the fluctuating part in the NO concentration, the laser beam was expanded to only 10 mm width using a -50 mm instead of the -25 mm concave lens. The higher energy density of the 10 mm compared to the 50 mm wide laser sheet increased the signal-to-noise ratio and improved the accuracy of the single exposure images. The laser sheet was used unfocused in order that partial saturation was avoided. This, however, was at the expense of spatial resolution. Two ∅50 mm 45° steering mirror directed the sheet to the entrance window of the Mk 2 engine. The mirrors were oxide coated and had a reflection efficiency of over 99 % at 226 nm. The back reflection of one of the cylindrical lenses was directed towards a UV-sensitive photodiode which was used to monitor the relative beam energy for every exposure.

7.2 Fluorescence Detection System

The fluorescence signal was imaged with a fibre-optic coupled intensified CCD-camera (Princeton Instruments). The intensifier was synchronised with the laser and gated for approximately 100 ns to discriminate against room light and combustion luminosity. The image was focused onto the intensifier with a Nikon f4.5 UV lens. The camera has a 15-bit dynamic range and a chip size of 578 x 384 pixels. Fluorescence from the $\gamma(0,2)$ band of NO at 238 - 258 nm was collected at a 90° angle to the incident laser

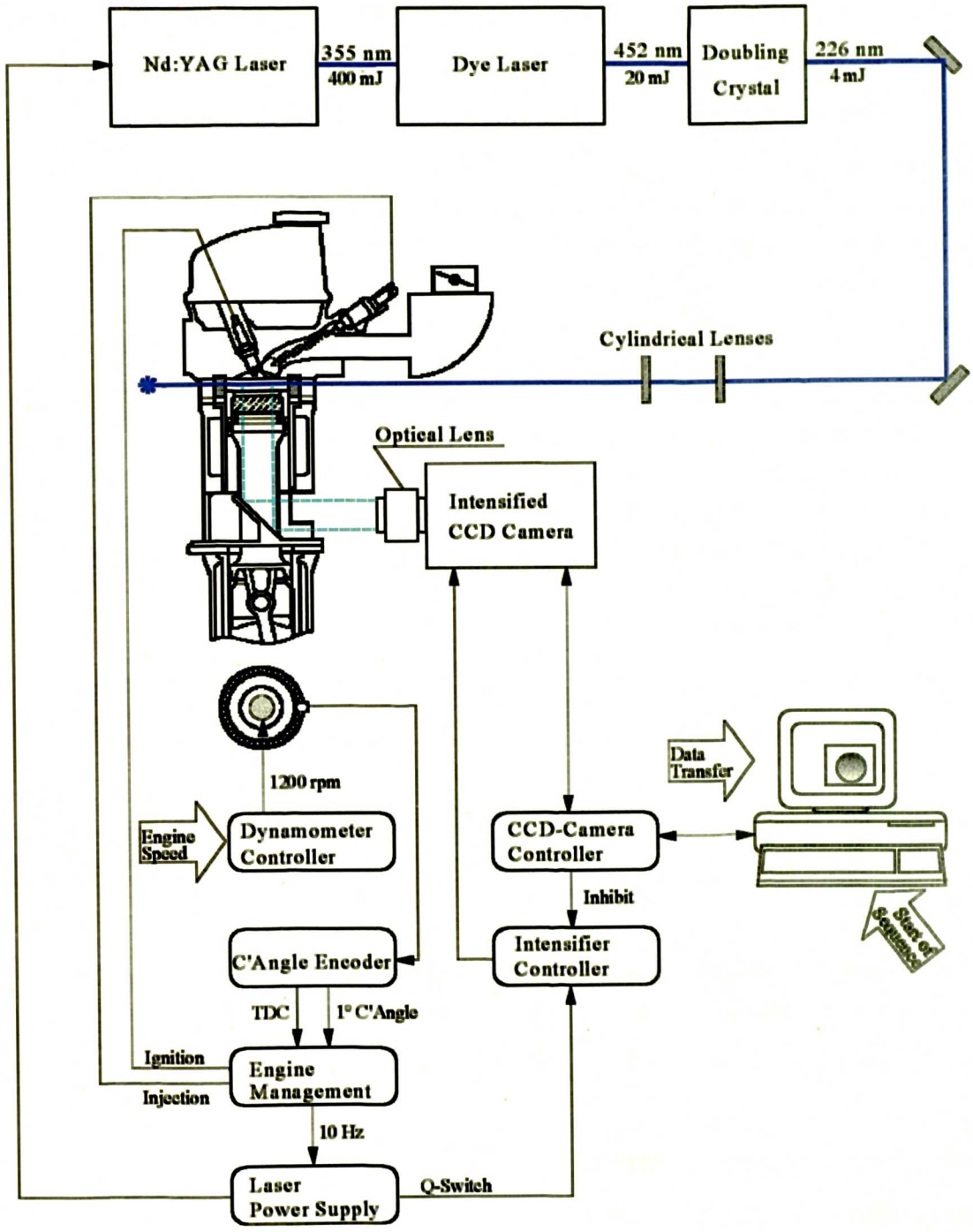

Fig. 7.2: Schematic of the instrumentation used to measure the NO concentration in the single-cylinder research engine.

radiation. A 45° mirror acted as a band-pass filter to discriminate laser radiation. The mirror had a reflection efficiency of above 90 % at 248 nm with a bandwidth of 10 nm.

7.3 Timing and Engine Control

The engine speed was regulated to a pre-set value by the controller of the dynamometer on which the engine was mounted. Therefore, the engine had to act as the master in the timing sequence. The ignition pulse from the engine controller was used to trigger the Nd:YAG laser. Since the Nd:YAG laser operated with minimum pulse-to-pulse fluctuations with a rep-rate of 10 Hz, the speed of the 4-stroke engine was set to 1200 rpm (20 Hz) for this experiment. The intensified CCD camera has no mechanical shutter. The intensifier which acts as a shutter was triggered at 10 Hz by the engine controller at ignition to synchronise with the laser. In order to prevent gating of the intensifier during readout, the camera controller was programmed to send an inhibit pulse to the intensifier at the end of the exposure time. The exposure time was set on the PC controlling the camera. The intensifier controller allows a precise delay to be set between the input pulse and the output gate. The delay was adjusted so that the laser pulse occurred in the centre of the 100 ns gate.

For ensemble-average imaging the sequence of events was:

1. The computer controlling the camera initiates a new exposure of shutter duration 10 s.
2. The camera controller sends a pulse to the intensifier enabling it to be triggered.
3. The intensifier is triggered at 10 Hz from the engine controller and gated 100 times during the 10 s exposure.
4. The camera controller sends a pulse to the intensifier to inhibit gating and subsequently the chip is read out and the image saved onto the hard disk.
5. The computer initiates a new exposure and the sequence is repeated.

7.4 Measurement Procedure

The procedure of a typical test run taking single shot images was as follows:

- Warm the engine cooling water to 58 °C using a heater in the coolant system.
- Switch on the fuel pump, to allow the accumulator to be filled and the fuel pressure to settle to a constant 2.5 bar.
- Re-align the dye laser until it delivers 3-4 mJ/pulse output energy.
- Check the laser sheet alignment - adjust if necessary.
- Crank the engine to inlet valve open position and fill the engine with calibration gas (N_2 with 1000 ppm NO).

- Fire the Nd:YAG laser from the internal trigger at 10 Hz.
- Tune dye laser to 225.970 nm wavelength (on resonance). Fine-tune to maximum signal in 0.001 nm steps (this allows for the temperature drift of the dye laser on a day-to-day basis).
- Obscure part of the laser beam with a fine wire. Re-focus camera and remove wire.
- Take a series of at least 10 images of this uniform seed concentration - these are the raw calibration images. Adjust the intensifier gain so that these images make the best use of the camera's dynamic range, while ensuring that the intensifier is not saturating.
- Tune the dye laser off resonance of NO (225.55 nm).
- Take a second series of at least 10 images - these contain the background signal which is subtracted from the raw calibration images. If the background signal is too high, the laser sheet must be altered to minimise the background noise level and the calibration images repeated.
- Switch on the vacuum pump and exhaust sensor heater.
- Open the throttle on the inlet plenum chamber.
- Start the engine. Switch on the engine controller and bring engine speed up to 1200 rpm (check speed with oscilloscope using TDC signal from engine controller).
- Check that ignition and injection occur on the compression stroke - switch TDC mark on engine controller if necessary. Set the injection timing for the first test condition.
- Switch Nd:YAG to external trigger (from engine controller).
- Take a series of background images.
- Close the throttle on the inlet plenum chamber and adjust the inlet manifold depression.
- Switch on injection, adjust the injection pulse length to AFR 16 (as measured by the exhaust sensor).
- Fire the engine until it has settled down (approximately 2 minutes). Re-adjust the injection pulse width and the inlet manifold depression if necessary.
- Tune the laser to resonance wavelength of NO.
- Take a series of images.
- Switch the injection off and open the throttle.
- Tune the laser off resonance wavelength of NO and take a series of background images.
- Repeat for other conditions.

- Switch Nd:YAG to internal trigger.
- Stop the engine and switch off engine controller.
- Crank the engine to the same position as for the previous calibration images. Take another set of calibration background images.
- Tune the laser on resonance of NO. Fill the engine with calibration gas. Take a further set of calibration images.

Chapter 8

Engine Application of NO LIF - Results

Results from the visualisation of the Nitric Oxide distribution in the SI research engine at ignition are presented. They comprise of ensemble-averaged two-dimensional NO concentrations and cyclic fluctuations in NO concentration. Improvements and possible future extensions of the measurement technique are discussed.

8.1 Measurements

In order to obtain a measure of the distribution and fluctuation of the residual gas concentration at the time of ignition, laser induced fluorescence (LIF) measurements of NO were performed in the cylinder of the Mk 2 one-cylinder research engine using a transition at 226 nm and collecting fluorescence between 238 nm and 258 nm.

The maximum NO level generated in an SI engine peaks at approximately AFR 16 which results at low load to about 500 to 1000 ppm. At AFR 20 the NO concentration will be lower by a factor of four to five (Heywood 1988). During the inlet stroke the residuals are diluted with the fresh charge by about 10 to 1. This will leave NO concentrations of between 50 and 100 ppm for AFR 16 at the time of ignition, where the measurements were taken. At such concentration levels the signal-to-noise ratio proved to be too low to be meaningful for single exposure imaging with the laser sheet expanded to 50 mm width. In order to obtain spatial information of the NO distribution, 100 single 2-dimensional images were accumulated on the chip of the CCD for succcssive cycles in a plane 5 mm below the spark plug. Ten of these accumulated images were taken at ignition (680° CA ATDC) for injection at 0° and 405° CA ATDC and at an AFR of 16 at low load (inlet depression 415 mmHg).

In order to measure the fluctuation of the residual gas concentration, cycle-resolved information on the NO concentration had to be obtained. Therefore, to increase the power density, the laser beam was expanded to a 10 mm wide ribbon, thus improving the signal-to-noise ratio. 58 single exposure images, centred about 5 mm below the spark plug, were taken at the time of ignition (680° CA ATDC) with injection at 405° CA ATDC at the same AFR and load condition as for the 2D measurements.

The engine was operated for all measurements with a speed of 1200 rpm in order to minimise the laser pulse-to-pulse fluctuations (see 7.3) and pure iso-octane was used as the fuel.

These operating conditions are slightly different compared to the fuel concentration measurements in Part 2 (AFR 20, 1500 rpm). Operation at AFR 16 compared to AFR 20 did, beside maximising the NO concentration in the residual gas, reduce the cyclic fluctuation in peak pressure from 20 % to 5 % and therefore reduce cyclic variations of the NO concentration in the burnt gas due to variations in combustion temperature. The effect of engine speed on the burnt gas fraction remaining in the cylinder is dependent on the valve-overlap. For small valve-overlap periods, as for the engine used in this work (Fig. 4.2), the residual gas fraction is not very sensitive to engine speed (Galliot 1990).

8.2 Image Processing

All images obtained were corrected for mean background by subtracting a background image obtained in the motored engine by tuning the laser off-resonance. The mean laser structure and the non-uniform collection efficiency of the intensified CCD camera was normalised with a calibration image obtained from a uniform NO/N_2 concentration in the stationary engine.

The 10 multiple exposure fluorescence images, each consisting of 100 accumulated images, were averaged. The resulting image effectively represents the mean of 1000 single images. The 58 single exposure fluorescence images were reduced onto a single pixel line. This removed the issue of pulse-to-pulse fluctuations of the laser sheet. Therefore each line represents the NO concentration in a measurement volume of approximately 10 x 2 mm in the vicinity of the spark plug.

8.3 Results

Single Shot Measurements

The average of 58 NO fluorescence lines is shown in Figure 8.1 together with the average of 10 background lines. The fluorescence signal from exciting the $Q_2(22.5)$ transition of NO is very weak. The fluorescence was about 2.5 times higher than the background signal. The background contains mainly scattered laser light from surfaces and Rayleigh scattering. Fluorescence was detected using a 45° mirror with a reflectivity of 90 % between 238 nm and 258 nm. The strong background signal suggests that scattered laser light (226 nm) was not completely rejected by this filter.

This is illustrated by the spike in the middle of signal and background in Figure 8.1. The spike stems from scattered laser light off the spark plug which extends into the combustion chamber. Although the laser sheet was not hitting the spark plug, stray laser light will have been reflected by the spark plug. Due to the spark plugs irregular

shape the angle and intensity of the reflection will be a function of the pulse-to-pulse fluctuations of the laser sheet intensity and profile, changing the background signal from shot to shot. Since the corrections for the background contribution are made on the basis of a mean background, the data will not be quantitative in this region. The NO fluorescence signal contained a high frequency component which was mainly due to shot noise on the intensifier and the CCD (Fig. 8.2). This high frequency component was removed by filtering the signal with a fast Fourier transform (fft).

The standard deviation for each pixel of the 58 lines was calculated and the fluctuation of the NO fluorescence around the mean from cycle to cycle obtained (Fig. 8.3). On average the cycle-by-cycle fluctuation was 18.1 % in the fft-filtered signal (Fig. 8.4). The expected fractional error for the line measurement is 6.5 % (see *Section 8.6*). Taking the fractional error into account the expected fluctuation in the NO fluorescence-signal is 17 %. The fluctuation around the mean of 10 images obtained from an uniform NO/N_2 concentration in the research engine was about 2 % (Fig. 8.5). This fluctuation is a measure of the repeatability of the measurement and consists of pulse-to-pulse laser fluctuations and shot noise from the intensified CCD camera. In a separate measurement, the fluctuation of the fuel concentration was found to be on average 10.5 % in a similar measurement volume (Fig. 8.6).

Averaged 2-dimensional measurements

Figure 8.7 and 8.8 show the mean of 1000 single 2-dimensional images, for injection at 0° and 405° CA ATDC respectively, taken at ignition 5 mm below the spark plug. The regions of high intensity at the secondary inlet valve are an artefact and are also present in the background images; but background subtraction did not remove the effect completely. The precise origin of the artefact is unclear. It may be due to reflections of stray laser light from the valve region of the cylinder head. As with the scatter off the spark plug in the case of the line measurements, the irregular shape of the cylinder head in the valve region may lead to fluctuating background signals due to pulse-to-pulse fluctuations of the laser sheet. Since the background corrections are made on the basis of a mean background, the data in these images does not give reliable information in this particular region.

The overall pattern for the images, taken at the different injection timings, is as expected very similar. For both injection strategies, the NO fluorescence-signal is significantly higher in the inlet half of the cylinder. The average gradient across the image is 20 % between the exhaust and inlet sides and 8 % between primary and secondary half of the cylinder (Fig. 8.9). Therefore, the highest residual concentrations are in the primary inlet quadrant, while the lowest concentrations are in the secondary exhaust quadrant. This is almost a mirror image of the fuel distribution (Fig. 8.10).

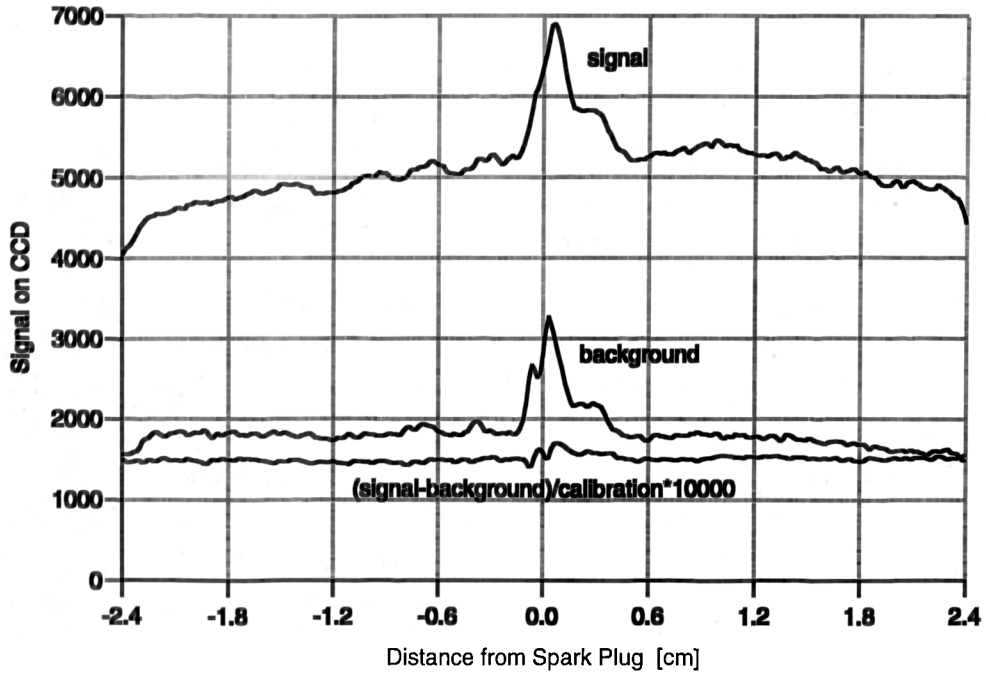

Fig. 8.1: Collected signal for on-resonance excitation (mean of 58 raw images) and off-resonance excitation (mean of 10 background images) together with the resulting final NO fluorescence signal. The lines represent the average signal, measured in the engine at the time of ignition, within a 10 mm wide laser sheet centred 5 mm below the spark plug.

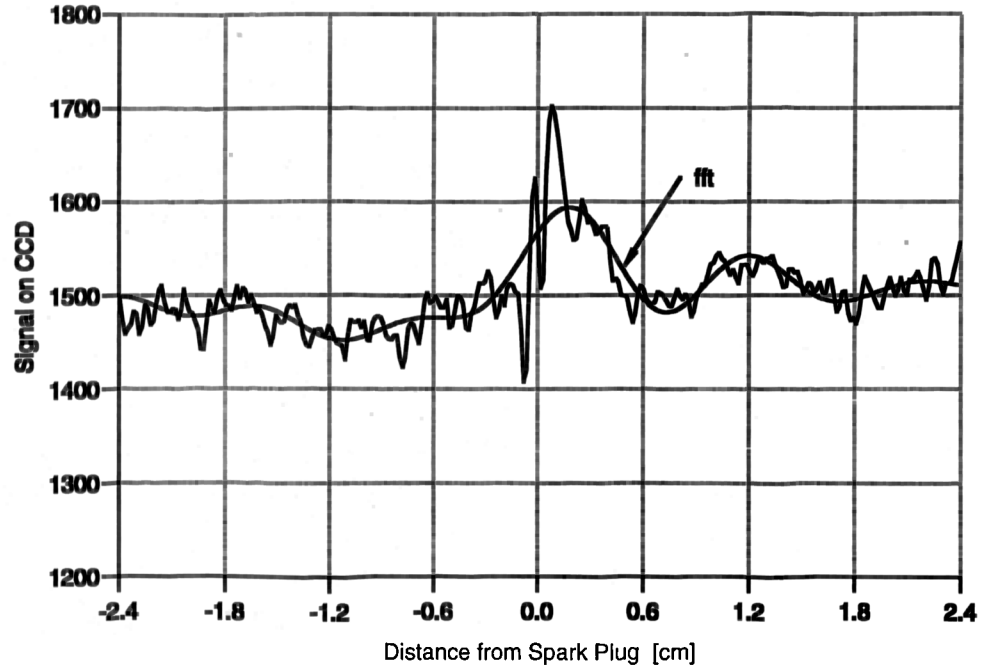

Fig. 8.2: The average of 58 NO fluorescence lines and the average of the same lines after filtering with a fast Fourier transform.

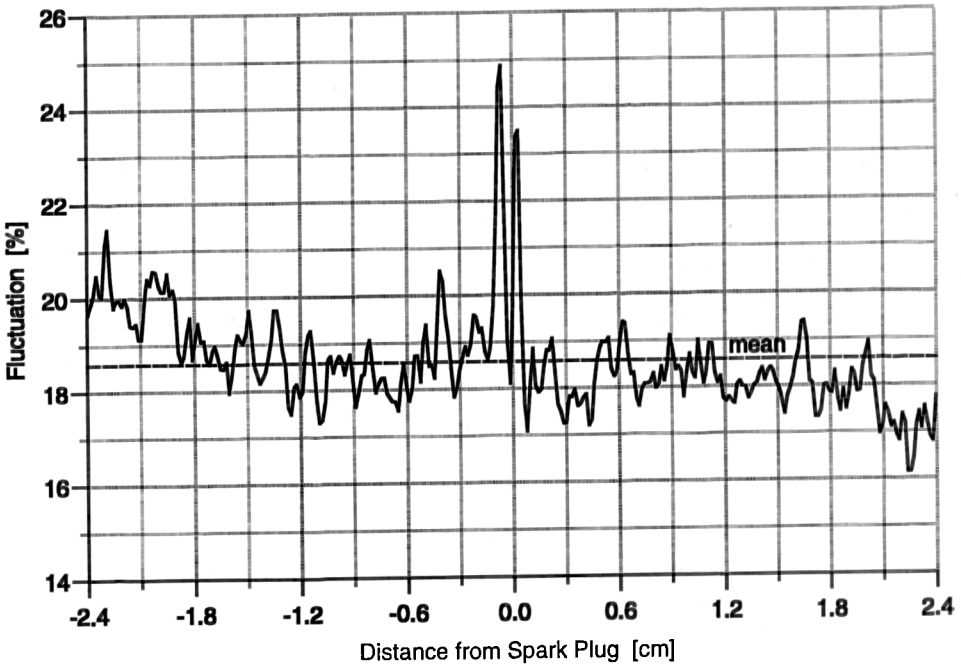

Fig. 8.3: Fluctuation of the NO fluorescence signal around the mean of 58 single lines. The standard deviation was calculated for each pixel along the line. The mean fluctuation is 18.6 %.

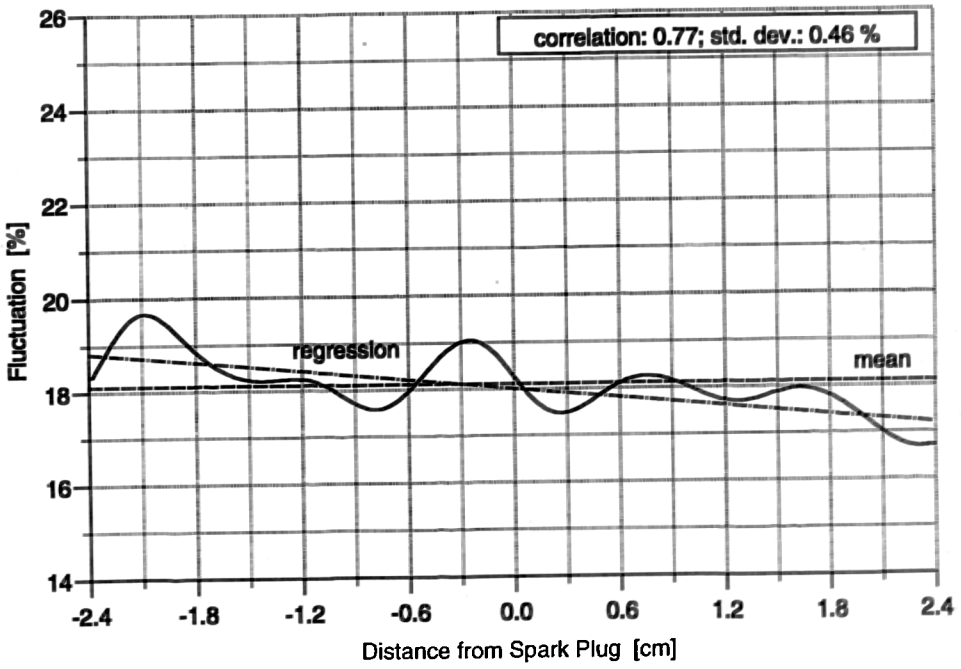

Fig. 8.4: Fluctuation of the NO fluorescence signal around the mean of 58 single fft-filtered lines. The mean fluctuation is 18.1 %.

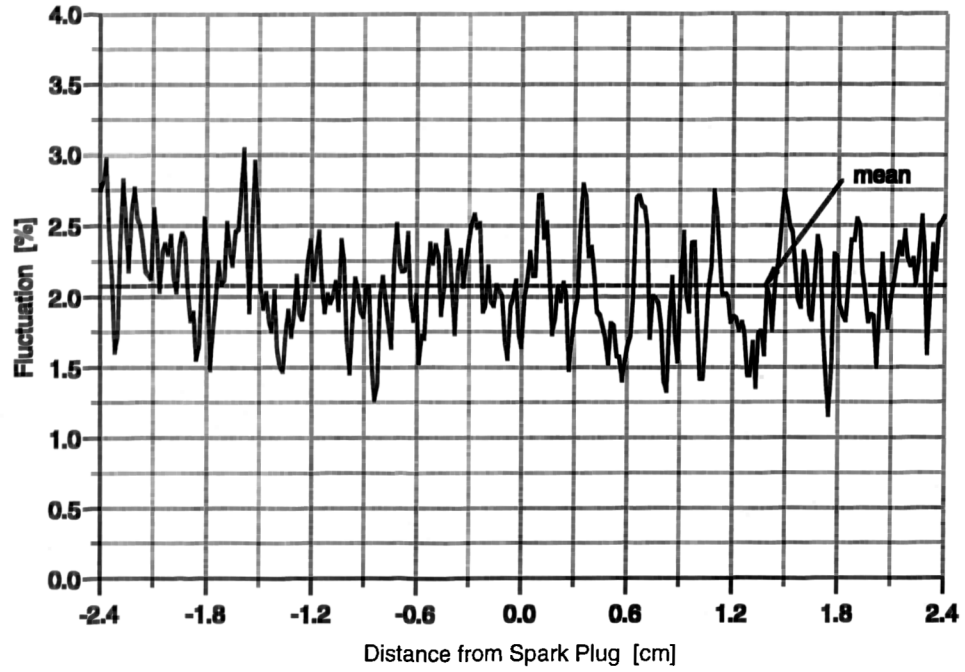

Fig. 8.5: Fluctuation around the mean of 10 fluorescence images taken from a homogeneous NO/N_2 mixture in the engine cylinder. Signal represents the average of a 10 mm wide sheet centred 5 mm below the spark plug.

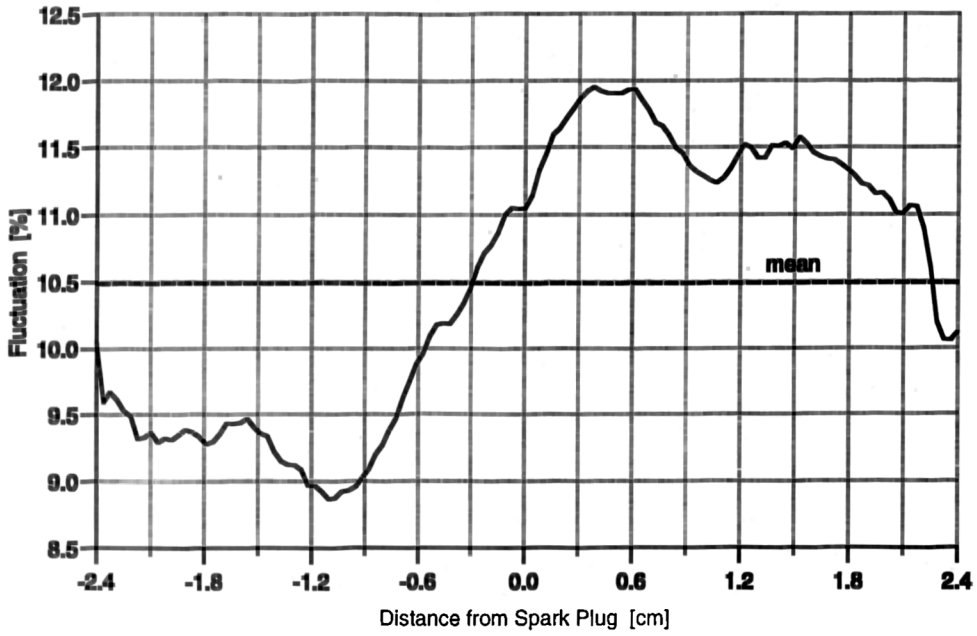

Fig. 8.6: Fluctuation around the mean of 200 single fuel LIF images (AFR 19, n = 1500 rpm). The signal represents the average of a 10 mm wide sheet centred 0.7 mm below the spark plug. The mean fluctuation is 10.5 %.

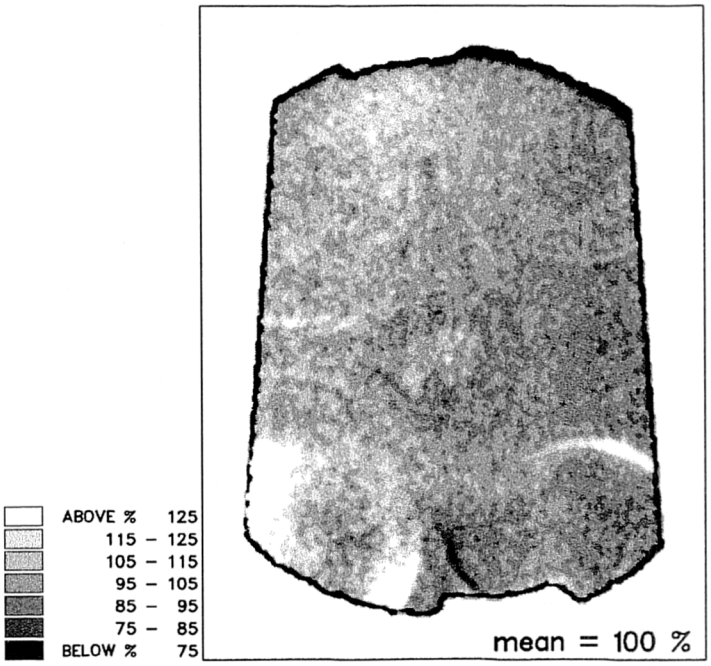

Fig. 8.7: NO fluorescence signal averaged over 1000 cycles in a plane 5 mm below the spark plug at the time of ignition (Ignition 680° CA, Injection 0° CA).

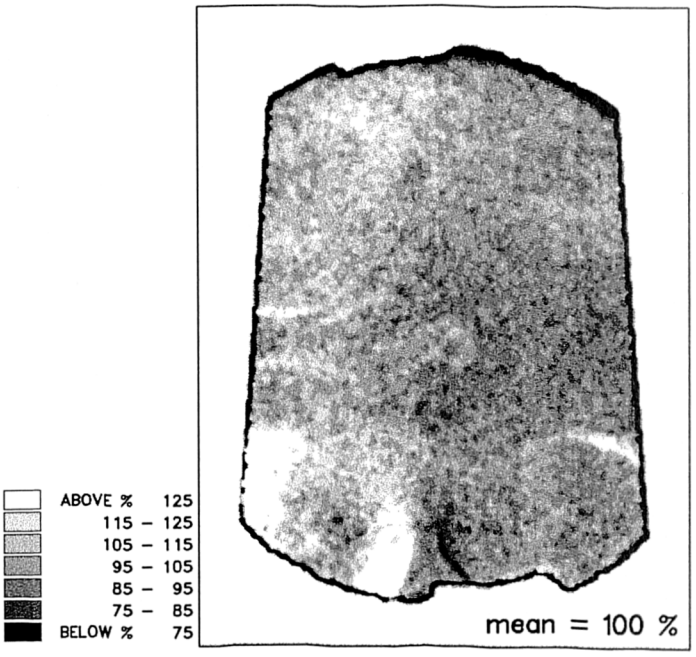

Fig. 8.8: NO fluorescence signal averaged over 1000 cycles in a plane 5 mm below the spark plug at the time of ignition (Ignition 680° CA, Injection 405° CA).

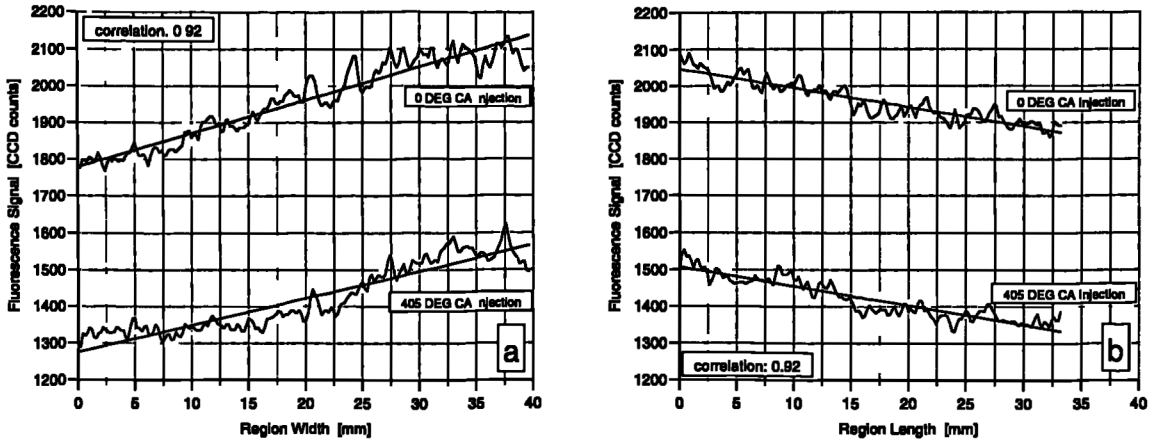

Fig. 8.9: Average gradient of the NO fluorescence signal across the images: **a)** positive gradient (20%) from exhaust to inlet side (left to right; **b)** negative gradient (-8%) from primary to secondary half, parallel to the pent-roof gable, in laser direction (top to bottom). The linear regression has in both cases a correlation coefficient of 0.92.

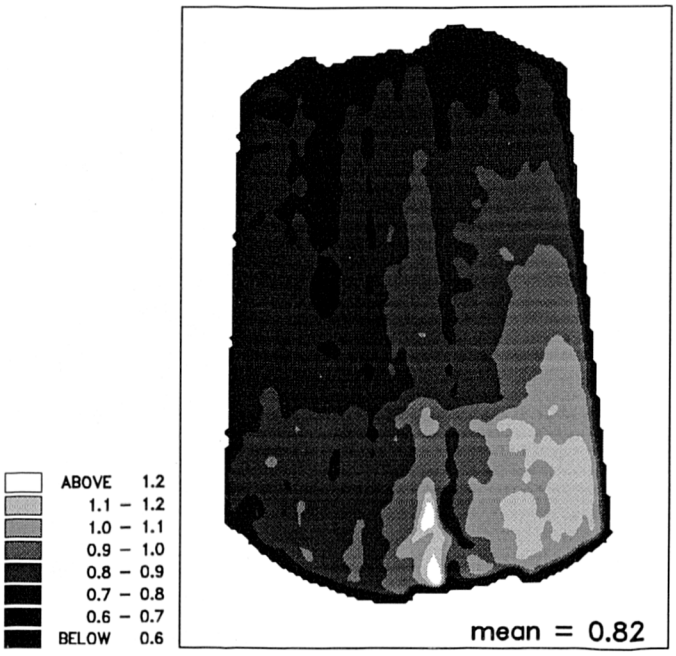

Fig. 8.10: Fuel concentration on an equivalence ratio scale, averaged over 125 consecutive cycles in a plane 5 mm below the spark plug at the time of ignition (AFR 19, ignition 680° CA, injection 405° CA, n = 1500 rpm).

8.4 Absorption & Quenching

Absorption of the laser light was found to be insignificant. Measurement of the laser energy before and after the probed volume, both in the engine and in preliminary cell studies, showed no difference between tuning on and off resonance. This is not surprising given that the ground state population of the $Q_2(22.5)$ transition is very small and hence the absorption cross-section is low.

In preliminary cell tests, iso-octane did not show any fluorescence or quenching effect on the fluorescence of NO excited at a wavelength of 226 nm. Oxygen, water vapour and carbon dioxide have big quenching cross sections for nitric oxide laser induced fluorescence (Drake 1993). Nitric oxide is also a very efficient self quenching species; however, the low concentration level in the engine renders self-quenching insignificant. CO_2 and H_2O are the major constituents of the residual gas and O_2 of air; therefore the NO fluorescence will be composition dependent. Fortunately the effect of quenching on the fluorescence signal can be calculated.

Fluorescence Yield as Function of Mixture Composition
The fluorescence emission I_f for a two-level system can be expressed as:

$$I_f = N_{NO} \cdot I_L \cdot B_{Lu} \cdot \frac{A}{A+Q} \cdot \frac{1}{1+\frac{I_L}{I_L^{sat}}}, \tag{8.1}$$

where N is the number of molecules of the fluorescing species, I_L the laser intensity, B_{lu} the Einstein coefficient for the rate of absorption, A the Einstein coefficient for spontaneous emission and Q the quenching coefficient.

$$Q = \sum_i N_i \cdot \sigma_i \cdot v_i , \tag{8.2}$$

where N is the number of molecules of the quenching species, σ the quenching cross section and v the relative velocity of the species. With the laser intensity being much smaller than the saturation intensity ($I_L << I_L^{SAT}$), equation 8.1 becomes:

$$I_f = N_{NO} \cdot I_L \cdot B_{Lu} \cdot \frac{A}{A+Q}. \tag{8.3}$$

The relative fluorescence signal of two different gas compositions, for the same fluorescence species concentration and measurement condition, can be written as:

$$\frac{I_1}{I_2} = \frac{A_2 + Q_2}{A_1 + Q_1}. \tag{8.4}$$

The Einstein coefficient for spontaneous emission is much smaller than the quenching rate ($A_{NO} \approx 3.3\text{-}4.6 \cdot 10^{6}\ s^{-1}$; $Q_{NO} \approx 1\text{-}200 \cdot 10^{28}\ s^{-1}$) and equation 8.4 can therefore be simplified to:

$$\frac{I_1}{I_2} = \frac{Q_2}{Q_1} = \frac{\sum (N_i \cdot \sigma_i \cdot v_i)_2}{\sum (N_i \cdot \sigma_i \cdot v_i)_1} \tag{8.5}$$

where the number of quenching molecules $N_i = n \cdot N_{AVOGADRO}$. Density is:

$$\frac{n}{V} = \frac{p}{\tilde{R} \cdot T} \qquad and \qquad \frac{n}{V} = \sum \left(\frac{n}{V}\right)_i . \tag{8.6}$$

The number density of the quenching species can be expressed as a function of species mole fraction X_i:

$$\left(\frac{n}{V}\right)_i = X_i \cdot \frac{n}{V} \tag{8.7}$$

and inserting in equation 8.5 results in:

$$\frac{I_1}{I_2} = \frac{N_A \cdot \left(\frac{n}{V}\right)_2 \cdot \sum (X_i \cdot \sigma_i \cdot v_i)_2}{N_A \cdot \left(\frac{n}{V}\right)_1 \cdot \sum (X_i \cdot \sigma_i \cdot v_i)_1} . \tag{8.8}$$

If $p_1 = p_2$ and $T_1 = T_2$ then the density remains constant:

$$\boxed{\frac{I_1}{I_2} = \frac{\sum (X_i \cdot \sigma_i \cdot v_i)_2}{\sum (X_i \cdot \sigma_i \cdot v_i)_1}} \tag{8.9}$$

Correction for Quenching Environment

The LIF measurement of the average NO distribution showed a gradient of 20 % between inlet and exhaust side (Figure 8.9). Galliot (1990) measured residual gas fractions of between 5 - 10 % at full load and about 20 % at part-load condition (0.45 bar inlet pressure) in an engine with a compression ratio of 8.3:1 and a valve overlap of 3° CA operating at 1500 rpm. These engine parameters and operation conditions match very closely those used for this investigation. Assuming an average residual gas fraction in the cylinder of 20 %, the charge composition can be calculated by using the residual gas composition from Figure 6.1 for an fuel/air equivalence ratio ϕ of 0.875 (*see Table 5*). The effect on the fluorescence yield due to the difference in the quenching environment across the image was calculated with Equation 8.9, using quenching cross sections from Drake (1993):

$$\frac{I_1}{I_2} = \frac{0.1615 \cdot 29.8 \cdot 6.36 + 0.0381 \cdot 107.4 \cdot 7.12 + 0.0231 \cdot 61.2 \cdot 5.65}{0.1685 \cdot 29.8 \cdot 6.36 + 0.0339 \cdot 107.4 \cdot 7.12 + 0.0189 \cdot 61.2 \cdot 5.65} = 1.052$$

Table 5: Mixture compositions and quenching factors

	N_2	O_2	H_2O	CO_2
Quenching Cross Sections[1] *(T = 296 K)* σ [Å^2]	0.014	29.8	107.4	61.2
Average Velocity of Collision Partners[2] v [10^{25} m/s]	6.58	6.36	7.12	5.65
Air Composition *(60 % humidity)* [%]	78.50	20.00	1.50	0.00
Residual Composition:[3] *(AFR 16)* [%]	75.00	2.50	12.00	10.50
Mixture 1: *(82 % Air + 18 % Residuals)* [%]	77.87	16.85	3.39	1.89
Mixture 2: *(78 % Air + 22 % Residuals)* [%]	77.73	16.15	3.81	2.31

[1] taken from Drake et al 1993 [2] see note at foot of page [3] taken from Figure 6.1

The fluorescence signal in the residual-rich inlet region will be 5 % lower than in the residual-lean region due to quenching. Therefore the gradient in residual concentration will be 25 % rather than 20 % as indicated by the images. Iterative linear interpolation between expected gradient and quenching leads to convergence for a difference in the quenching rate of 7 % between the lowest and highest concentration value. **Therefore the gradient in residual concentration from exhaust to inlet side is expected to be 27 %.** Between the primary and secondary sides, the measured gradient was 8 % (Figure 8.9). With the above values, iterative linear interpolation between expected gradient and quenching leads to convergence for a difference in the quenching rate of 3 % between the lowest and highest concentration value. **The gradient in residual concentration from the primary to the secondary side is expected to be 11 %.**

The fluctuation in the NO concentration from cycle-to-cycle was measured to be 17 % around the mean concentration (Figure 8.4). The fluorescence signal of NO will be quenched more heavily for residual concentrations above the mean and less heavily for concentrations below the mean. Therefore the quenching rate is a systematic addition to the measured fluctuation. If the mean residual concentration corresponds to 20 % of

---

[2] The relative velocity v of the quenching species is defined as:

$$v_i = \sqrt{\frac{8 \cdot k \cdot T}{\pi \cdot \mu_i}} \qquad \left[\frac{m}{s}\right],$$

where k (=1.3806226e23 J/K) is the Bolzmann constant, T the temperature and μ the reduced mass of the pair:

$$\frac{1}{\mu_i} = \frac{1}{\mu_1} + \frac{1}{\mu_2} = \frac{N_A}{M_1} + \frac{N_A}{M_2} \qquad \left[\frac{1}{kg}\right],$$

where N_A is the Avogadro number and M_i the molecular mass of the two species (quenching and fluorescence pair).

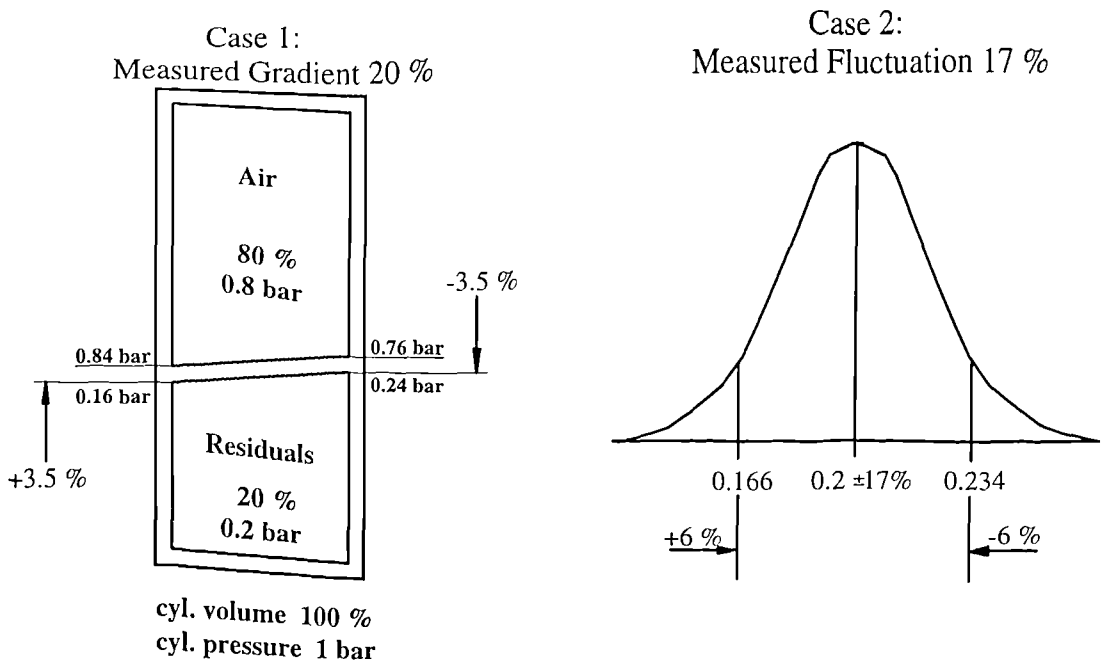

Fig. 8.11: Schematic of the influence of mixture composition on quenching.

the cylinder volume, iterative calculation of the quenching effect based on the measured residual concentration fluctuation using equation 8.9 leads to a difference in the quenching rate of 6 % between the mean concentration and the mean concentration plus one standard deviation (σ). **Therefore the fluctuation in the residual concentration around the mean value is estimated to be 23 %.**

8.5 Interpretation of Results

Laser induced fluorescence measurement of NO in the one-cylinder research engine gave some insight into the NO distribution and fluctuation at the time of ignition:

- The ensemble-averaged 2D-images showed, that on average the NO concentration is non-uniform in a plane across the cylinder bore.
- The single exposure measurements showed that substantial cycle-by-cycle fluctuations in NO concentration exist.

The fluctuation in the NO concentration is not equal to the fluctuation in residual concentration, since the amount of NO generated is dependent on the combustion temperature of the previous cycle, which will in turn vary from cycle-to-cycle. Therefore the cycle-to-cycle variation in the measured signal includes the variation in the overall NO concentration and the variation in the spatial distribution of NO due to non-uniformity of the residual gas within the cylinder. Chen (1976) showed that cyclic variations in peak pressure are linked to cyclic variations in nitric oxide concentrations in the exhaust gas. The faster combusting cycle is hotter and therefore generates more nitric oxide (Heywood 1988). Single shot temperature measurements by CARS in a SI

engine showed a linear correlation between combustion temperature and maximum pressure at light-load operation (Marie 1987). Therefore, fluctuations in peak pressure are an adequate measure for the cyclic variation in NO formation. In-cylinder pressure measurements showed fluctuations in peak pressure at the chosen running conditions to be on average about 5 %. Thus, the contribution of the cyclic variation in combustion to the measured fluctuation in NO is expected to be small:

$$\sigma_N = \sqrt{\sigma^2 - \sigma_p^2} = \sqrt{23\%^2 - 5\%^2} = 22.5\%$$

The mean level of the residual gas fraction in the unburned gas will affect the flame speed which is dependent on the diluent fraction and the unburned gas temperature (Metaghalchi 1982, Rhodes 1985). Flame radii and velocity measurements in conjunction with in-cylinder pressure measurements by Witze (1988) showed higher flame velocities and higher peak pressures earlier in the cycle for fully scavenged cycles compared with incompletely scavenged cycles. This result indicates that the diluting effect of the residual gas is more important for the burning velocity than the effect due to higher unburned gas temperatures. It follows that higher residual gas fractions lead to lower combustion temperatures and hence lower NO concentrations in the burned gas and the opposite for a lower residual fraction. The residual fraction in the unburned gas is dependent on load condition valve overlap period, compression ratio and for large valve overlap on engine speed. Therefore, for a given engine operation condition, the fluctuation in the mean level of the residual gas fraction from cycle-to-cycle will be higher than the fluctuation in the mean level of the NO concentration. The fluctuation in the mean level of the residual gas fraction is expected to be smaller than the fluctuation in peak pressure, since, as explained above, the extent of dilution with residuals affects the flame speed and therefore peak pressure. Galliot (1990) measured mean residual fraction fluctuations of about 1 % for an engine running at 1500 rpm with an inlet pressure of 0.4 bar and a valve overlap of 39° CA. For smaller valve overlaps, as for the engine used in the current work, these fluctuations are expected to be smaller. Therefore the measured fluctuation in the NO concentration of 25 % is attributed to imperfect mixing of the residual gas with the fresh charge.

Galliot (1990) measured a residual fraction of about 20 % in an engine with a compression ratio of 8.3, a valve overlap of 3° CA operated with 1500 rpm at 0.4 bar inlet pressure. These parameters are very similar to those of this experiment and in the following analysis a residual fraction of 20 % is assumed.

In a separate measurement, the fuel distribution was found to fluctuate by about 10 % around the mean in a similar measurement volume, 0.7 mm below the spark plug (Fig. 8.6, inj. 405° CA). However, the influence of the fluctuations in fuel concentration on the fluctuations in residual concentration is very small, because the difference in partial pressure between the fuel and residual gas is about one order of magnitude. Assuming a residual fraction of 20 %, and a homogenous mixture of air and residuals, with the fuel concentration fluctuating by 10 % cycle-by-cycle, the residual gas concentration would fluctuate by only 0.13 % (Fig. 8.12, Case 1). In the opposite case, where a

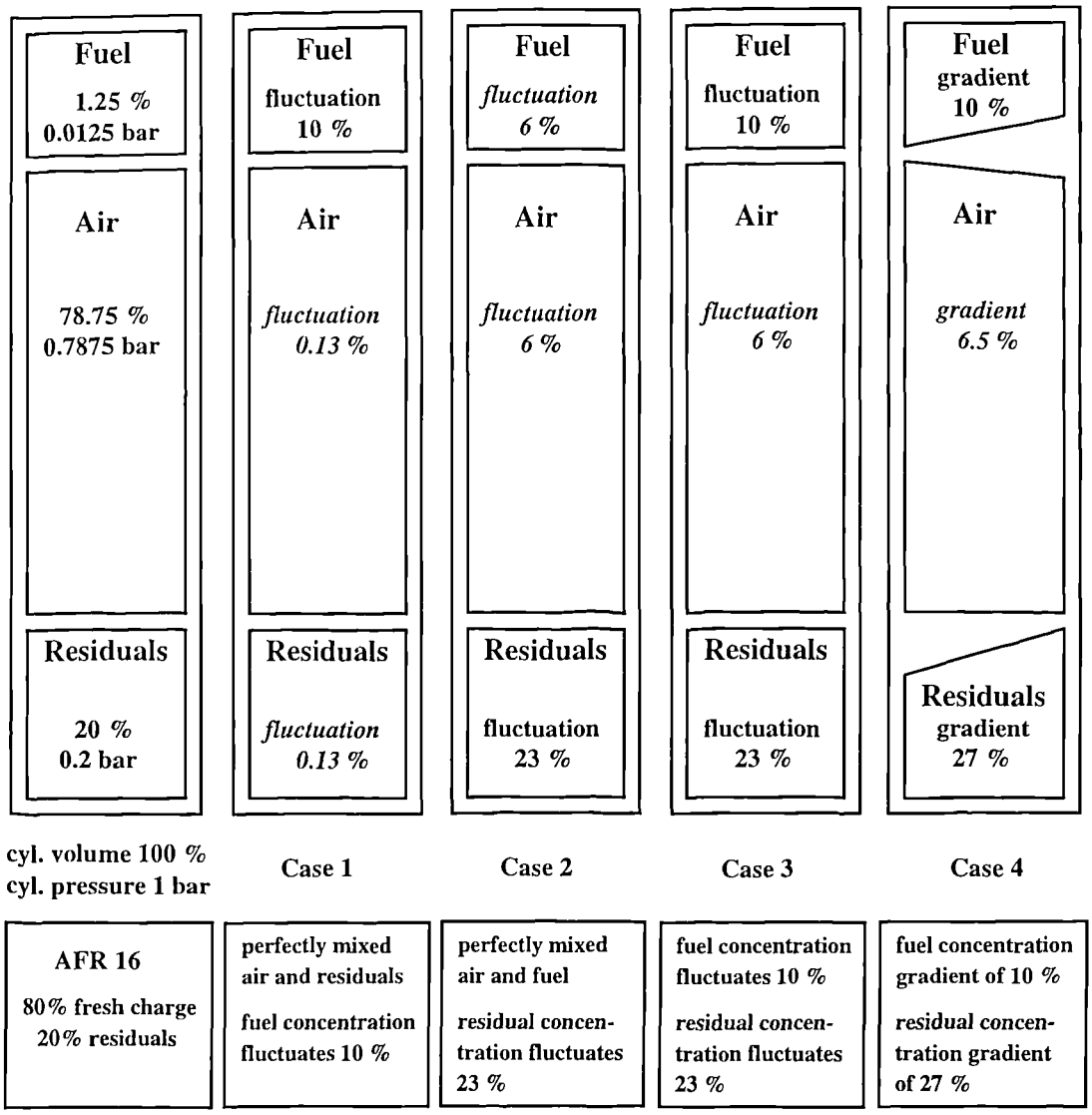

Fig. 8.12: Schematic on mixing between residual gas, fuel and air.

perfect mixture of air and fuel was mixed with residual gas, with a fluctuation of 23 %, the fuel concentration would be expected to fluctuate by 6 % (Fig. 8.12 Case 2). The separate measurements of fuel and residual concentrations in a line across the cylinder showed fluctuations of 10 % and 23 % respectively in the vicinity of the spark plug. Therefore, the air concentration (and thus the oxygen concentration) is likely to fluctuate on average about 6 % (Fig. 8.12, Case 3). The ensemble-averaged 2D-images showed a gradient between exhaust and inlet side of about 27 % for the residual gas and a reverse gradient of about 10 % for the fuel distribution. This will cause a gradient of about 6.5 % in air concentration across the image (Fig. 8.12, Case 4), with more air in the exhaust half of the cylinder.

These considerations show that even with a perfectly premixed air/fuel mixture the local fuel concentration would fluctuate by 6 % due to incomplete mixing of residual gas with the fresh charge (Fig. 8.12 Case 2). This is reflected in the fuel concentration measurements which showed in a similar measurement volume the smallest fluctuations

in the fuel concentration to be 8.5 % in the case of injection behind the closed inlet valve at 0° CA (Fig. 5.19). Similarly Williams (1991) observed fluctuations in the local fuel-air-ratio of 6 % despite using a premixed propane/air mixture. This is also consistent with Keck (1987) where cyclic fluctuations in the laminar flame speed of the early flame kernel were observed. Since in this work a premixed propane/air mixture was used no fluctuations in the air/fuel equivalence ratio were expected and the fluctuations in the flame speed were attributed to incomplete mixing of the fresh charge with residuals.

The fluctuations in the residual concentration of 23 % causes fluctuations in the air concentration of 6 % which affects the local AFR. For equal heat capacity added to the unburned mixture, burned gases have a much larger effect on the reduction of the laminar burning velocity (Fig. 8.13, Rhodes 1985). While the excess air helps combustion, the residual gas just absorbs energy and impedes the diffusion of chemical species and heat (Rhodes 1985). For example in an indolene-air mixture, the laminar burning velocity of a stoichiometric mixture is reduced by 23 %, as it is leaned out to an equivalence ratio of 0.8. Adding combustion products of the same heat capacity reduces the laminar flame speed by 52 % (Fig. 8.13). However, the molar specific heat of the combustion products of a stoichiometric mixture is about 10 % larger than that of air. Therefore, adding residuals of the same density as air, reduces the burning velocity by 58 % in this example. The higher temperature of the residual gas reduces density but the effect on burning velocity is likely to be compensated by an increase in heat capacity. Therefore, the fluctuation in the local AFR caused by incomplete mixing of air and residual gas will cause fluctuations in the laminar burning velocity.

In lean mixtures fluctuations in the fuel concentration in the vicinity of the spark plug were found to be a major cause for cyclic fluctuation in combustion (*Chapter 5.2*). Since incomplete mixing of residual gas with the fresh charge causes cyclic fluctuations in the fuel concentration it also limits the lean operation of a SI engine. In *Chapter 5.2* it was shown that, close to the spark plug, fluctuations in the fuel concentration of 10% mark the difference between a slow burning cycle and a fast burning cycle (Fig. 5.24, 5.25.). Therefore, fluctuations in the fuel concentration of 6 % caused by incomplete mixing with residual gas are significant for cyclic variability in combustion. For in-homogeneous fuel/air mixtures the residual fluctuations have an additional effect of changing the local AFR. Therefore, in stratified charge engines, the fluctuation in fuel concentration close to the spark plug does not give a complete picture of the magnitude of fluctuations in the mixture composition which influence the laminar burning velocity. This is reflected in the correlation coefficient between fuel concentration in the vicinity of the spark plug and peak pressure of 0.7 being significantly below 1 (see *Chapter 5.2* Fig. 5.30, 5.31).

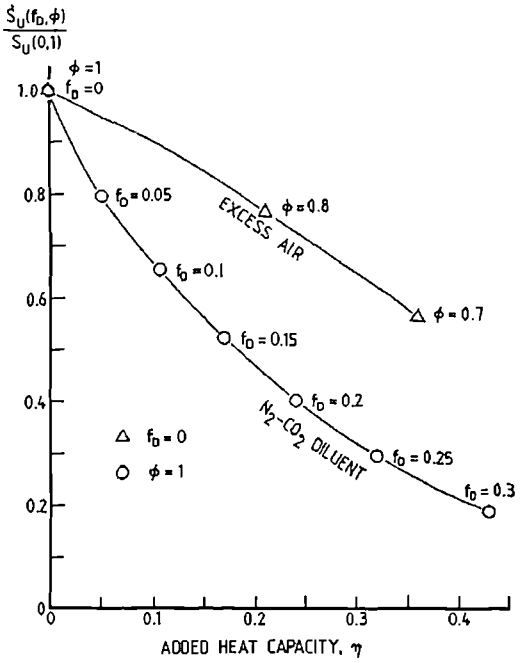

Fig. 8.13: Reduction in the laminar burning speed of a RMFD 303-air mixture due to the addition of various amounts of excess air or N_2-CO_2 diluent (Rhodes 1985).

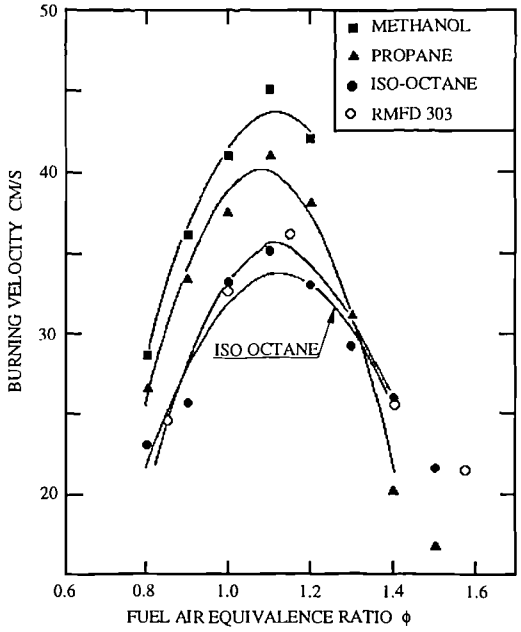

Fig. 8.14: Dependence of the burning velocity of mixtures of iso-octane, methanol, propane and RMFD 303 (Metaghalchi 1982).

In the stratified charge Honda VTEC-E engine local rich mixtures exist in a plane close to the spark plug (Fig. 5.3b, 5.4b). The burning velocity in iso-octane peaks at an equivalence ratio of 1.1 (Fig. 8.14, Metaghalchi 1982). Fluctuations in the air concentration caused by non-uniform mixing with residual gas will therefore change the stoichiometry and influence the burning velocity also in rich mixtures.

The laminar flame speed is also strongly dependent on temperature (Metaghalchi 1982, Rhodes 1985). The local temperature in the unburned gas will be dependent on the distribution and concentration of the hot residual gas. Although the data of Witze (1988) indicates that dilution is the more important factor, further studies, comparing residual concentrations with engine performance, may clarify which of the two effects, dilution or temperature, will be dominating.

The ensemble-averaged NO concentration images show a gradient from the exhaust to the inlet side and from the secondary to the primary side, with the highest NO concentrations on the inlet side in the primary inlet quadrant. This is nearly a mirror image of the fuel distribution. The result can be explained by the tumble and swirl motion of the intake air as observed by Hardalupas (1995).

The crank angle resolved 3D fuel images (*Chapter 5.1*) showed that during the inlet stroke, as indicated by the fuel motion, there was a strong axial air flow from the primary inlet valve along the exhaust side directed to the piston. The flowfield as measured by Hardalupas (1995) (Fig. 5.8) showed that by 540° CA, which is BDC of

intake, the flow has developed a strong clockwise swirl and the tumble results in piston-directed velocities along the exhaust side and head-directed velocities along the inlet side of the cylinder. Thus, during the inlet stroke, the air flow will gradually dilute the residual gas in the exhaust half of the cylinder, creating an axially-stratified air/residual mixture which continues to be convected by the tumble vortex towards the inlet side and up towards the cylinder head, thereby creating a residual-richer mixture in the inlet half of the cylinder. The magnitude of the swirl was measured to be such that the in-cylinder gas will rotate through approximately one revolution around the cylinder axis over a 360° CA rotation period. From the onset of the swirl motion, around BDC, up until ignition the residual-lean mixture in the exhaust half of the cylinder will be convected clockwise by 90° -120° towards the inlet side, explaining the lower residual concentration below the secondary inlet valve compared to the primary inlet valve region.

This implies that little mixing occurs across the perpendicular cylinder axis. That the mixing is indeed poor can be inferred from the crank angle resolved 3D fuel images (*Chapter 5.1*) where little cross-bore mixing of the fuel was observed during compression. The swirling pathlines during compression in Figure 5.8, are all close to concentric circles and therefore the amount of mixing that can be expected to occur, due to motion in the plane of the bore, is small (Hardalupas 1995). As for the fuel concentration measurements, additional studies in an engine with a non-swirl inlet port/valve configuration should be performed in order to clarify the influence of swirl on mixing.

8.6 Error Analysis of Data

Each of the final NO concentration images (F) was formed from four separate images:

- a raw data image (R),
- a background taken with the engine motoring (B),
- a calibration image (C)
- and a background for the calibration image (B_{cal}).

Each of these can potentially add to the total noise on the final NO image. The errors that will arise from the background images and the calibration image can be evaluated by measuring the fluctuation in sets of these images (denoted σ) and comparing them to the mean values. The fractional error in the raw data image is harder to estimate, but will be at least as large as the one for the calibration image. The final NO images were calculated as:

$$F = \frac{R - B}{C - B_{cal}} \tag{8.10}$$

The expected fractional error in measuring F will be:

$$\frac{\varepsilon_F}{F} = \sqrt{\left(\frac{\varepsilon_R}{R-B}\right)^2 + \left(\frac{\sigma_B}{R-B}\right)^2 + \left(\frac{\sigma_C}{C-B_{cal}}\right)^2 + \left(\frac{\sigma_{Bcal}}{C-B_{cal}}\right)^2} \tag{8.11}$$

Single Exposure Measurements

The data set comprises of 58 single exposure data images, 10 single exposure images each for background, calibration and calibration background. Below are the mean, and the fluctuation around that mean, for each of the data sets:

	CCD Counts
- Mean raw data image intensity (R)	5116
- Mean background intensity (B)	1835
- Mean calibration image intensity (C)	21230
- Mean calibration background intensity (B_{cal})	1399
- Fluctuation in raw images (ε-estimated as 2.6% of R)	133
- Fluctuation in background images (σ_B)	133
- Fluctuation in calibration images (σ_C)	453
- Fluctuation in calibration background images (σ_{Bcal})	65

With the above values, equation 8.11 gives an **expected fractional error of 6.5%** for the final images. The resulting values for the final image F (calculated from eq. 8.10) are:

	CCD Counts
- Mean final image intensity (F)	1502
- Fluctuation in final images (σ_F)	279 (18.6%)
- Uncertainty in final images (ε_F)	97 (6.5%)

The expected fluctuation in the signal F will be:

$$\sigma = \sqrt{\sigma_F^{\,2} - \varepsilon_F^{\,2}} \qquad (8.12)$$

With the above values, equation 8.12 gives an **expected cyclic fluctuation of 17%** for the NO concentration around the mean value.

Ensemble Averaged Multiple Exposure 2D-Images

NO-data, background, calibration and calibration background measurements comprise of 10 images each, which represent the average of 100 single images accumulated on the CCD-chip. Below are the mean and the fluctuation for each of the data sets:

	CCD Counts
- Mean raw data image intensity (R)	16283
- Mean background intensity (B)	10175
- Mean calibration image intensity (C)	28488
- Mean calibration background intensity (B_{cal})	8667
- Fluctuation in raw images (σ_R)	974
- Fluctuation in background images (σ_B)	737
- Fluctuation in calibration images (σ_C)	1266
- Fluctuation in calibration background images (σ_{Bcal})	661

With the above values, equation 8.11 gives an **expected error of 21%** for the final images.

The bigger error on the 2D data in comparison to the single-shot data is due to the lower signal-to-noise ratio (1.6 rather than 2.5). However, all of the fluctuations in the raw images of the 2D data - which are effectively a mean of 100 images - were attributed to the measurement error. This is probably too pessimistic, since samples of 100 images might not be enough to average out cyclic fluctuations in the NO concentration. Averaging the 10 data images will reduce the error, since random noise will cancel out:

$$\frac{\sigma}{\overline{Y}} = \frac{\sqrt{10 \cdot (\sigma_i)^2}}{\sqrt{\left(\sum_{i=1}^{10} Y_i\right)^2}} = \sqrt{\frac{10 \cdot 0.21^2}{10^2}} = 0.066 \qquad (8.13)$$

If all the error in the 10 NO-data images is random, then the **expected uncertainty will be 6.6 %** for the averaged images in Figure 8.7 and 8.8.

8.7 Considerations & Improvements

The previous discussion revealed the major limitation of the measurement system to be the low signal-to-noise ratio. This led to unsatisfactory error levels and inhibited measurement of single exposure planar images. Instantaneous planar NO concentration measurements would show the variation in the NO distribution compared to the mean distribution.

The accuracy of planar single exposure measurements of the "natural" NO in the engine, can be improved by optimising the fluorescence detection system. In this study a f4.5 UV-lens focused the image onto the intensifier. Using a f1.0 collection optics would increase the collection efficiency by a factor of 10 compared with the standard f4.5 optics. However, there are no standard f1.0 UV lenses available. This requires the design of an appropriate custom lens system. However, the effect of the collection efficiency on the signal-to-noise ratio is limited, since also the collection of stray laser light will be improved. In the present study a 45° mirror with a reflectivity of over 90 % between 238 nm and 258 nm separated the laser radiation from the fluorescence signal. The discrimination efficiency between fluorescence and background luminescence can be improved by using more than one separation mirror. A second 45° mirror with a peak reflectivity at 248 nm and a bandwidth of 10 nm would reduce the collection efficiency by at least 10 %, but would cut the unwanted background signal by an order of magnitude. Such a filter system collects fluorescence mainly from the $\gamma(0,2)$ band. However, since the NO fluorescence is broad-band (Reisel 1993), a long pass filter with a transmission efficiency of over 99 % above a cut-off wavelength of 231 nm could further increase the amount of collected fluorescence and reduce the amount of background scatter collected.

In addition, to improve the signal-to-noise ratio the fuel or the intake air could be seeded with a component which generates significant amounts of NO during combustion. Therefore two components were considered; acetonitrile (CH_3CN) to be mixed with the fuel and ammonia (NH_3) to be mixed with the intake air. For example, 1 % of ammonia mixed with the air delivered to the engine will produce approximately 8000 ppm NO during combustion. After dilution of the residual gases with fresh charge approximately, 400 ppm of NO will be available as fluorescence marker for the residual distribution at the time of ignition. This would raise the NO concentration in the residual gas by a factor of 5 to 10. Unfortunately, both components are polar and therefore are efficient fluorescence quenchers for NO. This is likely to negate the gain of signal due to the higher NO concentration. It will also bias the measurement towards the residual-rich regions, since the acetonitrile/ammonia concentration will be highest in air/fuel rich regions.

8.8 Alternative Strategy for Residual Imaging

The imaging of residual gas species proved to be difficult due to the low concentration levels during the compression stroke. Also, variation in the residual gas composition from cycle-to-cycle makes interpretation of the fluctuating part of the fluorescence

signal of one particular species difficult. Therefore, a completely different approach to residual imaging is suggested for consideration.

By seeding both the air and the fuel (iso-octane) with the same amount of 3-pentanone per mole, a homogeneous pentanone concentration is expected in a non-combusting engine. Thus in a combusting engine, any inhomogeneities in the distribution and any fluctuations in the concentration of the seed must be due to the incomplete mixing of the fresh charge with residual gas or cyclic fluctuations in the residual concentration. These inhomogeneities and fluctuations can be measured by planar LIF of 3-pentanone. The lower limit of the accuracy of this method is determined by the pulse-to-pulse fluctuations in the laser sheet and shot noise on the intensifier/CCD which has been previously measured as 2% (see Fig. 5.16). 3-pentanone is the preferred seed, since its vaporisation characteristics closely match those of iso-octane (see *Section 3.3*). This minimises potential errors due to the separation of fuel and seed. If this method is to succeed, a seeding system has to be designed which will provide a homogeneous air/pentanone mixture. The quality and potential accuracy of the seeder system can easily be measured in a motoring engine.

8.9 Conclusions on Residual Imaging

- A method for imaging the "natural" NO concentration as a marker for the residual gas by Laser Induced Fluorescence has been developed and applied to an optical one-cylinder research engine.
- The results gave some insight into the residual gas distribution:
  - on **average** the residual gas is in-homogeneously distributed in the cylinder.
  - there is a significant fluctuation in the mixing of fresh mixture with residual gas on a **cycle-to-cycle** basis.
- The measured fluctuation in the mixing of fresh charge and residual gas cause significant cyclic fluctuation in local fuel concentration.
- In a stratified charge engine incomplete mixing of residual gas with fresh mixture has a significant effect on the local AFR.
- Cyclic fluctuations in the mixing between residual gas and fresh charge are large enough to limit the lean operation of a SI engine.
- The influence of swirl on mixing between air and residual gas could be important.
- The low signal-to-noise ratio limits the accuracy of the measurement and prevents cycle-resolved 2D measurements of natural NO.
- The current method could be improved by designing more efficient collection optics (f1.0) and using a more efficient filter to separate laser light from fluorescence.
- Alternative strategies for visualisation of the residual concentration should be considered.

PART IV

SUMMARY & REFERENCES

Chapter 9

Summary

Previously, the contribution to combustion variability arising from the nonuniformity of the fuel-air mixture taken into the cylinder has been examined either *indirectly* by the impact of different mixture preparation methods on combustion quality, performance and emissions, or *directly* by in-cylinder measurements of the *local* air-fuel ratio fluctuations. Although these works indicate that there is substantial variation in the local fuel concentration at the spark electrodes, and that differences in mixture preparation can be important to engine behaviour, the contribution to cyclic combustion variability and performance due purely to mixture nonuniformity has not been clearly established. Factors influencing the mixture formation have been studied mostly indirectly by measuring their impact on performance or emission. The mixture formation process itself has not been clearly understood. Further, the issue of nonuniformity in residual gas concentration has not been considered in any depth. Thus an experimental program was undertaken in order to develop a picture of the mixture formation process in a near-production engine. It was intended to quantify the influence of the mixture formation on cyclic variability and performance. Further, it was intended to address separately spatial distribution and variations in burned residual gas concentration within the cylinder.

Planar laser induced fluorescence was chosen as diagnostic technique to achieve these goals. For the investigation on mixture formation and mixture nonuniformity the concentration of a fluorescence marker added to the fuel was measured in a 2-dimensional slice of the cylinder in an optical research engine. The technique was applied to a lean-burn one-cylinder SI engine with a 4-valve pent-roof cylinder head configuration. 3-Pentanone mixed with iso-octane was used as the fuel. In order to investigate the mixture formation process, mean fuel distributions were measured in four planes between 0.7 and 15.2 mm below the spark plug during the inlet and compression stroke. This gave a quasi 3-dimensional picture of the mixture formation in the cylinder of an operating engine. The measurements were performed with injection during inlet valve closed and open periods which allowed the effect of injection timing on mixture formation to be studied. The results showed that for 4-valve pent-roof cylinder head configurations with swirl inlet flows, fuel impinging on

the cylinder wall opposite to the inlet valves is a major cause of fuel stratification. The fuel film formed on the cylinder wall evaporates during compression, leading to a locally richer mixture. Injection timing was found to influence the amount of fuel impinging on the cylinder wall and hence the subsequent mixture distribution. To complete the data base on mixture formation in 4 valve pent-roof cylinder head configurations and to clarify the influence of the flowfield, similar measurements with non-swirl inlet flows are proposed.

To determine the influence of the mixture formation on engine performance and cyclic variability, the fuel concentration in a plane close to the spark plug was measured at ignition and after ignition on a large number of cycles for different injection timings. It was shown quantitatively that the mixture formation in a small region in the vicinity of the spark plug has a dominating effect on the subsequent pressure development for lean mixtures. The results also showed that variations in the mixture concentration in the vicinity of the spark plug are a major reason for cyclic variations in combustion. Injection timing was found to influence the degree of cyclic dispersion in mixture distribution.

The burned area in the images taken after ignition correlated well with the subsequent cycle performance. This supports the view that the early flame kernel development has a dominating effect on the bulk combustion. In nearly all measurements, the burned area was found to be displaced towards the fuel-lean side of the combustion chamber. This suggests that after the flame has been established, factors other than the fuel concentration are important for the flame development.

With the above LIF measurements the mixing of the fuel in the cylinder of a SI engine could be described and its influence on engine performance quantitatively determined. However, the fuel not only mixes with air. It also mixes with residual gas left in the cylinder from the previous cycle. In order to better understand the mixing of residuals with the fresh charge, a laser induced fluorescence technique was developed to measure natural NO distribution where the NO is assumed to mark the residual gas. Measurements were performed for the crank angle of ignition and were made close to the spark plug.

The results revealed, that at the time of ignition, the residual gas is on average not homogeneously mixed with the fresh charge and that significant cyclic variation in the local residual gas concentrations exist. The measured fluctuations in the mixing of residual gas with fresh charge causes significant cyclic fluctuations in local fuel concentration. The average residual distribution, as well as the cyclic fluctuations in residual concentration, are large enough to influence the local mixture composition. It is implicit from the mean residual distribution in a plane perpendicular to the cylinder axis, that little cross-bore mixing occurs. This suggests that in accord to the fuel concentration measurements, swirl motion of the intake air has an inverse effect on mixing. Further studies involving measurements of NO concentrations in an engine with no inlet swirl are required.

The accuracy of imaging the NO concentration as a measure for the residual gas concentration was limited by a low signal-to-noise ratio which inhibited the collection of cycle-resolved planar images. Cycle-resolved planar imaging would be important in gaining information on fluctuations in the residual distribution and to investigate the influence of residual fluctuations on engine performance. To improve the accuracy of the residual imaging a more efficient UV collection optic may be used in conjunction with a more effective filter to separate laser radiation from fluorescence signal. Imaging the NO concentration by PLIF shows considerable potential as a residual gas marker. However, further work is required to improve the accuracy of the method.

Nomenclature

AFR	Air-to-Fuel Ratio
ArF	Argon-Fluoride
ATDC	after Top-Dead Centre
BDC	Bottom-Dead Centre
b.p.	boiling point
BTDC	before Top-Dead Centre
CA	Crank Angle
CARS	Coherent Anti-Stokes Raman Spectroscopy
CCD	Charge-Coupled Device
DI	Direct Injected
EGR	Exhaust Gas Recirculation
fft	fast Fourier transform
IC engine	Internal Combustion engine
IDI	Indirect Injected
imep	indicated mean effective pressure
KrF	Krypton-Fluoride
LDA	Laser Doppler Anemometry
LIF	Laser-Induced Fluorescence
MBT	Maximum Brake-Torque
n	engine speed
Nd:YAG	Neodymium-Yttrium-Aluminium-Garnet
PAH	Polycyclic Aromatic Hydrocarbons
PDA	Phase Doppler Anemometry
PIV	Particle Image Velocimetry
PLIF	Planar Laser-Induced Fluorescence
rpm	revolutions per minute
SI-engine	Spark-ignition engine
SVC	Swirl Control Valve
TDC	Top Dead Centre
XeCl	Xenon-Chloride

Acknowledgements

Douglas Greenhalgh gave me the opportunity to work on this project. His insights, inspiration, support and encouragement kept me going. When I entered his office feeling the experiments had been a failure, somehow I felt the other way round by the time I left. I am truly grateful.

Nigel Tait introduced me to scientific research, supported me with the experiments, was always willing to help me when I ran out of ideas and kept his patience when I could not keep up with his pace.

Russell Locket was a fruitful source for physics and spectroscopic knowledge and an eager participant in numerous stimulating discussions (scientific and non-scientific).

Nick Farrugia sorted out countless computer breakdowns and shared with me his office and computer in the crucial last months.

Steve Welsh helped improving the language of this book.

Thanks to all my friends and colleagues for making life and work at Cranfield such a pleasure.

I also thank Robert Hicks from Leeds University for helpful discussions regarding the simulation of in-cylinder temperature and the application of the LEEDS ENGINE SIMULATION MODEL.

Honda R&D Co. LTD. in Japan sponsored this project and provided several engines. I am grateful for the generous assistance, financial and technical support.

I would like to thank Mr. Kiyosi Ishii from Honda R&D for his inspiration and generous support.

Thanks to my parents for always being there.

References

Amann C A, *Classic Combustion Diagnostics for Engine Research*, SAE 850395, 1985

Andresen P, Meijer G, Schlüter H, Voges H, Koch A, Hentschel W, Oppermann W, Rothe E, *Fluorescnce Imaging Inside an Internal Combustion Engine using Tunable Excimer Lasers*, Applied Optics, Vol. 29, No. 16, pp 2392-2404, 1990

Arcoumanis C, Hull D R, Whitelaw J H, *An Aproach to Charge Stratification in Lean Burn, SI-Engines*, SAE 941878, 1994

Arcoumanis C, Enotiadis A C, *In-Cylinder Fuel Distribution in a Port-Injected Model Engine using Rayleigh Scattering*, Experiments in Fluids 11, pp 375-387, Springer-Verlag, 1991

Arcoumanis C, Hu Z, Vafidis C, Whitelaw J H, *Tumbling Motion: A Mechanism for Turbulence Enhancement in SI-Engines*, SAE 900060, 1990

Arnold A, Buschmann A, Cousyn B, Decker M, Vannobel F, Sick V, Wolfrum J, *Simultaneous Imaging of Fuel and Hydroxyl Radicals in an In-Line Four Cylinder SI-Engine*, SAE 932696, 1993

Arnold A, Dinkelacker F, Heitzmann T, Monkhouse P, Schäfer M, Sick V, Wolfrum J, *DI Diesel Engine Combustion Visualized by Combined Laser Techniques*, Twenty-Fourth Symposium (International) on Combustion/The Combustion Institute, pp 1605-1612, 1992

Arnold A, Becker H, Suntz R, Monkhouse P, Wolfrum J, *Flame Front Imaging in an IC Engine Simulator by Laser Induced Fluorescence of Acetaldehyde*, Optical Letters Vol. 15, No. 15, pp 831-833, 1990

Asanuma T, Obokata T, *Gas Velocity Measurements of a Motored and Firing Engine by Laser Anemometry*, SAE 790096, 1979

Ayusawa T, Nemoto T, Koo Y, Hong Jo S, *Relationship between Local Air-Fuel Ratio and Combustion Character in SI Engines*, SAE 780147, 1978

Baritaud T A, Heinze T A, *Gasoline Distribution Measurements with PLIF in a SI-Engine*, SAE 922355, 1992

Bates S C, *Flame Imaging Studies in a Spark-Ignition Four-Stroke Internal Combustion Optical Engine*, SAE 890154, 1989

Becker H, Arnold A, Suntz R, Monkhouse P, Wolfrum J, Maly R, Pfister W, *Investigation of Flame Structure and Burning Behaviour in an IC Engine Simulator by 2D-LIF of OH Radicals*, Appl. Phys. B 50, 473-478, 1990

Bradley D, Hynes J, Lawes M, Sheppard C G W, *Limitations to Turbulence - Enhanced Burning Rates in Lean Burn Engines*, C46/88 IMechE, 1988

Bryce D, *Development and Application of Laser Diagnostics for Iso-Thermal Mixing and Soot*, PhD Thesis Cranfield University, to be published 1996

Buchave P, *Particle Image Velocimetry*, Chapter from "Optical Diagnostics for Flow Processes" (Eds.: Lading, Buchave, Wigley), Plenum Press, N.Y., 1994

Burgman T M, Klein-Douwel R, Huigen G, van Walwijk E, ter Meulen J J, *Laser-Induced-Fluorescence Imaging of NO in an n-Heptane- and Diesel-Fuel-Driven Diesel Engine*, Appl. Phys. B 57, pp 405-410, 1993

Cattolicia R J, *Visualisation of Flame Front Propagation by Laser -Induced Fluorescence Imaging of Nitrogen Dioxide*, Combust. Sci. and Tech., Vol. 54, pp 61 - 68, 1987

Cattolicia R J, *Combustion-Torch Ignition: Fluorescence Imaging of NO_2*, Twenty-First Symposium (International) on Combustion, pp 1551 - 1559, The Combustion Institute, 1986

Cole J B, Swords M D, *Measurement of Concentration Fluctuations in an Internal Combustion Engine*, J. Phys. D: Appl. Phys, Vol 71, pp 659 - , 1980

Chang A Y, DiRosa M D, Davidson D F, Hanson R K, *Rapid Tuning cw Laser Technique for Measurements of Gas Velocity, Temperature, Pressure, Density and Mass Flux Using NO*, Applied Optics, Vol. 30, No. 21, 1991

Chen K K, Krieger R B, *A Statistical Analysis of the Influence of Cyclic Variation on the Formation of Nitric Oxide in Spark Ignition Engines,* Combust. Sci. and Tech., Vol. 12, pp 125-134, 1976

Collings N, *A new Technique for Measuring HC Concentration in Real Time, in a Running Engine*, SAE 880517, 1988

Daneshyar H, Mendes-Lopes J M C, Ludford G S S, Tromans P S, *The Influence of Straining on a Premixed Flame and its Relevance to Combustion in Si-Engines*, C50/83 IMechE, 1983

Dodge L G, Dusek J, Zabielski M F, *Line Broadening and Oscillator Strength Measurements for the Nitric Oxide $\gamma(0,0)$ Band*, J. Quant. Spectrosc. Radiat. Transfer, Vol. 24, pp 237 249, Pergamon Press Ltd., 1980

Drake M C, Ratcliffe J W, *High Temperature Quenching Cross Sections for Nitric Oxide Laser-Induced Fluorescence Measurements*, J. Chem. Phys., Vol. 98 (5), pp 3850-3865, 1993

Dyer T M, *New Experimental Techniques for In-Cylinder Engine Studies*, SAE 850396, 1985

Earp R K, *Determination of the Position of Knock Using Pressure Transducer and Modelling Techniques*, MSc Thesis, Cranfield University, 1994

Eckbreth A C, *Laser Diagnostics for Combustion, Temperature and Species*, Abacus Press, 1987

Emmenthal K D, Grabe H J, Oppermann W, Schäpertöns H, *Motor mit Benzin-Direkteinspritzung und Verdampfungskühlung für das VW-Forschungsauto IRVW-Futura*, MTZ Motorentechnische Zeitschrift, Vol. 50, Nr. 9, pp 426 - 430, 1989

Engleman R, Rouse P E, Peek H M, Baiamonte V D, *Beta and Gamma Band Systems of Nitric Oxide*, LA-4364 UC-34 Physics TID-4500, Los Alamos Scientific Laboratory, NM, 1970

Farrugia N, *Vector-Scalar Imaging in Combustion Using PIV and LIF*, PhD Thesis, Cranfield University, 1996

Fansler T D, French D T, Drake M C, *Fuel Distribution in a Firing Direct Injected SI-Engine Using Laser Induced Fluorescence Imaging*, SAE 950110, 1995

Felton P G, Mantzaras J, Bomse D S, Woodin R L, *Initial Two-Dimensional Laser Induced Fluorescence Measurements of OH Radicals in an Internal Combustion Engine*, SAE 881633, 1988

Foster D E, *Velocity Measurements in the Wall Boundray Layer of a Spark-Ignited Research Engine*, SAE 872105, 1987

Galliot F, Cheng W K, Cheng C O, Stzenderowicz M, Heywood J B, Collings N, *In-Cylinder Measurements of Residual Gas Concentration in a SI-Engine*, SAE 900485, 1990

Gatowski J A, Heywood J B, *Effects of Valve Shrouding and Squish on Combustion in a SI-Engine*, SAE 852093, 1985

Gatowski J A, Heywood J B, Deleplace C, *Flame Photographs in a SI-Engine*, Combustion and Flame Vol. 56, p. 71-81, 1984

Greenhalgh D A, *Inelastic Scattering Laser Diagnostics; CARS, Planar LIF and Planar LII*, Chapter from "Optical Diagnostics for Flow Processes" (Eds.: Lading, Buchave, Wigley), Plenum Press, N.Y., 1994

Greenhalgh D A, *Quantitative CARS Spectroscopy*, Chapter from "Advances in Non-linear Spectroscopy" (Eds. Clarke, Hester), J. Wiley & Sons, London, 1988

Gülder Ö L, *Correlations of Laminar Combustion Data for Alternative SI-engine Fuels*, SAE 841000, 1984

Haagensen S, Valland H, Almas T, *Spark Ignition engine Cyclic Variability Measurements using Optical Probes*, I.Mech.E Seminar 'Experimental Methods in Engine Research and Development',London, pp 7 - 18, 1991

Hadded O, Denbratt I, *Turbulence Characteristics of Tumbling Air Motion in 4-Valve SI-Engines and their correlation with Combustion Parameters*, SAE 910478, 1991

Hall M J, Bracco F V, *A Study of Velocities and Turbulence Intensities Measured in Firing and Motored Engines*, SAE 870453, 1987

Hamai K, Kawajiri H, Takashi I, Nakai M, *Combustion Fluctuation Mechanism Involving Cycle-To-Cycle Spark Ignition Variation due to Gas Flow Motion in SI-Engines*, Twenty-first Symposium (International) on Combustion, pp. 505-512, 1986

Hansen D A, Lee E K C, *Radiative and Nonradiative Transition in the First Excited Singlet State of Symmetrical Methyl-Substituted Acetones*, J. Chem. Phys., Vol. 62, No. 1, 1975

Hardalupas Y, Taylor AMKP, Whitelaw J H, Ishii K, Miyano H, Urata Y, *Influence of Injection Timing on In-Cylinder Fuel Distribution in a Honda VTEC-E Engine*, SAE 950507, 1995

Harding S C, *Investigation of Mixing and Combustion in an Optical LPP Combuster*, PhD Thesis Cranfield University, to be published 1996

Heitor M V, Starner S H, Taylor AMKP, Whitelaw J H, *Velocity, Size and Turbulent Flux Measurement by Laser-Doppler Velocimetry*, Chapter from "Instrumentation for Flows with Combustion" (Ed.: AMKP Taylor), Academic Press Ltd., 1993

Heywood J B, *Internal Combustion Engine Fundamentals*, McGraw-Hill, 1988

Horie K, Nishizawa K, Ogawa T, Akazaki S, Miura K, *The Development of a High Fuel Economy and High Performance Four-Valve Lean Burn Engine*, SAE 920455, 1992

Hu Z, Vafidis C, Whitelaw J H, Chapman J, Head R A, *Correlation between In-Cylinder Flow, Performance and Emissions Characteristics of a Rover Pentroof Four-Valve Engine*, C448/026 IMechE, 1992

Inoue T, Matsushita S, Nakanishi K, Okano H, *Toyota Lean Combustion System - 3rd Generation System*, SAE 930873, 1993

Iwamoto Y, Danno Y, Hirako O, Fukui T, Murakami N, *The 1.5-Liter Vertical Vortex Engine*, SAE 920670, 1992

Johansson B, Neij H, Aldén M, Juhlin G, *Investigations of the Influence of Mixture Preparation on Cyclic Variations in a SI-Engine Using Laser Induced Fluorescence*, SAE 950108, 1995

Johnston S C, *Precombustion Fuel/Air Distribution in a Statified Charge Engine using Laser Raman Spectroscopy*, SAE 790433, 1979

Johnston S C, Robinson C W, Rorke W S, Smith J R, Witze P O, *Application of Laser Diagnostics to an Injected Engine*, SAE 790092, 1979

Kadota T, Zhao F, Tsuzaki H, *Mixture Strength Measurements in the Combustion Chamber of a SI-Engine via Rayleigh Scattering (2nd Report, Results for Liquid Fuel Injection)*, JSME International Journal Series II Vol. 34 No. 1 pp 87-94, 1991

Kadota T, Zhao F, Miyoshi H, *Mixture Strength Measurements in the Combustion Chamber of a SI-Engine via Rayleigh Scattering (3rd Report, Results in the Motored Engine)*, JSME International Journal Series II Vol. 34 No. 1 pp 95-102, 1991

Kadota T, Toyomi S, Memon M, Sumida O, *Mixture Strength Measurements in the Combustion Chamber of a SI-Engine via Rayleigh Scattering*, JSME International Journal Series II Vol. 32 No. 1 pp 134-141, 1989

Keck J C, Heywood J B, Noske G, *Early Flame Development and Burning Rates in Spark Ignition Engines and Their Cyclic Variability*, SAE 870164, 1987

Kiyota Y, Akishino K, Ando H, *Concept of Lean Combustion by Barrel-Stratification*, SAE 920678, 1992

Kume T, Iwamoto Y, Iida K, Murakami M, Akishino K, Ando H, *Combustion Control Technologies for Direct Injection SI Engine*, SAE 960600, 1996

Kuratle R, Märki B, *Influencing Parameters and Error Sources during Indication on Internal Combustion Engines*, SAE 920233, 1992

Kychakoff G, Knapp K, Howe R D, Hanson R K, *Flow Visualisation in Combustion Gases Using Nitric Oxide Fluorescence*, AIAA Journal, Vol. 22, pp 153 - 154, 1984

Lawrenz W, Köhler J, Meier F, Stolz W, Wirth R, Bloss W, Maly R R, Wagner E, Zahn M, *Quantitative 2D LIF Measurements of Air/Fuel Ratios during the Intake Stroke in a Transparent SI-Engine*, SAE 922320, 1992

Le Coz J F, *Cycle-to-Cycle Correlations between Flow Field and Combustion Initiation in an SI-Engine*, SAE 920517, 1992

Lebel M, Cottereau M J, *Study of the Effect of the Residual Gas Fraction on Combustion in a SI Engine Using Simultaneous CARS Measurements of Temperature and CO_2 Concentration*, SAE 922388, 1992

Lempert W, Diskin G, Kumar V, Glesk I, Miles R, *Two -Dimensional Imaging of Molecular Hydrogen in a H2-Air Diffusion Flame Using Two-Photon Laser_Induced Fluorescence*, Opt. Lett., Vol 16, 1991

Liou T M, Santavicca D A, *Cycle Resolved Turbulence Measurements in a Ported Engine with and without Swirl*, SAE-Paper 830419, 1983

Long M B, *Multidimensional Imaging in Combusting Flows by Lorenz-Mie, Rayleigh and Raman Scattering*, Chapter from "Instrumentation for Flows with Combustion" (Ed.: AMKP Taylor), Academic Press Ltd., 1993

zur Loye A O, Santavicca D A, *Temperature and Concentration Measurements in an Internal Combustion Engine Using Laser Raman Spectroscopy*, American Institute of Aeronautics & Astronautics No. AIAA-83-1551, 1983

Lozano A, Yip B, Hanson R K, *Acetone: A Tracer for Concentration Measurements in Gaseous Flows by Planar Laser-Induced Fluorescence*, Experiments in Fluids, Vol. 13, pp 369 - 376, 1992

Lucht R P, Teets R E, Green R M, Palmer R E, Ferguson C R, *Unburned Gas Temperatures in an Internal Combustion Engine. I: Cars Temperature Measurements*, Combust. Sci. and Tech., Vol. 55, pp 41 - 61, 1987

Marie J J, Cottereau M J, *Single-Shot Temperature Measurements by Cars in an I.C. Engine for Normal and Knocking Conditions*, SAE 870458, 1987

Matsui K, Tanaka T, Ohigashi S, *Measurement of Local Mixture Strength at Spark Gap of SI-Engines*, SAE 790483, 1979

Matsushita S, Inoue T, Nakanishi K, Kato K, Kobayashi N, *Development of the Toyota Lean Burn Combustion System*, SAE 850044, 1985

McBride B J, Sanford G, Reno M A, *Coefficients for Calculating Thermodynamic and Transport Properties of Individual Species*, NASA Technical Memorandum 4513, 1993

McMillin B K, Palmer J L, Hanson R K, *Two-Dimensional Temperature Measurements of Shock Tube Flows Using Planar Laser-Induced Fluorescence Imaging of Nitric Oxide*, AIAA 22nd Fluid Dynamics, Plasma Dynamics & Lasers Conference, 1991

Merdjani S, Sheppard C G W, *Gasoline Engine Cycle Simulation Using the Leeds Turbulent Burning Velocity Correlations*, SAE 932640, 1993

Metaghalchi M, Keck J C, *Burning Velocities of Mixtures of Air with Methanol, Isooctane and Indolene at High Pressure and Temperature*, Combustion and Flame 48, pp 191-210, 1982

Mikulic L A, Quissek F, Fraidl G K, Carstensen H, *Sequentielle Einspritzstrategien für verbrauchsoptimierte Ottomotorkonzepte*, MTZ Motorentechnische-Zeitschrift 51 7/8, pp 286-293, 1990

Morley C, *The Application of Laser Fluorescence Detection of Species in Atmospheric Pressure Flames*, Combustion and Flame, Vol. 47, 1982

Neij H, Johansson B, Aldén M, *Development and Demonstration of 2D-LIF for Studies of Mixture Preparation in SI Engines*, Combustion and Flame, Vol. 99, pp 449 - 457, 1994

Nino E, Gajdeczko B F, Felton P G, *Two-Colour Particle Image Velocimetry in an Engine With Combustion*, SAE 930872, 1993

Ohyama Y, Ohsuga M, Kuroiwa H, *Study on Mixture Formation and Ignition Process in Spark Ignition Engine using Optical Combustion Sensor*, SAE 901712, 1990

Paul P H, Lee J P, Hanson R K, *Molecular Velocity Imaging of Supersonic Flows Using Pulsed Planar Laser Induced Fluorescence of NO*, Opt. Lett., Vol. 14, pp 417 - 419, 1989

Pischinger S, Heywood J B, *How Heat Losses to the Spark Plug Electrodes Affect Flame Kernel Development in an SI-Engine*, SAE 900021, 1990

Pischinger S, Heywood J B, *A Study of Flame Development and Engine Performance with Breakdown Ignition Systems in a Visuslization Engine*, SAE 880518, 1988

Pundir B P, Zvonow V A, Gupta C P, *Effect of Charge Non-Homogeneity on Cycle-by-Cycle Variations in Combustion in SI-Engines*, SAE 810774, 1981

Quader A A, *The Axially-Stratified-Charge Engine*, SAE 820131, 1982

Quader A A; *What Limits Lean Operation in SI-Engines - Flame Initiation or Flame Propagation?*, SAE 760760, 1976

Quader A A; *Lean Combustion and the Misfire Limit in SI-Engines*, SAE 741055, 1974

Rask R B, *Laser Doppler Anemometer Measurements in an Internal Combustion Engine*, SAE 790094, 1979

Reeves M, Garner C P, Dent J C, Halliwell N A, *Particle Image Velocimetry Measurements of Barrel Swirl in a Production Geometry Optical IC Engine*, SAE 940281, 1994

Reisel J R, Carter C D, Laurendeau N M, *Laser-Saturated Fluorescence Measurements of Nitric Oxide in Laminar, Flat, $C_2H_6/O_2/N_2$ Flames at Amospheric Pressure*, Combust. Sci. and Tech., Vol. 91, pp 271-295, 1993

Reuss D L, Adrian R J, Landreth C C, French D T, Fansler T D, *Instantaneous Planar Measurements of Velocity and Large-Scale Vorticity and Strain Rate in an Engine Using Particle-Image Velocimetry*, SAE 890616, 1989

Rhodes D B, Keck J C, *Laminar Burning Speed Measurements of Indolene-Air-Diluent Mixtures at High Pressures and Temperatures*, SAE 850047, 1985

Seitzman J M, Hanson R K, *Planar Fluorescence Imaging in Gases*, Chapter from "Instrumentation for Flows with Combustion" (Ed.: AMKP Taylor), Academic Press Ltd., 1993

Seitzman J M, Haumann J, Hanson R K, *Quantitative Two-Photon LIF Imaging of Carbon Monoxide in Combustion Gases*, Applied Optics, Vol. 26, No. 14, pp 2892 - 2899, 1987

Seitzman J M, Kychakoff G, Hanson R K, *Instantaneous Temperature Field Measurements Using Laser-Induced Fluorescence*, Optics Letters, Vol. 10, No. 9, pp 439 - 441, 1985

Shimizu R, Seiichi M, Furuno S, Murayama M, Kojima S, *Measurement of Air-Fuel Mixture Distribution in a Gasoline Engine Using LIEF Technique*, SAE 922356, 1992

Shoji H, Saima A, Sasao T, Arai J, Ikeda S, Iwasaki M, *Clarification of the Combustion Reaction Mechanism in a SI Engine by Spectroscopic Analysis*, JSAE Review, Vol. 13, No. 2, pp 4 - 9, 1992

Shoji H, Saima A, Sasao T, Arai J, Ikeda S, Iwasaki M, *The Behaviour of Radical Luminescence Intensity in a SI Engine*, JSAE Review, Vol. 13, No. 1, pp 14-19, 1992

Sleightholme G R, *In-Cylinder Measurement of Charge Inhomogeneity in a SI-Engine*, SAE 900484, 1990

Spicher U, Krebs R, *Optical Fiber Technique as a Tool to Improve Combustion Efficiency*, SAE 902138, 1990

Suntz R, Becker H, Monkhouse P, Wolfrum J, *Two-Dimensional Visualization of the Flame Front in an Internal Combustion Engine by Laser-Induced Fluorescence of OH Radicals*, Appl. Phys. B 47, pp 287-293, Springer Verlag 1988

Swords M D, Kalghatgi G T, Watts A J, *An Experimental Study of Ignition and Flame Development in a Spark Ignited Engine*, SAE Paper 821220, 1982

Sztenderowicz M L, Heywood J B, *Mixture Nonuniformity Effects on S.I. Engine Combustion Variability,* SAE Paper 902142, 1990

Tagalian J, Heywood J B, *Flame Initiation in a Spark-Ignition Engine*, Combustion and Flame 64, pp 243-246, 1986

Tait N P, *Development of Planar Laser Diagnostic Techniques for Fuel and Soot Imaging in Combustion Application*, PhD Thesis, Cranfield University, 1994

Tait N P, Greenhalgh D A, *PLIF Imaging of Fuel Fraction in Practical Devices and LII Imaging of Soot*, Ber. Bunsenges. Chem. 97, No. 12, 1993

Tait N P, Greenhalgh D A, *2D Laser Induced Fluorescence Imaging of Parent Fuel Fraction in Nonpremixed Combustion*, Twenty-Fourth Symposium (International) on Combustion/The Combustion Institute, pp 1621-1628, 1992

Vafidis C, Vorropoulos G, Whitelaw J H, *Effects of Intake Port and Combustion Chamber Geometry on In-Cylinder Turbulence in a Motored Reciprocating Engine*, Symp. on Fluid Flow Heat Transfer in Reciprocating Machinery, ASME FED, Vol. 62, pp 9 - 15, 1987

Williams D R, Gover M P, *The Effect of Variations in Local Air Fuel Ratio on Cyclic Variability in a Firing Production Engine*, Procedings pp 143-150 of IMechE Seminar on Methods in Engine Research and Development, London, 1991

Winkelhofer E, Fraidl G K, Plimon A, *Monitoring of Gasoline Fuel Distribution in a Research Engine*, Proc. Instn. Mech. Engrs. Vol. 206 p. 107-115, 1992

Witze P O, Hall M J, Wallace J S, *Fibre-Optic Instrumented Spark Plug for Measuring Early Flame Development in SI-Engines*, SAE 881638, 1988

Witze P O, *The Effect of Spark Location on Combustion in a Variable Swirl Engine*, SAE 82004, 1982

Wurster W, Gruden D, *Die Verbrennung im Otto- und Dieselmotor mit direkter Einspritzung*, 9. Internationales Wiener Motorensymposium 1988, Fortschritt-Berichte VDI-Verlag Reihe 12 Nr. 99, 1988

Yamada T, Hayakawa N, Kami Y, Kawai T, *Universal Air-Fuel Ratio Heated Exhaust Gas Oxygen Sensor and further Applications*, SAE 920234, 1992

Yamaguchi J, *Mitsubishi DI Gasoline Engine Prototype*, Automotive Engineering, Vol. 103, No. 9, pp 25 - 29, 1995

Young M B; *Cyclic Dispersion in the Homogeneous-Charge SI-Engine - a Literature Survey*, SAE-Paper 810020, 1981

List of Papers

Berckmüller M, Tait N P, Greenhalgh D A, *The Time History of the Mixture Formation Process in a Lean Burn Stratified-Charge Engine*, Transactions of the SAE International Fuels & Lubricants Meeting & Exposition, San Antonio, Texas, 1996

Berckmüller M, Tait N P, Greenhalgh D A, *A Study of the Influence of Local Fuel Concentration on the Performance of a Lean Burn Engine*, Proceedings of the 'Joint Meeting of the Portugese, British, Spanish, and Swedish Sections of the Combustion Institute', Funchal, Madeira, 1996

Berckmüller M, Tait N P, Lockett R D, Greenhalgh D A, Ishii K, Urata Y, Umiyama H, Yoshida K, *In-Cylinder Crank-Angle-Resolved Imaging of Fuel Concentration in a Firing SI Engine Using Planar Laser-Induced Fluorescence*, Twenty-Fifth Symposium (International) on Combustion/ The Combustion Institute, pp. 155-156, 1994

Berckmüller M, Tait N P, Greenhalgh D A, Ishii K, Urata Y, Umiyama H, Yoshida K, *In-cylinder Imaging of Fuel Concentration using Planar Laser-Induced Fluorescence*, C485/027 IMechE, 1994